

©Copyright 2023

Meredith Durbin

# Empirical Approaches to the Near-Infrared Tip of the Red Giant Branch

Meredith Durbin

A dissertation  
submitted in partial fulfillment of the  
requirements for the degree of

Doctor of Philosophy

University of Washington

2023

Reading Committee:

Julianne J. Dalcanton, Chair

Rachael L. Beaton

Benjamin F. Williams

Program Authorized to Offer Degree:

Astronomy



University of Washington

**Abstract**

Empirical Approaches to the Near-Infrared Tip of the Red Giant Branch

Meredith Durbin

Chair of the Supervisory Committee:

Julianne J. Dalcanton

Department of Astronomy

The infrared tip of the red giant branch (IR-TRGB) is a powerful tool for measuring distances to galaxies in the local Universe. However, establishing its absolute “anchor” with sufficient precision and accuracy has proved challenging due to lingering sources of systematic uncertainty in both theoretical predictions and empirical calibrations. Here I describe three studies aimed at improving observational constraints on the IR-TRGB. First, I develop a computational method for self-consistently measuring TRGB magnitudes and colors, and the covariance thereof, in multiwavelength stellar photometry catalogs. Traditional detection methods either marginalize over color, or else rely on assuming a fiducial color dependence, both of which may result in different stellar populations dominating the TRGB signal at different wavelengths. Next, I explore two complementary approaches to reconciling observations of the IR-TRGB as measured with ground- and space-based instruments respectively. The former are impacted by absorption features in Earth’s atmosphere, where the latter are not. Furthermore, there is an extremely limited range of magnitudes at which current facilities can achieve the requisite data quality from both locations. To this end, I derive transformation equations between respective photometric systems using synthetic photometry of observed stellar spectra, and then present initial results from a three-year observing campaign designed to directly compare space- and ground-based observations of bright RGB stars in the Magellanic Clouds.

# TABLE OF CONTENTS

	Page
List of Figures . . . . .	iii
List of Tables . . . . .	xi
Glossary and Acronyms . . . . .	xii
Chapter 1: Introduction . . . . .	1
1.1 Cosmological Context . . . . .	1
1.2 The Cosmic Distance Ladder . . . . .	2
1.3 The Tip of the Red Giant Branch as a Distance Indicator . . . . .	3
1.4 Thesis outline . . . . .	4
Chapter 2: MCR-TRGB: A Multiwavelength-Covariant, Robust Tip of the Red Giant Branch Measurement Method . . . . .	8
2.1 Introduction . . . . .	8
2.2 Data . . . . .	13
2.3 TRGB Measurement . . . . .	24
2.4 Results . . . . .	31
2.5 Discussion . . . . .	45
2.6 Conclusions and Future Work . . . . .	58
Chapter 3: Empirical <i>HST</i> -2MASS Filter Transformations: I. Synthetic Photometry . . . . .	60
3.1 Introduction . . . . .	60
3.2 Data . . . . .	61
3.3 Synthetic Photometry . . . . .	73
3.4 Results . . . . .	80
3.5 Discussion . . . . .	83

3.6	Conclusions . . . . .	92
Chapter 4:	Empirical <i>HST</i> -2MASS Filter Transformations: II. A Direct Calibration in the Magellanic Clouds . . . . .	93
4.1	Observations, data reduction, and photometry . . . . .	98
4.2	Results . . . . .	116
4.3	Discussion . . . . .	126
4.4	Conclusions . . . . .	133
Chapter 5:	Conclusions . . . . .	135
5.1	Summary . . . . .	135
	Bibliography . . . . .	137
Appendix A:	MCR-TRGB: Tests on Artificial Data . . . . .	171
A.1	Luminosity function sampling . . . . .	172
A.2	Metallicity . . . . .	174
A.3	Photometric uncertainties . . . . .	175
A.4	XDGMM vs. Sobel edge detection . . . . .	176
A.5	Adjustments to measurements . . . . .	177
Appendix B:	MCR-TRGB: Figure Sets . . . . .	179
Appendix C:	Synthetic Photometry Table . . . . .	218
Appendix D:	Extinction Map Comparisons . . . . .	270

# LIST OF FIGURES

Figure Number		Page
2.1	Footprints of the <i>HST</i> observations originally presented in D09 and D12, which we reanalyze in this work. ACS/WFC footprints are shown by thin white lines, and WFC3/IR footprints are in thick orange. Background images are PanSTARRs $z + g$ for all targets except NGC 300 & NGC 7793-HALO-6, which use DSS2. All background images were retrieved through the HiPS thumbnail service provided by the Université de Strasbourg. . . . .	11
2.2	Distributions of the RMS scatter of alignment residuals for F814W, F110W, and F160W. Both near-IR filters have a residual scatter on the order of $0.025''$ , or $\sim 0.2$ WFC3/IR pixels. In F814W the alignment RMS has a peak closer to $0.01''$ , but there is a long tail of images with higher scatter, likely due to variations in exposure depth and source densities. . . . .	15
2.3	Hess diagram of input AST photometry in the near-IR. The densest portions (orange to yellow) are from the CMDs, whereas the uniform sampling is purple. . . . .	20
2.4	Left panels: NIR Hess diagrams of three galaxies in our sample, with the selections of stars included in our surface density calculations highlighted. Right: corresponding stellar surface density maps for each target. All density maps are scaled to the same limits (0 to 1.5 RGB stars per square arcsecond) to highlight the range of stellar densities in our sample. Gaps in the density images show where contaminating sources such as foreground stars and background galaxies were rejected. The complete figure set (23 images) is available in the online journal. . . . .	21
2.5	Changes in photometry between D12 and this work for HS117 (top), NGC 300 (middle), and NGC 4163 (bottom), with the D12 magnitude on the x-axis and $\Delta m$ on the y-axis. The color-coding indicates the DOLPHOT crowding parameter of the new photometry, which is the number of magnitudes subtracted from the initial measurement due to neighboring sources. The rolling mean and median are shown by the solid and dashed lines respectively. The complete figure set for both F110W and F160W (46 images) is available in the online journal. . . . .	23

2.6	A demonstration of filter-by-filter RGB selections for NGC4163. Each of the 9 panels contains a color-magnitude combination used to determine $P(\text{RGB})$ for stars in the color-magnitude range. The points in each panel are color-coded by the final probability as indicated on the color-bar. The best-fit PARSEC synthetic RGB in each combination is shown. The complete figure set (23 images) is available in the online journal. . . . .	25
2.7	Tip star selection with edge detection for three demonstrative galaxies in our sample. From top to bottom, HS117, NGC 300, and NGC 4163. For each galaxy, three panels are shown, from left to right, the CMD of high-probability RGB stars, the raw (gray) and smoothed (black) luminosity function, and the Sobel edge response ( $\eta$ ). The initial magnitude of the TRGB is identified as the magnitude at $\eta_{\text{max}}$ , which is identified as the dashed line in each panel. TRGB candidate stars are selected within the blue band, the width of which is determined by the photometric uncertainty at the tip and by the number of stars on the upper RGB as described in the text. The complete figure set (23 images) is available in the online journal. . . . .	30
2.8	Results of XDGMM fits to candidate TRGB stars for HS117 (top), NGC 300 (middle), and NGC 4163 (bottom). For each galaxy the fits are shown for the following color-magnitude combinations: F814W, F814W–F160W (left), F110W, F814W–F110W (center), and F160W, F110W–F160W (right). The solid horizontal lines in each panel identify the mean magnitudes of the tip from XDGMM (which are typically very close to the Sobel-detected edge), and the overplotted ellipses show the 95% color-magnitude confidence regions of the two-dimensional fitted tip. We note that because this method uses a set of candidate tip stars selected based on their magnitudes in a single band (either F814W or F110W), the 2-D ellipses may not follow the visual impression of the tip in other bandpasses. This is especially apparent when the color-width of the RGB is of order the color uncertainties, which is typical in the NIR. . . . .	32
2.9	Comparison of the revised tip F160W apparent magnitudes and F110W – F160W colors from this work (blue points) to those of D12 (orange points). Arrows indicate per-target correspondence between D12 and the new measurements. The blue ellipses show the 68% confidence regions on the measurements of this paper from XDGMM fitting, and the bottom right errorbars indicate the median photometric uncertainties in color and magnitude for an individual star. For NGC 300 (unfilled points) we plot $M_{\text{F160W}} + 1$ rather than $M_{\text{F160W}}$ , as it is $\sim 1$ mag brighter than the remainder of the sample. On average, our mean color-magnitude tip results are redder and slightly fainter than D12. . . . .	33

2.10	Left: changes in the $M_{\text{F160W}}$ tip magnitudes compared to changes in the $M_{\text{F110W}}$ TRGB magnitudes between this work and D12. Right: changes in the $M_{\text{F160W}}$ tip magnitudes between this work and D12 against the NIR color measured in this work. Both panels show histograms with overlaid kernel density estimates of the marginal distributions of the quantities on each axis, linear fits with shaded confidence intervals, and scale bars with typical photometric uncertainties. . . . .	34
2.11	Comparison of D12 color-color relation to the TRGB color-color relation determined in this work, with $\text{F110W} - \text{F160W}$ against $\text{F814W} - \text{F110W}$ (left) and $\text{F814W} - \text{F160W}$ (right). As in Figure 2.9, orange points are from D12, blue points are from this work, arrows connect the corresponding results, and the blue shading indicates our two-dimensional uncertainties from XDGMM. We show a linear fit to the D12 values (as done in that work) and a generalized logistic fit to values from this work to highlight the changes in morphology in our new color-color relations. . . . .	36
2.12	Comparison of revised NIR color-absolute magnitude relations to D12 with revised absolute magnitudes derived using the same distances as in D12. Blue points are values from the current work and orange points are from D12. The corresponding color-coded lines show linear fits to each dataset and the shaded regions show 95% confidence intervals. Again, we see that our results are slightly redder and slightly fainter than D12 using their distances. This color-color relation is distance-independent. . . . .	39
2.13	Revised absolute tip magnitudes using distance moduli calibrated to $M_{\text{F814W}}$ versus $\text{F814W} - \text{F160W}$ derived from synthetic photometry from the MIST (orange) and PARSEC (green) model suites. Each solid line represents a set of theoretical tip star colors and absolute magnitudes at a single age. In the left panel, we tie the observed colors to an absolute magnitude in either isochrone set to determine $\mu_{\text{F814W}}$ . On the right, we use $\mu_{\text{F814W}}$ to determine $M_{\text{TRGB}}^{\text{F160W}}$ and plot against our $\text{F110W} - \text{F160W}$ color; we find that these measurements are systematically offset from the corresponding isochrone models. . . . .	42
2.14	We invert the demonstration of Figure 2.13. In the left panel, we tie the observed colors to an absolute magnitude in either isochrone set to determine $\mu_{\text{F160W}}$ . On the right, we use $\mu_{\text{F160W}}$ to compute $M_{\text{TRGB}}^{\text{F814W}}$ and plot against our $\text{F814W} - \text{F160W}$ color; we again find that our measurements are systematically offset from the corresponding isochrone models. Taken with Figure 2.13, this suggests that distance moduli calibrated to models in one band will systematically mispredict the corresponding tip behavior in other bands. . . . .	43

2.15	Histograms and overlaid biweight kernel density estimates of $\Delta\mu$ , where $\Delta\mu$ is the difference between distance moduli derived in this work and the distance moduli used in D12. The top panel shows $\Delta\mu$ using distance moduli calibrated to $M_{F814W}$ and the bottom shows $\Delta\mu$ using distance moduli calibrated to $M_{F160W}$ . These differences are much larger than those measured using the same distances (Figure 2.12) and thus can be interpreted as differences between model predictions of tip magnitudes. . . . .	45
2.16	As in Figure 2.13, we infer absolute F160W magnitudes via adopted F814W absolute magnitudes. Here the F814W absolute magnitudes are calibrated to the F814W vs. F606W–F814W $QT$ relation presented by Jang & Lee (2017b) for the subset of our sample with F606W coverage. We overplot MIST (orange) and PARSEC (green) synthetic photometry for comparison. Left: The $QT$ relation with adopted $M_{F814W}$ values. Center: Inferred $M_{F160W}$ vs. F110W–F160W. Right: Distance-independent F110W–F160W vs. F606W–F814W color-color plot. . . . .	50
2.17	Left: Bolometric luminosity vs. effective temperature for the MIST (orange) and PARSEC (green) model tip stars used in this work (ages 8 - 14 Gyr and $-2 \leq [\text{Fe}/\text{H}] \leq -0.25$ dex). PARSEC luminosities are found to be consistently $\sim 1.1$ times brighter than MIST at the same age and metallicity. Center: (F110W–F160W) vs. (F814W–F110W) color-color plots for MIST and PARSEC tip star predictions. Right: Color-color results of this work overlaid on MIST and PARSEC predictions. . . . .	52
3.1	Schematic comparison of near-infrared stellar spectra (black lines, Verro et al. 2022a) and their integrated fluxes (colored points, plotted at respective effective wavelengths) for three broad classes of cool and luminous giants. These include non-pulsating AGB and upper RGB stars (upper three), and thermally pulsating carbon-rich (center) and oxygen-rich (lower) AGB stars respectively. Transmission curves for the 2MASS $JHK_S$ and <i>HST</i> F110W, F160W bandpasses are shown as filled curves at the bottom, and regions with significant atmospheric telluric absorption are marked by gray vertical bands. . . . .	62
3.2	Fractional distance uncertainties as a function of distance (linear on the lower axis, modulus on the upper) for all library stars. Colors and symbols correspond to host objects, which are Galactic field or bulge stars, open and globular clusters, and the Magellanic Clouds. Note that many of the distance uncertainties are asymmetric; we show the mean values here. . . . .	67

3.3	Sky maps of our final cross-library sample, color coded by adopted $E(B - V)$ values. We show all-sky maps in Galactic coordinates for Milky Way stars in three distance bins of 0-0.1 kpc, 0.1-1 kpc, and 1-20 kpc. Magellanic Cloud stars are shown in separate insets in the lower right in equatorial coordinates.	70
3.4	Summary stellar properties (effective temperature $T_{\text{eff}}$ , metallicity $[\text{Fe}/\text{H}]$ , and surface gravity $\log(g)$ ) of the merged spectral libraries. We note that these literature measurements are extremely heterogenous, and these data are used primarily to understand the ranges of stellar properties over which our library can provide insight. Stars with known photometric variability are plotted in orange, whereas stars not known to be variable are shown in blue. . . . .	72
3.5	Differences between observed and synthetic magnitudes in <i>Gaia</i> (E)DR3 $BP$ , $G$ , $RP$ (left) and 2MASS $JHK_S$ (right) as functions of observed magnitude for select CALSPEC stars. Blue points indicate empirical spectrophotometry (available for effectively all CALSPEC stars in the optical), and orange indicates spectra extrapolated from theoretical models (e.g. missing WFC3/IR and/or NICMOS data), which we exclude from calculations and show only for reference. Blue dashed lines and solid bands show weighted means and standard deviations of the photometric offsets, as reported in Table 3.2. . .	75
3.6	Left: absolute $H$ vs. $J - K_S$ CMD of all available 2MASS photometry for our full sample. Here, dark blue points indicate sources with high-quality 2MASS photometry in all bands (“Qf1g=AAA”), and light blue indicates non-optimal quality flags in one or more bands. Center: the same CMD for our synthetic photometry suite. Blue points indicate spectra with no data caveats. Orange indicates CALSPEC library stars that were observed only with STIS, where the spectra are filled in outside the STIS wavelength range ( $\gtrsim 1 \mu\text{m}$ ) using theoretical spectra. Green indicates XSL spectra that were corrected for slit loss via spline fitting (Verro et al. 2022b), and red indicates XSL spectra uncorrected for slit loss. Right: The same in $J - H$ vs. $J - K_S$ color-color space. . . . .	77
3.7	Color-magnitude diagrams of our final fitting sample (left) and stars excluded from fitting (right), colormapped by literature effective temperature. . . . .	79
3.8	Filter transformation fits to $F110W - J$ (top row), $F125W - J$ (center row), and $F160W - H$ (bottom row) as functions of $J - K_S$ , $J - H$ , $F110W - F160W$ , and $F125W - F160W$ color from left to right. Points used in the fitting are shown in dark blue with light blue covariance ellipses. Solid black lines show the resulting piecewise linear transformations with 68% confidence intervals in grey, and dashed black lines mark the breakpoint locations. . . . .	81



3.9	Comparisons to previously published transformations for F125W – $J$ (Riess 2011, upper panel) and F160W – $H$ (lower panel; Riess 2011 in blue, and Dalcanton et al. 2012a in orange). Results of this work are shown in gray. . .	85
3.10	Residuals of our <i>HST</i> -2MASS filter transformations with respect to $J - K_S$ color for our fitting sample (773 spectra of 648 unique stars). Colormaps show relevant stellar parameters where available, including effective temperature $T_{\text{eff}}$ , metallicity $[\text{Fe}/\text{H}]$ , surface gravity $\log(g)$ , and reddening $E(B - V)$ . Reddenings are as described in §3.2.2; all other parameters are adopted as-is from literature sources. . . . .	86
3.11	As Figure 3.10 with respect to $J - H$ color on the $x$ -axis. . . . .	87
3.12	As Figure 3.10, but showing residuals for stars excluded from our fitting sample (424 spectra of 643 unique stars). Note the changes in both $x$ - and $y$ -axis ranges relative to figures 3.10 and 3.11. . . . .	88
3.13	As Figure 3.12, with $J - H$ color on the $x$ -axis. Again, note differences in $x$ - and $y$ -axis ranges between this and previous figures. . . . .	89
3.14	Synthetic 2MASS color-magnitude diagram (left) and filter transformation residuals (center, right) with several subtypes of evolved stars used as primary distance indicators highlighted by color. These include C- and O-rich TP-AGB variables in blue and orange respectively; first-ascent RGB stars in green; RR Lyrae variables in red; and classical Cepheids in pink. Repeat observations of the same stars are connected with solid lines. . . . .	91
4.1	Comparison of imaging data from 2MASS 6X $J$ (left), LCO/FourStar $J$ (center), and <i>HST</i> WFC3/IR F125W (right) of the same field in the Small Magellanic Cloud (SMC_AV_14_1 in our nomenclature). The <i>HST</i> image is a single exposure, whereas 2MASS and FourStar are stacked mosaics. Bright RGB and AGB stars are circled in solid blue and dashed orange respectively, with classifications taken from the OGLE-III catalog of long-period variable stars (Soszyński et al. 2009, 2011). . . . .	96
4.2	Spectral response curves for selected near-infrared wide- and medium-band imaging filters on <i>HST</i> WFC3/IR, 2MASS, LCO/FourStar, and Paranal/VISTA (upper to lower panels). Regions strongly affected by absorption features in Earth’s atmosphere (tellurics) are marked by gray vertical bars, with boundaries taken from Verro et al. (2022a, Table 1). We focus on the wide passbands in this work (F110W, F125W, and F160W on <i>HST</i> , and $JHK_S$ on the ground), and will present additional medium band data (F153M, $J1$ , $J2$ , and $H_S$ ) in a future paper. . . . .	97

4.3	Locations of all pure parallel <i>HST</i> pointings obtained as part of this work (white points), overlaid on the <i>Gaia</i> DR3 source density map in the vicinity of the Magellanic Clouds (Gaia Collaboration et al. 2022a). The actual WFC3/IR footprints are smaller on the sky than the size of the markers. . . . .	102
4.4	Per-exposure RMS scatter of <b>TweakReg</b> astrometric solutions relative to <i>Gaia</i> DR3, in units of WFC3/IR pixels (plate scale $0.13'' \text{ pixel}^{-1}$ ). Scatter points and marginal density plots are color-coded by filter. . . . .	109
4.5	Median offsets between 2MASS and raw FourStar magnitudes as a function of airmass, colored by the date of the FourStar observations. . . . .	114
4.6	Fractions of sources in our <i>HST</i> photometry with matches in 2MASS 6X (blue), VMC (orange), and FourStar (green) catalogs. . . . .	116
4.7	Color-magnitude diagrams of our complete <i>HST</i> catalogs in the Large (left) and Small (right) Magellanic Clouds in the F110W, F110W–F160W plane. Stars that saturate in the first read in F110W (down to just above 14th magnitude) are marked with large points, and unsaturated stars with smaller and lighter ones. . . . .	117
4.8	As Figure 4.7, but with F125W on the $y$ axis. Saturation occurs at F125W $\approx 13$ . . . . .	118
4.9	As Figure 4.7, but with F160W on the $y$ axis. Saturation occurs at F160W $\approx 12$ . . . . .	119
4.10	As Figure 4.7 for $H$ , $J - H$ on LCO/FourStar. . . . .	120
4.11	As Figure 4.10 for $K_S$ , $J - K_S$ on LCO/FourStar. The population of stars dimmer than $K_S \sim 18.5$ is from a small subset of deeper areas with repeated pointings. . . . .	121
4.12	Color-magnitude diagrams of our final crossmatched sample for the Large (upper row) and Small (lower row) Magellanic Clouds. Catalogs from left to right: WFC3/IR F160W vs. F110W–F160W, FourStar $H$ vs. $J - H$ , and the same bands with 2MASS. Both <i>HST</i> and FourStar reach at least two magnitudes below the red clump ( $H \sim 17$ ), whereas 2MASS stops just short of it. Note the large crowding uncertainties at the 2MASS magnitude limit, where faint stars are upscattered due to photometric blending with nearby sources. . . . .	122
4.13	Differences between FourStar and 2MASS $JHK_S$ bands as functions of FourStar $J - K_S$ and $J - H$ color. . . . .	124
4.14	First-order transformations between FourStar and VMC $JK_S$ bands as functions of FourStar $J - K_S$ color. . . . .	124
4.15	Linear fits to WFC3/IR F110W – $J$ vs. $J - K_S$ for the FourStar, VMC, and 2MASS $J$ and $K_S$ filters (top to bottom). . . . .	128
4.16	As Figure 4.15 for F125W – $J$ vs. $J - K_S$ . . . . .	129

4.17	Linear fits to $F160W - H$ vs. $J - K_S$ for FourStar and 2MASS. . . . .	129
4.18	As Figure 4.17 for $F110W - J$ vs. $J - H$ . . . . .	130
4.19	As Figure 4.17 for $F125W - J$ vs. $J - H$ . . . . .	131
4.20	As Figure 4.17 for $F160W - H$ vs. $J - H$ . . . . .	131
4.21	Comparisons of this work to published transformations for $F125W - J$ (Riess 2011, Durbin et al. in prep, upper panel) and $F160W - H$ (Riess 2011; Dalcanton et al. 2012a, Durbin et al. in prep, lower panel). . . . .	132
A.1	TRGB measurement bias: star counts . . . . .	173
A.2	TRGB measurement bias: color . . . . .	174
A.3	TRGB bias: photometric scatter . . . . .	175
A.4	TRGB measurement bias: XDGMM vs. edge detection . . . . .	176
D.1	Pair plots of $E(B - V)$ measurements for stars common to different extinction catalogs. Stars with high-quality measurements in both $E(B - V)$ maps per pair are shown by blue points, and stars with data quality flags in one or both maps are shown in light gray. Summary data for individual tables are given in Table D.1, and median absolute deviations of pairwise differences in Table D.2. . . . .	273

## LIST OF TABLES

Table Number		Page
2.3	Apparent TRGB magnitudes . . . . .	37
2.4	Absolute TRGB magnitudes from D12 distances . . . . .	41
3.1	Summary of spectral library datasets used in this work. . . . .	63
3.3	Filter transformation results . . . . .	82
4.1	Summary of WFC3/IR and FourStar observations. . . . .	98
4.2	Typical 1-orbit <i>HST</i> exposure sequence . . . . .	103
4.3	<b>hst1pass</b> parameters . . . . .	104
4.4	WFC3/IR zeropoints . . . . .	108
4.5	Typical LCO/FourStar Exposure Sequence . . . . .	111
4.6	Filter transformations: FourStar . . . . .	125
4.7	Filter transformations: <i>HST</i> . . . . .	127
A.1	Applied bias corrections . . . . .	178
C.1	Synthetic 2MASS and <i>HST</i> magnitudes . . . . .	218
D.1	Summary of extinction data sources . . . . .	271
D.2	Median absolute deviations of pairwise $E(B - V)$ differences for 3D maps and single-star fits . . . . .	272

## GLOSSARY AND ACRONYMS

ACS	Advanced Camera for Surveys
AGB	Asymptotic Giant Branch
ANGST	ACS Nearby Galaxy Survey Treasury
<i>HST</i>	<i>Hubble Space Telescope</i>
IR	InfraRed
<i>JWST</i>	<i>James Webb Space Telescope</i>
LMC	Large Magellanic Cloud
MW	Milky Way
NIR	Near-InfraRed
PSF	Point Spread Function
RGB	Red Giant Branch
<i>Roman</i>	<i>Nancy Grace Roman Space Telescope</i>
SMC	Small Magellanic Cloud
TP-AGB	Thermally Pulsing Asymptotic Giant Branch
TRGB	Tip of the Red Giant Branch
WFC3	Wide Field Camera 3

## ACKNOWLEDGMENTS

My sincerest gratitude to a great many people:

Julianne Dalcanton, for the unwavering grace, commitment, and intellectual generosity you have shown not only to me, but to everyone you've led through strange and often difficult times. Also for your impeccable taste in cat pictures and trashy fantasy TV, both of which improved my graduate school experience tremendously.

Rachael Beaton, for going above and beyond as a mentor and collaborator in every way. I am honored to have shared in this work with you, and I look forward to the rest of it.

Ben Williams, for the infinite patience through countless debugging sessions, and for stepping up as my acting UW advisor after Julianne's departure.

The UW Astronomy graduate students whose advocacy and companionship have had no small part in keeping me here: Grace Telford, Tyler Gordon, Dino Bektešević, Rudy Garcia, Nell Byler, Kristen Garofali, Samantha Gilbert-Janizek, Margaret Lazzarini, Bethlee Lindor, Brianna and Myles McKay, Lupita Tovar Mendoza, Debby Tran, Matt Wilde, and Diana Windemuth, among others.

My former colleagues and mentors at STScI, from whom I first learned so many of the skills that have been indispensable to me throughout this work, and who have answered many a helpdesk query from me since then. Special thanks to Susan Kassin for encouragement and mentorship over nearly a decade now.

Crystal Mannfolk, Russell Ryan, and the staff of Las Campanas Observatory for their assistance with the observations of Chapter 4.

My dear friend Tessa Briggs, for years of simply unshakable confidence and support.

And of course my parents, Jane Robinson and Greg Durbin, for everything.

## DEDICATION

To Mom and Dad. Love you to the stars and back.

From the landscape: a sense of scale.

From the dead: a sense of scale.

---

Richard Siken, “Detail of the Woods”



## Chapter 1

# INTRODUCTION

### 1.1 *Cosmological Context*

Nearly a century after its initial theoretical articulation and empirical measurement (Friedmann 1922; Lemaître 1927; Hubble 1929), the quantity currently known as the Hubble or Hubble-Lemaître constant,  $H_0$ , remains a topic of active investigation in contemporary astrophysics and cosmology.  $H_0$  is most simply described as the rate of expansion of the universe; formally, it parameterizes the relationship between distant galaxies’ recessional velocities  $v$ , or the speed at which they appear to be traveling away from us due to expansion of the intervening spacetime (the “Hubble flow”), and their proper distances  $D$  at the time of observation:

$$v = H_0 D \tag{1.1}$$

In the past decade, measurements of  $H_0$  derived from two complementary techniques—one anchored in the “local-” or “late-universe”, and the other in the early universe—have simultaneously reached unprecedented precision at the percent-level, and yet diverged from each other by  $\gtrsim 4\sigma$ , with late-universe values skewing systematically larger (Planck Collaboration et al. 2020; Aiola et al. 2020; Di Valentino et al. 2021; Efstathiou 2021; Freedman 2021; Perivolaropoulos & Skara 2022). This discrepancy may signal either as-yet-unknown physics—the standard  $\Lambda$ CDM cosmological model cannot explain such a change—or else lingering sources of systematic bias that have been heretofore underestimated or unaccounted for in any or all existing measurements. Although many solutions to this conundrum have been proposed, at the time of this writing a broad consensus has yet to emerge in the literature.

## 1.2 The Cosmic Distance Ladder

In academic and popular discourse, the *cosmic distance ladder* serves as an umbrella metaphor for the diverse and ever-expanding assemblage of techniques by which distances to astrophysical objects may be inferred, from Earth’s nearest planetary companions to the farthest observable galaxies. In this paradigm, techniques applicable at different scales are conceived of as rungs, building progressively outwards upon each other from geometric parallaxes in the near field to velocities in the Hubble flow in the far field.

Between these two extremes, a number of “intermediate” rungs rely on classes of astrophysical objects or phenomena most popularly termed “standard candles” (or sometimes, more properly, *standardizable* ones). Broadly, these are objects whose intrinsic luminosities are either a) nearly constant across all members of a class, at least under certain physical and/or observational conditions, or else b) can be reliably constrained using other distance-independent properties. Their utility as distance indicators relies on the inverse square law of radiation, which states that the intensity of electromagnetic output from an isotropically radiating point source—as effectively all stars can be approximated as in this context—decreases proportionally to the square of the distance traveled. Therefore, a standard candle’s distance can be measured solely by comparing its intrinsic (“absolute”) and observed (“apparent”) luminosities. In logarithmic units this is typically articulated as

$$\mu \equiv 5 \log_{10}(D) - 5 \tag{1.2}$$

$$= m - M \tag{1.3}$$

where  $\mu$  is distance modulus,  $D$  is proper distance in parsecs (1 parsec = 3.26 light years),  $m$  is apparent magnitude, and  $M$  is absolute magnitude.

The best-established distance ladder pathway to  $H_0$  employs two such types of standard candles: classical Cepheid variable stars and Type Ia supernovae (SNe Ia). First, distances to galaxies which host both Cepheid variables and SNe Ia are determined from geometric calibrations of nearby Cepheids; these in turn are used to establish an absolute SNe Ia

calibration, which can then finally be applied to distant SNe Ia in the Hubble flow to arrive at  $H_0$  (Freedman et al. 2001; Riess et al. 2009; Burns et al. 2018; Scolnic et al. 2022). The current highest-precision measurement from this method (and the local universe in general) reports a formal uncertainty below 1.5% (Riess et al. 2022).

In recent decades, another standard candle has emerged as a complement to Cepheids, able to provide an independent SNe Ia calibration of comparable precision: the tip of the red giant branch (TRGB, Lee et al. 1993; Freedman et al. 2019, 2020). Two independent estimates with this technique have so far measured  $H_0$  to within 2.5% systematic uncertainty, with values in between those determined from Cepheids and the early universe respectively (although statistical consistencies differ; Freedman et al. 2019, 2020; Freedman 2021; Anand et al. 2022). While these differences are smaller than the overall  $H_0$  tension, understanding sources of variation both *between* and *within* techniques that ultimately calibrate the same quantities is central to establishing the consensus local universe distance scale.

### ***1.3 The Tip of the Red Giant Branch as a Distance Indicator***

Stars of  $\sim 0.8$  to 2 solar masses begin their first “ascent” of the red giant branch (RGB) after they have fused all available hydrogen in their cores into helium. As the star continues fusing hydrogen in a shell around the core, the core contracts until it reaches electron degeneracy, at which point it continues to accumulate mass and heat without changes in volume. Meanwhile, the outer layers expand and cool, causing the star to appear increasingly red and luminous. This process is brought to an abrupt halt once the core reaches  $\sim 10^8$  K and ignites runaway helium fusion via the triple alpha process in an event known as the helium flash. The energy released from the core in this process effectively restructures the star from the inside out, until the degeneracy in the core is lifted and the star settles onto the core helium-burning horizontal branch (Härm & Schwarzschild 1964; Thomas 1967; Salaris et al. 2002; Salaris & Cassisi 2005). In ancient ( $\gtrsim 4$  Gyr) and metal-poor ( $[M/H] \lesssim -0.5$ ) stellar populations, the helium flash occurs only under tightly constrained core temperature and mass conditions, resulting in a near-constant maximum bolometric luminosity on the red giant branch (Serenelli et al.

2017; Beaton et al. 2018). Observationally speaking, this manifests as a sharp decrease in star counts at the bright end of the RGB sequence, which can be statistically detected and measured in external galaxies.

Relative to Cepheids, the TRGB offers two main observational advantages. First, nearly all galaxy types host the ancient, metal-poor populations in which the TRGB method is most effectively applied, whereas Cepheids are much shorter-lived, occurring only in galaxies with recent star formation ( $\lesssim 100$  Myr). Second, Cepheids’ use as distance indicators relies on their periodic variability (Leavitt & Pickering 1912), which requires repeat observations over weeks or months to characterize; the TRGB has no such constraint.

Current applications of the TRGB to  $H_0$  use observations taken at optical wavelengths, where the absolute magnitude of the TRGB is least dependent on stellar properties (Salaris & Cassisi 1997, 2005; Beaton et al. 2016, 2018). However, these studies are still hampered by interstellar extinction at the precision level now required (Yuan et al. 2019; Freedman et al. 2020; Górski et al. 2020). Moving into the infrared (IR) reduces this systematic by a factor of 2 or greater. Furthermore, where the optical TRGB is fainter than Cepheids, the IR-TRGB is as bright as the faint end of the Cepheid sequence, further increasing its efficiency advantage (Beaton et al. 2018; Freedman et al. 2020). With new and upcoming infrared facilities including *JWST*, the *Nancy Grace Roman Space Telescope*, and eventually ground-based Extremely Large Telescopes (Beaton et al. 2019a), the IR-TRGB is poised to enable uniform distance measurements for unprecedented volumes of the nearby Universe—provided it can be sufficiently well-calibrated.

## 1.4 Thesis outline

### 1.4.1 MCR-TRGB

In Chapter 2 (originally published as Durbin et al. 2020, hereafter D20) I present an end-to-end reevaluation of the IR-TRGB color-absolute magnitude relations first presented by Dalcanton et al. (2012a, hereafter D12). To this end, I re-reduced the D12 dataset with

updated calibration and photometry techniques, and developed a method to self-consistently detect and fit TRGB magnitudes and colors in multiwavelength catalogs. The results, when compared to two state-of-the-art suites of general-purpose isochrone predictions, nonetheless revealed  $\sim 0.1$  mag discrepancies between observations and theory for both color-magnitude and optical-IR color-color relations of TRGB stars. These findings were consistent with theoretical investigations’ conclusions that stellar physics implementations and bolometric corrections remain a dominant source of uncertainty in absolute TRGB predictions (Capozzi & Raffelt 2020; Serenelli et al. 2017; Straniero et al. 2020). Since this study’s publication, exciting progress has been made in reducing uncertainties, both from the theoretical side (Di Luzio et al. 2022; Lopes & Lopes 2021; Pietrinferni et al. 2021; Saltas & Tognelli 2022; Dennis & Sakstein 2023a,b) and on the empirical optical calibration as well (Hoyt 2023).

#### 1.4.2 Empirical HST-2MASS Filter Transformations I and II: Overview

Connecting near-field trigonometric parallaxes to extragalactic SNe Ia host measurements is an essential step in calibrating the cosmic distance ladder at the precision required to address remaining uncertainties in near-field  $H_0$  measurements. This poses particular challenges for the IR-TRGB for two reasons: 1) the ground-based infrared filters anchoring the nearest *geometric* TRGB calibrators diverge from their spaceborne counterparts due to varying absorption features in the Earth’s atmosphere (“tellurics”); and 2) while the relative brightness of the infrared TRGB confers an advantage in distant galaxies, in the near field this same feature poses a challenge. The statistical nature of the TRGB requires observations of dozens to hundreds of stars, if not more. At present, there is only a narrow magnitude range in which current infrared facilities can obtain adequate precision and population statistics from both space and the ground without incurring extreme observational overheads. In Chapters 3 and 4, I explore two complementary approaches to deriving empirical filter transformations between *HST* and ground-based photometric systems, not only for TRGB-like stars but a robust sample of many stellar types and populations for comparison as well.

### 1.4.3 NIR Filter Transformations I. Synthetic Photometry

In Chapter 3 I present 2MASS-WFC3/IR filter transformations predicted from synthetic photometry of four empirical optical-IR spectral libraries. This sample comprises over 1000 individual stars, which together span nearly the full HR diagram and include stellar populations from the solar neighborhood out to the Magellanic Clouds at a broad range of ages, metallicities, and other relevant stellar properties (Turnshek et al. 1990; Rayner et al. 2009; Villaume et al. 2017; Verro et al. 2022c). The final synthetic magnitudes and fitted transformations incorporate several sources of random and systematic uncertainties, including those of the library spectral data themselves, and from line-of-sight extinction and other astrophysical and calibration considerations (Delchambre et al. 2022; Gordon et al. 2003; Vergely et al. 2022a; Bailer-Jones et al. 2021; Martins 2018). For most library stars, transformations were well-fit by piecewise-linear functions with two to three breakpoints, but strong molecular features in cool stars (both low-mass dwarfs and luminous giants with temperatures under  $\sim 3500$  K) can cause deviations from these relations of up to several tenths of a magnitude, often in ways that do not map one-to-one with broadband color.

### 1.4.4 NIR Filter Transformations II. A Direct Calibration in the Magellanic Clouds

In Chapter 4, I show preliminary results of a three-year program designed to obtain high-quality NIR photometry of cool giants in the Large and Small Magellanic Clouds using both *HST* WFC3/IR and the FourStar camera on Las Campanas Observatory’s 6.5m Baade telescope (Persson et al. 2013). While the synthetic photometry technique explored in Chapter 3 is a well-tested and highly efficient method for predicting filter transformations, fully empirical calibrations are of course preferred when possible. The *HST* component of these observations was completed only a few weeks before the time of this writing, and to date we have obtained FourStar photometry for about half of the available *HST* fields, mainly in the SMC. (A majority of the LMC fields were observed only in the last several months of the *HST* program, and certain constraints of the observation mode meant that we could not

determine their precise coordinates ahead of time.) While we do not yet have the population statistics for a more sophisticated analysis, initial results show overall good agreement with prior results, and that the data quality is more than adequate for the task.

#### *1.4.5 Conclusions and Appendices*

I briefly discuss my conclusions and possible avenues for future work in Chapter 5.

Appendix A discusses tests of the technique developed in Chapter 2 on artificial data, and Appendix B shows figures for the full galaxy sample in this chapter, which are limited to a small representative subset in the body of the text. Appendix C gives the full set of synthetic magnitudes used in 3, and Appendix D compares a number of available extinction estimates for these data.

## Chapter 2

# MCR-TRGB: A MULTIWAVELENGTH-COVARIANT, ROBUST TIP OF THE RED GIANT BRANCH MEASUREMENT METHOD

### 2.1 Introduction

The tip of the red giant branch (TRGB) is defined as the truncation of the RGB phase of stellar evolution. The TRGB is reached when the helium flash ignites, terminating the expansion and cooling of the outer layers (Salaris & Cassisi 2006). Helium ignition occurs at a more or less fixed temperature, and thus the maximum bolometric luminosity ( $L_{\text{bol}}$ ) produced by the core is well-constrained (see e.g., Sweigart & Gross 1978; Vandenberg et al. 2000; Salaris & Cassisi 2006; Serenelli et al. 2017). However, both the bolometric luminosity and the observed luminosity in a given bandpass will vary from star to star depending on the effective temperature, atmospheric chemistry, and on which elements and molecules selectively absorb and emit flux. While the TRGB can be used as a “standardizable candle”, care must be taken to understand the wavelength dependence of the observed TRGB luminosity (see Serenelli et al. 2017, for a discussion of additional physical details).

Baade (1944), when first resolving M 31 into stars, noticed a field of red-stars of roughly equal brightness, which we now associate with the TRGB of “old” stellar populations. However, the optical TRGB (OPT-TRGB) was not used as a distance indicator until Lee et al. (1993), who leveraged precise color-magnitude diagrams (CMDs) of globular clusters from Da Costa & Armandroff (1990) to demonstrate an effective technique to “detect” the truncation of the RGB sequence observationally, and thereby determine a distance to the host system.

The Lee et al. (1993) methods are conceptually simple; to detect the truncation of the



RGB sequence, one identifies the magnitude at which there is a sharp jump in star counts, as expected for the edge of the RGB sequence. Lee et al. (1993) applied an edge-detection algorithm that approximates the first-derivative of a discrete function (a Sobel filter; Sobel & Feldman 1968) to measure the point of greatest change in the RGB luminosity function, which they identified as the apparent magnitude of the TRGB. Since Lee et al. (1993), algorithms to detect the TRGB and calibrations of the absolute TRGB have evolved (a review and comparison is given in Beaton et al. 2018), but the core of the technique has stayed the same. In general, the OPT-TRGB employed in the  $I$  filter is thought to have a near-constant magnitude  $M_I \sim -4$  mag for most old ( $t > 5$  Gyr) and metal-poor ( $[\text{Fe}/\text{H}] < -0.5$  dex) stellar populations – populations that are nearly ubiquitous in galaxies of all Hubble types and luminosity classes (Kunder et al. 2018). These properties have made the detection of the OPT-TRGB an effective distance determination method out to  $\sim 31$  Mpc (Jang & Lee 2017a).

While the OPT-TRGB is a powerful tool with several key science drivers (for example, Tully et al. 2013; Trujillo et al. 2019; Anand et al. 2019b; Freedman et al. 2019, among others), extending this method to the near-infrared (IR-TRGB, hereafter) has several advantages: (i) the stars themselves are  $\sim 1 - 1.5$  mag brighter and comparable in luminosity to  $P \sim 10$  day Cepheids (see Fig. 30 in Beaton et al. 2018); (ii) the impact of extinction is reduced by up to a factor of 6 (Indebetouw et al. 2005) (Casagrande & Vandenberg 2014), permitting exploration of galaxies behind high extinction (see e.g., Anand et al. 2019a) and reducing any dust-based systematics; and (iii) the next generation of astronomical facilities, whether 30-m class telescopes on the ground, wide-field telescopes in space, or large-aperture telescopes in space, are likely to realize their highest efficiency in the near- to mid-infrared. Thus, there is enormous potential for the IR-TRGB, although there remain challenges to its implementation at high precision.

The first detailed characterization of the IR-TRGB in the Hubble Space Telescope (*HST*)’s WFC3/IR filters was presented in Dalcanton et al. (2012a, D12 hereafter) in which 23 galaxies with optical imaging from the ACS Nearby Galaxy Survey Treasury (ANGST, Dalcanton

et al. 2009, hereafter D09) were supplemented with WFC3/IR imaging in the F110W and F160W filters (Dalcanton 2009, GO-11719). D12 detected the IR-TRGB applying a Sobel filter to F110W–F160W color-magnitude diagrams, and then converted the dust-corrected apparent magnitudes to an absolute scale via distances derived in D09, using the OPT-TRGB calibrated to models described in Girardi et al. (2008). D12 found a strong correlation between the absolute F160W magnitude of the IR-TRGB and the F110W-F160W color, such that redder TRGB stars had a brighter absolute magnitude. The correlation was expected due to metallicity variations among the sample, such that more metal rich stars had redder colors, pushing a larger fraction of their bolometric flux into the NIR. However, the D12 IR-TRGB was brighter than contemporaneous theoretical models by 0.05 to 0.10 mag and, generally, was notably different from globular cluster observations that had been converted from 2MASS into the WFC3/IR system. The general conclusion from this paper was that while the IR-TRGB was promising, there were significant unresolved issues. A subsequent and similar analysis by Wu et al. (2014), however, essentially found the same underlying mag-color relationship for the IR-TRGB, albeit these authors argued for a break in the slope at  $F110W-F160W = 0.95$  mag.

More recent, ground-based work in the 2MASS filter system by Hoyt et al. (2018), Madore et al. (2018), and Górski et al. (2018) produced empirical color-magnitude relations for the IR-TRGB. These, however, are significantly different from those determined for WFC3/IR on HST. In their review, Beaton et al. (2018) compared the WFC3/IR and 2MASS IR-TRGB slopes to demonstrate that these independent WFC3/IR and 2MASS calibrations largely agree when considered within a given filter system and that the apparent differences are more likely due to inherent differences between the filter systems. As a result, calibrations from the ground-based 2MASS systems are likely inapplicable to the space-based WFC3/IR system.

In addition to advancing empirical measurements of the IR-TRGB, recent papers have also updated theoretical relationships derived from stellar models. A key work is that of Serenelli et al. (2017), which directly compared the theoretical IR-TRGB for a range of

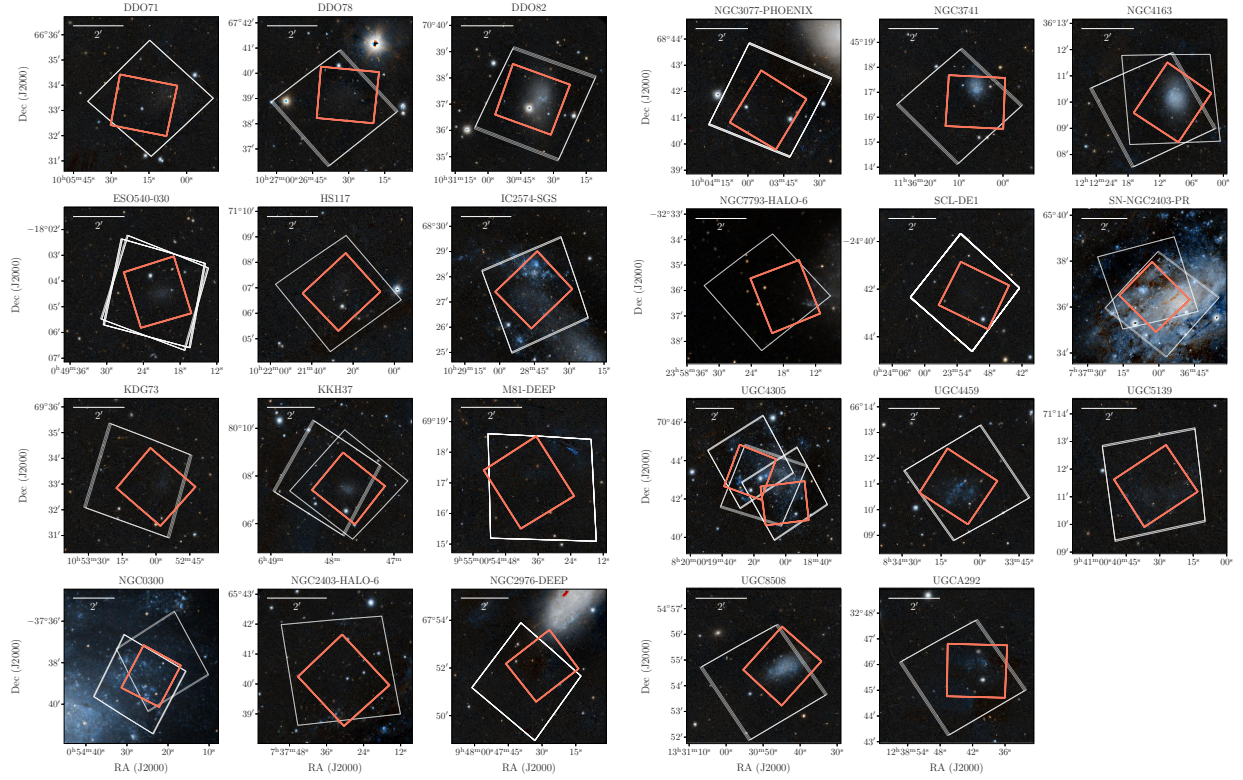


Figure 2.1: Footprints of the *HST* observations originally presented in D09 and D12, which we reanalyze in this work. ACS/WFC footprints are shown by thin white lines, and WFC3/IR footprints are in thick orange. Background images are PanSTARRs  $z+g$  for all targets except NGC 300 & NGC 7793-HALO-6, which use DSS2. All background images were retrieved through the HiPS thumbnail service provided by the Université de Strasbourg.

metallicities and ages in the BaSTI (Pietrinferni et al. 2013) model suite. Serenelli et al. (2017) report both physical and color-magnitude relationships for the IR-TRGB, but note that uncertainties in the bolometric corrections and stellar  $T_{\text{eff}}$  scale make direct use of these relationships challenging (as discussed further in Beaton et al. 2018). McQuinn et al. (2019) studied the variation in the TRGB with age and metallicity from the optical to the mid-IR using simulated photometry based on the PARSEC (Bressan et al. 2012; Marigo et al. 2017) model suite, and found that rectifying the photometry to a fiducial tip reduced the range of variations in the measured F160W TRGB to 0.04 mag. Thus, while the potential for the IR-TRGB is well-recognized (see e.g., Beaton et al. 2018, among others), the empirical evidence for its reliability remains unclear.

D12 presented a number of concerns regarding their analysis that ranged from the relatively new data processing and calibration of WFC3/IR data, to crowding in the images (for which the higher-resolution optical images are clearly deeper and more complete). However, since D12, major large-scale projects like the Panchromatic Hubble Andromeda Treasury (PHAT; Dalcanton et al. 2012b; Williams et al. 2014), the Cosmic Assembly Near Infrared Deep Extragalactic Legacy Survey (CANDELS; Grogin et al. 2011; Koekemoer et al. 2011), and the Ultra Deep Field (Koekemoer et al. 2013; Borlaff et al. 2019), have led to substantial improvement both in our technical knowledge of the WFC3/IR camera and in the development of multiwavelength data-processing techniques that significantly improve the WFC3/IR photometric quality. Additionally, there have been multiple internal efforts to improve WFC3/IR calibration and data products (for a comprehensive overview see Mack 2018). It is the purpose of this work to apply these techniques to the D12 dataset and revisit the discrepancies identified in D12 regarding the IR-TRGB (Durbin 2017). We also take advantage of and expand upon recent works (e.g. Hoyt et al. 2018; Madore et al. 2018; Freedman et al. 2020) that have demonstrated the effectiveness of calibrating the TRGB in multiple bandpasses by selecting a set of fiducial “tip stars” and fitting their multiwavelength behavior; we present a generalized version of this method here.

The outline of this chapter is as follows. Section 2.2 describes the observations, image

processing, photometry, and artificial star tests. Section 2.3 presents techniques to isolate the RGB, identify candidate TRGB stars, and trace their multiwavelength behavior. Section 2.4 presents the final measured TRGB apparent magnitudes and colors, and compares the absolute magnitudes and distance moduli obtained from previously published distances and then from calibration to two sets of theoretical isochrones. Section 2.5 presents a discussion of our results, attempts to resolve concerns from D12, and discusses lingering concerns regarding the full realization of the IR-TRGB. Section 2.6 presents a summary of our work and discusses directions of future research. Throughout the main text, we limit visualizations to a representative set of galaxies; figures for the full sample are given as figure sets.

## 2.2 Data

### 2.2.1 Observations

We re-reduced the optical and near-infrared *HST* imaging data described in D09 and D12. The D12 observations were a WFC3/IR imaging follow-up (SNAP-11719) to the optical ACS/WFC data presented in D09. The F110W+F160W observations cover 26 pointings in 22 Local Volume galaxies with a range of star-formation histories. The majority of the galaxies are low-metallicity dwarfs, with the exception of M81. Table 2.1, reproduced from D12, presents summary information about the galaxies in our sample, including coordinates, angular diameter, apparent  $B$  magnitude, foreground reddening, T-type, HI line widths, and group membership. We note that not all of these galaxies have the purely old stellar populations that are considered optimal for measuring the TRGB.

We analyzed 24 of the 26 datasets that were included in D12. To maintain uniformity in the final dataset and analyses, we excluded two targets (NGC404 and NGC2403-DEEP) because their optical data were taken by WFPC2 rather than ACS. Additionally, we combined the two pointings of Holmberg II (UGC4305-1 and UGC4305-2 in D12) into a single target UGC4305 here, as they have slight overlap in the NIR and substantial overlap in the optical. All targets have ACS imaging in F814W (comparable to Johnson-Cousins  $I$ ) and at least one

Table 2.1: Sample galaxies

Galaxy	Alt. Name(s)	RA (J2000)	Dec (J2000)	Diam. ''	$B_T$	$A_V$ mag	$m - M$ mag	$T$ km s <sup>-1</sup>	$W_{50}$	Group
DDO53	U4459	08:34:06.5	66:10:45	1.6	14.55	0.104	27.79	10.0	25	M81
DDO78		10:26:27.9	67:39:24	2.0	15.80	0.058	28.18	-3.0		M81
DDO82	U5692	10:30:35.0	70:37:10	3.4	13.57	0.112	27.90	9.0		M81
HoI	U5139, DDO63	09:40:28.2	71:11:11	3.6	13.64	0.137	27.95	10.0	29	M81
HoII	U4305	08:19:05.9	70:42:51	7.9	11.09	0.087	27.65	10.0	66	M81
HS117		10:21:25.2	71:06:58	1.5	16.50	0.316	27.91	10.0	13	M81
I2574	U5666, DDO81	10:28:22.4	68:24:58	13.2	10.84	0.100	27.90	9.0	115	M81
KDG2	E540-030, KK9	00:49:21.1	-18:04:28	1.2	16.37	0.064	27.61	-1.0		ScI
KDG63	U5428, DDO71	10:05:07.3	66:33:18	1.7	16.01	0.270	27.74	-3.0	19	M81
KDG73		10:52:55.3	69:32:45	0.6	17.09	0.052	28.03	10.0	18	M81
KKH37		06:47:45.8	80:07:26	1.2	16.40	0.204	27.56	10.0	20	
M81	N3031, U5318	09:55:33.5	69:04:00	26.9	7.69	0.232	27.77	3.0	422	M81
N300		00:54:53.5	-37:40:57	21.9	8.95	0.034	26.50	7.0	149	14+13
N2403	U3918	07:36:54.4	65:35:58	21.9	8.82	0.110	27.50	6.0	231	M81
N2976	U5221	09:47:15.6	67:54:49	5.9	11.01	0.241	27.76	5.0	97	M81
N3077	U5398	10:03:21.0	68:44:02	5.4	10.46	0.188	27.92	10.0	65	M81
N3741	U6572	11:36:06.4	45:17:07	2.0	14.38	0.066	27.55	10.0	81	14+07
N4163	U7199	12:12:08.9	36:10:10	1.9	13.63	0.055	27.29	10.0	18	14+07
N7793		23:57:49.4	-32:35:24	9.3	9.70	0.054	27.96	7.0	174	ScI
Sc22	Sc-dE1	00:23:51.7	-24:42:18	0.9	17.73	0.042	28.11	10.0		ScI
U8508	IZw60	13:30:44.4	54:54:36	1.7	14.12	0.042	27.06	10.0	49	14+07
UA292	CVnI-dwA	12:38:40.0	32:46:00	1.0	16.10	0.043	27.79	10.0	27	

Table 2.1 notes: Reproduced from D12, with updates to  $A_V$  from Schlafly & Finkbeiner (2011). Name, position, diameter,  $B_T$ ,  $W_{50}$ , and T-type taken from Karachentsev et al. (2004).  $m - M$  from D09 and Karachentsev et al. (2003) for NGC 7793; Group membership from Karachentsev (2005) or Tully et al. (2006).

of the F475W, F555W, and F606W filters (comparable to SDSS  $g$ , Johnson-Cousins  $V$ , and broad Johnson-Cousins  $V$  respectively). Figure 2.1 shows the footprints of the ACS/WFC (white) and WFC3/IR (orange) on either PanSTARRS or DSS2 imaging for each of the 23 distinct targets used here.

Table 2.2 describes the ACS/WFC and WFC3/IR observations used for this work including references to the original proposals, total F814W exposure time, and offsets of the observation from the galaxy center.

We retrieved all data in the form of calibrated individual exposures (`*flt` files for WFC3/IR and CTE-corrected `*flc` files for ACS/WFC) from the Mikulski Archive for Space Telescopes (MAST) with Astroquery (Ginsburg et al. 2017, 2019) on January 28, 2019, and obtained up-to-date reference files with the HST CRDS `bestref` tool (Swam et al. 2004).

### 2.2.2 Alignment & Photometry

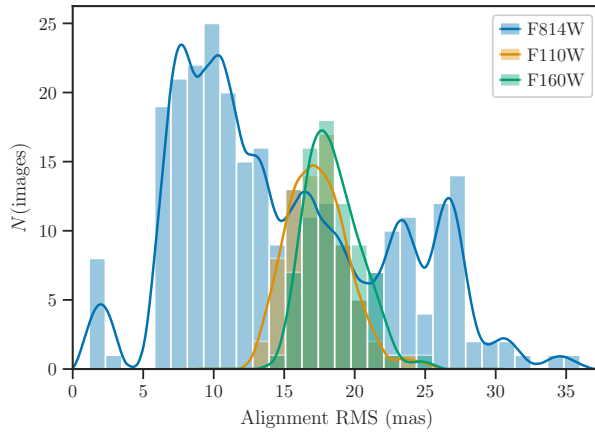


Figure 2.2: Distributions of the RMS scatter of alignment residuals for F814W, F110W, and F160W. Both near-IR filters have a residual scatter on the order of  $0.025''$ , or  $\sim 0.2$  WFC3/IR pixels. In F814W the alignment RMS has a peak closer to  $0.01''$ , but there is a long tail of images with higher scatter, likely due to variations in exposure depth and source densities.

We aligned all exposures using **TweakReg** and **Drizzlepac** 2.0 (Hack et al. 2013; Avila et al. 2015). **TweakReg** aligns images by calculating an affine transform (shifts, rotation, and

Table 2.2: Observations

Galaxy	Target name	Date obs.	Offset (')	$T_{\text{exp}}$ (s)	$\Sigma_{\text{min}}$	$\Sigma_{\text{max}}$	$N_{\star}$	Opt.	Opt. filters
								PID	
KDG63	DDO71	2010-04-21	16:33:04	0.97	9000	0.00	0.86	68477	9884 F606W, F814W
DDO78	DDO78	2010-04-20	15:13:25	0.34	2292	0.02	0.54	56458	10915 F475W, F814W
DDO82	DDO82	2010-05-07	07:27:41	0.38	2442	0.01	2.99	187699	10915 F475W, F606W, F814W
KDG2	ESO540-030	2009-12-17	12:32:10	0.15	7840	0.00	0.60	28087	10503 F606W, F814W
HS117	HS117	2010-02-24	02:35:38	0.13	900	0.00	0.46	13011	9771 F606W, F814W
I2574	IC2574-SGS	2010-02-25	03:34:37	3.28	6400	0.10	1.40	286852	9755 F555W, F814W
KDG73	KDG73	2010-06-09	18:17:42	0.43	2274	0.00	0.22	12721	10915 F475W, F814W
KKH37	KKH37	2009-09-29	11:12:38	0.09	3441	0.00	1.36	30966	10915, F475W, F606W, 9771 F814W
M81	M81-DEEP	2010-06-13	01:26:19	13.88	29953	0.02	0.23	63093	10915 F475W, F606W, F814W
N300	NGC0300	2010-04-19	18:17:32	6.26	2982	0.05	0.59	197750	10915, F475W, F555W, 9492 F606W, F814W

Table 2.2 notes: Here the date observed is the date of the last IR exposure; the offset is the distance between the center of the IR footprint and the galaxy coordinates as given in Table 2.1; the exposure time is the total F814W exposure time (all IR observations have uniform exposure times of 600s in F110W and 900s in F160W); and  $N_{\star}$  is the number of stars that were detected in all of F814W, F110W, and F160W.



scale) that best describes the transformation between astrometric catalogs from two images, one of which is treated as the fiducial “reference” image. It then calculates an updated WCS solution for the non-reference image using the affine transform.

By default, **TweakReg** extracts astrometric source catalogs from input images with a point source extraction routine based on DAOFIND (Stetson 1987), which is optimized for point source detection. However, many of our exposures are too sparsely populated with bright stars to produce a reliable cross-filter alignment solution from point sources alone, requiring the addition of background galaxies to the astrometric source catalogs.<sup>1</sup> We therefore followed the procedure described in Lucas (2015) to align images on Source Extractor (Bertin & Arnouts 1996) catalogs rather than **TweakReg**-produced catalogs. Source Extractor’s detection algorithm is largely morphology-agnostic, which enables the robust detection of both point and extended sources. We used SEP (Barbary 2016), a Python and C reimplementations of core Source Extractor algorithms, to derive all catalogs used in alignment.

We chose ACS/WFC F814W as our “reference” filter for all targets, as it is the only optical filter common to all targets, and in most cases it is the deepest and most likely to contain sources that are detected across multiple filters. We aligned all frames for each target with the following steps:

1. Extract initial source catalogs from all F814W exposures with SEP and align these with **TweakReg**;
2. Combine all aligned F814W exposures into a single distortion-corrected reference image with **AstroDrizzle**, and extract a deep reference catalog from the drizzled image;
3. Realign all F814W exposures to the reference image using catalogs from the cosmic ray cleaned (**\*crclean**) images produced by **AstroDrizzle**;

---

<sup>1</sup>Although it is true that extended sources are less optimal for alignment, as their morphologies may vary across filters affecting their calculated centroids, they are nonetheless useful in the absence of sufficient point sources.

4. Align all other exposures to the reference image with `TweakReg`.

We did not attempt to derive an absolute astrometric solution for any of our targets, as the majority are severely limited by the  $\sim 2' \times 2'$  WFC3/IR field of view and do not have enough bright sources to reliably match against external astrometric catalogs such as *Gaia*. For the purposes of this work, internally consistent alignment on a per-target basis is sufficient.

Figure 2.2 compares the RMS scatter of the alignment residuals for the common filters of F814W, F110W, and F160W. The residuals for the two WFC3/IR filters are very similar, with a residual scatter of  $\sim 0''.025$  or 0.2 WFC3/IR pixels. The residuals for F814W are more scattered, with a peak at  $0''.01$  (0.2 ACS/WFC pixels) and a long tail, likely due to differences in the underlying image datasets themselves (e.g., different exposure depths and source densities).

We carried out photometry on the aligned images with the pipeline described in Williams et al. (2014), which wraps the *HST* photometry package DOLPHOT (Dolphin 2000). Briefly, DOLPHOT uses a set of fiducial PSF models that are empirically scaled for each frame to account for frame-to-frame differences, such as those induced by “breathing” (Hasan & Bely 1994). The cross-camera wrapper utilizes a single underlying source list such that DOLPHOT can iteratively measure each individual source simultaneously across frames employing techniques optimized for crowded fields. As described in Williams et al. (2014), the output photometry for each source requires additional characterization to have realistic uncertainties incorporating all concerns; these are derived via artificial star tests that are described in the following subsection.

The key difference in the procedure adopted here compared to that of D12 is that we perform *simultaneous cross-camera photometry* rather than reducing the datasets independently and then matching catalogued sources. Due to the differences in the native angular resolution between ACS/WFC and WFC3/IR ( $0''.05/\text{pixel}$  vs.  $0''.13/\text{pixel}$  respectively), the simultaneous procedure should produce a more complete and robust WFC3/IR dataset due

to improved deblending and more complete source lists.

We rejected large contaminating sources, such as bright foreground stars and background galaxies, by convolving the images with a 2D Gaussian kernel with width  $0''.75$  (15 WFC3/IR pixels) and extracting sources from the convolved images with SEP. We used the ellipse parameters  $a$ ,  $b$ , and  $\theta$  of the sources to mask potentially contaminated pixels, with  $a$  and  $b$  multiplied by 5 to ensure that a sufficient fraction of the contaminating flux was masked.

### 2.2.3 Artificial Star Tests

The primary sources of photometric uncertainty in these data are total exposure depth, which determines the Poisson noise of photon counts, and stellar surface density, which affects the likelihood of a star being blended with surrounding sources. The former are well-captured by DOLPHOT’s accounting of photon-counting uncertainties. The latter, however, require additional tests to fully characterize, especially given that blending is typically the dominant source of bias and uncertainty in crowding-limited data.

We evaluated the photometric biases, scatter, and completeness of our data with a series of artificial star tests (ASTs). We generated 20,000 artificial stars to be injected into the image stack for each target, for a total of 460,000 ASTs. We prioritized the near-IR RGB when selecting artificial star magnitudes. Half were drawn directly from simulated absolute photometry generated with MATCH (Dolphin 2002) from PARSEC models. The other half were assigned random magnitudes within our F110W-F160W selection box, with optical magnitudes taken from simulated stars with comparable near-IR photometry. Figure 2.3 shows a CMD of the full set of input NIR photometry. All absolute input magnitudes were then adjusted by the per-filter foreground reddening and D12 distance modulus for each target and assigned random pixel coordinates within the NIR image footprints, excluding the locations of masked contaminating sources such as extended background galaxies and bright foreground stars. These input stars were then inserted into the image stack in batches of 1000 at a time and processed identically to the original photometry.

As the AST input locations were assigned at random, they do not necessarily reflect the

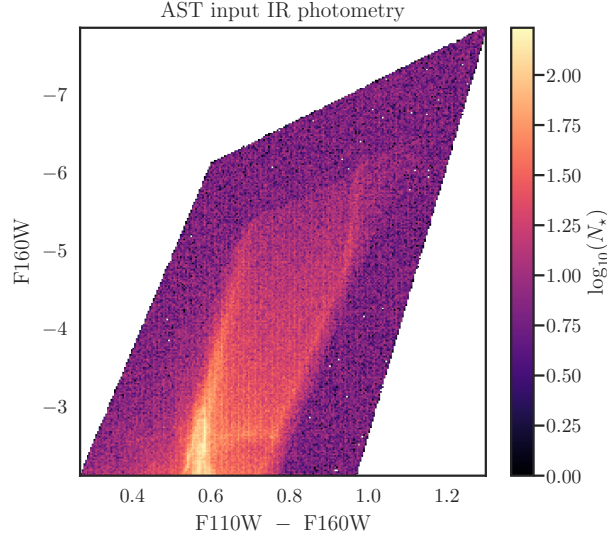


Figure 2.3: Hess diagram of input AST photometry in the near-IR. The densest portions (orange to yellow) are from the CMDs, whereas the uniform sampling is purple.

true distributions of density and depth for any single target. We therefore resampled the full set of AST results to match the distribution of these quantities for each target as closely as possible, as follows.

We evaluated stellar surface densities using kernel density estimation (Rosenblatt 1956; Parzen 1962) with the Python package `KDEpy` (Odland 2018). We selected the photometry to be used for density estimation using the same near-IR selection box as in the ASTs, with the additional criteria of having a mean near-IR signal-to-noise greater than 3. We then constructed stellar surface density maps by convolving source coordinates with a Gaussian kernel with a width of  $5''$ , and tagged all photometry with their local densities. Density maps for three example targets are shown in Figure 2.4. In the analysis presented in Section 2.3 we used only photometry with local densities less than  $1.5 \text{ stars}/\square''$ , except for the high-density target SN-NGC2403-PR, where we used a maximum local density of  $3 \text{ stars}/\square''$ .

While all near-IR exposures were taken with identical exposure times and are therefore of comparable depth, there is considerable variation in the optical exposure depths, which in

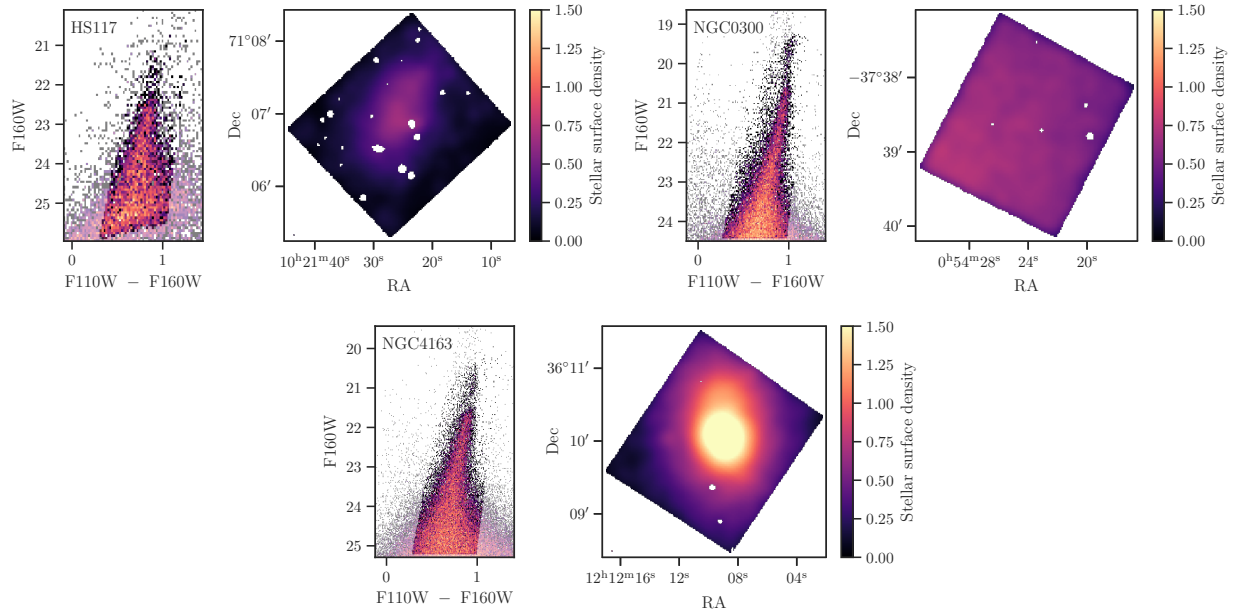


Figure 2.4: Left panels: NIR Hess diagrams of three galaxies in our sample, with the selections of stars included in our surface density calculations highlighted. Right: corresponding stellar surface density maps for each target. All density maps are scaled to the same limits (0 to 1.5 RGB stars per square arcsecond) to highlight the range of stellar densities in our sample. Gaps in the density images show where contaminating sources such as foreground stars and background galaxies were rejected. The complete figure set (23 images) is available in the online journal.

turn may affect DOLPHOT’s source detection and subsequent deblending of near-IR sources. To characterize exposure depth, we use the weight maps generated by **Astrodrizzle** for the combined F814W reference images to assign fiducial total exposure times to the locations of each source.

For each target we separated to the photometry into 10 bins according to density vs. depth using K-means clustering (Arthur & Vassilvitskii 2007; Sculley 2010), and resampled the full set of ASTs to match the observed distributions of densities and depths.

We then use the resampled ASTs to assign fiducial photometric uncertainties, biases, and completenesses to all of our photometry. We define the photometric bias to be the median of the differences between observed and input AST magnitudes, the photometric error to be the interquartile range of the same, and the completeness to be the fraction of stars with non-null observed magnitudes. We calculate these quantities as a function of AST input magnitudes in each filter.

We subtract filter-appropriate foreground extinctions from all photometry, with values obtained from Schlafly & Finkbeiner (2011); the corresponding  $V$ -band extinctions are listed in Table 2.1. We assume negligible internal extinction for all targets, as the majority of our targets are either low-metallicity dwarfs or halos of spiral galaxies. Target SN-NGC2403-PR is an exception, but in that case we find that the photometric uncertainties due to crowding are large enough that an attempt to analyze or correct for internal extinction would likely not be productive.

#### *2.2.4 Comparison to D12 photometry*

Here we directly compare this generation of photometry to that of D12 by crossmatching individual stars. We first convert the IR pixel coordinates of the original photometry to the WCS defined by our realigned images. We select an initial sample of stars within 1 mag of the D12 TRGB values and maximum per-filter old-to-new magnitude differences of 0.5 mag, and match on RA and Dec using a kd-tree (Bentley 1975) with a maximum distance of  $2''$ . We then find the robust coordinate transformation parameters between the new and

old photometry using RANSAC regression (Fischler & Bolles 1987) on the matched initial sample with a maximum residual value of  $0''.1$ . We apply this transformation to the full set of old photometry coordinates and match the transformed coordinates again with a kd-tree, this time with a maximum distance of  $0''.1$ . Figure 2.5 shows the changes in magnitude as a function of the original D12 magnitudes in F160W, with the D12 TRGB  $\pm 0.1$  mag highlighted.

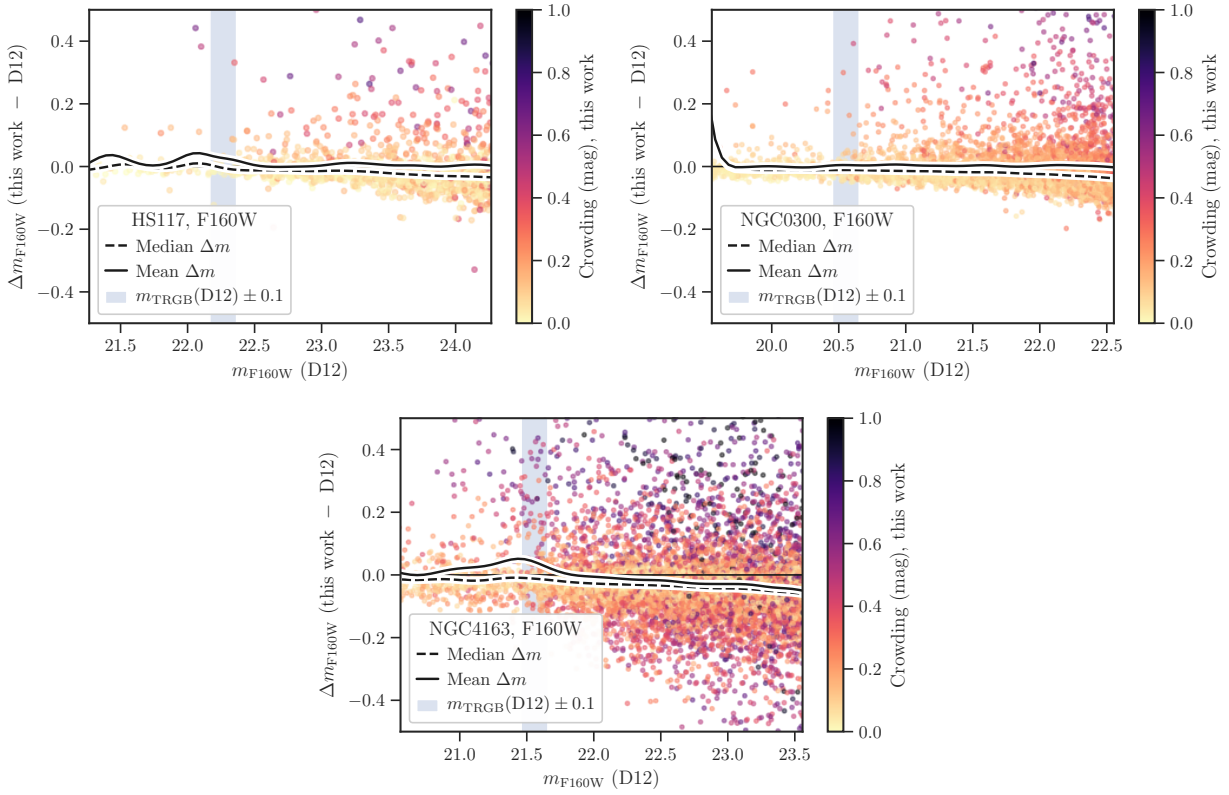


Figure 2.5: Changes in photometry between D12 and this work for HS117 (top), NGC 300 (middle), and NGC 4163 (bottom), with the D12 magnitude on the x-axis and  $\Delta m$  on the y-axis. The color-coding indicates the DOLPHOT crowding parameter of the new photometry, which is the number of magnitudes subtracted from the initial measurement due to neighboring sources. The rolling mean and median are shown by the solid and dashed lines respectively. The complete figure set for both F110W and F160W (46 images) is available in the online journal.

Interestingly, we find that near the tip, the median magnitude difference is typically very small (on the order of 0.01 mag) but negative for uncrowded stars, indicating that this generation of photometry is slightly brighter than the previous. However, even the sparsest fields show a population of high-crowding stars that are several tenths of a magnitude dimmer than their D12 counterparts.

### **2.3 TRGB Measurement**

In this section we describe the steps we use to measure the apparent magnitudes and colors of the IR-TRGB. We adopt a multiwavelength approach, which we call “MCR-TRGB”, that we summarize for the reader in advance of detailed descriptions. First, we isolate the RGB sequence from the other stellar populations. From the RGB sample, we do a tip detection to select stars in the vicinity of the TRGB. This initial sample is then separated into potential sub-populations to isolate those that have colors and magnitudes consistent with being TRGB stars. The color and magnitude distributions of the candidate tip stars are then fitted jointly for all applicable color-magnitude spaces to build the final color-magnitude calibrations. This approach has several advantages over traditional Sobel edge-detection for the purpose of this work, which we discuss in detail in Section 2.5.

Throughout this section, the methods are demonstrated using galaxies that span a range in metallicity and RGB shape. Identical figures for each of the 23 galaxies in the sample are provided as figure sets.

#### *2.3.1 Initial RGB Star Selection*

A maximally complete and minimally contaminated sample of RGB stars is essential for characterizing the TRGB and the RGB luminosity function near the tip. Unfortunately there are many stars that have colors and magnitudes similar to RGB stars, such as red helium-burning (RHeB) and asymptotic giant branch (AGB) stars. These “contaminant” populations can blur the TRGB edge or distort its measured magnitude (see discussion in D12).



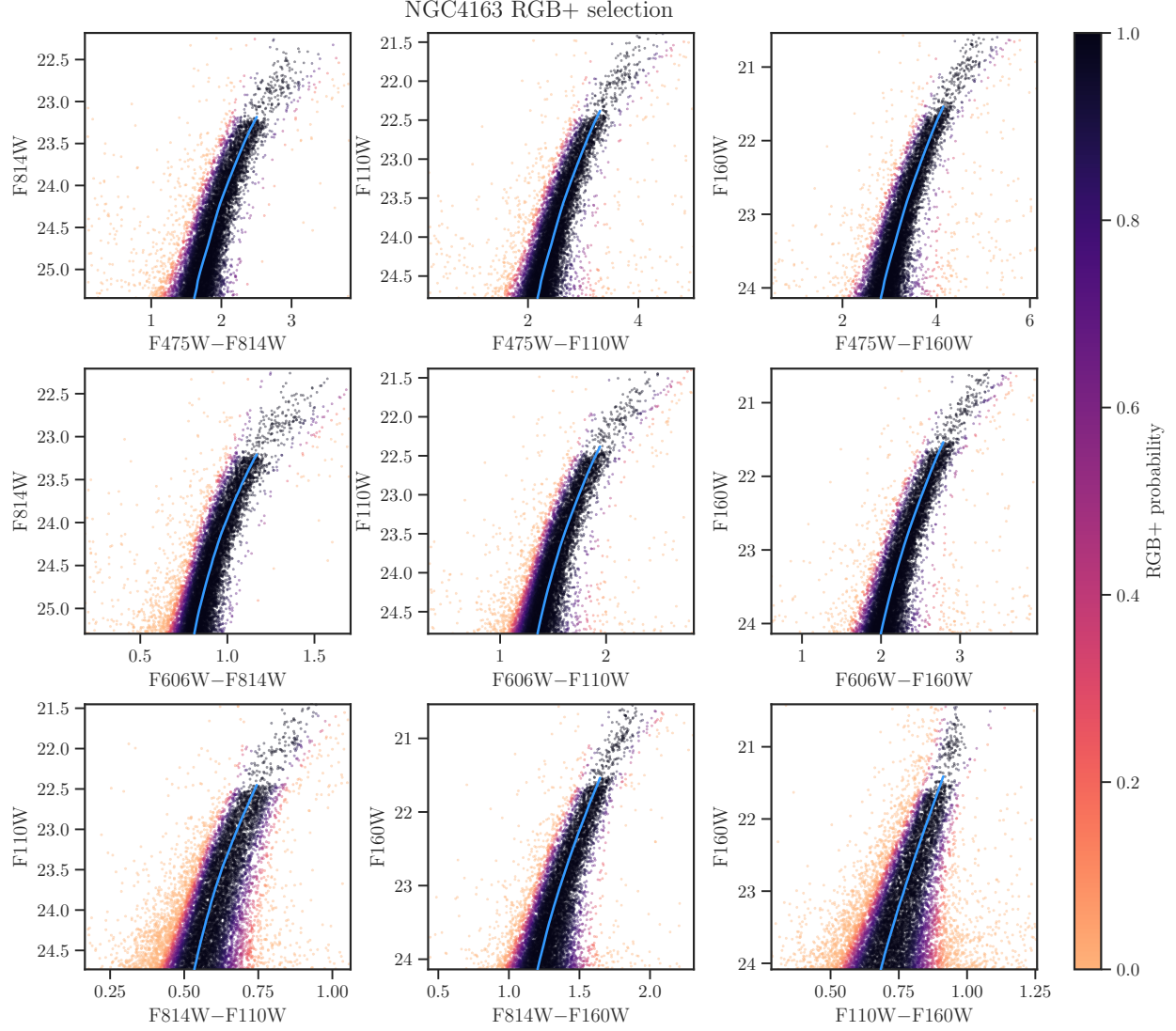


Figure 2.6: A demonstration of filter-by-filter RGB selections for NGC4163. Each of the 9 panels contains a color-magnitude combination used to determine  $P(\text{RGB})+$  for stars in the color-magnitude range. The points in each panel are color-coded by the final probability as indicated on the color-bar. The best-fit PARSEC synthetic RGB in each combination is shown. The complete figure set (23 images) is available in the online journal.

Typically, RGB stars are selected using strict binary color-magnitude cuts; we describe two particular examples. D12 initially select stars with colors in the range  $0.6 < F110W - F160W < 1.1$  mag and magnitudes brighter than 1 mag below their initial TRGB estimate, and then make further rejections based on the standard deviations of a linear fit to the remaining stars in color-magnitude space. The Carnegie-Chicago Hubble Program (Hatt et al. 2017; Jang et al. 2018; Hatt et al. 2018a,b; Freedman et al. 2019) makes color cuts with a fiducial RGB slope and a color width chosen visually to encompass the edges of the RGB near the tip.

Here, we leverage the multiwavelength information available for our targets to probabilistically identify stars that fall along characteristic RGB color-magnitude sequences. For each target we construct a set of *red* vs. *blue-red* CMDs using F814W, F110W, and F160W as the red filters, and using all available optical filters other than F814W as the blue. We also construct CMDs in F814W vs. F814W–F160W, F110W vs. F814W–F110W, and F110W vs. F110W–F160W for all targets. The number of unique color-magnitude combinations varies from 6 to 12 depending on the number of available optical filters for each target. We apply broad initial color and magnitude cuts based on the D12 TRGB measurements. Figure 2.6 provides example CMDs after cuts for NGC 4163 in the color-magnitude combinations used for this analysis.

Next, we define an RGB locus in each filter combination by fitting a predicted RGB color-magnitude sequence to the photometry in each color-magnitude combination independently. We minimize the median distance between the observed photometry and a grid of synthetic photometry derived from PARSEC (Marigo et al. 2017) isochrones of ages 4 to 14 Gyr and  $[\text{Fe}/\text{H}] -3.0$  to  $-0.2$  dex, which have been limited to RGB stars brighter than  $M_{F110W} = -2$  mag and converted to apparent magnitudes using the distance moduli from D12. The panels of Figure 2.6 have their best-fit isochrone-predicted RGB sequences overlaid in blue. As our goal is to trace the RGB color-magnitude locus across all available bandpasses rather than to measure any underlying properties of the stellar populations, we do not force a single age and metallicity combination to fit all color-magnitude combinations. (We note that the

metallicities of the “best-fit” isochrones for a single target can vary filter-to-filter by up to nearly a full dex, especially in the case of low-metallicity targets where the upper RGB color only weakly depends on metallicity; see subsection 2.5.3 for further discussion of filter-to-filter differences between observed and predicted photometry at the TRGB.)

An initial “RGB-sequence probability” is then assigned to each star based on the distance between its observed position in color-magnitude space and the nearest point on the predicted RGB for each color-magnitude combination. The points in the panels of Figure 2.6 are color-coded by these probabilities.

The purpose of this process is to construct a luminosity function with which to make an initial TRGB estimate, as described in subsection 2.3.2. We therefore extrapolate the fitted RGB sequences out to at least 1.5 mag brighter than the measured D12 TRGB apparent magnitudes in all filters. As a result, stars brighter than the TRGB that fall along the predicted color-magnitude loci will be assigned high RGB-sequence probabilities. These probabilities should be understood as estimates of a star’s proximity to the color-magnitude relations characteristic of each target’s RGB sequence, rather than as identifications of only the stars that are truly on the RGB.

The individual RGB-sequence probabilities are then averaged across all color-magnitude combinations to produce global RGB-sequence probabilities, which we call  $P(\text{RGB})+$ .

### 2.3.2 *Edge Detection*

We make an initial selection of candidate tip stars by applying a Sobel edge detection to the RGB-weighted luminosity function (LF). For each target we choose the filter with the sharpest LF; that is, the filter in which the tip magnitude is least dependent on color. This is F814W for most targets, and F110W for targets with  $F110W - F160W > 0.95$  mag, as measured in D12). We first construct a luminosity function (shown in the middle column of Figure 2.7) by marginalizing  $P(\text{RGB})+$  over color as a function of magnitude. We use a bin size of 0.01 mag, which is a factor of  $\sim 5$  smaller than the typical magnitude uncertainty.

For each galaxy, the middle panels of Figure 2.7 show the raw LF (blue), where the

noise is consistent with Poisson fluctuations. We first smooth the LF with a Savitzky-Golay filter (Savitzky & Golay 1964), a low-pass filter originally developed to suppress noise in spectroscopic data by fitting a polynomial within a rolling window. This technique effectively removes Poisson noise spikes while preserving sharp features such as the TRGB edge. However, there may be remaining spurious edges from photometric variance or stochastic sampling of the luminosity function, particularly in sparse data. To reduce the impact of these false edges, we smooth the LF once more using GLOESS (Gaussian-windowed, Locally Weighted Scatterplot Smoothing); for an in-depth description see Hatt et al. (2017) and references therein. Briefly, GLOESS is an implementation of one-dimensional Gaussian kernel density estimation, which we have modified to accept a variable kernel width. We select a fiducial kernel width using the `KDEpy` implementation of the Improved Sheather-Jones algorithm (Botev et al. 2010), which chooses an optimal kernel width based on the overall density of the data. We then multiply this fiducial width by the square of the photometric uncertainties scaled by their median value as a function of magnitude, which de-emphasizes LF variation fainter than the TRGB, where photometric uncertainties are higher. The final smoothed LF, shown overlaid in black on the raw LFs in Figure 2.7, is then used for the initial TRGB detection.

To detect the TRGB, we begin by applying a Sobel filter, which is one of the most widely used means of finding the tip (see summary and comparisons in Beaton et al. 2018). The Sobel filter approximates the first derivative of a discrete dataset via convolution with a kernel. In its simplest form, this kernel is  $[-1, 0, 1]$ , which effectively subtracts counts in the  $i - 1$  bin from the  $i + 1$  bin to determine the edge-response,  $\eta$ , for bin  $i$ . This kernel is applied to the smoothed LF, and the response is shown for each galaxy in the right panels of Figure 2.7. In Figure 2.7, the magnitude of maximum Sobel response,  $m(\eta_{\max})$ , is indicated by the dashed line across all panels.

We then select candidate tip stars near  $m(\eta_{\max})$  within a range we call  $\Delta\eta$ . The value of  $\Delta\eta$  is determined using two quantities: i) the median photometric error within  $\pm 0.1$  mag of  $m(\eta_{\max})$ ,  $\sigma_{\text{phot}}^{\eta_{\max}}$ , and ii), a minimum number of tip candidate stars  $N_{\star}^{\min}$ . We define  $N_{\star}^{\min}$  as

the square root of the number of stars 1 magnitude below  $m(\eta_{\max})$ , with a hard minimum of 30 stars. For each target, we make an initial selection of stars within  $\pm 1\sigma_{\text{phot}}^{\text{TRGB}}$ , and then iteratively expand the selection range by  $0.5\sigma_{\text{phot}}^{\text{TRGB}}$  on each side until either  $N_{\star}^{\min}$  is reached or  $\Delta\eta$  is over 0.2 mag. For the majority of our targets, the initial selection window of  $\pm 1\sigma_{\text{phot}}^{\text{TRGB}}$  is enough to meet  $N_{\star}^{\min}$ . Our final  $\Delta\eta$  is shown by the blue band in the panels of Figure 2.7 for our example pointings.

Out of the stars that fall within the fiducial tip magnitude range, we first select likely RGB stars as those with  $P(\text{RGB})+ > 0.6$ , which roughly corresponds to stars that were identified as RGB+ sequence candidates with over 90% probability in at least two-thirds of the filter combinations we used to assign RGB probabilities. We then reject stars with anomalous magnitudes in at least one filter with Local Outlier Factor outlier detection (Breunig et al. 2000), which evaluates the relative isolation of points using  $k$ -nearest neighbors. We take this trimmed sample of stars to be our final set of tip star candidates, which we then use to measure tip magnitudes and colors as described in the following section.

We note that this selection of likely RGB tip stars is performed based on the results of applying the Sobel filter to the filter where the tip is “flat” with color. The Sobel filter, by design, looks for an sharp edge in a one-dimensional distribution. Two dimensional implementations of the Sobel Filter exist, but still require conversion of our CMDs into a binned form. Thus, application of the one-dimensional Sobel filter to a distribution that has magnitude-color behavior may not fully detect the true edge in the distribution. Lastly, where there is strong magnitude-color trend, because our colors are more imprecise than our magnitudes, the intrinsic slope can be distorted by the color-spread in our data. Thus, in the next section, we develop a method to utilize the tip stars we have just identified to trace the intrinsic TRGB slope across our set of color-magnitude combinations.

### 2.3.3 Multiwavelength tip fitting

We characterize the color and magnitude distributions of our candidate tip stars using Extreme Deconvolution (XDGM, Bovy et al. 2011), a modification of Gaussian mixture mod-

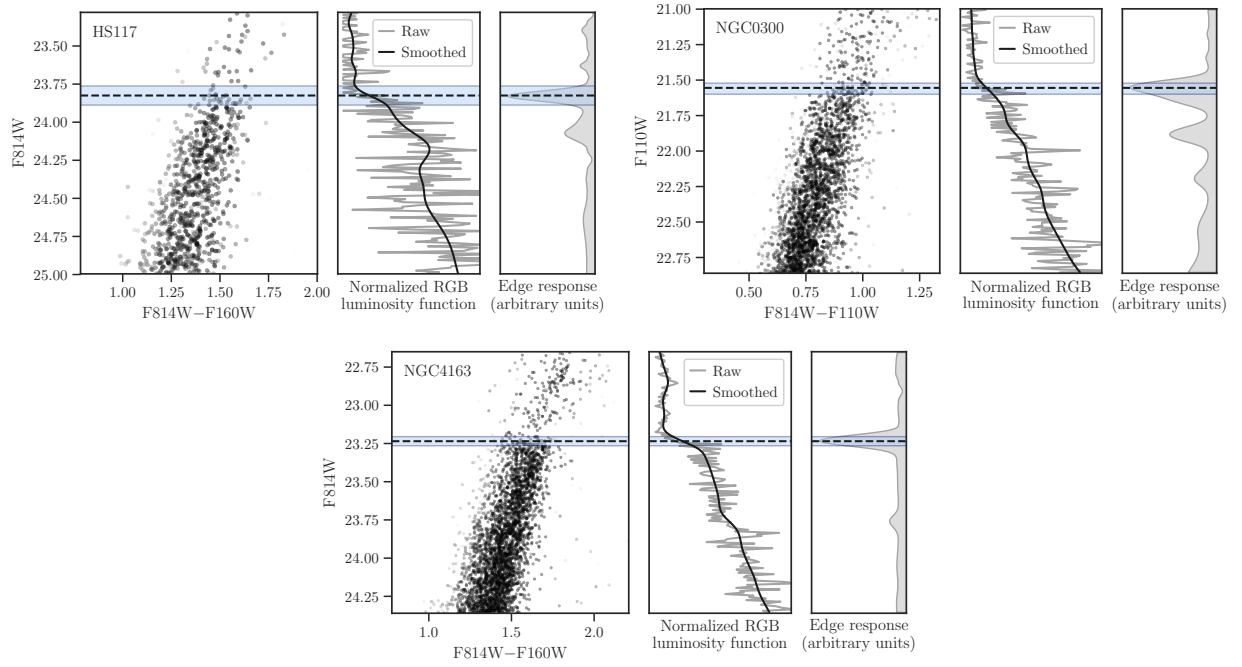


Figure 2.7: Tip star selection with edge detection for three demonstrative galaxies in our sample. From top to bottom, HS117, NGC 300, and NGC 4163. For each galaxy, three panels are shown, from left to right, the CMD of high-probability RGB stars, the raw (gray) and smoothed (black) luminosity function, and the Sobel edge response ( $\eta$ ). The initial magnitude of the TRGB is identified as the magnitude at  $\eta_{\max}$ , which is identified as the dashed line in each panel. TRGB candidate stars are selected within the blue band, the width of which is determined by the photometric uncertainty at the tip and by the number of stars on the upper RGB as described in the text. The complete figure set (23 images) is available in the online journal.

eling that accounts for uncertainties in the input data. Specifically, we use XDGMM to fit a single six-dimensional Gaussian to the F814W, F110W, and F160W magnitudes and the F814W–F160W, F814W–F110W, and F110W–F160W colors of the tip star candidates. Although the underlying distribution of tip stars in this parameter space is not intrinsically Gaussian, we find that a single Gaussian is a reasonable approximation for the majority of our tip star samples. Additionally, for the faintest and sparsest of our targets, low star counts and photometric uncertainties on the same order as the width of the tip star selection windows do not allow us to place reasonable constraints on more complex models, such as multi-component Gaussian mixtures. We discuss potential alternative modeling approaches in subsection 2.5.2.

For the uncertainties we use as inputs to XDGMM, we divide each star’s individual photometric uncertainties by  $P(\text{RGB}+)$ , effectively weighting the input points by  $P(\text{RGB}+)$ . We emphasize that XDGMM, as a tool, allows us to take into account these uncertainties and weights on the RGB+ likelihood to trace the tip in filters where the Sobel edge is less effective due to color-magnitude slopes.

We take the means of the fitted distributions to be our final apparent tip magnitudes and colors. Results of these fits are shown for our sample galaxies in Figure 2.8, where we plot ellipses showing the 95% confidence regions of the XDGMM fits in three color-magnitude combinations. The width, height, and position angle of each ellipse are derived from two-dimensional slices of the full six-dimensional covariance matrix.

Potential systematic and statistical biases of this method are discussed in Section A; overall, we find that the results are comparable to those of edge detection in most cases.

## 2.4 Results

### 2.4.1 Apparent TRGB magnitudes and colors

In this section we compare the TRGB apparent magnitudes and colors we have measured using the techniques developed in this paper to those used in D12. All revised apparent

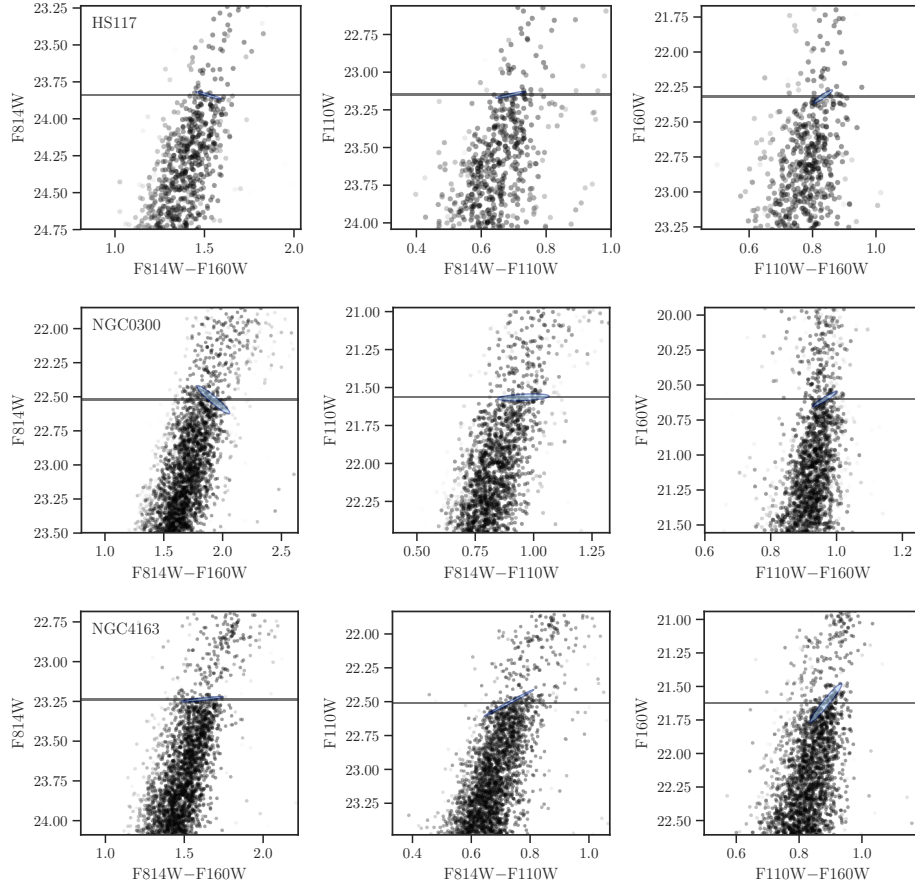


Figure 2.8: Results of XDGMM fits to candidate TRGB stars for HS117 (top), NGC 300 (middle), and NGC 4163 (bottom). For each galaxy the fits are shown for the following color-magnitude combinations: F814W, F814W–F160W (left), F110W, F814W–F110W (center), and F160W, F110W–F160W (right). The solid horizontal lines in each panel identify the mean magnitudes of the tip from XDGMM (which are typically very close to the Sobel-detected edge), and the overplotted ellipses show the 95% color-magnitude confidence regions of the two-dimensional fitted tip. We note that because this method uses a set of candidate tip stars selected based on their magnitudes in a single band (either F814W or F110W), the 2-D ellipses may not follow the visual impression of the tip in other bandpasses. This is especially apparent when the color-width of the RGB is of order the color uncertainties, which is typical in the NIR.



magnitudes and errors are reported in Table 2.3.

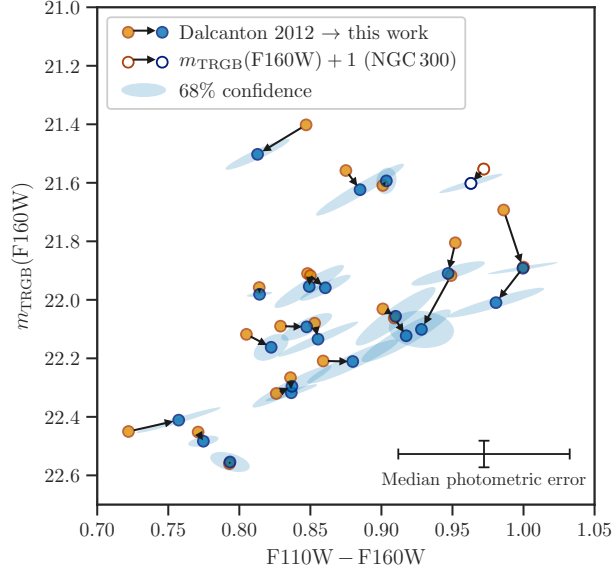


Figure 2.9: Comparison of the revised tip F160W apparent magnitudes and F110W – F160W colors from this work (blue points) to those of D12 (orange points). Arrows indicate per-target correspondence between D12 and the new measurements. The blue ellipses show the 68% confidence regions on the measurements of this paper from XDGMM fitting, and the bottom right errorbars indicate the median photometric uncertainties in color and magnitude for an individual star. For NGC 300 (unfilled points) we plot  $M_{\text{F160W}} + 1$  rather than  $M_{\text{F160W}}$ , as it is  $\sim 1$  mag brighter than the remainder of the sample. On average, our mean color-magnitude tip results are redder and slightly fainter than D12.

First, Figure 2.9 compares the change in apparent F160W magnitude and F110W–F160W color between this work (blue points) and D12 (orange points) for each target in our sample. The 68% confidence intervals are shown for our measurements and demonstrate that the difference between this work and D12 is almost always larger than our measurement uncertainties, albeit, as shown in the lower right, most are within the color-magnitude photometric error circle for an individual source at the tip.

The origin of these offsets can be determined by comparing the individual differences between the photometry. Figure 2.10 compares the relative change between the measure-

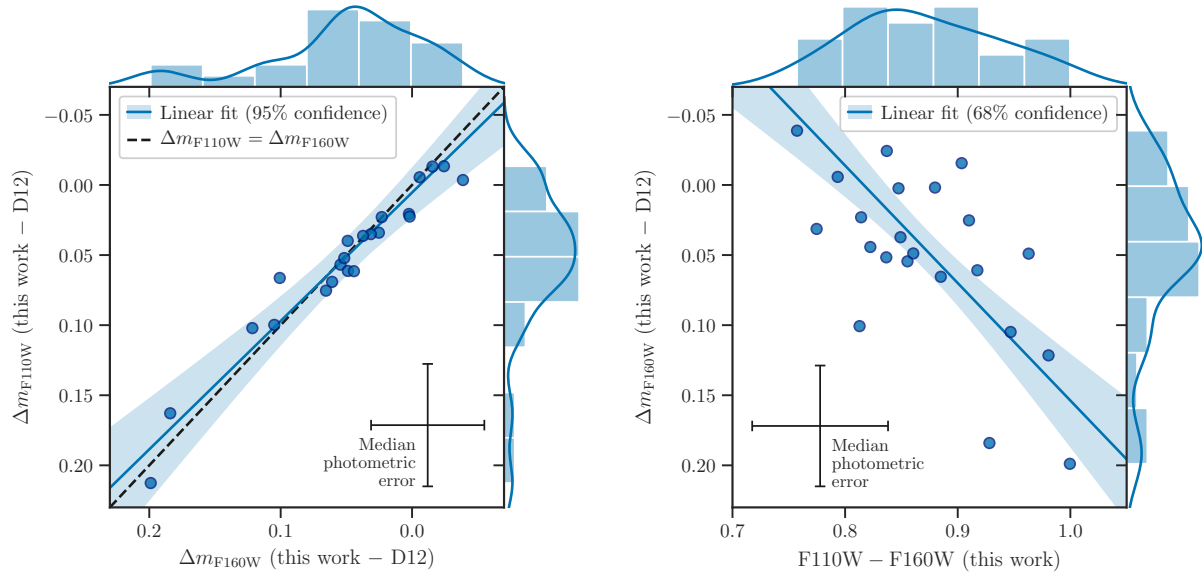


Figure 2.10: Left: changes in the  $M_{F160W}$  tip magnitudes compared to changes in the  $M_{F110W}$  TRGB magnitudes between this work and D12. Right: changes in the  $M_{F160W}$  tip magnitudes between this work and D12 against the NIR color measured in this work. Both panels show histograms with overlaid kernel density estimates of the marginal distributions of the quantities on each axis, linear fits with shaded confidence intervals, and scale bars with typical photometric uncertainties.

ments of this work and that of D12 for the F110W (x-axis) and F160W (y-axis). For both  $\Delta m_{\text{F160W}}$  and  $\Delta m_{\text{F110W}}$  (defined as this work minus D12), the median difference is approximately +0.05 mag; histograms are shown in Figure 2.10 on each axis. Interestingly, the offsets are highly correlated; in the left panel, a one-to-one line is shown in black-dashed line with a fit to the results given in blue solid, and the 95% confidence interval (shown in the shaded region) encompasses the one-to-one line. The offsets also show some color dependence, with stars at redder TRGB colors skewing systematically dimmer in this work relative to D12. We attribute this largely to differences in the populations that dominate the TRGB in the optical vs. the IR. As most of our measurements are tied to the lower-metallicity stars selected from the F814W TRGB edge, it makes sense that differences relative to direct IR-TRGB edge measurements would become more pronounced in metal-rich populations.

Figure 2.11 displays the F814W–F110W (left) and F814W–F160W (right) to F110W–F160W color-color diagrams for the results of this work (blue) compared to that of D12 (orange). Relative to D12, the measurements from this work move the color-color relations to the left in this diagram – bluer in F814W–F110W and F814W–F160W and slightly redder in F110W–F160W.

In Figure 2.11 we provide reference lines to highlight the color behavior, using a linear function for the D12 photometry and a logistic function for our new photometry. (We caution that these fitting relations should not be taken as physically meaningful.)

#### 2.4.2 *The TRGB color-absolute magnitude relation*

To derive the color dependence of the NIR TRGB absolute magnitude, we must adjust the apparent magnitudes in Figure 2.9 by the appropriate distance modulus for each galaxy.

We first present a revised NIR color-absolute magnitude relation adopting the same distances as in D12, and then explore the use of the most up-to-date stellar models to derive revised distance moduli and absolute magnitudes.

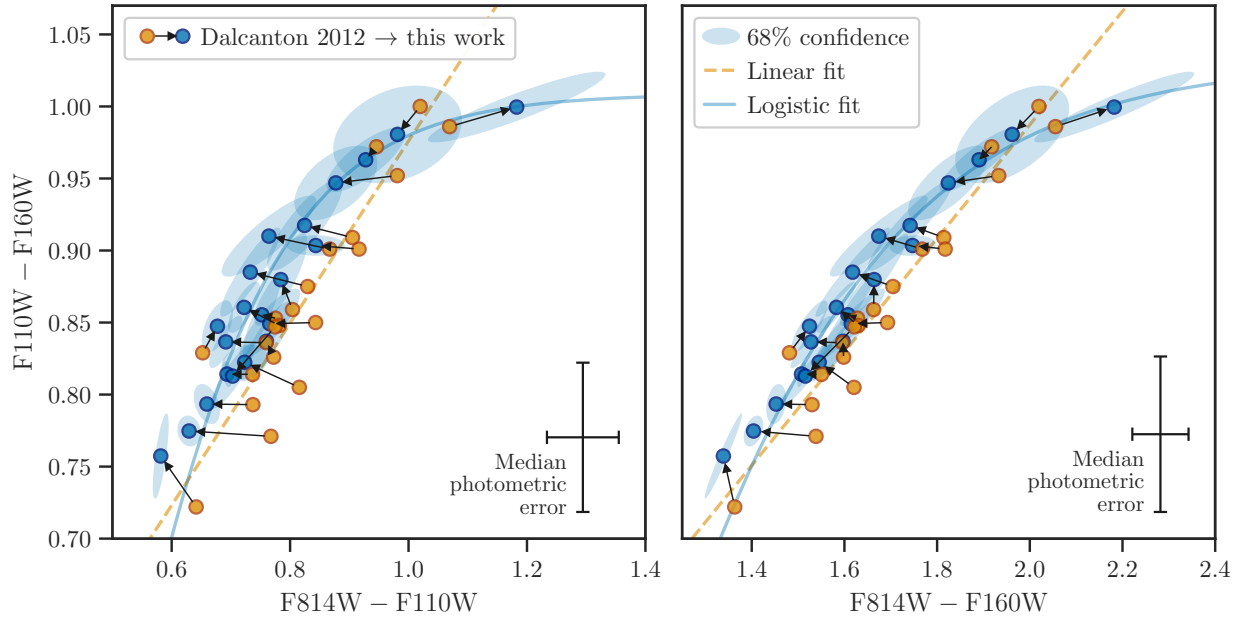


Figure 2.11: Comparison of D12 color-color relation to the TRGB color-color relation determined in this work, with  $F110W - F160W$  against  $F814W - F110W$  (left) and  $F814W - F160W$  (right). As in Figure 2.9, orange points are from D12, blue points are from this work, arrows connect the corresponding results, and the blue shading indicates our two-dimensional uncertainties from XDGM. We show a linear fit to the D12 values (as done in that work) and a generalized logistic fit to values from this work to highlight the changes in morphology in our new color-color relations.

Table 2.3: Apparent TRGB magnitudes

Target	F814W			F110W			F160W			$N_{\star}$
	$m$	$\sigma_{\text{fit}}$	$\sigma_{\text{phot}}$	$m$	$\sigma_{\text{fit}}$	$\sigma_{\text{phot}}$	$m$	$\sigma_{\text{fit}}$	$\sigma_{\text{phot}}$	
DDO71	23.742	0.002	0.015	22.990	0.022	0.047	22.134	0.040	0.048	1478
DDO78	23.730	0.005	0.032	22.966	0.050	0.042	22.056	0.066	0.042	1948
DDO82	23.864	0.005	0.044	23.040	0.041	0.051	22.123	0.060	0.051	4525
ESO540-030	23.617	0.007	0.036	22.940	0.023	0.039	22.092	0.031	0.043	631
HS117	23.845	0.011	0.036	23.154	0.009	0.045	22.318	0.019	0.040	592
IC2574-SGS	23.875	0.005	0.040	23.091	0.031	0.062	22.211	0.050	0.057	5227
KDG73	23.887	0.021	0.031	23.258	0.023	0.046	22.483	0.024	0.052	312
KKH37	23.542	0.004	0.032	22.819	0.020	0.044	21.959	0.030	0.048	902
M81-DEEP	24.074	0.103	0.013	22.892	0.021	0.039	21.892	0.024	0.035	551
NGC0300	22.493	0.043	0.017	21.565	0.009	0.022	20.602	0.022	0.022	1350
NGC2403-HALO-6	23.340	0.020	0.027	22.497	0.036	0.027	21.593	0.036	0.028	378
NGC2976-DEEP	23.734	0.055	0.027	22.857	0.016	0.044	21.910	0.028	0.040	1771
NGC3077-PHOENIX	23.972	0.080	0.016	22.990	0.015	0.044	22.010	0.034	0.041	1136
NGC3741	23.488	0.004	0.034	22.795	0.005	0.043	21.981	0.006	0.043	798
NGC4163	23.241	0.007	0.030	22.508	0.039	0.038	21.623	0.059	0.039	2429
NGC7793-HALO-6	23.868	0.007	0.051	23.029	0.046	0.032	22.101	0.042	0.038	866
SCL-DE1	24.007	0.028	0.015	23.348	0.034	0.049	22.554	0.030	0.052	454
SN-NGC2403-PR	23.416	0.076	0.067	22.457	0.030	0.100	21.489	0.032	0.079	1641
UGC4305	23.569	0.004	0.034	22.803	0.034	0.050	21.954	0.049	0.049	4883
UGC4459	23.708	0.004	0.034	22.985	0.028	0.044	22.162	0.031	0.048	1292
UGC5139	23.893	0.003	0.021	23.133	0.031	0.047	22.296	0.048	0.050	2015
UGC8508	23.018	0.005	0.027	22.315	0.021	0.032	21.503	0.035	0.034	1402
UGCA292	23.750	0.021	0.028	23.168	0.023	0.044	22.411	0.035	0.048	177

### *Adopting D12 distances*

The distance moduli used in D12 were determined using the F814W TRGB, which enables a fully self-consistent study of the TRGB across bandpasses. With the exception of NGC 7793, these distances were originally published in Dalcanton et al. (2009), whereas the distance for NGC 7793 is from Karachentsev et al. (2003), which also uses the F814W TRGB. The absolute calibration of the F814W (ground-based *I*-band) TRGB at  $< 5\%$  precision is unclear (Jang & Lee 2017b; Beaton et al. 2018; Freedman et al. 2019; Yuan et al. 2019; Reid et al. 2019; Freedman et al. 2020). Historically, it has been assumed to be a constant value of approximately  $M_{\text{TRGB}}^I \sim -4.05$  mag (Lee et al. 1993; Salaris & Cassisi 1997). However, this magnitude is only anticipated to be roughly constant for uniformly old and metal-poor populations (Beaton et al. 2018; Serenelli et al. 2017; Salaris & Cassisi 2006); more specifically,  $[M/H] < -0.5$  dex and  $> 4$  Gyr.

The stellar populations in the D12 sample, however, span a wide range of ages and metallicities that preclude the assumption of a single value for the TRGB F814W luminosity. Rather than adopting a single value for  $M_{\text{TRGB}}^{\text{F814W}}$ , Dalcanton et al. (2009) used the mean optical colors of stars within 0.2 mag of the apparent F814W TRGB to choose fiducial Girardi et al. (2008) isochrones with corresponding colors. Dalcanton et al. (2009) then determined the predicted F814W TRGB absolute magnitude for each galaxy from the isochrone sets, subtracted that from their measured F814W TRGB apparent magnitudes, and corrected for foreground extinction to obtain their distance moduli.

We calculate NIR TRGB absolute magnitudes by subtracting the D12 distance moduli from our apparent tip magnitudes, as reported in Table 2.4. The resulting NIR absolute magnitudes and color-magnitude relation are compared to that of D12 in Figure 2.12.

We fit a linear relation to the absolute F160W magnitudes and F110W–F160W colors determined in this work using orthogonal distance regression (ODR, Boggs et al. 1987), and find:

$$M_{\text{TRGB}}^{\text{F160W}} = -2.541(\text{F110W} - \text{F160W}) - 3.475 \quad (2.1)$$

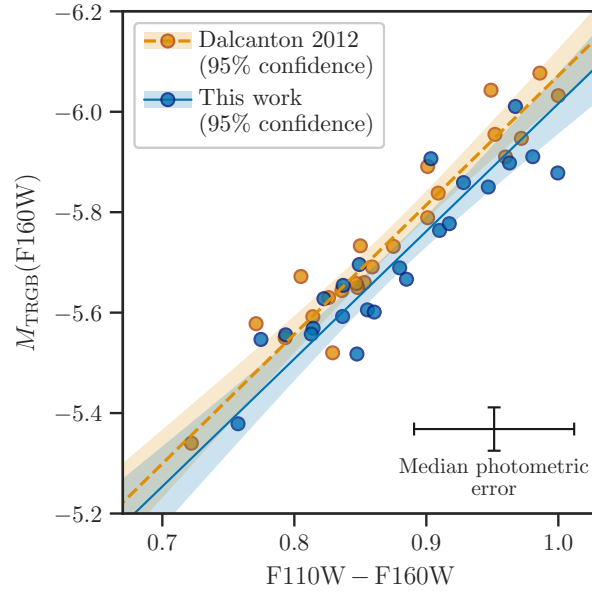


Figure 2.12: Comparison of revised NIR color-absolute magnitude relations to D12 with revised absolute magnitudes derived using the same distances as in D12. Blue points are values from the current work and orange points are from D12. The corresponding color-coded lines show linear fits to each dataset and the shaded regions show 95% confidence intervals. Again, we see that our results are slightly redder and slightly fainter than D12 using their distances. This color-color relation is distance-independent.

The uncertainties on our slope and zeropoint are  $0.057 \text{ mag color}^{-1}$  and  $0.050 \text{ mag}$ , respectively. Compared to the equivalent fit from D12 (their eq. 1),

$$M_{\text{TRGB}}^{\text{F160W}} = -2.576(\text{F110W} - \text{F160W}) - 3.496, \quad (2.2)$$

we find an  $0.02 \text{ mag}$  fainter zero-point ( $< 1\%$  in distance) and a change in the slope of less than  $0.04 \text{ mag color}^{-1}$ , both of which are well within our uncertainties. As expected, the difference in the zeropoint is roughly equivalent to the differences in measured TRGB photometry observed in Figure 2.9.

### *Recalibrating Distances to Recent Models*

Both the physical isochrones and the filter transformations described in Girardi et al. (2008) have undergone many revisions in the intervening years (Bressan et al. 2012; Marigo et al. 2017), and thus the F814W TRGB zeropoints adopted in D09 and D12 may no longer be appropriate. Here we apply a similar distance estimation method as in D09 to our revised measurements, using synthetic photometry from the model suites PARSEC v. 1.2S<sup>2</sup> (Bressan et al. 2012; Marigo et al. 2017) and MIST v. 1.2<sup>3</sup> (Choi et al. 2016), both of which are used routinely for stellar populations work. We retrieved the synthetic photometry directly from the cited web services. For both sets, we use isochrones with ages spanning 8 to 14 Gyr with  $\log(\text{age})$  spacing of 0.05 dex. The PARSEC metallicities span  $-2.2 \leq [\text{Fe}/\text{H}] \leq 0$  dex with a spacing of 0.1 dex, whereas the MIST metallicities span  $-2.0 \leq [\text{Fe}/\text{H}] \leq 0$  dex with a spacing of 0.25 dex. Both model suites use scaled-solar abundances, albeit with slightly different calibrations ( $Z_{\odot} = 0.0152$  and  $Y_{\odot} = 0.275556$  for PARSEC, and  $Z_{\odot} = 0.0142$  and  $Y_{\odot} = 0.2703$  for MIST). We use the evolutionary phase tags in each model set to select the predicted TRGB at each age/metallicity combination.

For each of these model sets, we estimate new sets of distance moduli using two color-magnitude combinations: (i) F814W vs. F814W–F160W and (ii) F160W vs. F110W–F160W.

---

<sup>2</sup>[http://stev.oapd.inaf.it/cgi-bin/cmd\\_3.3](http://stev.oapd.inaf.it/cgi-bin/cmd_3.3)

<sup>3</sup><http://waps.cfa.harvard.edu/MIST/index.html>



Table 2.4: Absolute TRGB magnitudes from D12 distances

Target	$\mu$ (D12)	$M_{F814W}$	$\sigma_{F814W}$	$M_{F110W}$	$\sigma_{F110W}$	$M_{F160W}$	$\sigma_{F160W}$
DDO71	27.740	-3.998	0.016	-4.750	0.052	-5.606	0.062
DDO78	27.820	-4.090	0.033	-4.854	0.065	-5.764	0.078
DDO82	27.900	-4.036	0.044	-4.860	0.066	-5.777	0.079
ESO540-030	27.610	-3.993	0.037	-4.670	0.046	-5.518	0.053
HS117	27.910	-4.065	0.037	-4.756	0.045	-5.592	0.044
IC2574-SGS	27.900	-4.025	0.040	-4.809	0.069	-5.689	0.076
KDG73	28.030	-4.143	0.037	-4.772	0.051	-5.547	0.057
KKH37	27.560	-4.018	0.032	-4.741	0.049	-5.601	0.056
M81-DEEP	27.770	-3.696	0.104	-4.878	0.045	-5.878	0.043
NGC0300	26.500	-4.007	0.046	-4.935	0.024	-5.898	0.031
NGC2403-HALO-6	27.500	-4.160	0.034	-5.003	0.045	-5.907	0.046
NGC2976-DEEP	27.760	-4.026	0.061	-4.903	0.047	-5.850	0.049
NGC3077-PHOENIX	27.920	-3.948	0.082	-4.930	0.047	-5.910	0.053
NGC3741	27.550	-4.062	0.035	-4.755	0.043	-5.569	0.044
NGC4163	27.290	-4.049	0.031	-4.782	0.055	-5.667	0.070
NGC7793-HALO-6	27.960	-4.092	0.052	-4.931	0.056	-5.859	0.057
SCL-DE1	28.110	-4.103	0.031	-4.762	0.060	-5.556	0.060
SN-NGC2403-PR	27.500	-4.084	0.101	-5.043	0.105	-6.011	0.086
UGC4305	27.650	-4.081	0.034	-4.847	0.060	-5.696	0.069
UGC4459	27.790	-4.082	0.034	-4.805	0.052	-5.628	0.057
UGC5139	27.950	-4.057	0.022	-4.817	0.056	-5.654	0.069
UGC8508	27.060	-4.042	0.027	-4.745	0.039	-5.557	0.049
UGCA292	27.790	-4.040	0.035	-4.622	0.049	-5.379	0.060

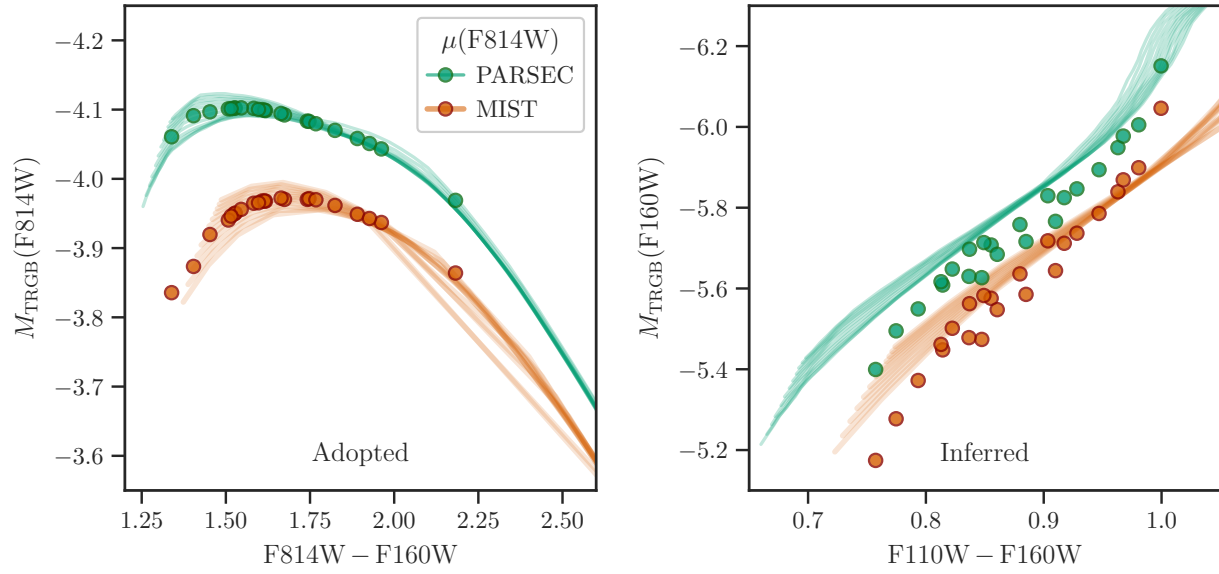


Figure 2.13: Revised absolute tip magnitudes using distance moduli calibrated to  $M_{\text{F814W}}$  versus  $\text{F814W}-\text{F160W}$  derived from synthetic photometry from the MIST (orange) and PARSEC (green) model suites. Each solid line represents a set of theoretical tip star colors and absolute magnitudes at a single age. In the left panel, we tie the observed colors to an absolute magnitude in either isochrone set to determine  $\mu_{\text{F814W}}$ . On the right, we use  $\mu_{\text{F814W}}$  to determine  $M_{\text{TRGB}}^{\text{F160W}}$  and plot against our  $\text{F110W}-\text{F160W}$  color; we find that these measurements are systematically offset from the corresponding isochrone models.

For most of our color measurements, there are multiple isochrones with TRGB colors that fall within the measurement uncertainties, each with slightly different absolute TRGB magnitudes. We calculate a fiducial tip absolute magnitude for each galaxy by taking the weighted mean of the isochrone absolute magnitudes, where the weights are defined by a Gaussian with a center at the measured tip color and a width from the color-uncertainty. Derived distance moduli for all color-magnitude combinations and model sets are reported in Table 2.5.

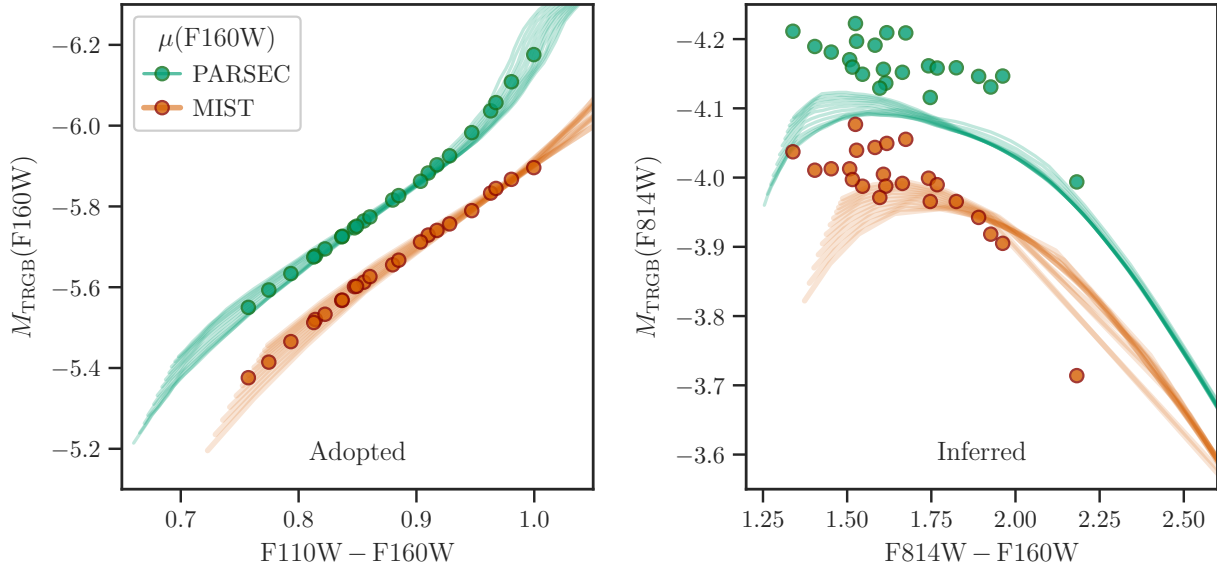


Figure 2.14: We invert the demonstration of Figure 2.13. In the left panel, we tie the observed colors to an absolute magnitude in either isochrone set to determine  $\mu_{\text{F160W}}$ . On the right, we use  $\mu_{\text{F160W}}$  to compute  $M_{\text{TRGB}}^{\text{F814W}}$  and plot against our  $\text{F814W}-\text{F160W}$  color; we again find that our measurements are systematically offset from the corresponding isochrone models. Taken with Figure 2.13, this suggests that distance moduli calibrated to models in one band will systematically mispredict the corresponding tip behavior in other bands.

The results of this procedure are shown in Figure 2.13 where the left panel shows the adopted values of  $M_{\text{TRGB}}(\text{F814W})-(\text{F814W}-\text{F160W})$  and the right panel shows the inferred values of  $M_{\text{TRGB}}(\text{F160W})-(\text{F110W}-\text{F160W})$ . In each panel, sets of synthetic photometry at single ages (8-13 Gyr), with metallicities spanning  $-2.0 < [\text{Fe}/\text{H}] < -0.25$  dex, are plotted as transparent lines, with PARSEC models plotted in green and MIST models in orange.

Overall, the mag-color behavior of the two sets is qualitatively similar, but the absolute magnitudes differ by  $\Delta M_{\text{F814W}} \sim 0.15$  mag, with PARSEC being brighter than MIST for the same color ( $\sim 8\%$  in distance).

The fits of our data to the predicted  $M_{\text{TRGB}}(\text{F814W})-(\text{F814W}-\text{F160W})$  distributions are shown as the points in the panels of Figure 2.13. From this, we determine a distance modulus to each galaxy, which we denote as  $\mu_{\text{F814W}}$ . In the right panel, we use  $\mu_{\text{F814W}}$  to translate  $m_{\text{TRGB}}(\text{F160W})$  to  $M_{\text{TRGB}}(\text{F160W})$ , and compare these values to the same isochrone sets used to derive  $\mu_{\text{F814W}}$ . The PARSEC-based distances place the observed NIR TRGB  $\sim 0.05$  mag fainter than predicted, but they do trace the same underlying variations with color. In contrast, the MIST-derived values are less offset overall in magnitude, but show shape deviations that become particularly pronounced at red colors.

Figure 2.14 repeats this process in reverse by determining a distance modulus,  $\mu_{\text{F160W}}$ , based off of the  $M_{\text{TRGB}}(\text{F160W})-(\text{F110W}-\text{F160W})$  model predictions (left panel) and then comparing the absolute  $M_{\text{TRGB}}(\text{F814W})-(\text{F814W}-\text{F160W})$  empirical relationship to the models in the right panel. In this case, different behavior is observed: for both model sets,  $M_{\text{TRGB}}(\text{F814W})$  from our data are too bright by  $\sim 0.1$  mag at the blue (low-metallicity) end, and there is a slight color offset of  $\sim 0.05$  mag.

Overall Figure 2.13 and Figure 2.14 suggest that the isochrone predictions are inconsistent both with each other and, when used internally to predict multi-band magnitudes, with our measurements. We will further discuss potential reasons for these apparent inconsistencies in subsection 2.5.3.

### *New Distance Moduli Compared to D12*

Figure 2.15 compares the distance moduli determined in the previous subsection to those from D12. The top panel compares the distances calibrated to F814W (the same filter in either case) and the bottom panel compares the distances from F160W. No difference ( $\Delta\mu = 0$  mag) is indicated by the vertical dashed line. In both cases, the PARSEC-based calibration is systematically larger than in D12 by median values of  $0.043(\pm 0.069)$  mag in F814W

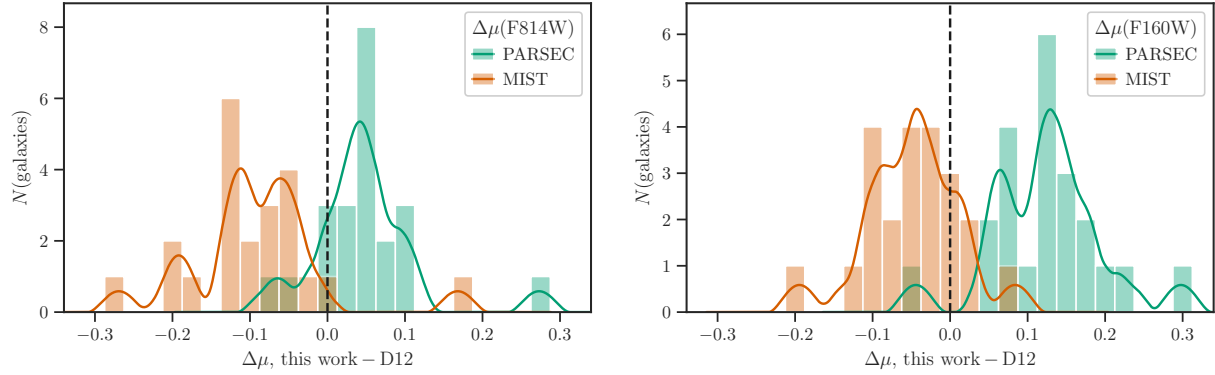


Figure 2.15: Histograms and overlaid biweight kernel density estimates of  $\Delta\mu$ , where  $\Delta\mu$  is the difference between distance moduli derived in this work and the distance moduli used in D12. The top panel shows  $\Delta\mu$  using distance moduli calibrated to  $M_{\text{F814W}}$  and the bottom shows  $\Delta\mu$  using distance moduli calibrated to  $M_{\text{F160W}}$ . These differences are much larger than those measured using the same distances (Figure 2.12) and thus can be interpreted as differences between model predictions of tip magnitudes.

and  $0.126(\pm 0.071)$  mag in F160W, corresponding to  $2(\pm 3)\%$  and  $6(\pm 3)\%$  greater distances, respectively. The MIST calibrations, on the other hand, are systematically smaller, with median differences of  $-0.096(\pm 0.084)$  mag in F814W and  $-0.045(\pm 0.063)$  mag in F160W ( $4(\pm 4)\%$  and  $2(\pm 3)\%$  closer respectively).

## 2.5 Discussion

In this section, we discuss the advantages and limitations of our adopted methods to trace the TRGB across multiple wavelengths. Once established, we then discuss more fundamental limitations to our investigation, which include knowledge of the absolute magnitude of the TRGB, details of the physical models underlying the isochrone suites, and possible systematics that are difficult to disentangle with the data at hand.

Table 2.5: New distance moduli

Target	PARSEC				MIST			
	F814W		F160W		F814W		F160W	
	$\mu$	$\sigma$	$\mu$	$\sigma$	$\mu$	$\sigma$	$\mu$	$\sigma$
DDO71	27.842	0.065	27.899	0.093	27.710	0.065	27.747	0.093
DDO78	27.822	0.093	27.939	0.100	27.700	0.093	27.785	0.100
DDO82	27.948	0.101	28.026	0.109	27.835	0.101	27.864	0.109
ESO540-030	27.719	0.072	27.839	0.080	27.566	0.072	27.694	0.080
HS117	27.948	0.072	28.042	0.075	27.796	0.072	27.885	0.075
IC2574-SGS	27.969	0.094	28.027	0.115	27.847	0.094	27.866	0.115
KDG73	27.978	0.072	28.077	0.090	27.761	0.072	27.898	0.090
KKH37	27.643	0.072	27.733	0.087	27.506	0.072	27.585	0.087
M81-DEEP	28.043	0.162	28.068	0.070	27.938	0.162	27.788	0.070
NGC0300	26.551	0.079	26.639	0.047	26.441	0.079	26.435	0.047
NGC2403-HALO-6	27.423	0.061	27.456	0.060	27.311	0.061	27.306	0.060
NGC2976-DEEP	27.804	0.098	27.893	0.079	27.696	0.098	27.699	0.079
NGC3077-PHOENIX	28.015	0.124	28.118	0.083	27.909	0.124	27.877	0.083
NGC3741	27.590	0.065	27.659	0.075	27.429	0.065	27.501	0.075
NGC4163	27.340	0.079	27.450	0.091	27.209	0.079	27.290	0.091
NGC7793-HALO-6	27.948	0.091	28.026	0.077	27.838	0.091	27.858	0.077
SCL-DE1	28.104	0.064	28.188	0.094	27.926	0.064	28.020	0.094
SN-NGC2403-PR	27.467	0.158	27.546	0.155	27.358	0.158	27.334	0.155
UGC4305	27.668	0.084	27.705	0.099	27.537	0.084	27.557	0.099
UGC4459	27.810	0.074	27.857	0.087	27.664	0.074	27.695	0.087
UGC5139	27.993	0.075	28.022	0.099	27.858	0.075	27.864	0.099
UGC8508	27.119	0.064	27.178	0.069	26.964	0.064	27.015	0.069
UGCA292	27.811	0.071	27.961	0.091	27.586	0.071	27.787	0.091

Table 2.5 notes: Quoted errors are the quadrature sum of the photometric and fitting errors.

### 2.5.1 *Advantages of the MCR-TRGB method*

MCR-TRGB simultaneously measures the distributions of a pre-selected group of stars across an arbitrary number of color-magnitude combinations. As a result, the method ensures self-consistency in the measured color-magnitude behavior as it is determined from the same underlying set of stars. In contrast, traditional edge detection is done on a per-filter basis, and it is not guaranteed to detect the tip using precisely the same stars across color-magnitude combinations. This limitation is particularly important in the cases of steeply-sloped tips where the corresponding color-baseline changes significantly relative to the color-uncertainty.

Fitting the full color-magnitude covariance has the further benefit of characterizing spread of colors and magnitudes both intrinsically, e.g., within a galaxy, and experimentally, e.g., with respect to our photometric precision. This differs from Sobel-based edge detection where it is difficult to properly account for measurement uncertainties in both magnitude and color. Moreover, Sobel-based edge detection does not automatically account for intrinsic color-magnitude variation across a given TRGB and, as a result, the Sobel-edges are generalized to a mean color on a per-filter basis.

Unlike the  $T$ -magnitude system of Madore et al. (2009), which rectifies the photometry to an assumed TRGB slope, MCR-TRGB relies only on the assumption that there is one filter in which the tip magnitude has a weak enough color dependence enough to make an initial selection of tip star candidates. This permits us to use the well-established Sobel method to find a “flat” edge to define candidate tip stars and then utilize those stars in regimes where the tip is more difficult to detect using Sobel-based methods. This provides a fundamental advantage toward revealing the underlying intrinsic behavior of TRGB stars to construct self-consistent color-magnitude calibrations.

We posit that MCR-TRGB is a more effective tool to define the underlying color-magnitude calibrations for local, well-studied, and well-observed galaxies than relying on techniques more suited for distant galaxies. Stated differently, if your goal is to provide the best characterization of the behavior of tip stars across multiple bands, MCR-TRGB

will perform better than standard Sobel-edge detection. It also provides a fully empirical basis to explore the ultimate precision of the TRGB as distance-measurement tool, from which we can gain understanding of both systematic and statistical biases for more distance measurements where there is a lower ability to probe these terms with available data.

### *2.5.2 Limitations of MCR-TRGB*

Our method requires multi-wavelength data and relatively good data quality, which makes it less generally applicable to all distance measurement applications. More specifically, MCR-TRGB requires fairly stringent initial rejection of potential contaminants, which may not be feasible for all datasets due to photometric uncertainties or the complexity of the underlying stellar populations. Moreover, the multiwavelength tracing of individual TRGB stars may also be infeasible for many contexts where the acquisition of multiband imaging is too expensive. Thus, as just discussed, we consider MCR-TRGB’s most significant role is as a tool to define the underlying systematics affiliated with TRGB-based distances as the community explores different color-magnitude regimes.

The XDGMM algorithm used in MCR-TRGB loses its ability to resolve the shape of an intrinsic distribution when the typical uncertainties on the input data points are comparable to the full range of the input data. This method loses its advantages for low signal-to-noise photometry, filter combinations with very short color baselines, and simple stellar populations with little color spread near the TRGB. (See Section A for further discussion.)

Another limitation of XDGMM is its assumption of Gaussianity. In practice, the intrinsic distribution of TRGB stars within a given magnitude range is far from Gaussian. More complex models of this distribution should be investigated, ideally on high-precision photometry of systems with well-populated RGB sequences. For example, a multi-component Gaussian mixture could be of use in distinguishing remaining contaminants, such as a low-density AGB “background”, from the TRGB population. Alternate fitting methods, such as Gaussian process regression, should also be considered. We reserve tests of this nature for future exploration using local galaxies with properties and observations that are better



matched to the requirements of drawing conclusions from such tests.

### 2.5.3 *Absolute Calibration*

In Section 2.4.2, Figures 2.13 and 2.14 introduce a puzzle with regards to using synthetic photometry as the absolute calibration for the TRGB. Inspection of Figures 2.13 and 2.14 reveal two concerns for the isochrone sets: (i) a systematic offset between PARSEC and MIST is present for the absolute magnitudes regardless of filter, such that PARSEC is consistently brighter than MIST, and (ii) there is a relative filter-to-filter offset between the models' predictions and our measurements, such that the absolute NIR magnitudes of our measurements derived by adopting the models' optical predictions do not correspond to the models' NIR predictions, and vice versa. Understanding these differences requires considering how stellar interior models, which predict stellar structure, are mapped to stellar atmospheres used to construct the synthetic photometry shown in Figures 2.13 and 2.14. An excellent discussion of this process is given by Casagrande & VandenBerg (2014).

Before examining the models more closely, we note that such offsets should not be surprising when viewed in the context of the larger literature. Even in the well-studied F814W/*I*-band, there is a current debate in the value of the absolute magnitude of the TRGB, which is central to determining  $H_0$  (e.g., see Freedman et al. 2019; Yuan et al. 2019; Reid et al. 2019; Freedman et al. 2020, and references therein). Even the most detailed and careful calibrations have total uncertainties at the 0.05 mag level due to various systematic terms. The range of recently used F814W absolute values spans  $\sim 0.10$  mag (as reviewed by Beaton et al. 2018). These discrepancies in the absolute magnitude of the tip can propagate into stellar models depending on exactly how the isochrone sets cross-check their own absolute scales. As reviewed by Beaton et al. (2018), such discrepancies also affect the RR Lyrae and horizontal branches, which imparts uncertainty on the absolute scale for globular clusters (as are explored in detail by Casagrande & VandenBerg 2014). Therefore, no theoretical predictions can be expected immune to the downstream effects of systematics in the empirical distance scale.

In this subsection, we first present a preliminary comparison of our results to the empirical TRGB relation derived for the  $(F606W-F814W)-M_{F814W}$  color-magnitude plane by Jang & Lee (2017b), and discuss its implications with regard to assessing differences in the models' behavior. We then consider two aspects of the synthetic photometry that might contribute to the discrepancies in Figures 2.13 and 2.14: (i) differences in adopted stellar atmospheres, which affect the conversion from bolometric luminosity to observed fluxes in specific filters, discussed in section 2.5.3, and (ii) differences in the underlying stellar evolution physics, discussed in section 2.5.3.

#### *Comparison to empirical optical results*

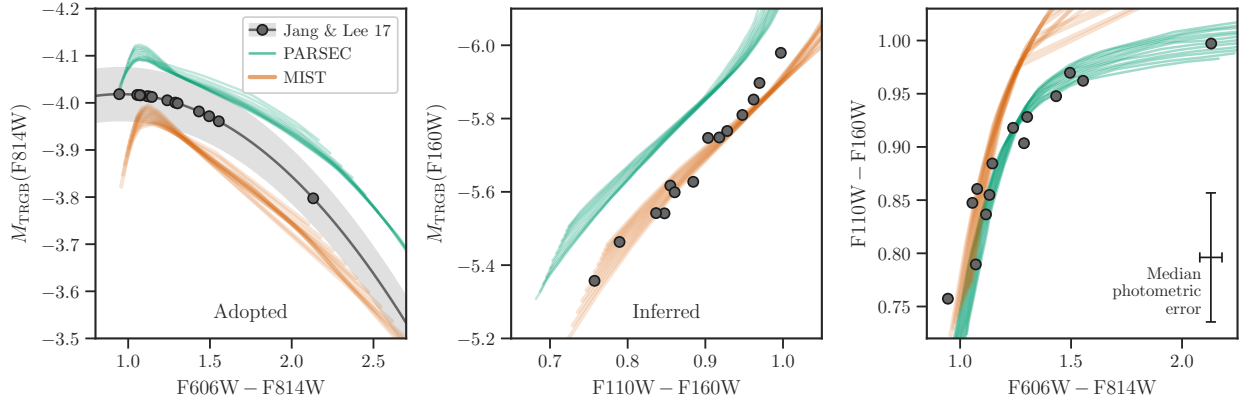


Figure 2.16: As in Figure 2.13, we infer absolute F160W magnitudes via adopted F814W absolute magnitudes. Here the F814W absolute magnitudes are calibrated to the F814W vs.  $F606W-F814W$   $QT$  relation presented by Jang & Lee (2017b) for the subset of our sample with F606W coverage. We overplot MIST (orange) and PARSEC (green) synthetic photometry for comparison. Left: The  $QT$  relation with adopted  $M_{F814W}$  values. Center: Inferred  $M_{F160W}$  vs.  $F110W-F160W$ . Right: Distance-independent  $F110W-F160W$  vs.  $F606W-F814W$  color-color plot.

The discrepancies between our measurements and both sets of synthetic photometry in Figures 2.13 and 2.14 make it unclear which model should be preferred, if either. As an alternative, we turn to the empirical F814W TRGB calibration presented by Jang & Lee

(2017b). Like the majority of existing empirical F814W/ $I$  calibrations, it is based on a specific optical color baseline (F606W–F814W), which precludes us from adopting it for our entire sample, as F814W is the only optical filter common to all our targets. However, the subset of our sample with F606W observations (14 out of 23 targets) allows us to make a preliminary comparison as a benchmark against theoretical calibrations.<sup>4</sup>

Jang & Lee (2017b) employ a quadratic functional form (the  $QT$  system) for the  $M_{\text{F814W}}$  vs. (F606W–F814W) relation, which they calibrate over an extensive color range of  $0.8 < \text{F606W} - \text{F814W} < 3$  mag. We show the results of adopting the  $QT$  relation for the galaxies in our sample with F606W coverage in Figure 2.16.

Figure 2.16 shows that the Jang & Lee calibration falls squarely between the PARSEC and MIST predictions in F814W. Adopting the distances from this calibration, we then plot the inferred absolute magnitude in the F160W band in the center panel. The resulting F160W TRGB absolute magnitudes agree quite well with the MIST predictions in the NIR. We explore this apparent color mismatch further in the right panel, which compares the optical F606W–F814W colors to the NIR F110W–F160W colors for the 14 galaxies with F606W data. Although the center panel of Figure 2.16 appears to favor MIST predictions in the NIR at all but the reddest colors, the optical-IR color-color behavior strongly favors PARSEC.

### *Bolometric corrections*

We make a direct comparison of the models’ physical predictions in the left panel of Figure 2.17, which compares the MIST and PARSEC model TRGB in temperature-luminosity space for the same range of ages and metallicities as in Figures 2.13 and 2.14. We see that the models are offset from each other in  $T_{\text{eff}}$  and  $\log(L/L_{\odot})$ , indicating differences in the underlying stellar structure, with PARSEC running approximately  $\sim 10\%$  more luminous and 50-150 K warmer than MIST at the same age and metallicity. (For comparison, Choi et al.

---

<sup>4</sup>A more detailed analysis that incorporates recently revised distances to the two absolute-scale zeropoint anchors used by Jang & Lee (2017b) is currently in preparation.

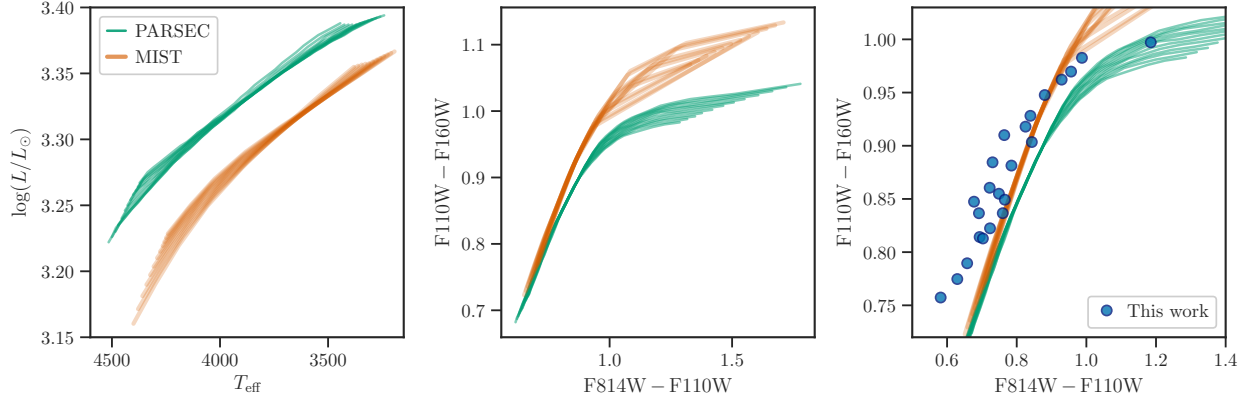


Figure 2.17: Left: Bolometric luminosity vs. effective temperature for the MIST (orange) and PARSEC (green) model tip stars used in this work (ages 8 - 14 Gyr and  $-2 \leq [\text{Fe}/\text{H}] \leq -0.25$  dex). PARSEC luminosities are found to be consistently  $\sim 1.1$  times brighter than MIST at the same age and metallicity. Center:  $(F110W - F160W)$  vs.  $(F814W - F110W)$  color-color plots for MIST and PARSEC tip star predictions. Right: Color-color results of this work overlaid on MIST and PARSEC predictions.

(2018a) find uncertainties on the absolute  $T_{\text{eff}}$  scale of  $\pm 100$  K due to boundary conditions.) The PARSEC predictions also show a slightly larger spread in  $T_{\text{eff}}$  than MIST over the same range of age and metallicity.

We attempt to isolate filter-to-filter differences between the models' predictions by examining their color-color behavior. The middle panel of Figure 2.17 shows the  $F814W - F110W$  to  $F110W - F160W$  color-color behavior of the two model sets. There is a divergence on the order of 0.1 mag for stars with  $F814W - F110W > 1$  mag, indicating significant differences in the model atmospheres of cooler stars. Close inspection of the bluer side shows that although the color-color relations have similar slopes, they are slightly offset from one another at the same metallicity.

We compare these color-color predictions to our measurements in the right panel of Figure 2.17, which overlays the color-color results derived via the MCR-TRGB technique. Unlike Figures 2.13 and 2.14, the color-color relations are distance-independent, which alleviates concerns about the absolute scale of the measurements. The observed TRGB is systemati-

cally redder than predicted in F110W–F160W and/or systematically bluer in F814W–F110W (which appears to effectively rule out unaccounted-for extinction as a source of disagreement). Comparison to the right panel of Figure 2.16, which shows good agreement between observations and PARSEC predictions for F606W–F814W and F110W–F160W colors, suggests that PARSEC’s predicted TRGB colors are overall accurate in the optical and IR independently, but that there may be offsets in the relative cross-calibration between the two wavelength regimes in either the stellar atmosphere models or in our data. More specifically, if PARSEC’s predicted F110W and F160W absolute magnitudes were shifted to be  $\sim 0.1$  mag dimmer (or if our NIR measurements were 0.1 mag brighter) with no changes to the optical, the predicted and observed F814W–F110W colors would be brought into alignment, with no change to the F110W–F160W or F606W–F814W colors.

The stellar atmospheres used to generate synthetic photometry are encoded as bolometric corrections, which transform bolometric luminosities into filter-specific quantities. The bolometric corrections depend primarily on  $\log(g)$ ,  $T_{\text{eff}}$ , and both  $[\text{Fe}/\text{H}]$  and  $[\alpha/\text{H}]$ . While the differences in predicted bolometric luminosities shown in the left panel of Figure 2.17 suggest that PARSEC and MIST would still predict different absolute magnitudes for a tip star of a given age and metallicity, bolometric corrections and the stellar  $T_{\text{eff}}$  scale are likely to be a source of some of the filter-to-filter offsets we observe.

As of this writing, the PARSEC web service (CMD v. 3.3) uses PHOENIX (Allard et al. 2012) bolometric corrections for stars with  $T_{\text{eff}} < 5500$  K ( $\sim 1000$  K warmer than the warmest TRGB stars), and MIST uses ATLAS12 (Kurucz 2014). Chen et al. (2019b) have explored how the PHOENIX (Allard et al. 2012) and ATLAS9 (Kurucz 2014) model atmospheres affect predicted colors and magnitudes of PARSEC isochrones in optical and IR passbands. Their Figure 2 shows that the PHOENIX bolometric corrections produce RGB colors that are biased red by up to 0.1 mag in  $V - I$ , which translates to an artificially bright TRGB in the NIR consistent with what we see in Figures 2.13 and 2.14. Although Chen et al. (2019b) claim that the PHOENIX bolometric corrections are preferable for giants because they are computed with spherical geometry, Fu et al. (2018, section 3.2.3) find that the PHOENIX bolometric

corrections cannot reproduce the observed RGB colors in 47 Tuc, which they term the “RGB-too-red” problem. While we have been unable to locate any similar such studies of MIST’s predictions for the RGB, Fu et al. (2018) caution that **ATLAS12** atmospheres may be unreliable for  $T_{\text{eff}} < 4000$  K, which may explain the divergence we see between the MIST and PARSEC predictions at  $F814W-F110W > 1$  in the center panel of Figure 2.17.

Similar evidence for the importance of bolometric corrections for the optical TRGB was explored by Serenelli et al. (2017), who directly compared the predicted absolute magnitudes of the *I*-band TRGB from the BaSTI models (Pietrinferni et al. 2013) using four sets of bolometric corrections (see their fig. 8). They see differences at the  $\sim 10\%$  level when applying different sets of bolometric corrections to models using the same underlying physics, comparable to the amplitude of discrepancies we see here. Although this investigation focused on the optical, their finding of  $\sim 0.1$  mag discrepancies aligns with the scale of the adjustments needed to bring our measurements and the models’ predictions into alignment.

While further quantitative investigation is clearly required, we conclude that bolometric corrections are a likely source of a substantial part of the optical-IR discrepancies we observe in Figures 2.13 and 2.14.

### *Physical properties of TRGB stars*

The left-most panel of Figure 2.17 suggests that there are currently real differences in the predicted stellar structure at the TRGB due to the different physical assumptions between the models, even before differences in atmospheres or bolometric corrections are included. Our comparison of PARSEC and MIST broadly agrees with the conclusions from a more detailed model-focused study by Serenelli et al. (2017), who investigated both the physical and computational factors contributing to differences between the predicted TRGB luminosities of two sets of stellar models (BaSTI and GARSTEC). Serenelli et al. (2017) were able to produce identical predictions of tip stars’ physical properties from two different model suites only when certain physical processes, such as neutrino energy loss and electron screening, as well as some numerical criteria such as integration timestep, were implemented consistently

between stellar evolution codes (the full set of which they term “concordance physics”). While a comparable investigation of such sources of difference between MIST and PARSEC is well outside the scope of this work, we find it reasonable to conclude that some aspects of their physical differences are likely due to limitations in our current understanding of certain “cutting edge” topics in stellar astrophysics, and may also be in part due to differing computational approaches. Tip stars, in addition to being both cool and luminous, are at an evolutionary transition point, and so may be especially sensitive to these details.

Another possible source of disagreement between the models’ predictions and our data is elemental abundances, including the helium fraction  $Y$  and  $\alpha$  enhancement, the latter of which is of particular concern at  $[\text{Fe}/\text{H}] \lesssim -1$  dex ( $\text{F110W} - \text{F160W} \lesssim 0.9$  mag for PARSEC). At present, neither MIST nor PARSEC have publicly available  $\alpha$ -enhanced models, although they are slated to be included in future releases of both (Choi et al. 2016; Fu et al. 2018). Serenelli et al. (2017) report that, at least after the adoption of their concordance physics,  $\alpha$  enhancement produces what they consider to be negligible effects on the TRGB bolometric luminosity ( $< 1\%$  difference between  $[\alpha/\text{Fe}] = 0.4$  and  $[\alpha/\text{Fe}] = 0$  at fixed  $[\text{M}/\text{H}]$ ),  $T_{\text{eff}}$  ( $< 2\%$  difference), and predicted  $VIJK$  magnitudes ( $< 0.01$  mag difference at constant color). Similarly, they find that a change in the helium fraction  $Y$  of 0.01 (approximately the range over which estimates of the primordial helium mass fraction vary) has no more than a 1% effect on TRGB temperatures and luminosities. Nonetheless, as forthcoming versions of PARSEC will offer options for variable  $\alpha$  enhancement and helium abundance (Fu et al. 2018) as well as updated bolometric corrections<sup>5</sup>, we anticipate that a direct analysis of these quantities’ impacts on predictions of TRGB behavior as they pertain to this work will be both easily achievable and informative.

---

<sup>5</sup>The PHOENIX bolometric corrections currently employed in the PARSEC web service only take total  $Z$  into account in their color transformations (Fu et al. 2018), which is problematic for understanding potential photometric effects of varying abundance ratios. ATLAS12 model atmospheres for  $\alpha$ -enhanced PARSEC isochrones down to  $T_{\text{eff}} = 4000$  K are currently in development (Fu et al. 2018; Chen et al. 2019b).

#### 2.5.4 *TP-AGB contamination*

While we believe that our method of determining  $P(\text{RGB})+$  is overall effective at rejecting contaminating populations, such as red supergiants and the bulk of the AGB, there may be some amount of remaining contamination, particularly from thermally-pulsing AGB (TP-AGB) stars, which we briefly discuss here.

Although TP-AGB stars are generally intrinsically brighter than the TRGB, extinction from circumstellar dust can substantially impact their observed magnitudes and bring them closer to luminosities typical of the upper RGB. However, as they are also heavily reddened, their colors are inconsistent with RGB stars (Boyer et al. 2017, see their fig. 8), so it is likely that our method of TRGB candidate selection successfully rejected most, if not all, of these stars.

TiO absorption is another factor that may bring certain TP-AGB stars, particularly M-type stars at high metallicity, closer in luminosity to the TRGB (Boyer et al. 2019). While the bulk of our targets are low-metallicity dwarf galaxies, this may be an issue for some of the larger galaxies in our sample, such as M81.

Finally, TP-AGB stars may cross the TRGB when they reach the minimum point in their pulsation cycle. In this case, the fact that our NIR data were taken several years later than our optical data is an advantage; TP-AGB stars at their minimum in our optical observations are unlikely to be at their minimum in the NIR, and vice versa.

#### 2.5.5 *Limited Empirical Constraints on TRGB Magnitude Stability*

We briefly discuss other physical concerns that may affect the colors and magnitudes of TRGB stars, including binarity, low amplitude pulsational variability, mass loss, and planetary engulfment.

First, the presence of a companion star may affect the intrinsic photometric properties of a TRGB star through mass transfer in a binary interaction. Preliminary investigations suggest that the photometric effects of the former phenomenon are overall secondary to



the variation of TRGB magnitude with metallicity (Eldridge 2019, private communication). Thus, we qualitatively conclude that binarity is likely to be a source of some amount of residual scatter in our measurements rather than a primary driver of TRGB variation across populations.

Second, as recent high-precision, high-cadence photometry has demonstrated, low-amplitude variability exists for many to most stellar types. Pulsational variability was first proposed for stars on the upper RGB by Ita et al. (2002) and has since been observationally confirmed (Ita et al. 2004; Lebzelter & Wood 2005; Wood 2015). Variability may contribute some amount of uncertainty to TRGB measurements by effectively blurring the TRGB edge. However, there are few established constraints on relevant characteristics, such as typical periods, amplitudes, fractions of stars that exhibit variability, and dependence on stellar properties such as age and metallicity. We have thus disregarded TRGB variability as a potential systematic in this work due to lack of empirical constraints. We expect that any overall effects are small compared to our dominant sources of uncertainty.

RGB stars are known to experience mass loss driven by chromospheric activity (Origlia et al. 2007; Groenewegen 2012; Pasquato et al. 2014), which may be amplified by either of the first two properties. Jimenez et al. (2020) predict that variations in the mass loss parameter  $\eta$  at the TRGB may affect individual stars' luminosities by over 5%, although they estimate that the net effect on measured TRGB distances does not exceed 2%, and that it is strongly metallicity-dependent. Additionally, although mass loss has been correlated with the blueshifting of optical and near-IR spectral lines such as  $H\alpha$  and the calcium triplet (McDonald & van Loon 2007; Wood 2015), the impact of this blueshifting on broadband photometry has not been quantified.

Jimenez et al. (2020) also consider planetary engulfment, wherein an RGB star consumes one or more planets in close orbit as it expands. They predict that the increased turbulence in the star's convective envelope, corresponding to an increase in mixing length, may result in a net decrease in TRGB luminosity by up to 5% for a single star that has consumed a giant planet. However, they conclude that both detailed hydrodynamical simulations and

further studies of planetary system formation are required to accurately constrain potential impacts of this phenomenon on the TRGB as a distance indicator.

Again, we expect that these effects are overall well within the uncertainties of this work, but may need to be taken under consideration in future high-precision TRGB studies.

## 2.6 Conclusions and Future Work

### 2.6.1 Conclusions

We have developed a method to measure TRGB magnitudes and colors in multiple filters simultaneously. This method, MCR-TRGB, was designed to use a set of likely RGB stars, which were defined where traditional TRGB-detection methods using edge-detection can be employed reliably, to study the multi-wavelength behavior of the TRGB using those same stars. We applied MCR-TRGB to a re-reduction of optical+NIR *HST* data originally presented in D12; these new reductions use the optical observations, which have higher spatial resolution and are generally more complete at the TRGB, to produce more complete and precise photometry in the infrared-bands. When using the same distances as D12, we find only minor adjustments to the color-magnitude behavior of the IR-TRGB. However, the D12 absolute magnitudes were determined relative to color-magnitude predictions from stellar models. Thus, we compared three different absolute-magnitude calibrations of the measured TRGB magnitudes, one using the same distance moduli as in D12, and two using distance moduli derived from the predicted TRGB absolute magnitudes from two commonly used isochrone sets (PARSEC and MIST). We find that the isochrone-based absolute calibrations are inconsistent with each other at the  $\sim 0.1$  mag level, consistent with previous work in this domain, and that both sets of isochrones are internally inconsistent with our measurements of the TRGB magnitudes and colors when optical and infrared measurements are used together. We further caution that adoption of model-based absolute calibrations for the TRGB, a conservative 10% systematic included in the calibrations for the TRGB based on differences between the isochrone sets at the TRGB. We find that these tensions persist even with

the application of a state-of-the-art empirical calibration. From examining the distance-independent color-color behavior of our data against model predictions, we conclude that bolometric corrections and the underlying stellar  $T_{\text{eff}}$  scale are likely to explain a large part of the inconsistencies we have found.

### 2.6.2 Future work

An empirical absolute TRGB calibration in WFC3/IR bandpasses remains elusive. A fully model-independent calibration, as in Jang & Lee (2017b), is clearly necessary. However, there are a limited number of systems that are distant enough that their apparent TRGB magnitudes are easily observable with *HST*, but nearby enough to have distances that are well-constrained by other means.

Another limitation of our study is the lack of precise independent distances to the galaxies in this work. Indeed, the majority of these systems *only* have distances determined from the TRGB itself. Some of these galaxies are within a volume for variable-star based distances with *HST*, though we are cautious about their precision given the metallicity dependence of such relations and the difficulty of inferring stellar metallicities for galaxies at these distances (for RR Lyrae see Beaton et al. 2018).

Our initial goal in this work was to relate empirical results on the multi-wavelength TRGB to the physical characteristics of the underlying stellar populations, such as age and metallicity. We found that goal challenging due to the internal mismatches we observe in the isochrone sets, given that the aforementioned physical parameters are ultimately inferred via comparison to those from isochrone sets once a distance, also often isochrone-dependent, is assumed.

## Chapter 3

# EMPIRICAL *HST*-2MASS FILTER TRANSFORMATIONS I. SYNTHETIC PHOTOMETRY

### 3.1 Introduction

Near-infrared (NIR) spectrophotometry of stars is increasingly important to a wide range of astrophysical issues. Recent and upcoming missions with NIR capabilities, such as *JWST* and *Roman*, will resolve orders of magnitude more stars at higher precision and greater distances than their closest predecessors.

In practice, however, the potential of these and other space-based observations is frequently limited by the ability to link new photometry to the rich legacy of ground-based observations (e.g. 2MASS, Skrutskie et al. 2006). The widely-used *JHK* filter set and its near relatives are largely shaped to accommodate the atmospheric windows where the Earth’s atmosphere is transparent. Space-based instruments, however, do not share these constraints, and can sample the full range of the stellar spectrum. Even for space-based filters expressly designed to mimic their ground-based counterparts, subtle differences can arise from the atmospheric absorption that typically defines ground filters’ blue and red edges. Similarly, spatial and temporal variations in Earth’s atmosphere add complexity to the task of consistently calibrating ground-based NIR photometry, both night-to-night and across observatories.

Interpreting even precisely calibrated NIR photometry is particularly challenging for the cool and luminous giants that dominate the integrated rest-frame infrared light of intermediate-aged to ancient stellar populations. In such stars, low surface gravities ( $\log g \lesssim 1$ ) and effective temperatures ( $T_{\text{eff}} \lesssim 4000$  K) give rise to deep and wide atomic and molecular absorption features that can have profound impacts on spectral shapes as measured

with typical broadband filters. Figure 3.1 shows example spectral sequences for three broad subclasses of such stars: non-pulsating asymptotic giant branch (AGB) or bright first-ascent red giant branch (RGB) stars (“quasi-static” giants, following Verro et al. 2022a), and thermally pulsing AGB (TP-AGB) stars with carbon- and oxygen-rich atmospheres. We overlay synthetic integrated fluxes for each spectrum in the ground-based 2MASS  $JHK_S$  and *Hubble Space Telescope* (*HST*) F110W and F160W filters. While the integrated fluxes in overlapping *HST* and 2MASS bandpasses approximately agree for the quasi-static giants, they begin to diverge as molecular feature strength increases in both TP-AGB subtypes. Furthermore, even non-pulsating giants exhibit variability over a range of amplitudes, timescales, and modes due to asteroseismic oscillations, further complicating their photometric calibration.

In this paper, we begin a systemic empirical cross-calibration of the ground-based 2MASS filter set with a subset of popular broadband filters on the the infrared channel of *HST*’s Wide Field Camera 3 (WFC3/IR). We take advantage of several empirical spectral libraries that have been released in the past two decades, which together include stars ranging in temperature from below 3000 K to over 60,000 K. At the higher temperatures, the sample is dominated by main sequence stars and white dwarfs, and at cool temperatures, the sample is approximately evenly split between low-mass dwarfs and evolved giants.

§3.2 describes the data products used in this work, including all spectral libraries, distance and extinction estimates, and other literature data used in determining and interpreting our final synthetic magnitudes and colors. §3.3 describes our synthetic photometry production and validation process. In §3.4 we present best-fit global 2MASS $\leftrightarrow$ *HST*/WFC3-IR magnitude and color transformations. We compare to previously published relations and examine residuals with respect to stellar properties in §3.5, and discuss conclusions and future work in §3.6.

### 3.2 Data

In this section, we describe the datasets used in this work: empirical spectral libraries (§3.2.1); distance and reddening measurements (§3.2.2); and other compiled literature pa-

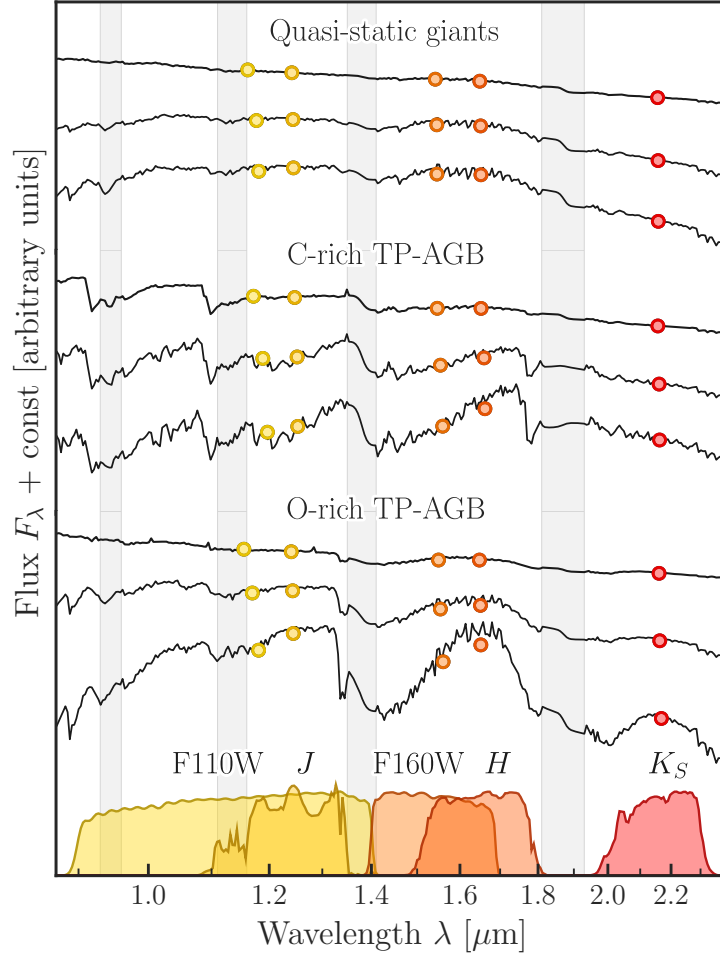


Figure 3.1: Schematic comparison of near-infrared stellar spectra (black lines, Verro et al. 2022a) and their integrated fluxes (colored points, plotted at respective effective wavelengths) for three broad classes of cool and luminous giants. These include non-pulsating AGB and upper RGB stars (upper three), and thermally pulsating carbon-rich (center) and oxygen-rich (lower) AGB stars respectively. Transmission curves for the 2MASS  $JHK_S$  and HST F110W, F160W bandpasses are shown as filled curves at the bottom, and regions with significant atmospheric telluric absorption are marked by gray vertical bands.

Table 3.1: Summary of spectral library datasets used in this work.

	(E)IRTF	XSL DR3	CALSPEC	All
Facility	IRTF/SPEX	VLT/X-shooter	STIS NICMOS WFC3/IR	—
Wavelengths [ $\mu\text{m}$ ]	0.8–2.5+	0.3–2.45	0.1–1.0 0.8–2.5 0.8–1.7	—
Spectral resolution	$\sim 2000$	$\sim 10000$	$> 500$ $\sim 200$ $\sim 170$	—
Absolute fluxing?	Yes, to 2MASS	No	Yes	—
Reference(s)	Rayner et al. (2009) Villaume et al. (2017)	Verro et al. (2022b)	Turnshek et al. (1990)	—
Spectral types	primarily late-type	many	primarily dwarfs	—
Total spectra	431	736	102	1269
Unique stars	422	614	102	1061
$J - K_S$ color range	$-0.1 - 2.5$	$-0.2 - 2.4$	$-0.3 - 0.9$	$-0.3 - 2.5$

rameters (§3.2.3).

### 3.2.1 Empirical Spectral Libraries with NIR Coverage

Empirical spectral libraries are critical benchmarks for understanding many facets of stellar atmospheres, evolution, and populations (Trager 2012). Many existing libraries offer excellent coverage of optical and near-UV wavelengths (e.g. Yan et al. 2019; Wang et al. 2018; Sánchez-Blázquez et al. 2006; Falcón-Barroso et al. 2011; Prugniel & Soubiran 2001, 2004; Prugniel et al. 2007; Gregg et al. 2006; Valdes et al. 2004; Le Borgne et al. 2003; Bagnulo et al. 2003). However, there is a relative dearth of comparable libraries available for the near-infrared. Such observational libraries are essential, given that theoretical spectra are known to have difficulty reproducing observed NIR SEDs and spectral features of cool and luminous giants (Alvarez et al. 2000; Tej et al. 2003; Bonatto et al. 2004; Maraston 2005; Levesque et al. 2006; Lyubenova et al. 2012; Aringer et al. 2016; Gonneau et al. 2017; Baldwin et al. 2018; Dahmer-Hahn et al. 2018; Coelho et al. 2020; Lançon et al. 2021; Aringer et al. 2019; Eftekhari et al. 2022; Eriksson et al. 2023).

The spectral library datasets adopted in this work were selected to have continuous spectral coverage in the range of at least  $0.8 \lesssim \lambda \lesssim 1.8 \mu\text{m}$ , with the SED continuum preserved. In addition to the descriptions to follow, basic characteristics of the libraries and the stars adopted from them are provided in Table 3.1. For all of the stars selected from the libraries, we also search the literature and archives such as SIMBAD for relevant optical and infrared photometry, stellar parameters and classifications, and distances and line-of-sight extinctions. Because this information is extensive and potentially of use for other purposes, we include machine-readable tables of our final compiled database in Appendix C.

### CALSPEC

CALSPEC is a library of spectrophotometric standards that forms the basis of the *HST* absolute flux calibration scale (Turnshek et al. 1990; Bohlin et al. 2001; Bohlin 2007; Bohlin & Cohen 2008; Bohlin et al. 2014; Bohlin & Deustua 2019, and references therein). The majority



of observed spectra are taken with the Space Telescope Imaging Spectrograph (STIS), the infrared channel of the Wide Field Camera 3 (WFC3/IR), and/or the Near Infrared Camera and Multi-Object Spectrometer (NICMOS) instruments. STIS covers 0.011-1.03  $\mu\text{m}$  at low to medium resolution with a number of gratings/grisms; only the G750L and G750M span into the IR ( $\sim 0.5$ - 1.  $\mu\text{m}$ ) with resolutions of  $\sim 500$ -1000 and  $\sim 5000 - 9000$ , respectively. The WFC3/IR grisms G102 and G140 together span 0.8-1.7  $\mu\text{m}$ , at resolutions of  $R = 210$  at 1  $\mu\text{m}$  and 130 at 1.4  $\mu\text{m}$ . The NICMOS grisms span from 0.8-2.5  $\mu\text{m}$  with resolution  $R \sim 200$ . Most CALSPEC stars have counterpart theoretical spectra available as well (Bohlin et al. 2017), and regions of the empirical spectra that lack observational coverage are filled in with model predictions where available. We do not retain stars without empirical WFC3/IR and/or NICMOS data in our final analysis, but show them in §3.3.2 for comparison.

In addition to CALSPEC’s sub-percent absolute and relative calibration and widespread use as standards (e.g. Holberg & Bergeron 2006; Casagrande et al. 2010; Bessell & Murphy 2012; Tonry et al. 2012; Scolnic et al. 2018), its lack of atmospheric absorption makes it an extraordinarily valuable anchor, as the other spectral libraries we use are all from ground-based observatories.

Throughout this work, we use the February 2023 CALSPEC release<sup>1</sup>, which includes the Vega spectrum `alpha_lyr_stis_011.fits`. We use this spectrum as our reference for the Vega magnitude system in all bands.

### *IRTF and Extended IRTF Libraries*

The original IRTF Spectral Library<sup>2</sup> (Rayner et al. 2009) contains 226  $R \sim 2000$  spectra of 225 late-type stars at mostly solar metallicity, taken by the SpeX prism spectrograph at the NASA Infrared Telescope Facility on Mauna Kea (Rayner et al. 2003) with coverage from 0.8-2.5+  $\mu\text{m}$ . We adopt the data as presented in the library, which relied on the data

---

<sup>1</sup><https://web.archive.org/web/20230312225336/https://www.stsci.edu/hst/instrumentation/reference-data-for-calibration-and-tools/astronomical-catalogs/calspec>

<sup>2</sup>[http://irtfweb.ifa.hawaii.edu/~spex/IRTF\\_Spectral\\_Library/](http://irtfweb.ifa.hawaii.edu/~spex/IRTF_Spectral_Library/)

processing tool described in Cushing et al. (2004), the telluric correction described in Vacca et al. (2003), and the uncertainty propagation described in Vacca et al. (2004).

The Extended IRTF Library (EIRTF, Villaume et al. 2017)<sup>3</sup> expands the metallicity range of the original library, adding spectra of 206 stars with  $-1.7 < [\text{Fe}/\text{H}] < 0.6$  taken with the same instrument. Both phases of the IRTF libraries are flux calibrated to 2MASS photometry (see Rayner et al. 2009, §2.3).

### *X-Shooter Spectral Library*

The X-Shooter Spectral Library<sup>4</sup> (Chen et al. 2014a; Gonneau et al. 2020a; Verro et al. 2022b) was designed to bridge the optical and NIR for studies of intermediate to old-aged stellar populations. As such, it spans a wide range of spectral types and luminosity classes with an emphasis on cool giants, including first-ascent red giants, red supergiants, and both oxygen- and carbon-rich thermally-pulsing asymptotic giant branch (TP-AGB) stars (Gonneau et al. 2016; Lançon et al. 2018). As of the third data release (Verro et al. 2022b), the library comprises 830 spectra of 683 unique stars observed with the ultraviolet, visible, and near-IR arms of the VLT/X-shooter spectrograph simultaneously. The final set of arm-merged spectra offer  $R \sim 10,000$  spectral coverage from 0.35 to 2.48  $\mu\text{m}$ . Of these, 736 (89%; 614 unique stars) are fully corrected for wavelength-dependent instrumental flux losses (as described in Gonneau et al. 2020a).

Detailed comparisons between XSL and other empirical spectral libraries, as well as between synthetic and observed *Gaia* and 2MASS broadband colors, find overall agreement of 5% or better for common non-variable stars in all cases, and 1% or better in many (Gonneau et al. 2020a; Verro et al. 2022b). Comparisons with model atmospheres and literature fundamental parameters, however, highlight ongoing difficulties in reproducing both overall SED shapes and specific spectral features for stars at low temperatures ( $T_{\text{eff}} \lesssim 4000$  K) and surface gravities ( $\log g \lesssim 1$ ) (Gonneau et al. 2017; Arentsen et al. 2019; Lançon

---

<sup>3</sup>[http://irtfweb.ifa.hawaii.edu/~spex/IRTF\\_Extended\\_Spectral\\_Library/](http://irtfweb.ifa.hawaii.edu/~spex/IRTF_Extended_Spectral_Library/)

<sup>4</sup><http://xsl.astro.unistra.fr/index.html>

et al. 2021).

### 3.2.2 Distances and Reddenings

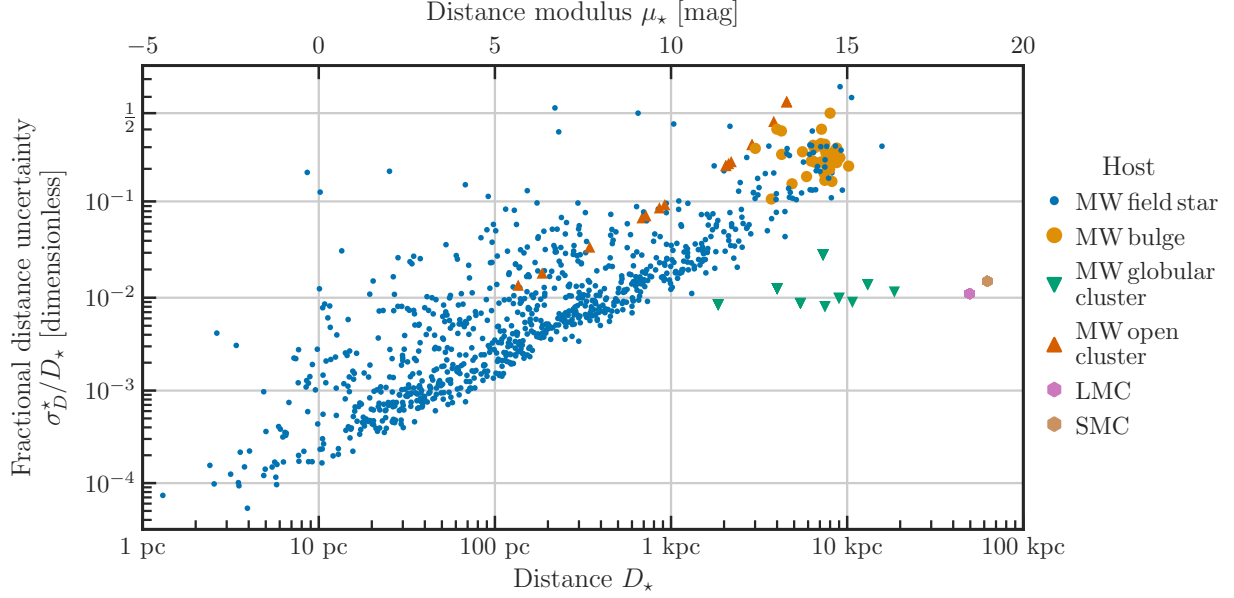


Figure 3.2: Fractional distance uncertainties as a function of distance (linear on the lower axis, modulus on the upper) for all library stars. Colors and symbols correspond to host objects, which are Galactic field or bulge stars, open and globular clusters, and the Magellanic Clouds. Note that many of the distance uncertainties are asymmetric; we show the mean values here.

While absolute-scale synthetic fluxes are neither necessary nor practical for our purposes, line-of-sight reddenings are important for interpreting synthetic colors. All of the spectral libraries in §3.2.1 provide dereddened spectra with the exception of CALSPEC, which offers reddened model spectra instead (and whose targets are largely low-extinction regardless). However, we opt to deredden all of the spectra as uniformly as possible using independent  $E(B - V)$  estimates for inter-library consistency.

For the majority of Galactic stars, we are able to utilize three-dimensional dust maps to obtain the best estimate of reddening along the line-of-sight to the star. Thus, the process

of adopting reddening has two steps: first, the determination of the distance to the star and second, the estimation of the reddening from maps.

### *Distances*

For the vast majority of Galactic field stars we use geometric distances from Bailer-Jones et al. (2021). These distances use a Bayesian framework to invert the *Gaia* EDR3 trigonometric parallaxes and derive realistic uncertainties using a Galactic disk prior. We find available distances for 1030 stars in this catalog, but 136 of these are superseded by distances to parent objects as described below, such that only 894 stars have distances adopted directly from Bailer-Jones et al. (2021).

For stars that are members of Galactic stellar clusters, we use the mean distances derived in Cantat-Gaudin & Anders (2020) and Baumgardt & Vasiliev (2021) for open and globular clusters respectively. Both of these works combine astrometric and kinematic information for individual stars to determine aggregate cluster distances. Cantat-Gaudin & Anders (2020) provided catalogs with membership probabilities at a star-by-star level, and we adopt the cluster distance for library stars that have cluster membership probabilities greater than 50%, which 17 stars in our sample do. For globular cluster candidate stars, we determine cluster membership by first querying SIMBAD for hierarchical parent membership probabilities. For stars with available membership data, we supersede the Bailer-Jones et al. (2021) distance if the median cluster membership probability is greater than 50%. For 9 candidates without membership data, we compare individual Bailer-Jones et al. (2021) distances to those derived for the parent clusters, and accept the cluster distances for all but two stars whose individual distances differ from the cluster distance by more than a factor of two.

For Magellanic Cloud stars, we do not require distance information to obtain reddening values, as 2D extinction maps offer sufficient correction. For completeness, we adopt the detached eclipsing binary distances from Pietrzyński et al. (2019,  $m - M = 18.477 \pm 0.004 \pm 0.026$ ) and Graczyk et al. (2020,  $m - M = 18.977 \pm 0.016 \pm 0.028$ ) for 51 and 25 stars in the Large and Small Magellanic Clouds respectively.

For the remaining 34 stars without distances from any of these sources, 14 have parallax distances from *Gaia* DR2 (Bailer-Jones et al. 2018), and 13 from *Hipparcos* (van Leeuwen 2007). Seven have distances derived from various other methods, primarily luminosity fitting (Sahai et al. 2007; Schmidt et al. 2010; Torres et al. 2010; Davies & Beasor 2020; Maíz Apellániz et al. 2022).

We were unable to locate any literature distance information for only 1 star, UCAC2 18505584. As this star is towards the Galactic bulge, we conservatively assume its distance is  $8 \pm 4$  kpc.

In summary, distances for 894 stars were adopted from Bailer-Jones et al. (2021), 57 stars from cluster distances, 76 from Magellanic Clouds eclipsing binary distances, and 34 from other sources.

Figure 3.2 shows average fractional distance uncertainties ( $\sigma_D^*/D_*$ ) against distance moduli ( $\mu_*$ ) for our preferred distances for all library stars. Many of these distances have asymmetric upper and lower uncertainties; we describe how we incorporate asymmetric distance uncertainties into our star-by-star  $E(B - V)$  estimates where possible in §3.2.2. For Galactic field and bulge stars, uncertainty largely scales with distance, as expected. The best-measured of these are below 1% distance uncertainty out to  $\sim 1$  kpc, and 10% at  $\sim 10$  kpc. The uncertainties on open cluster distances scale similarly, as we adopt the most conservative reported uncertainties based on assumed parallax offsets of  $\Delta\omega = \pm 0.1$  mas (Cantat-Gaudin & Anders 2020). The globular cluster distances of Baumgardt & Vasiliev (2021), on the other hand, incorporate information from multiple distance determination techniques wherever available, of which parallax inversion is only one. Several of these distances reach 1% uncertainty out to  $\sim 10$  kpc, and all are within 5%. Finally, the detached eclipsing binary distances to the Large and Small Magellanic Clouds have 1- to 2% formal uncertainties. These are almost certainly underestimates for individual stars given line-of-sight depth variations, especially in the SMC (Ripepi et al. 2017, 2022, and references therein). However, the larger distance uncertainties are not a concern for reddening corrections, as the Magellanic Clouds reddening map is distance-independent.

### Reddenings

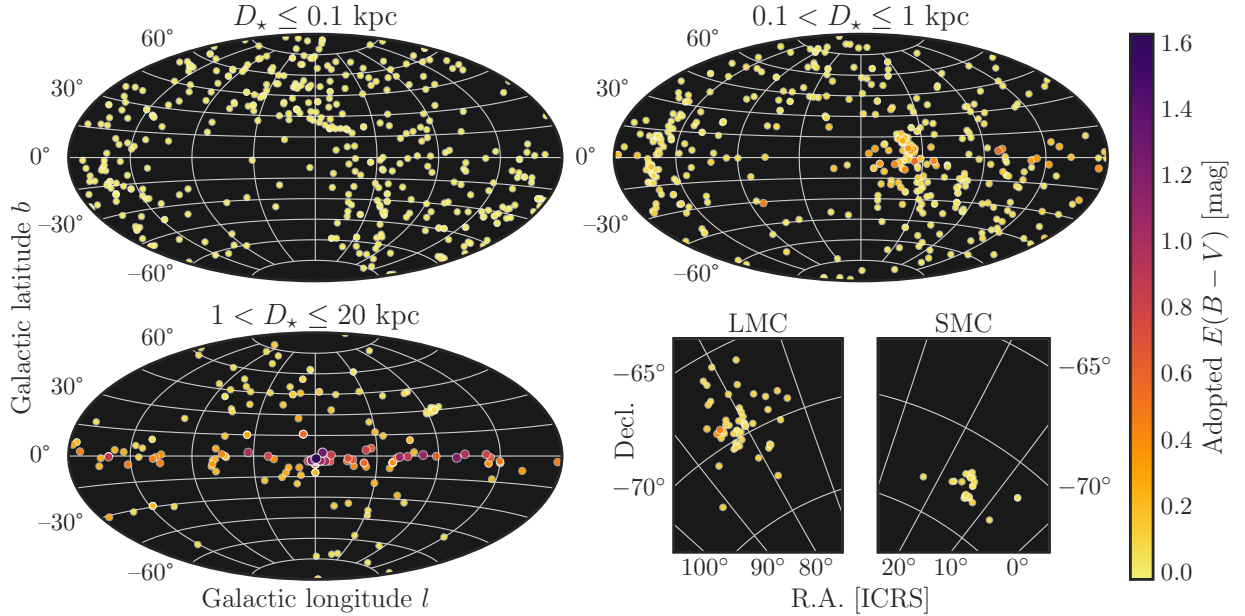


Figure 3.3: Sky maps of our final cross-library sample, color coded by adopted  $E(B - V)$  values. We show all-sky maps in Galactic coordinates for Milky Way stars in three distance bins of 0-0.1 kpc, 0.1-1 kpc, and 1-20 kpc. Magellanic Cloud stars are shown in separate insets in the lower right in equatorial coordinates.

With distances in hand, we can now obtain line-of-sight reddening estimates for our sample. For the majority of Galactic disk and bulge stars, including cluster stars, we use the 3D all-sky map from Vergely et al. (2022b)<sup>5</sup>, which uses a hierarchical inversion algorithm to derive line-of-sight extinctions over a  $10 \times 10 \times 0.8$  kpc volume around the Sun to stars with high-quality *Gaia* EDR3 parallaxes and *Gaia* and 2MASS photometry. This map revises Lallement et al. (2022) with an improved calibration for cool giant stars specifically, and Lallement et al. (2022) itself updates Lallement et al. (2019). We use this map for 808 stars in total.

For the 178 Galactic stars that fall outside the boundaries of the Vergely et al. (2022b)

---

<sup>5</sup>Available at <https://explore-platform.eu/sdas>.

map, we use the *Gaia* DR3 total Galactic extinction map (TGE, Delchambre et al. 2022). This map combines individual extinction measurements inferred from low-resolution BP/RP spectra (Andrae et al. 2022) of giants outside the Galactic plane ( $|b| > 300$  pc or Galactocentric radius  $R > 16$  kpc).

Finally, for Magellanic Cloud stars we use the 2D map presented by Skowron et al. (2021), which is derived from OGLE-IV red clump color excess measurements.

In Appendix D we compare our final adopted  $E(B - V)$  values both to those adopted or measured by the original libraries, and to those from several other widely used maps and stellar parameter fitting techniques as well. We find that different  $E(B - V)$  estimates have typical median absolute deviations (MADs) of 0.05-0.1 mag, with some exceptions. This translates to a  $\sim 2$ -5% MAD in  $E(J - K_S)$ , assuming  $E(J - K_S)/E(B - V) = 0.42$  (Yuan et al. 2013).

A similar intercomparison of the values from Skowron et al. (2021) with other such measurements in the Magellanic Clouds (e.g. Imara & Blitz 2007; Haschke et al. 2011; Choi et al. 2018b; Joshi & Panchal 2019; Bell et al. 2019; Chen et al. 2022) would be of potential interest as well. We do not pursue it here because the proportion of Magellanic Clouds stars in our sample is low (below 10%), and many of those spectra are affected by data quality issues regardless.

### 3.2.3 Global Sample Properties

In addition to distances and reddenings, we have compiled relevant literature data for our sample from VizieR and SIMBAD. These include stellar parameters such as effective temperature  $T_{\text{eff}}$ , metallicity  $[\text{Fe}/\text{H}]$ , and surface gravity  $\log(g)$ ; observed *Gaia* and 2MASS photometry; spectral type and other classifications; and binarity and variability information. We show a summary of  $T_{\text{eff}}$ ,  $\log(g)$ , and  $[\text{Fe}/\text{H}]$  coverage in Figure 3.4.

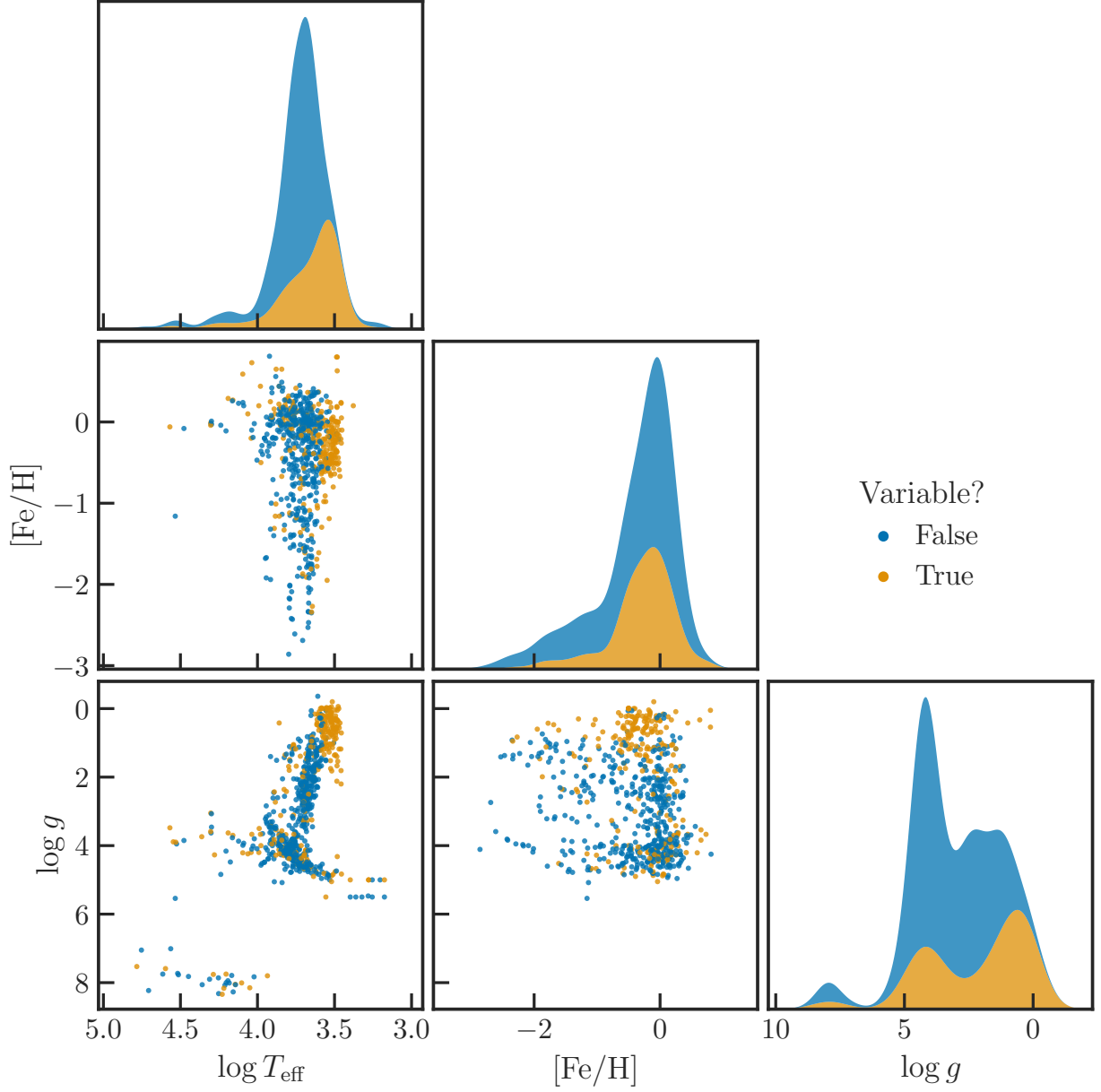


Figure 3.4: Summary stellar properties (effective temperature  $T_{\text{eff}}$ , metallicity  $[\text{Fe}/\text{H}]$ , and surface gravity  $\log(g)$ ) of the merged spectral libraries. We note that these literature measurements are extremely heterogeneous, and these data are used primarily to understand the ranges of stellar properties over which our library can provide insight. Stars with known photometric variability are plotted in orange, whereas stars not known to be variable are shown in blue.



### 3.3 Synthetic Photometry

Here we describe the process of producing and validating synthetic photometry from our ensemble library. For ease of reproducing or expanding on this work, all derived products have been made public; we describe those data in Appendix C.

#### 3.3.1 Synthetic Photometry Procedure

For a given spectrum with flux density  $f_\lambda(\lambda)$  and bandpass with dimensionless throughput  $P(\lambda)$ , the integrated flux density is defined as:

$$f_\lambda(P) \equiv \frac{\int f_\lambda(\lambda) P(\lambda) \lambda d\lambda}{\int P(\lambda) \lambda d\lambda} \quad (3.1)$$

(Strömgren 1937; Koornneef et al. 1986).

If we treat the spectrum  $f_\lambda(\lambda)$  as a vector  $\mathbf{f}_\lambda$ , and a set of bandpasses  $\mathbf{P}$  as a matrix with dimensions  $n_P \times n_\lambda$ , where  $n_P$  is the number of bandpasses and  $n_\lambda$  is the number of wavelength samples, then the integrated fluxes  $\mathbf{f}_P$  are simply:

$$\mathbf{f}_P = \mathbf{P} \cdot \mathbf{f}_\lambda \quad (3.2)$$

This approach allows us to calculate the covariance between integrated fluxes in different bandpasses as

$$\text{Cov}[\mathbf{f}_P] = \mathbf{P} \cdot \text{Cov}[\mathbf{f}_\lambda] \cdot \mathbf{P}^T \quad (3.3)$$

following Gaia Collaboration et al. (2022b).

We begin by resampling all spectra and transmission curves to the  $R = 100$  wavelength grid on which the *HST* flux uncertainty scale is defined (Bohlin et al. 2014), to improve computational efficiency and ease of uncertainty propagation. We used the `FluxConservingResampler` from the Python package `specutils`, which preserves integrated flux and associated uncertainties (Carnall 2017). For XSL spectra, we first fill in the deepest telluric-dominated regions (1.35 - 1.41 and 1.81 - 1.935  $\mu\text{m}$ ) via convolution with a Gaussian kernel.

Next, we correct the resampled spectra for interstellar extinction. Specifically, we estimate the total wavelength-dependent line-of-sight extinction  $A_\lambda$  using the  $E(B - V)$  values described in §3.2.2 as inputs to extinction laws implemented in the `dust-extinction` package.<sup>6</sup> We use the Fitzpatrick et al. (2019) law with  $R_V = 3.1$  for Galactic stars, and in the LMC and SMC we use the respective average laws from Gordon et al. (2003). We incorporate both the reported uncertainties on  $E(B - V)$  and, in the Galactic case, uncertainties of  $\pm 0.3$  on  $R_V$  into the final uncertainties on the deextinguished spectra.

Using equations 3.2 and 3.3, we are able to derive integrated fluxes and covariances for an arbitrary set of bandpasses  $\mathbf{P}$  over both the original and deextinguished spectra. For the remainder of this paper, we will focus primarily on the 2MASS  $JHK_S$  and *HST* WFC3/IR F110W, F125W, and F160W bandpasses. However, we also provide synthetic *Gaia* DR3  $BP$ ,  $G$ , and  $RP$  magnitudes for spectra with sufficient wavelength coverage in this paper. Comparable sets of transformations for *JWST*/NIRCam, *Roman*/WFI, and other ground-based systems will be presented in a follow-up paper.

### 3.3.2 Validation

Overall, the best check on synthetic magnitudes and colors is to compare them to corresponding measured values. In this section, we first cross-check our CALSPEC data against high-quality 2MASS and *Gaia* photometry, and then consider the global 2MASS color-magnitude and color-color fidelity of the full sample.

#### *CALSPEC zeropoints*

While an end-to-end recalibration in either direction (as in, e.g., Riess 2011; Maíz Apellániz & Weiler 2018; Maíz Apellániz & Pantaleoni González 2018; *Gaia* Collaboration et al. 2022b) is beyond the scope of this paper, here we briefly reproduce the 2MASS zeropoint adjustment procedure of Maíz Apellániz & Pantaleoni González (2018, hereafter MA18) and references

---

<sup>6</sup><https://web.archive.org/web/20230706195114/https://learn.astropy.org/tutorials/color-excess.html>

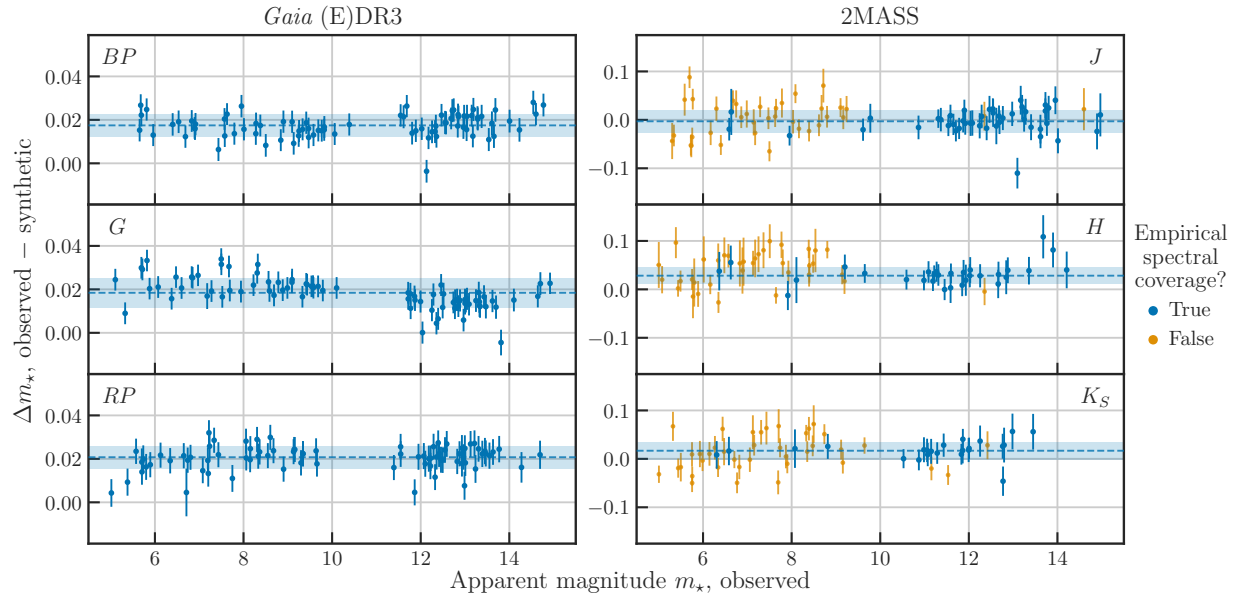


Figure 3.5: Differences between observed and synthetic magnitudes in *Gaia* (E)DR3 *BP*, *G*, *RP* (left) and 2MASS *JHK<sub>S</sub>* (right) as functions of observed magnitude for select CALSPEC stars. Blue points indicate empirical spectrophotometry (available for effectively all CALSPEC stars in the optical), and orange indicates spectra extrapolated from theoretical models (e.g. missing WFC3/IR and/or NICMOS data), which we exclude from calculations and show only for reference. Blue dashed lines and solid bands show weighted means and standard deviations of the photometric offsets, as reported in Table 3.2.

therein. We extend this procedure to *Gaia* (E)DR3 as well for additional verification, as in Fabricius et al. (2021, section 4.4.2).

We choose our comparison sample based on the criteria of MA18 with minor updates, namely: a) CALSPEC spectra with empirical IR spectrophotometry (limited to NICMOS in MA18; here we also include WFC3/IR); and b) uncertainties on observed magnitudes of 0.05 mag or less. For *Gaia*, we use all available CALSPEC stars with observed magnitudes  $5 < m_{\star} < 15$ . All criteria are applied on a per-band basis.

We calculate mean offsets and dispersions weighted by combined synthetic and observed magnitude uncertainties for each band, as summarized in Table 3.2 and shown in Figure 3.5. We find a consistent  $\sim 0.02$  mag offset between the synthetic and observed photometry in all *Gaia* bands, and offsets of up to 0.03 mag in 2MASS, although the latter are all statistically compatible with zero. We attribute these largely to differences in the respective adopted reference SEDs, consistent with previous studies of synthetic *Gaia* and 2MASS magnitudes (MA18, Casagrande & VandenBerg 2018) and historical changes to the CALSPEC Vega calibration (Bohlin et al. 2014, 2019).

#### *Global CMD and color-color fidelity*

Figure 3.6 compares the absolute observed 2MASS magnitudes (left) to their synthetic counterparts (right) in a  $M_H$  versus  $J-H$  color magnitude diagram. The right panel of Figure 3.6 separates the highest quality photometry, `Qflag = AAA` (Skrutskie et al. 2006), from that with flags in one or more bands; the best photometry is shown as dark blue, and the lower quality in lighter blue. Visually, the stars with lower photometric quality have larger scatter around prominent CMD features (e.g., the red giant branch, main sequence, and white dwarf cooling sequence) that are tightly traced by the high-quality photometry.

The left panel of Figure 3.6 uses our synthetic magnitudes, where the points are color-coded if there are quality flags within the spectral libraries themselves. Of note: the orange points are CALSPEC stars observed only with STIS, meaning that the spectrum beyond  $\sim 1 \mu\text{m}$  is synthetic (Bohlin et al. 2017); the green are XSL spectra corrected for slit-

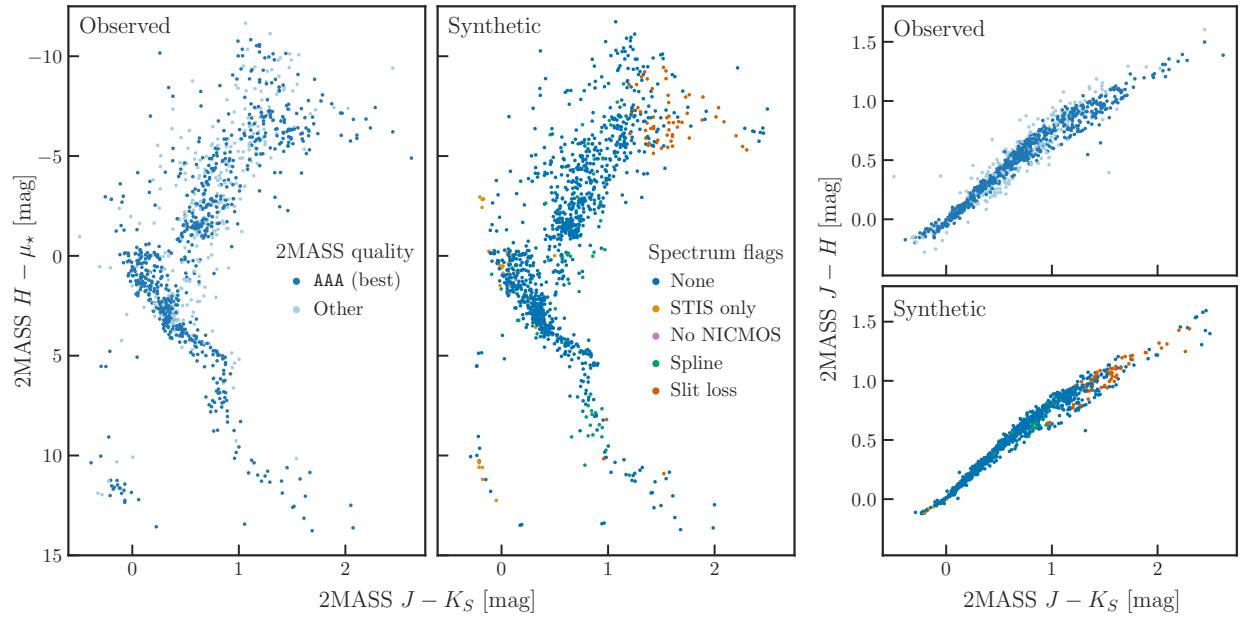


Figure 3.6: Left: absolute  $H$  vs.  $J - K_S$  CMD of all available 2MASS photometry for our full sample. Here, dark blue points indicate sources with high-quality 2MASS photometry in all bands (“Qflag=AAA”), and light blue indicates non-optimal quality flags in one or more bands. Center: the same CMD for our synthetic photometry suite. Blue points indicate spectra with no data caveats. Orange indicates CALSPEC library stars that were observed only with STIS, where the spectra are filled in outside the STIS wavelength range ( $\gtrsim 1 \mu\text{m}$ ) using theoretical spectra. Green indicates XSL spectra that were corrected for slit loss via spline fitting (Verro et al. 2022b), and red indicates XSL spectra uncorrected for slit loss. Right: The same in  $J - H$  vs.  $J - K_S$  color-color space.

Table 3.2: Summary of Gaia (E)DR3 and 2MASS observed and synthetic photometry differences for CALSPEC stars

Band	$\Delta ZP$	$\sigma(\Delta ZP)$	$\bar{\sigma}_{\text{obs}}$	$\bar{\sigma}_{\text{syn}}$	$N_{\star}$
<i>Gaia</i> <i>BP</i>	0.0175	0.0052	0.0030	0.0042	80
<i>G</i>	0.0184	0.0068	0.0028	0.0042	82
<i>RP</i>	0.0208	0.0052	0.0039	0.0045	80
2MASS <i>J</i>	−0.0030	0.0229	0.0248	0.0085	45
<i>H</i>	0.0283	0.0172	0.0258	0.0099	30
<i>K<sub>S</sub></i>	0.0168	0.0176	0.0244	0.0116	23

Table 3.2 notes:  $\Delta ZP$  and  $\sigma(\Delta ZP)$  are the error-weighted mean and standard deviation of the differences (in the direction observed – synthetic);  $\bar{\sigma}_{\text{obs}}$  and  $\bar{\sigma}_{\text{syn}}$  are the respective mean uncertainties; and  $N_{\star}$  is the number of stars used.

dependent flux loss with a spline function (Verro et al. 2022b); and the red are XSL spectra uncorrected for slit loss.

Generally, the scatter in the right panel of Figure 3.6 is reduced with the synthetic photometry, which is a comforting check on our processes. However, we emphasize that the absolute-scale synthetic magnitudes for XSL in particular should be treated with caution, as the XSL spectra are calibrated only for relative (wavelength-dependent) flux and not absolutely fluxed. We do not make more detailed comparisons here because of the relatively large sample of stars known to be variable, particularly on the upper giant branch (e.g., Figure 3.4) and the comparison here would likely only serve to highlight cases where the spectra and photometry were taken at inconsistent phase points.

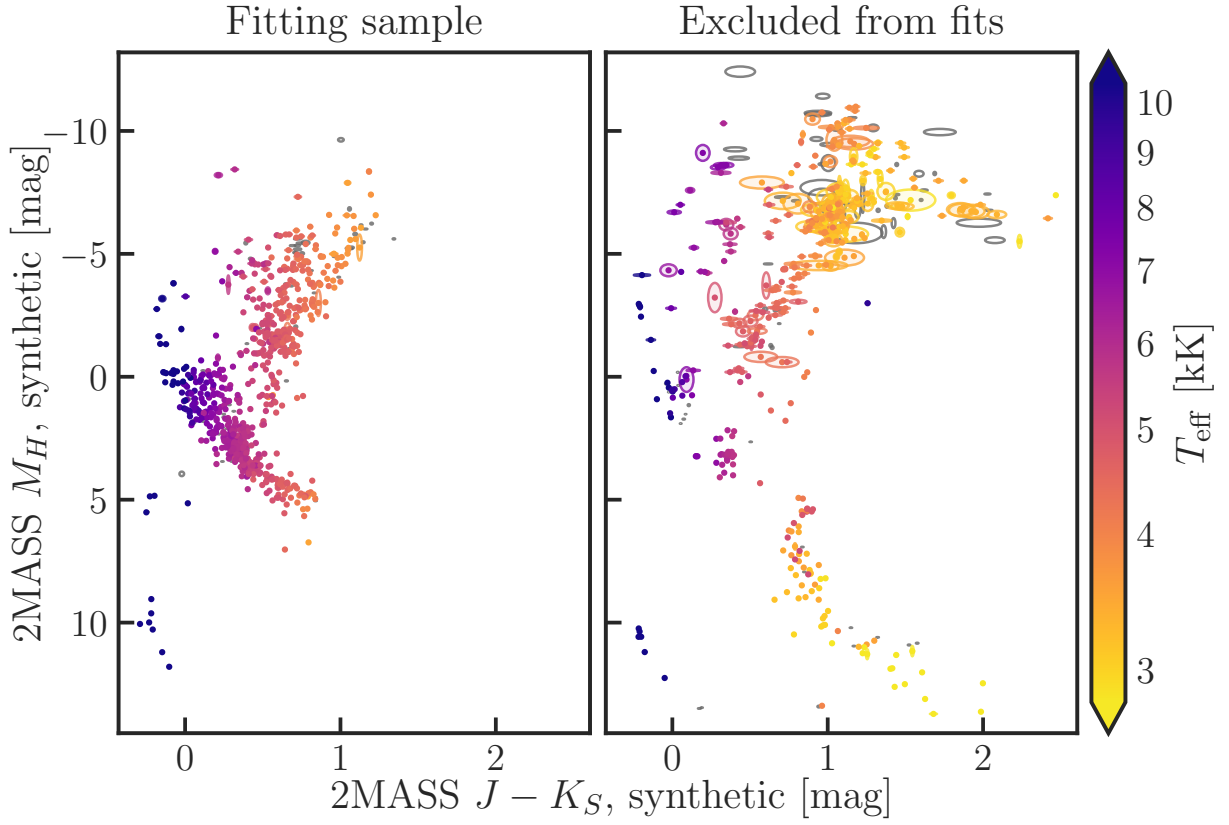


Figure 3.7: Color-magnitude diagrams of our final fitting sample (left) and stars excluded from fitting (right), colormapped by literature effective temperature.

### 3.4 Results

#### 3.4.1 Fitting sample selection

To construct general-purpose filter transformations, we require a subset of library stars with high-quality spectra covering as broad a swath of the HR diagram as possible. Given the heterogeneity of available information for stars in our library, we combine several complementary kinds of classification data to accept or reject stars for our final calibration sample. We selected the fitting sample based on the following criteria:

1. Synthetic magnitude uncertainties under 0.05 mag in all bands;
2. No spectral quality flags (see Figure 3.6);
3. No known atypical SED features, based on available SIMBAD object class and spectral type information. Specifically, we reject stars with any of the following literature classifications:
  - (a) Ae or Be stars, which often show IR excesses from circumstellar decretion disks;
  - (b) dwarves of type M or later, including L and T dwarves;
  - (c) C-, R-, and S-type stars; these are mainly AGB stars of varying masses, but also include carbon-enhanced metal poor (CEMP) and other chemically peculiar non-AGB stars;
  - (d) other extreme giant types, including Miras, OH/IR and post-AGB stars, and supergiants of any temperature;
  - (e) any other stars with  $T_{\text{eff}} < 3500$  K.

Together, these yield a sample of 773 high-quality spectra of 648 unique stars in total. Color-magnitude diagrams of accepted and rejected stars are shown in Figure 3.7. The fitting sample is dominated by main sequence and red giant branch stars the color range  $-0.3 < J - K_S < 1.35$ .



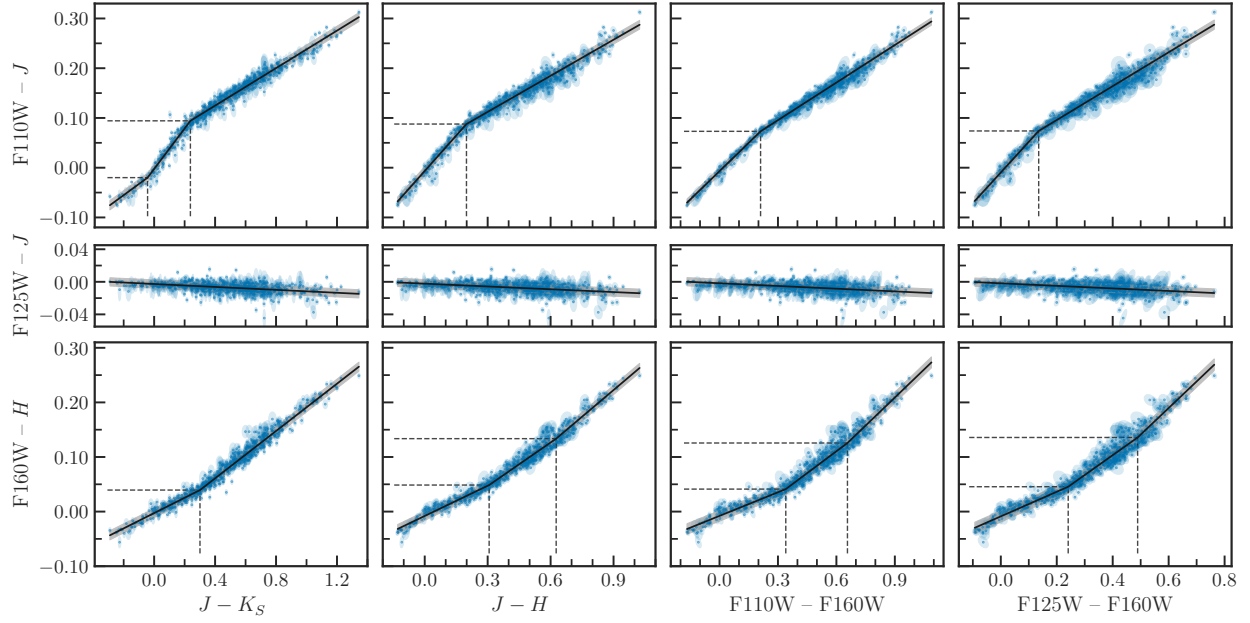


Figure 3.8: Filter transformation fits to  $F110W - J$  (top row),  $F125W - J$  (center row), and  $F160W - H$  (bottom row) as functions of  $J - K_S$ ,  $J - H$ ,  $F110W - F160W$ , and  $F125W - F160W$  color from left to right. Points used in the fitting are shown in dark blue with light blue covariance ellipses. Solid black lines show the resulting piecewise linear transformations with 68% confidence intervals in grey, and dashed black lines mark the breakpoint locations.

### 3.4.2 Fitting process

We plot differences between comparable *HST* and 2MASS magnitudes as functions of color for our fitting sample in Figure 3.8. In general, they follow consistent and well-defined relations, albeit not necessarily linear ones.

Deviations from linearity are most clearly seen in  $F110W - J$  vs.  $J - K_S$  (the upper leftmost panel of Figure 3.8). Here, the noticeably steeper slope at  $0 \lesssim J - K_S \lesssim 0.25$  corresponds to the  $0.82 \mu\text{m}$  Paschen jump, which is strongest in A-type stars (Taylor 1986; Straizys 1998). The slope change at the blue end of this feature is only detectable in  $F110W - J$  vs.  $J - K_S$ , as F110W is the most blue-sensitive filter and  $J - K_S$  the widest available color baseline. However, we consistently observe slope changes at colors of about 0.2 to 0.35 mag in  $F110W - J$  and  $F160W - H$  for all color baselines.

Table 3.3: Filter transformation results

$Y$	$X$	$X_0$	$X_1$	$c_0$	$c_1$	$\sigma_{\text{seg}}$	$N_{\star}$	$\sigma_{\text{global}}$
F110W – $J$	$J - H$	-0.13	0.20	-0.0066	0.4743	0.0091	153	0.0088
		0.20	1.02	0.0396	0.2419	0.0087	620	”
	$J - K_S$	-0.29	-0.04	-0.0103	0.2244	0.0078	29	0.0088
		-0.04	0.24	-0.0025	0.4065	0.0117	137	”
		0.24	1.34	0.0494	0.1885	0.0080	607	”
	F110W – F160W	-0.17	0.21	-0.0069	0.3797	0.0059	125	0.0073
		0.21	1.09	0.0200	0.2518	0.0075	648	”
	F125W – F160W	-0.09	0.14	-0.0096	0.6162	0.0090	128	0.0093
		0.14	0.76	0.0278	0.3404	0.0094	645	”
F125W – $J$	$J - H$	-0.13	1.02	-0.0023	-0.0115	0.0050	773	0.0050
	$J - K_S$	-0.29	1.34	-0.0027	-0.0090	0.0051	773	0.0051
	F110W – F160W	-0.17	1.09	-0.0018	-0.0111	0.0051	773	0.0051
	F125W – F160W	-0.09	0.76	-0.0018	-0.0156	0.0051	773	0.0051
F160W – $H$	$J - H$	-0.13	0.31	-0.0080	0.1845	0.0063	268	0.0081
		0.31	0.63	-0.0330	0.2659	0.0089	386	”
		0.63	1.02	-0.0704	0.3256	0.0094	119	”
	$J - K_S$	-0.29	0.30	-0.0027	0.1402	0.0064	217	0.0082
		0.30	1.34	-0.0257	0.2166	0.0089	556	”
	F110W – F160W	-0.17	0.34	-0.0079	0.1442	0.0076	224	0.0096
		0.34	0.66	-0.0496	0.2668	0.0100	407	”
		0.66	1.09	-0.0992	0.3424	0.0113	142	”
	F125W – F160W	-0.09	0.24	-0.0087	0.2253	0.0074	246	0.0102
		0.24	0.49	-0.0420	0.3634	0.0108	409	”
		0.49	0.76	-0.1022	0.4864	0.0131	118	”

NOTE—Filter transformations take the functional form  $Y = c_0 + c_1 X$  for  $X_0 < X \leq X_1$ , where  $X$  is a broadband color and  $Y$  is the difference between comparable filters.  $\sigma_{\text{seg}}$  is the weighted RMS dispersion of the residuals in each segment (e.g. with  $X_0 < X \leq X_1$ ), and  $\sigma_{\text{global}}$  is the same for the full piecewise relation.  $N_{\star}$  is the number of stars per segment.

A more subtle change in  $F160W - H$  also appears near 0.5 - 0.65 mag for all colors except  $J - K_S$ . We attribute this to the  $1.6 \mu\text{m}$  “bump”, where the  $H$ – continuum opacity reaches a minimum as the dominant absorption mode transitions from photoionization to free-free (John 1988; Allende Prieto 2023). This produces a well-defined peak in cool stars’ SEDs, which is strongest in intermediate M-type giants and supergiants (Rayner et al. 2009). The  $H$  band is nearly centered on this feature, but  $F160W$  falls about  $0.1 \mu\text{m}$  bluewards of its peak, resulting in slightly dimmer  $F160W$  magnitudes relative to  $H$ .

We fit transformations using the Python library `pwlfit` (Jekel & Venter 2019), which solves for a system of piecewise linear equations continuous over the data domain.<sup>7</sup> The current version as of this writing, v0.2.0, offers the options to fit for optimal breakpoint locations given a desired number of line segments, and to incorporate weights in the least-squares regression. For a synthetic color  $X$  and  $HST$ -2MASS magnitude difference  $Y$ , we weight by the inverse variance

$$w_{X,Y}^{-2} = \sigma_X^2 + \sigma_Y^2 - \text{cov}(X, Y) \quad (3.4)$$

where  $\text{cov}(X, Y)$  is obtained by propagating the uncertainties from Equation 3.3.

Our fitting results are summarized in Table 3.3, and overplotted in black in Figure 3.8.

### 3.5 Discussion

#### 3.5.1 Comparison with Literature Relations

Earlier works have carried out similar exercises to what we have done here using theoretical stellar atmospheres.

Riess (2011) derived first-order transformations between  $F125W$ ,  $F160W$  and  $JH$  as part of an investigation of the WFC3/IR count rate nonlinearity (CRNL, also known as reciprocity failure). They used synthetic photometry of Castelli & Kurucz (2003) model atmospheres

---

<sup>7</sup>For a detailed description of the `pwlfit` algorithm and implementation, please see <https://web.archive.org/web/20211203035946/https://jekel.me/2018/Continuous-piecewise-linear-regression/>. The original description of the method may be found at <https://web.archive.org/web/20171116164225/https://www.golovchenko.org/docs/ContinuousPiecewiseLinearFit.pdf>

with  $-0.15 < J - H < 0.8$ ,  $T_{\text{eff}} \geq 3500$  K,  $\log(g)=4.5$ , and solar metallicity and abundance ratios. With these they fit the following color terms:

$$J - \text{F125W} = +0.012(\pm 0.020)(J - H) \quad (3.5)$$

$$H - \text{F160W} = -0.204(\pm 0.040)(J - H) \quad (3.6)$$

To interpret tip of the red giant branch (TRGB) color-magnitude absolute calibrations, Dalcanton et al. (2012a) derived transformations using Padova isochrone predictions (Girardi et al. 2008) for 10 Gyr stars at the TRGB with  $0.6 < J - H < 1.15$ . Within this color range, the model transformations between  $JH$  and F110W, F160W were fit by:

$$\begin{aligned} \text{F160W} - H &= 0.2031 + 0.401(J - H - 0.9) \\ &\quad + 0.3498(J - H - 0.9)^2 \end{aligned} \quad (3.7)$$

$$\begin{aligned} J - H &= 0.9418 + 0.841(\text{F110W} - \text{F160W} - 1.0) \\ &\quad - 0.9053(\text{F110W} - \text{F160W} - 1.0)^2 \end{aligned} \quad (3.8)$$

We show comparisons between equations 3.5-3.7 and our results in Figure 3.9. We find overall excellent agreement with Riess (2011) in both bands, and only a very slight offset relative to Dalcanton et al. (2012a) in  $\text{F160W} - H$  ( $\sim 0.02$  mag at  $J - H = 0.8$ , but less at both bluer and redder colors).

### 3.5.2 *Stellar properties*

We now examine these transformations with respect to fundamental stellar properties. In Figures 3.10 through 3.13 we show residuals of the transformations color-coded by effective temperatures, surface gravities, and metallicities from the literature, as well as our adopted reddenings. Figures 3.10 and 3.11 show residuals of our fitting sample, and figures 3.10 and 3.11 show residuals of stars excluded from the fits (i.e., those plotted in the right panel of Figure 3.7). Stars without literature parameters are shown as open gray covariance ellipses.

Figures 3.10 and 3.11 show that the fitting sample residuals are nearly all within 0.05 mag of our final filter conversions, and the majority are within 0.025 mag. However, there may

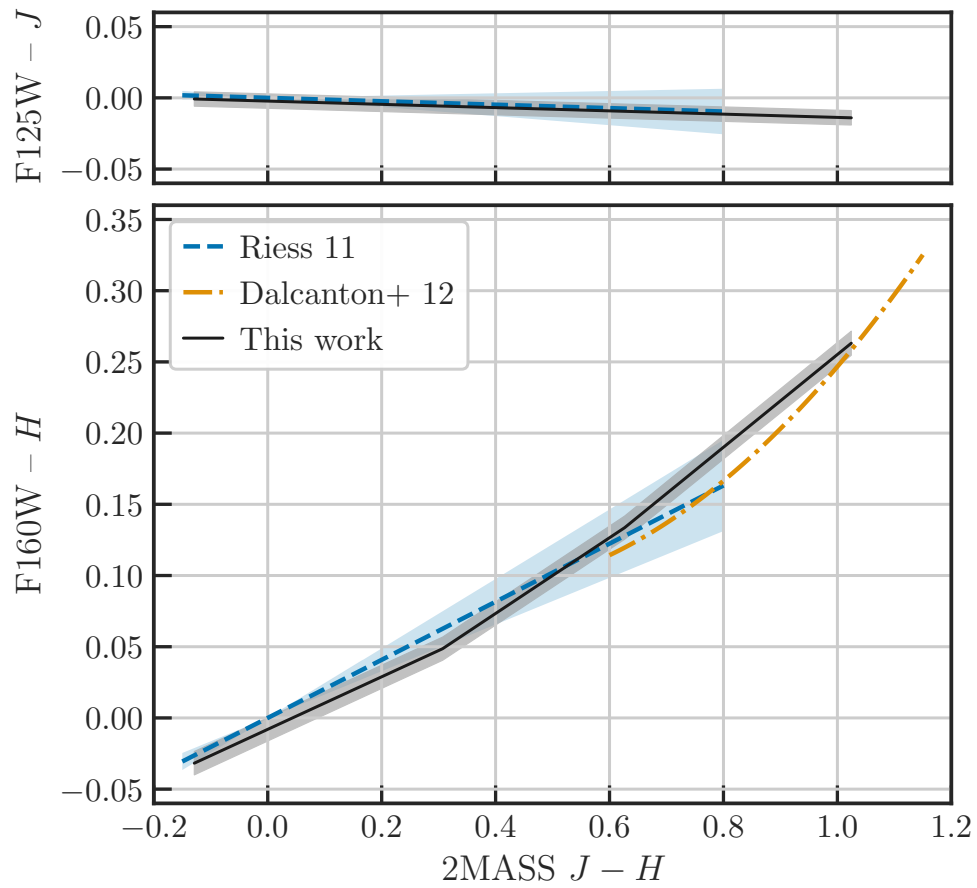


Figure 3.9: Comparisons to previously published transformations for  $F125W - J$  (Riess 2011, upper panel) and  $F160W - H$  (lower panel; Riess 2011 in blue, and Dalcanton et al. 2012a in orange). Results of this work are shown in gray.

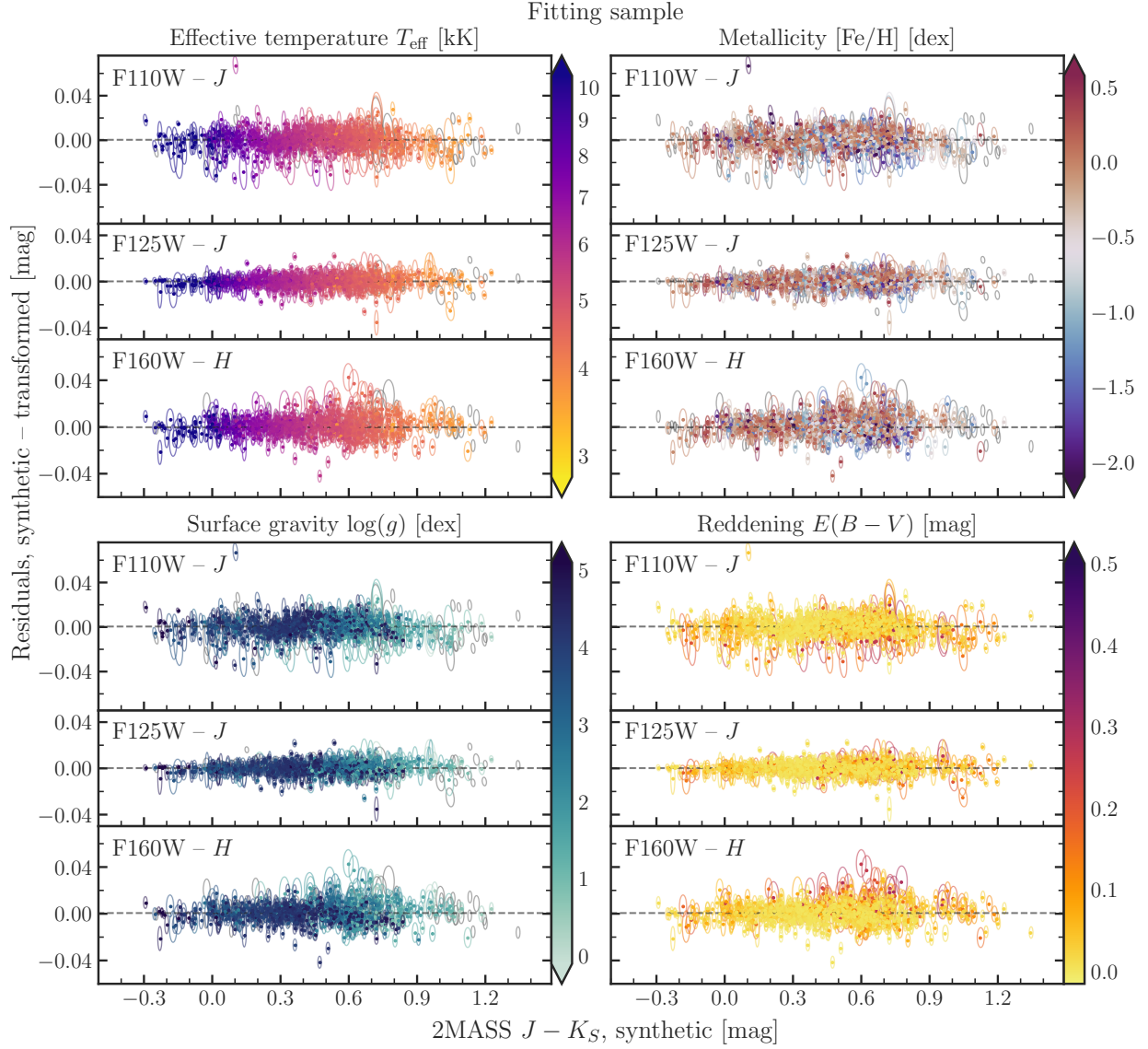


Figure 3.10: Residuals of our *HST*-2MASS filter transformations with respect to  $J - K_S$  color for our fitting sample (773 spectra of 648 unique stars). Colormaps show relevant stellar parameters where available, including effective temperature  $T_{\text{eff}}$ , metallicity  $[\text{Fe}/\text{H}]$ , surface gravity  $\log(g)$ , and reddening  $E(B - V)$ . Reddenings are as described in §3.2.2; all other parameters are adopted as-is from literature sources.

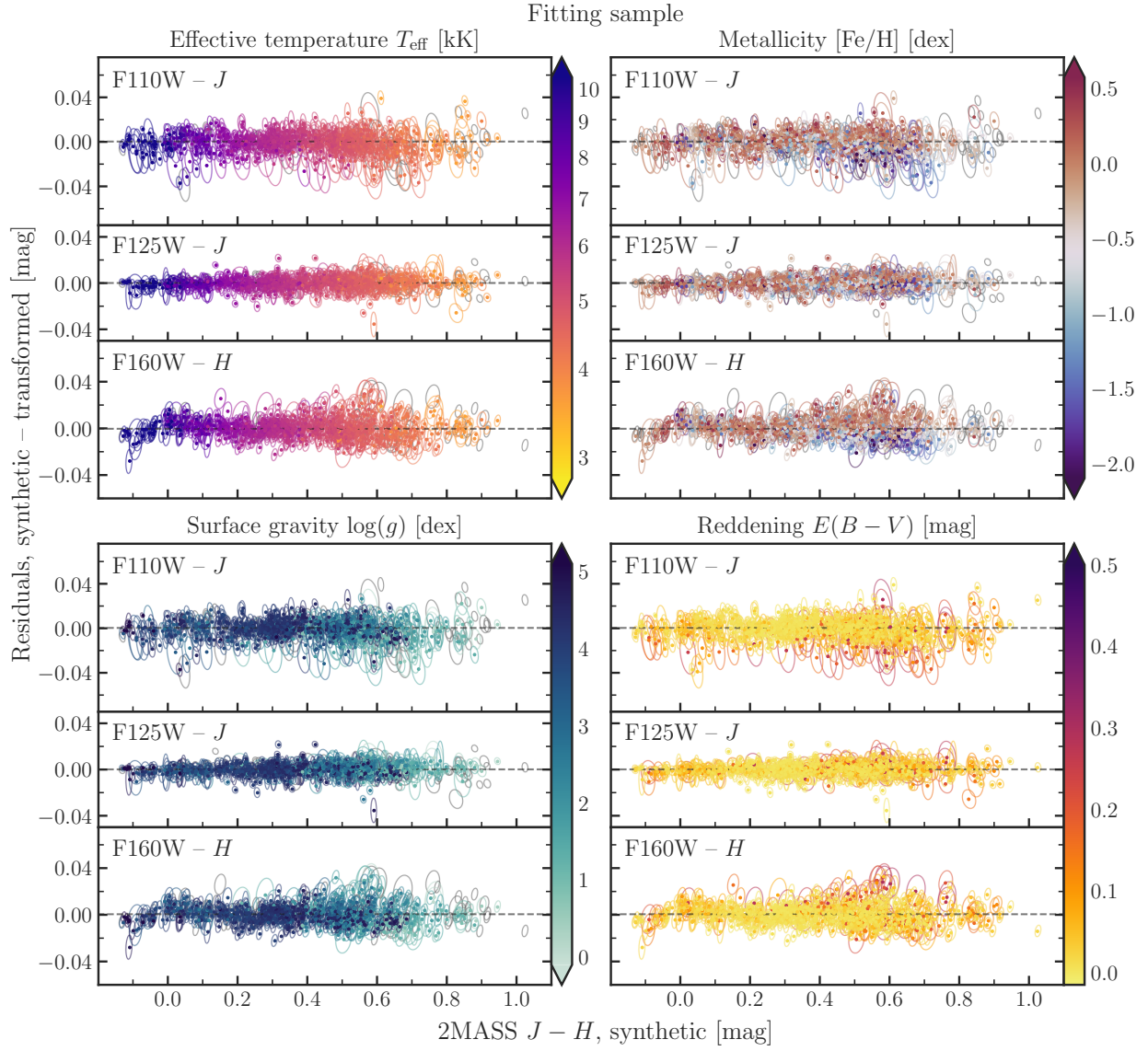


Figure 3.11: As Figure 3.10 with respect to  $J - H$  color on the  $x$ -axis.

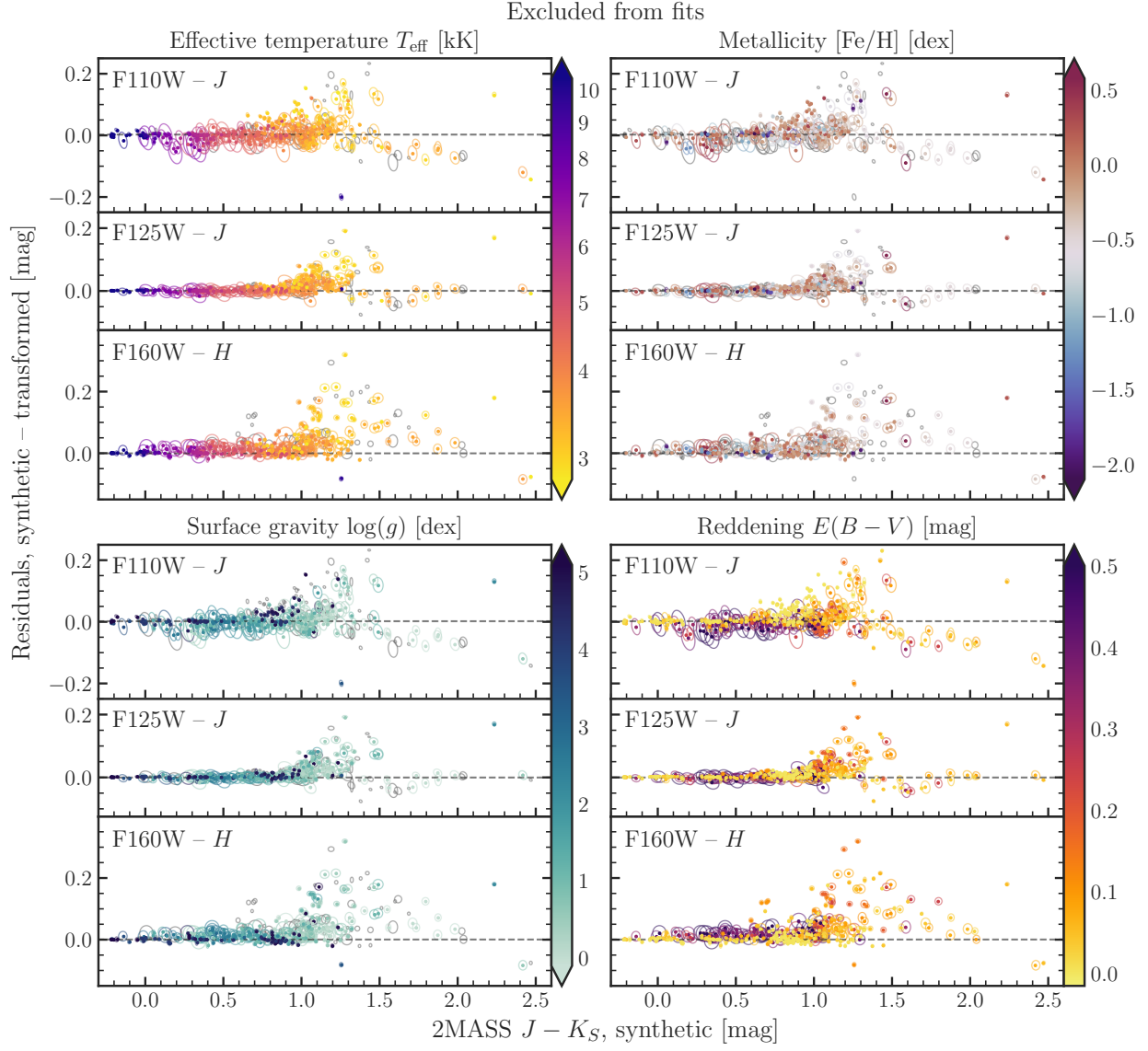


Figure 3.12: As Figure 3.10, but showing residuals for stars excluded from our fitting sample (424 spectra of 643 unique stars). Note the changes in both  $x$ - and  $y$ -axis ranges relative to figures 3.10 and 3.11.



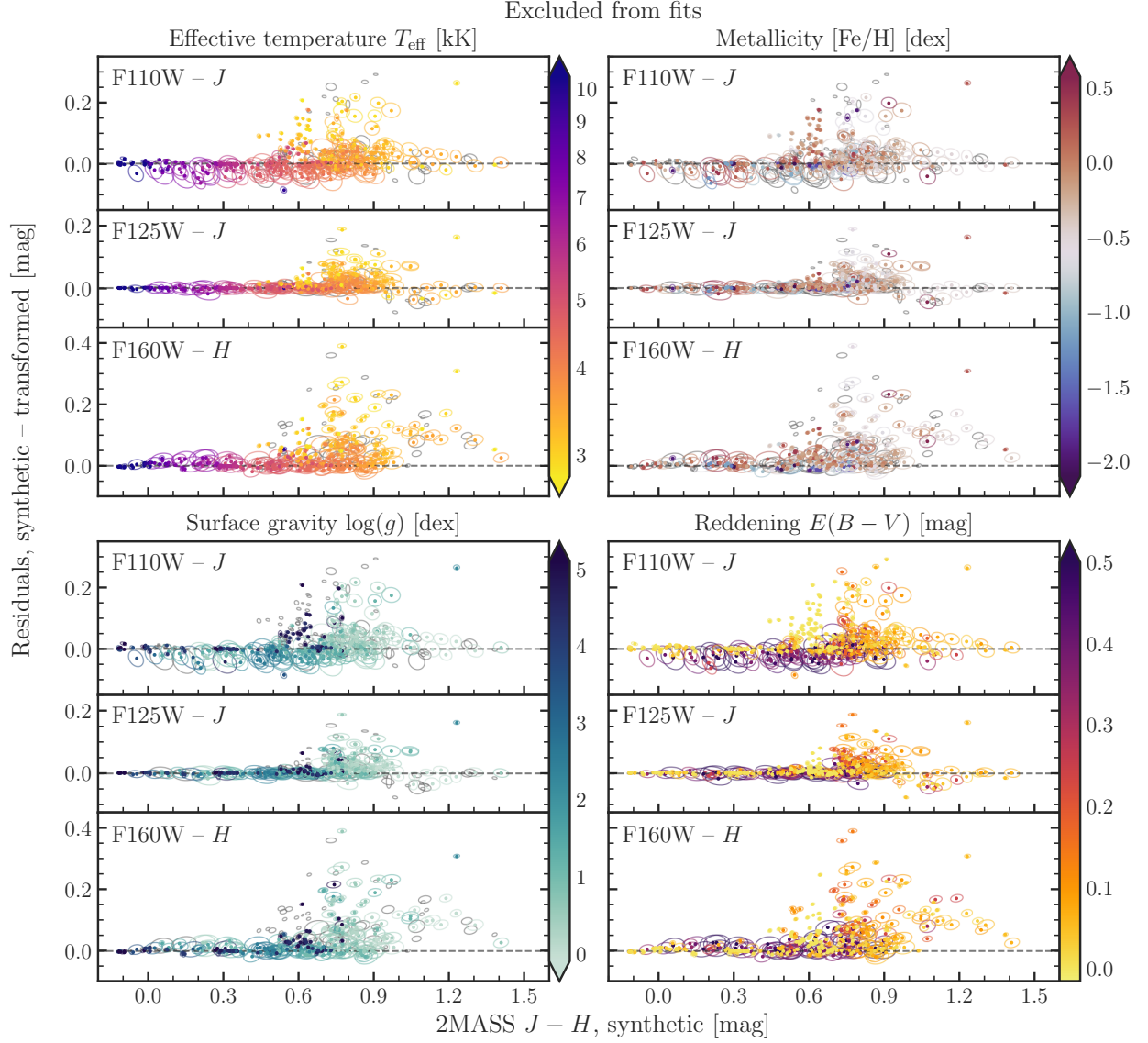


Figure 3.13: As Figure 3.12, with  $J - H$  color on the  $x$ -axis. Again, note differences in  $x$ - and  $y$ -axis ranges between this and previous figures.

also be slight differences in the residuals that correlate with stellar parameters, leading to either increased scatter or small biases that vary systematically with intrinsic quantities, like metallicity and surface gravity, or observed quantities like extinction. We note a possible metallicity dependence in the F110W– $J$  and F160W– $H$  residuals at  $0.4 \lesssim J - H \lesssim 0.8$  (upper right of Figure 3.11), with metal-poor stars appearing to fall preferentially below the nominal fit (that is, slightly brighter in *HST* filters relative to 2MASS than average), and metal-rich above (dimmer in *HST*). This is more or less expected, as higher metal content generally reddens stellar spectra and F110W and F160W both fall bluewards of  $J$  and  $H$  respectively. However, we do not attempt to quantify this effect further given the heterogeneity of available metallicity information and possible confounding effects of surface gravity, dust, and/or specific abundance patterns such as alpha enhancement.

In the excluded sample (Figures 3.12 and 3.13), the most noticeable feature is the much higher level of scatter in the residuals overall, and the color dependence thereof. In particular, the residual amplitude increases dramatically for red stars ( $J - K_S \gtrsim 1$  or  $J - H \gtrsim 0.5$ ) due to deep absorption features and variability (see Figure 3.14).

### 3.5.3 *Stellar classifications*

We now examine residuals for several subclasses of luminous evolved stars, many of which are commonly used in the literature as primary distance indicators. Figure 3.14 compares synthetic photometry residuals for carbon-rich (blue) and oxygen-rich (orange) TP-AGB stars, RGB stars (green), RR Lyrae variables (RRL, red), and classical Cepheids (pink). For stars with multiple library spectra taken at different phase points, we connect their synthetic magnitudes with solid lines to show variability effects.

As seen for the reddest stars in the previous section, it is clear that TP-AGB stars show dramatically higher color-magnitude scatter relative to other stellar types due to temperature- and abundance-dependent absorption features. Furthermore, the strength of these features—as well as the overall SED shape—can vary significantly in individual stars over the course of a thermal pulsation cycle; indeed, we see changes in band-to-band

residuals of up to  $\sim 0.2$  mag in several of the O-rich variables. We note that the XSL observations took simultaneous UV-optical-NIR spectra of such variables at multiple phase points to accurately model their net effects on the integrated light of simple stellar populations. These results highlight the need for similar observing strategies—and careful choices of filters—when cross-calibrating TP-AGB magnitudes between near-infrared photometric systems. This is especially salient in any distance-scale work that seeks to establish a common zeropoint between local calibrators best observed from the ground (e.g. Galactic stars with trigonometric parallaxes, the Magellanic Clouds) and space-based extragalactic observations of distant galaxies.

With the exception of the TP-AGB stars, however, we find that the transformations given in Table 3.3 hold well for RR Lyrae, Cepheids, and RGB stars, and require no additional uncertainties beyond those reported in Table 3.3.

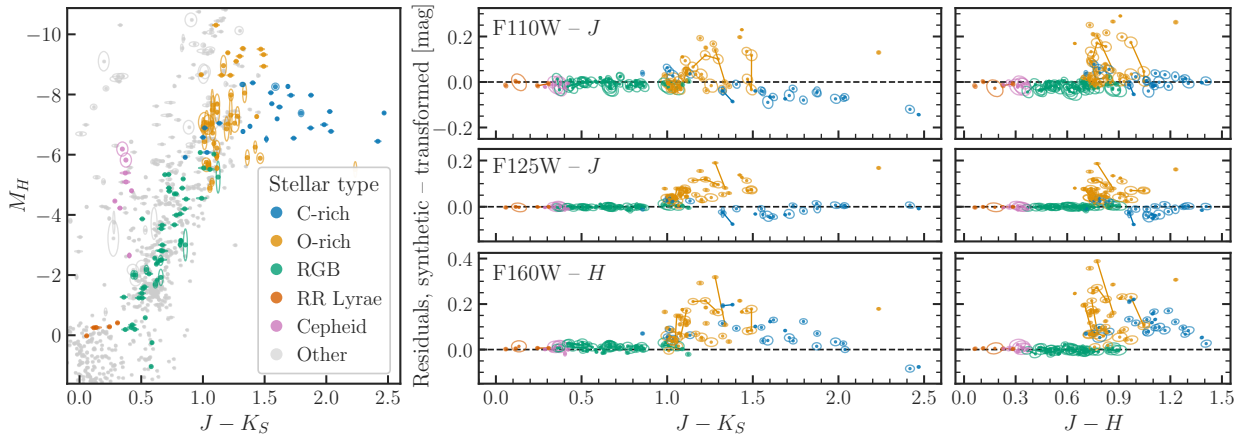


Figure 3.14: Synthetic 2MASS color-magnitude diagram (left) and filter transformation residuals (center, right) with several subtypes of evolved stars used as primary distance indicators highlighted by color. These include C- and O-rich TP-AGB variables in blue and orange respectively; first-ascent RGB stars in green; RR Lyrae variables in red; and classical Cepheids in pink. Repeat observations of the same stars are connected with solid lines.

### 3.6 Conclusions

We have derived new transformations between 2MASS and *HST* broadband filters based on synthetic photometry of empirical stellar spectra. While the majority of stars follow relations that are well-constrained as a function of broadband color, stars with  $T_{\text{eff}} \lesssim 3500$  K in particular diverge significantly from these nominal relations due to molecular absorption. This is especially apparent in the case of both carbon- and oxygen-rich thermally pulsing AGB stars; furthermore, such stars' extreme and often irregular variability poses additional challenges for directly cross-calibrating them between systems. While we cannot recommend a one-size-fits-all set of transformations for these stars, readers may find the individual synthetic magnitudes and literature parameters compiled in Appendix C of use in this regard, depending on the application.

#### 3.6.1 Future Work

We will use the data and methods presented here to predict similar transformations for a number of new and upcoming NIR photometric systems in a follow-up paper, including *JWST*/NIRCam, *Roman*/WFI, and *Euclid*/NISP.

While synthetic photometry is a well-tested and highly efficient method for predicting filter transformations, fully empirical calibrations are of course preferred when possible. In a future paper series (Beaton et al. in prep), we will directly compare *HST* WFC3/IR spectrophotometry of cool giants in the Magellanic Clouds to *JHK<sub>S</sub>* photometry of the same fields from the FourStar camera on Las Campanas Observatory's 6.5m Baade telescope.

## Chapter 4

# EMPIRICAL *HST*-2MASS FILTER TRANSFORMATIONS II. A DIRECT CALIBRATION IN THE MAGELLANIC CLOUDS

The past decade has seen a dramatic increase in the precision at which the Hubble constant ( $H_0$ ), a key cosmological parameter, can be measured. From its initial 10% measure at the conclusion of the *HST* Key Project (Freedman et al. 2001), the current state-of-the-art measurement from the local distance ladder is at 1.4% (Riess et al. 2022), and from modelling the anisotropies in the Cosmic Microwave Background drops this uncertainty by another factor of two to 0.6% (Planck Collaboration et al. 2020). Despite these dramatic improvements, the values themselves are in  $\sim 5\sigma$  tension (Riess et al. 2022). This tension could be signaling physics beyond the current concordance  $\Lambda$ -CDM or pointing to as-yet unrealized systematics in either measurement.

The standard for the local measurement of  $H_0$  is set by calibrating type Ia supernovae (SNe Ia) in the local volume ( $\sim 50$  Mpc) using a stellar standard candle and then applying that calibration to hundreds of SNe Ia in the smooth Hubble Flow (beyond  $\sim 80$  Mpc) (Riess et al. 2019; Freedman et al. 2019). The current standard for SNe Ia calibration is Cepheid-type variables, which can be observed both in the optical and near-infrared out to distances as great as  $\sim 50$  Mpc (Riess et al. 2016).

The growing tension in the value of  $H_0$  has inspired the rise of two competitive alternative techniques for measuring distances to local SNe Ia calibrators: (1) the statistical detection of the tip of the red giant branch (TRGB) in the optical (Beaton et al. 2016; Freedman et al. 2019; Freedman 2021), which can produce exquisitely precise distances (2-3%), but at  $M_I \sim -4$  mag is limited to only  $\sim 40$  Mpc; and (2) Mira-type variables, which require

long-baseline (hundreds of days) multi-epoch observations (Huang et al. 2018, 2020; Sanders 2023). The TRGB as observed in the near-infrared (IR-TRGB), instead of the optical (OPT-TRGB), is a resource-efficient solution to both expand the volume probed by standard candles (at  $M_H \sim -6.0$  mag; Hoyt et al. 2018; Dalcanton et al. 2012a; Wu et al. 2014) and, because only a single epoch of observations in two filters is required, greatly reduce the observational overheads required to obtain precise distances. Thus, the IR-TRGB combines the intrinsic brightness of variable stars with the statistical precision of the OPT-TRGB to enable large-scale distance measurement.

A major expansion of the use of the IR-TRGB is expected from the *Nancy Grace Roman Space Telescope*, whose proposed wide-area survey will provide  $\sim 5\%$  IR-TRGB distances to *any* galaxy within  $\sim 20$  Mpc. This will sharpen secondary distance indicators like the Tully-Fisher Relation (Tully et al. 2016; Singh et al. 2021) and the Fundamental Plane (Blakeslee et al. 2002). The IR-TRGB can also be pushed to much larger distances with *JWST* and the next generation of extremely large telescopes (ELTs). Distances accessible with the IR-TRGB technique for these facilities are sufficiently large that they are best communicated not in linear distance, but in redshift. Conservatively, *JWST* can reach out to  $cz \sim 2400$  km/s ( $z = 0.008$ ) in a 1-hour total integration, and ELTs to  $cz \sim 7200$  km/s ( $z \sim 0.024$ ). Accessing these volumes will produce several major advances in cosmological parameter derivation: (i) the TRGB can be used *directly* in the Hubble Flow (bypassing SNe Ia); (ii) hundreds, instead of  $\sim$ dozens, of SNe Ia can be calibrated over a large range of properties to better understand their intrinsic variations for application to dark energy studies; and (iii) techniques independent of the distance-ladder can be checked directly against the distance ladder to form a consensus distance scale (e.g., megamasers and gravitational wave standard sirens (Beaton et al. 2019a; Beasley et al. 2019), among others). Thus, the IR-TRGB enables the measurement of key quantities in cosmology in a vastly new way.

While the application of the IR-TRGB is straightforward, establishing the absolute system remains a challenge. The absolute system is set by objects (either individual stars or populations in galaxies) with distances determined via geometric techniques. Of these,

there are currently only a handful: (i) *Gaia* parallaxes of individual stars in the Milky Way (e.g. Li et al. 2022; Dixon et al. 2023); (ii) a 1.3% (2%) eclipsing binary distance to the Large (Small) Magellanic Cloud (Pietrzyński et al. 2013, 2019; Graczyk et al. 2020); (iii) a less precise eclipsing binary distance to M 31 (Vilardell et al. 2010); and (iv) a distance to NGC 4258 from modeling the megamaser within its black hole accretion disk (Reid et al. 2019). The geometric distances to M 31 and NGC 4258 are feasible to calibrate directly using the space-based filter systems, and these studies can be performed with existing datasets (e.g., Williams et al. 2018; Jang et al. 2021). Galactic field stars are challenging to use directly with space-based instrumentation, both due to their brightness and due to the sparse nature of the targets, which require wide-area mapping. There are special WFC3/IR observing modes that have been used to great success for small numbers of nearby calibrator stars, but the overheads are still far too extreme for the hundreds of stars required for a precise TRGB calibration (Rich et al. 2018; Riess et al. 2016; Casertano et al. 2016; Deustua et al. 2014). This leaves the Magellanic Clouds, in particular the LMC, as the best available anchors in which to determine a direct transformation between 2MASS and WFC3/IR from a set of commonly observed stars.

The Magellanic Clouds are ideal for making such a comparison for several reasons. First, their population characteristics are broadly typical of the environments where the IR-TRGB is most effectively applied: the halos of Milky Way-mass galaxies ( $\sim 1.5$  dex, with a large spread; Gilbert et al. 2014), sufficiently populated dwarf galaxies (Hatt et al. 2017), and the outskirts of early-type galaxies. The median metallicity of older stellar populations in the LMC (SMC) is  $-0.7$  ( $-1.2$ ) dex, and both objects have strong spreads ( $\sim 1.5$  dex) in  $M/H$  and  $\alpha/H$  over their full multi-degree extents (Nidever et al. 2020). Second, they are one of only a few well-populated extragalactic systems in which high-precision NIR photometry (at the 1% level or better) at the magnitude of the TRGB can be obtained from the ground. While adaptive optics can reach the depths and spatial resolutions required, precise absolute photometry remains a challenge.

In this paper we present initial results of a pure-parallel *HST* campaign designed to

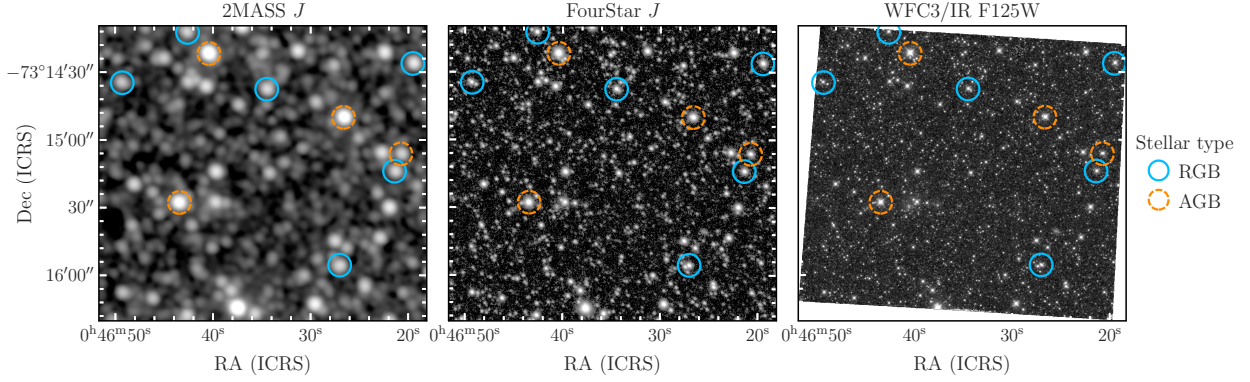


Figure 4.1: Comparison of imaging data from 2MASS 6X  $J$  (left), LCO/FourStar  $J$  (center), and *HST* WFC3/IR F125W (right) of the same field in the Small Magellanic Cloud (SMC\_AV\_14\_1 in our nomenclature). The *HST* image is a single exposure, whereas 2MASS and FourStar are stacked mosaics. Bright RGB and AGB stars are circled in solid blue and dashed orange respectively, with classifications taken from the OGLE-III catalog of long-period variable stars (Soszyński et al. 2009, 2011).

obtain high-quality NIR photometry and low-resolution spectroscopy of upper RGB stars in the Magellanic Clouds, along with counterpart ground-based observations from the FourStar camera on Las Campanas Observatory’s 6m Baade telescope (hereafter LCO/FourStar or simply FourStar). While a direct calibration between *HST* and 2MASS is not impossible, the 2MASS data are hampered by photometric blends and crowding at the magnitudes and stellar surface densities of interest. Figure 4.1 illustrates this with a side-by-side comparison of 2MASS, FourStar, and *HST* imaging data for a single *HST* pointing in the Small Magellanic Cloud, with known upper RGB and AGB stars circled. The FourStar image depth and resolution are much closer to that of *HST* than 2MASS. Notably, several of the RGB stars have nearby neighbors that are unresolved in 2MASS, but clearly resolved in FourStar and *HST*.

Figure 4.2 compares throughput curves for a subset of filters on the four instruments we consider here: *HST* WFC3/IR, 2MASS, LCO/FourStar, and Paranal/VISTA. While differences between  $JHK_S$  filters in the three ground systems are subtle (if not fully negligible),



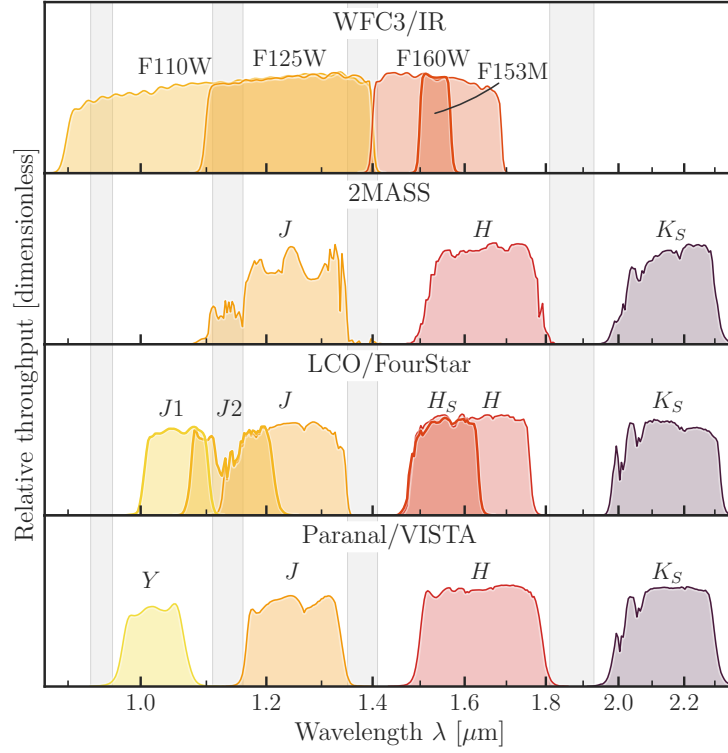


Figure 4.2: Spectral response curves for selected near-infrared wide- and medium-band imaging filters on *HST* WFC3/IR, 2MASS, LCO/FourStar, and Paranal/VISTA (upper to lower panels). Regions strongly affected by absorption features in Earth’s atmosphere (tellurics) are marked by gray vertical bars, with boundaries taken from Verro et al. (2022a, Table 1). We focus on the wide passbands in this work (F110W, F125W, and F160W on *HST*, and  $JHK_S$  on the ground), and will present additional medium band data (F153M,  $J1$ ,  $J2$ , and  $H_S$ ) in a future paper.

even their closest analogues on *HST* are noticeably different in wavelength coverage, reinforcing the importance of calibrating all filters with a common set of stars.

The paper is organized as follows. §4.1 describes the *HST* (§4.1.1) and FourStar (§4.1.2) observations, data reduction, and photometry procedures, and the production of the final crossmatched catalog (§4.1.3). §4.2 presents color-magnitude diagrams and cross-instrument filter transformations. We compare to literature results in §4.3, and give a summary and conclusions in §4.4.

#### 4.1 Observations, data reduction, and photometry

§4.1.1 describes the observing strategy, data processing, and photometry procedures for our *HST* campaign, and §4.1.2 describes the same for the counterpart ground-based observations. §4.1.3 describes the process of cross-matching photometry at the exposure and instrument levels to produce matched multiband catalogs.

All observations taken as part of this program are summarized in Table 4.1, and Figure 4.3 shows their locations on the sky overlaid on the *Gaia* DR3 source density map.

Table 4.1: Summary of WFC3/IR and FourStar observations.

Field Name	R.A. <sup>a</sup>	Decl. <sup>a</sup>	<i>HST</i> cycle			LCO observation date <sup>b</sup>		
	ICRS	ICRS	27	28	29	01-02	11-14	11-16
LMC_SK_-68_8_1	73.506357	-68.626855	X			X	X	
LMC_SK_-68_8_2	73.639922	-68.756230	X			X	X	
LMC_N11_026_1	74.238119	-66.323070	X			X	X	
LMC_SK_-68_16_1	74.541885	-68.449595	X			X	X	
LMC_HV_5622_1	77.596996	-68.961495	X			X	X	
LMC_SK_-71_19_1	80.622226	-71.270509	X			X	X	

<sup>a</sup> Coordinates are the centers of the *HST* pointings.

<sup>b</sup> All dates are for the year 2021.

Table 4.1 — continued

Field Name	R.A. <sup>a</sup>	Decl. <sup>a</sup>	<i>HST</i> cycle			LCO observation date <sup>b</sup>		
	ICRS	ICRS	27	28	29	01-02	11-14	11-16
LMC_SK_-69_140_2	82.058949	-69.281399	X			X	X	
LMC_LMCe078-1_1	84.301586	-69.160400	X	X		X	X	X
LMC_SK_-70_16_1	73.658110	-70.065153		X				
LMC_SK_-69_43_1	73.846232	-69.210118		X				
LMC_SK_-66_17_1	73.947106	-66.427066		X			X	
LMC_SK_-71_21_1	80.759676	-71.668570		X			X	
LMC_SK_-67_167_1	83.104615	-67.592718		X			X	
LMC_HD_269927C_1	84.551376	-69.524323		X			X	
LMC_SK_-67_266_1	86.628756	-67.300250		X			X	
LMC_SK_-66_17_3	73.904037	-66.501278			X		X	
LMC_N11_051_1	74.009610	-66.368952			X		X	
LMC_LH_9-89_1	74.064700	-66.446129			X		X	
LMC_SK_-66_18_1	74.069429	-66.056381			X			
LMC_N11_046_1	74.076943	-66.653721			X			
LMC_LMCe055-1_1	74.186453	-69.868456			X			
LMC_SK_-69_52_1	74.697892	-69.892836			X			
LMC_SK_-70_50_1	75.669415	-70.200188			X			
LMC_SK_-70_60_1	76.185237	-70.224231			X			
LMC_SK_-69_83_2	78.405105	-69.535491			X			
LMC_SK_-69_83_1	78.883831	-69.508190			X			
LMC_SK_-67_78_1	79.840998	-67.304241			X			
LMC_SK_-67_78_2	80.301049	-67.313528			X			

<sup>a</sup> Coordinates are the centers of the *HST* pointings.<sup>b</sup> All dates are for the year 2021.

Table 4.1 — continued

Field Name	R.A. <sup>a</sup>	Decl. <sup>a</sup>	<i>HST</i> cycle			LCO observation date <sup>b</sup>		
	ICRS	ICRS	27	28	29	01-02	11-14	11-16
LMC_LH_58-496_1	81.428546	-68.810599			X			
LMC_SK_-71_35_1	82.238915	-71.113195			X			
LMC_SK_-71_46_1	82.975567	-70.993524			X			
LMC_SK_-69_178_1	83.095613	-69.476595			X			
LMC_SK_-69_212_2	83.788259	-69.160495			X			
LMC_SK_-68_133_1	84.001863	-68.762075			X			
LMC_SK_-69_212_1	84.205169	-69.162533			X	X	X	
LMC_VFTS_355_1	84.621757	-68.998532			X	X	X	
LMC_[ST92]_5-52_1	84.764192	-69.639422			X			
SMC_AV_14_1	11.645862	-73.254116	X			X	X	X
SMC_AV_187_1	14.622625	-71.282483	X			X	X	
SMC_AV_235_1	15.182993	-72.797432	X			X	X	
SMC_AV_332_2	15.907979	-72.262273	X			X	X	
SMC_AV_332_1	15.915021	-72.196823	X			X	X	
SMC_AV_393_1	16.565307	-72.412196	X			X	X	
SMC_2dFS_2266_1	16.788492	-72.329429	X			X	X	
SMC_AV_440_1	17.528008	-71.869370	X			X	X	
SMC_AV_488_1	19.209163	-73.418120	X			X	X	
SMC_2dFS_3694_1	20.832438	-73.171903	X				X	
SMC_AV_85_1	12.867040	-72.805318		X				
SMC_AV_96_1	12.905838	-72.038137		X				
SMC_AV_148_1	13.161580	-72.662020		X				

<sup>a</sup> Coordinates are the centers of the *HST* pointings.

<sup>b</sup> All dates are for the year 2021.

Table 4.1 — continued

Field Name	R.A. <sup>a</sup>	Decl. <sup>a</sup>	<i>HST</i> cycle			LCO observation date <sup>b</sup>		
	ICRS	ICRS	27	28	29	01-02	11-14	11-16
SMC_AV_186_1	14.454051	-72.558794		X				X
SMC_AV_343_1	16.128977	-72.627007		X				X
SMC_AV_445_1	17.042607	-72.395550		X		X	X	
SMC_AV_472_1	18.533833	-72.721052		X			X	
SMC_AV_224_1	14.763455	-72.087255			X			X
SMC_AV_296_2	15.432402	-72.135818			X			X
SMC_2dFS_2553_1	17.293580	-73.170638			X			
SMC_SK_183_1	22.240860	-73.468530			X			
SMC_SK_187_1	22.897249	-73.308369			X			X
SMC_SK_187_2	23.007647	-73.348568			X			X

#### 4.1.1 WFC3/IR

The Wide Field Camera 3 instrument is a fourth-generation imager installed during the fourth *HST* servicing mission. Its infrared channel, WFC3/IR, is a 1024x1024 CMOS HgCdTe detector with a  $136'' \times 123''$  field-of-view and  $\sim 0.13''$  pixel<sup>-1</sup> plate scale. It includes fifteen wide, medium, and narrow filters as well as two grisms.

#### Program Design

Our observing campaign comprises *HST* proposals GO/PAR-15875, GO/PAR-16358, and GO/PAR-16928 (cycles 27 through 29 respectively; Beaton et al. 2019b, 2020, 2022). The program was designed as a pure-parallel to be executed alongside observations for the *Hubble* *UV Legacy Library of Young Stars as Essential Standards* (ULLYSES, Roman-Duval et al.

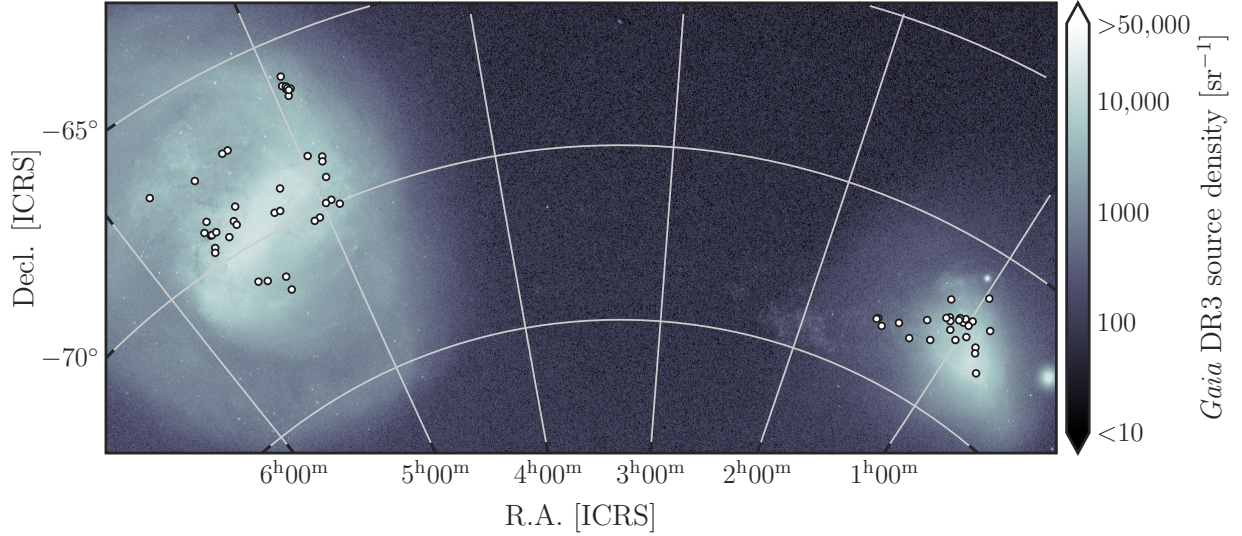


Figure 4.3: Locations of all pure parallel *HST* pointings obtained as part of this work (white points), overlaid on the *Gaia* DR3 source density map in the vicinity of the Magellanic Clouds (Gaia Collaboration et al. 2022a). The actual WFC3/IR footprints are smaller on the sky than the size of the markers.

2020)<sup>1</sup>. ULLYSES is a large Director’s Discretionary program devoting approximately 1,000 orbits to obtaining ultraviolet spectroscopy of a wide range of young stars, including OB stars in both Magellanic Clouds. By taking WFC3 exposures during the UV spectroscopy, we anticipated capturing of order 1-3 upper RGB stars (within 1 mag of the TRGB) per pointing, based on extant observations of the MCs.

As WFC3/IR is several arcminutes offset in the *HST* focal plane relative to the primary instruments, and the roll angles of the primaries were unconstrained, exact WFC3/IR field locations were not possible to specify beforehand. Similarly, repeat parallels attached to observations of the same primary target were not necessarily guaranteed to overlap each other, depending on the net difference in roll angle at the respective times of observation. Therefore, we adopt the field names for the primary targets, but append an extra digit to identify non-overlapping parallel fields for the same primary where needed.

---

<sup>1</sup><https://ullyses.stsci.edu>

Table 4.2: Typical 1-orbit *HST* exposure sequence

Name	Filter	Samp. seq.	N. reads	$T_{\text{exp}}$ [s]	Readout times [s]
J_Spec	G102	SPARS25	4	77.9	2.9, 27.9, 52.9, 77.9
J_Img	F125W	RAPID	7	20.5	2.9, 5.9, 8.8, 11.7, 14.7, 17.6, 20.5
H_Spec	G141	SPARS25	5	102.9	2.9, 27.9, 52.9, 77.9, 102.9
H_Img	F160W	RAPID	7	20.5	2.9, 5.9, 8.8, 11.7, 14.7, 17.6, 20.5
Hs_Img <sup>a</sup>	F153M	SPARS10	2	12.9	2.9, 12.9
wJ_Img	F110W	RAPID	5	14.7	2.9, 5.9, 8.8, 11.7, 14.7

<sup>a</sup> Introduced in Cycle 28.

Our exposure sequences for WFC3/IR were designed to avoid saturating the TRGB stars of interest. Following Hoyt et al. (2018), the magnitudes of the TRGB in the LMC (SMC) are between  $12.4 < H_{\text{LMC}} < 12.5$  ( $12.9 < H_{\text{SMC}} < 13.0$ ), which saturate in  $\sim 2.0$  s ( $\sim 3.1$  s) in F110W,  $\sim 3.4$  s ( $\sim 5.2$  s) in F125W, and  $\sim 3.5$  s ( $\sim 5.5$  s) in F160W based on the ETC. These times to saturation are very short, but all but one are longer than the minimum WFC3/IR full-frame exposure time of 2.9s, which is set by the time required to read out the chip. In this time, stars near the TRGB reach a predicted signal-to-noise of over 300. While it is possible to use subarrays to obtain shorter exposure times, our program is not centered on specific stars and, thus, the full area is needed to sample as many stars as possible.

*HST* observations were obtained in pure parallel mode for STIS or COS primary observations. The frame-by-frame details for pure parallel programs are set by the needs of the primary program, in particular the memory capacity of in-flight buffers. Thus, our program was limited to 32 individual reads of the WFC3/IR chip. A typical exposure sequence for a single-orbit observation is given in Table 4.2. This is the sequence used for 1-orbit visits; for 2-orbit visits the order of the F125W and F160W exposures were flipped to test for systematics due to taking observations through the Earth’s atmosphere. As noted in Table 4.2, the F153M filter was added at the beginning of Cycle 28.

### Photometry

We measured all WFC3/IR photometry using the `hst1pass` software (Anderson 2022). `hst1pass` is a publicly available FORTRAN routine designed to perform optimal point spread function (PSF) fitting on relatively bright, isolated sources in individual *HST* `flt` or `flc` exposures. Included with the software are a number of library *HST* PSFs derived using the effective PSF method (ePSF, Anderson & King 2000, 2006), with those provided for WFC3/IR described in Anderson (2016).

Table 4.3: `hst1pass` parameters

Name	Value	Description
HMIN	2	Minimum isolation in pixels
FMIN	500	Minimum flux (SNR~20)
PSF	PSFSTD	Library PSF file
GDC	STDGDC	Distortion model file
DOSATD	+ <sup>a</sup>	Measure saturated stars?
PMAX	9999999	Maximum central pixel flux
QMAX	0.25 <sup>b</sup>	Maximum PSF quality-of-fit
CMIN	-0.2	Minimum PSF central excess
CMAX	0.2	Maximum central excess
PERT	0/1 <sup>c</sup>	Perturb library PSF?

<sup>a</sup> +/- = True/False

<sup>b</sup> 0 being a perfect fit.

<sup>c</sup> 1 for sufficiently populated fields, otherwise 0.

Our `hst1pass` star finding and data quality parameters are summarized in Table 4.3. We briefly discuss the most relevant of these here. For in-depth descriptions of all parameters, please refer to Anderson (2022).



`hst1pass` takes three required arguments when operating on an input image or list of images. `HMIN` and `FMIN` are finding parameters, which specify the minimum radius at which a pixel can have no brighter neighbors and the minimum flux in the brightest 2x2 pixels respectively. `PSF` specifies either the PSF library file, or else a radius and sky annulus for aperture photometry.

A number of optional arguments allow tuning of certain photo- and astrometric quality parameters and the inclusion of additional reference files. `GDC` refers to a file with a model of the instrument geometric distortion, required to transform between instrumental and celestial coordinate frames and to correct photometry for distortion-induced pixel area variations. Like the library PSFs, these are provided along with the code for *HST* instruments. `DOSATD` specifies whether to perform aperture photometry on saturated stars, and `PMAX` sets the maximum allowed flux of the central pixel. The `QMAX`, `CMIN`, and `CMAX` parameters relate to PSF-fitting quality metrics. `q` is the PSF-weighted sum of the fit residuals, where a perfectly fit source has `q`=0. `c` is the excess of the central pixel relative to the best-fit PSF. Positive `c` values indicate too-sharp sources, such as cosmic rays in CCD data, and negative values indicate blurry or extended sources.

`hst1pass` allows an option to construct “perturbation” PSFs, which are empirical adjustments to the library PSFs to account for image-to-image variations from telescope jitter, focus changes (both from thermal expansion and contraction over the course of an orbit, or “breathing”, and from long-term secular focus changes), and other such spacecraft or instrument effects. A value of 0 for the `PERT` parameter indicates to use the library PSFs as-is. 1 indicates to derive a single perturbation PSF for the entire image, and higher values (up to 9) produce an  $n \times n$  perturbation PSF grid evenly spaced over the image area.

We initially ran all photometry with `PERT`=0, as recommended in the documentation, and then a second round with `PERT`=1. Not all of these second runs completed, as many exposures lack sufficient bright and isolated stars with which to construct a perturbation PSF. For exposures where the `PERT`=1 runs were successful, we found consistently higher photo- and astrometric quality. We adopt the `PERT`=1 photometry wherever available in the

rest of this work.

### *Zeropoints*

`hst1pass` provides strictly uncalibrated photometry by design. Users are encouraged to derive their own zeropoints both for the sake of understanding the associated uncertainties, and because the *HST* absolute photometric calibration is subject to ongoing refinement. Therefore, we adapt STScI’s recommended procedure for calculating custom zeropoints with the Python package `stsynphot` (STScI Development Team 2020)<sup>2</sup>.

`stsynphot` offers the option to predict ACS and WFC3 photometry for apertures much smaller than the “infinite” aperture that defines the full extent of the PSF. In this mode, synthetic fluxes are scaled by the fraction of flux the PSF contains at a given radius (“encircled energy”) relative to its flux at infinity. The on-orbit encircled energy calibration for WFC3/IR is discussed in Hartig (2009); `stsynphot` implements the values reported in their Table 6.

The `hst1pass` library PSFs for WFC3/IR are normalized to a 5.5 pixel radius (0.7″ on average for WFC3/IR<sup>3</sup>), as are all its downstream photometric outputs (Anderson 2016). However, this is not the same as the aperture used in the PSF-fitting process itself. For that `hst1pass` uses the innermost  $5 \times 5$  whole pixels, or an effective radius of  $r \approx 2.8$  pixels ( $\sim 0.36''$  on WFC3/IR).

We note that the `stsynphot` documentation<sup>4</sup> recommends using only the aperture radii at which encircled energy fractions have been measured for a given instrument (the nearest of these to our 0.7″ aperture being 0.6 and 0.8″). This is because it performs only first-order interpolation of the encircled energy fraction with respect to aperture radius, which the authors caution may be a poor approximation of its true form at small radii especially. However,

---

<sup>2</sup><https://github.com/spacetelescope/WFC3Library/tree/master/notebooks/zeropoints>

<sup>3</sup>WFC3/IR pixels are not square on the sky due to its substantial geometric distortion, with a  $\sim 10\%$  difference in scale between the image  $x$  and  $y$  axes.

<sup>4</sup>[https://stsynphot.readthedocs.io/en/stable/stsynphot/appendix\\\_specialkey.html\#encircled-energy; v1.2.0](https://stsynphot.readthedocs.io/en/stable/stsynphot/appendix\_specialkey.html\#encircled-energy; v1.2.0)

the most recent web version of the encircled energy table<sup>5</sup> provides values for a different set of aperture radii than those reported in Hartig (2009); the nearest of these to ours are 0.65 and 0.78". The page does not specify the origin of these values, but we speculate that an update to the 2009 calibration is in progress. Calamida et al. (2022) presented new encircled energy measurements for a subset of WFC3/UVIS filters that incorporated time-dependent photometric calibration information, but uncertainties in the WFC3/IR sensitivity evolution prevented them from doing the same there (see their section 4 and Som et al. 2021). Since then, Bajaj et al. (2022) have reported an IR sensitivity loss term of  $0.13 \pm 0.02\%$  year<sup>-1</sup>, with no evidence of wavelength dependence. For these reasons, we have chosen to derive initial zeropoints at the 0.7" radius regardless of the possible uncertainties it introduces. We conservatively estimate the uncertainty as half the difference between the zeropoints calculated at the `stsynphot`-recommended 0.6 and 0.8" apertures. We will make updates in a future data release should a new encircled energy calibration become available.

Our final zeropoint values are provided in Table 4.4. We use the newly implemented time-dependent photometric calibration (Calamida et al. 2022) to calculate zeropoints appropriate for the approximate midpoint of our full set of observations, MJD=59570 (December 22, 2021). Although we use the Vega magnitude system throughout this paper, we also provide the ST and AB systems for convenience, and we similarly include F153M for posterity despite limiting this initial work to our broadband data. Our reference Vega spectrum is `alpha_lyr_stis_011.fits`, and our operational CRDS<sup>6</sup> context is `hst_synphot_0055.imap`. The full `stsynphot` observation mode keyword pattern is `wfc3,ir,<band>,mjd#59570,aper#0.7`, where `<band>` is the filter name in all lowercase.

---

<sup>5</sup><https://web.archive.org/web/20230607225833/https://www.stsci.edu/hst/instrumentation/wfc3/data-analysis/photometric-calibration/ir-encircled-energy>

<sup>6</sup>Calibration Reference Data System; <https://hst-crds.stsci.edu/>

Table 4.4: WFC3/IR zeropoints

Filter	$\lambda$ [ $\mu\text{m}$ ]	Vegamag	STmag	ABmag	$\sigma$
F110W	1.1521	25.9297	28.3200	26.7046	0.0143
F125W	1.2481	25.1956	27.9045	26.1153	0.0131
F153M	1.5322	23.0438	26.5541	24.3197	0.0210
F160W	1.5366	24.5370	28.0516	25.8109	0.0201

NOTE—Zeropoints are for an  $0.7''$  aperture at MJD=59570.  $\lambda$  indicates pivot wavelength (Koornneef et al. 1986).

### *Astrometric alignment*

We adapted the workflow described in Bajaj (2017)<sup>7</sup> to align our *HST* data to *Gaia* with *TweakReg*. *TweakReg* is an alignment routine included in the *Drizzlepac* software (Gonzaga et al. 2012; STSCI Development Team 2012; Avila et al. 2015; Hoffmann et al. 2021). It derives transformations between coordinates of sources in a reference frame and sources in individual exposures using a triangle pattern matching algorithm, and optionally updates exposure headers’ WCS information with the “tweaked” astrometric solutions.

Here, we used *Gaia* DR3 coordinates as the reference catalog (ICRS, epoch J2016.0), and *hst1pass* pixel coordinates as exposure catalogs. We employed progressive quality cuts depending on numbers of available stars (per target for *Gaia*, and per exposure for *HST*). For *Gaia*, we restricted all reference catalogs to non-duplicated sources (`Dup == 0`) with the recommended `RUWE < 1.4`. For targets with more than 500 reference sources, we additionally required the maximum error of the 6-parameter astrometric solution to be less than 1 mas (`amax < 1`), and for over 1000 reference sources we required `amax < 0.5` mas. For *HST*, we required that the absolute central pixel excess relative to the PSF model be less than 0.1 (`C**2 < 0.1**2`), and quality-of-fit `q` values less than: 0.2 for exposures with 50+ detected

---

<sup>7</sup>[https://github.com/spacetelescope/gaia\\\_alignment](https://github.com/spacetelescope/gaia\_alignment)

sources; 0.15 for 250+ sources; and 0.1 for 500+ sources.

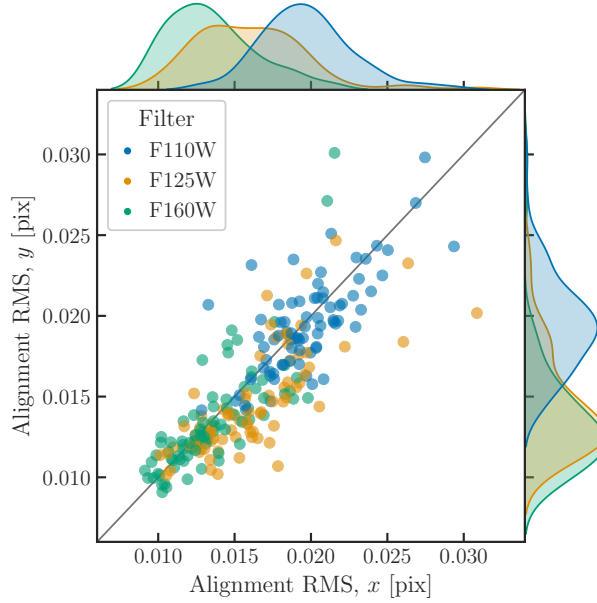


Figure 4.4: Per-exposure RMS scatter of **TweakReg** astrometric solutions relative to *Gaia* DR3, in units of WFC3/IR pixels (plate scale  $0.13'' \text{ pixel}^{-1}$ ). Scatter points and marginal density plots are color-coded by filter.

The  $x$  and  $y$  RMS dispersions of all alignment solutions are shown in Figure 4.4. Nearly all frames are aligned to within 0.03 pix (4 mas) on both axes, and the majority of F125W and F160W frames are aligned to within 0.02 pix ( $\sim 2.5$  mas). The scatter in F110W is systematically higher by about a factor of 2, likely due to greater numbers of both faint sources and saturated stars.

We considered incorporating proper motion information from *Gaia* into our alignment procedure, but we found that doing so offered only marginal benefits at best, even with strict quality cuts. For a number of fields, application of proper motions to the reference catalogs consistently increased the residual scatter. We attribute this largely to lingering scanning-law systematics in *Gaia* DR3 (see Gaia Collaboration et al. 2021), which we expect will continue to see substantial improvement in future data releases.

#### 4.1.2 LCO/FourStar

To complement each field observed with *HST* WFC3/IR, observations were acquired from the ground using the FourStar instrument on the Magellan-Baade telescope at Las Campanas Observatory (hereafter LCO/FourStar or simply FourStar; for a full description of the instrument, please see Persson et al. 2013). FourStar is a  $4\text{ K} \times 4\text{ K}$  NIR imager with Teledyne electronics and an all-refractive optical system. The  $10.8' \times 10.8'$  field-of-view is split over four HAWAII-2RG detectors, with a pixel scale of  $0.159'' \text{ pixel}^{-1}$ .

In addition to the  $JHK_S$  broadband filter set, five medium-width filters spanning the 1-1.8  $\mu\text{m}$  wavelength range are available. These were designed for the FourStar Galaxy Evolution Survey (ZFOURGE, Straatman et al. 2016)<sup>8</sup> to enable precise and accurate photometric redshift measurements unachievable with wider filters. Similarly, the finer sampling of stellar SEDs enables luminous giant subtypes to be much more reliably identified than with broadband data (e.g. Boyer et al. 2013, 2019). All six FourStar filters obtained in this survey ( $JHK_S$  and the medium bands  $J1$ ,  $J2$ , and  $H_S$ ) are shown in Figure 4.2.

While the  $JHK_S$  data are easily calibrated to 2MASS with only minimal if any color terms (see §4.1.2 and §4.2.2), color and airmass terms must be jointly fitted in the case of the medium band data. As we observed all targets in one filter at a time (§4.1.2), different bands were taken at different airmasses over the course of the night, further complicating their relative calibration. For that and other reasons, we focus on the  $JHK_S$  filters in this work, and will incorporate the medium band data in a future data release. As part of this future release, we will include data from a secondary campaign of standard star observations, with which we will further constrain the medium bands' zeropoints and color terms.

#### Program design

Because the roll-angle for the *HST* parallel observations was not constrained, the precise coordinates of the WFC3/IR fields were only known once the observations were taken. Thus,

---

<sup>8</sup><https://zfouge.tamu.edu/>

the ground-based observations occurred after the *HST* observations (once the coordinates were known), typically in the B LCO semester when both the LMC and SMC are accessible for the full night. A basic observing log of the LCO/FourStar campaign is given in Table 4.1, with the exposure times and dither sequences repeated at each position given in Table 4.5.

The ground observations were planned to reach signal-to-noise  $\sim 100$  for the upper giant branch targets of interest in all six filters ( $J1$ ,  $J2$ ,  $J$ ,  $H_S$ ,  $H$ ,  $K_S$ ). A 5-pt dither sequence was used to achieve five images of length  $<10$  s each and the specifics are given in Table 4.5. Custom macros were used to minimize overheads. The macro would move to all fields in a region of the sky (usually the LMC or SMC) and execute a single filter sequence (Table 4.5) at each location. The script was used once per filter because filter moves on FourStar take several seconds and, in some switches, require focus offsets, which also add time. We did not guide or do real time focus adjustments because any given position was not held long enough; thus between each run of the macro, we reset to the initial coordinates and performed a Shack-Hartmann focus after known focus offsets (if required).

Table 4.5: Typical LCO/FourStar Exposure Sequence

Filter	Exptime [s]	Sequence
$J1$	5.822	5-pt dither
$J2$	5.822	5-pt dither
$J$	4.366	5-pt dither
$H_S$	5.822	5-pt dither
$H$	4.366	5-pt dither
$K_S$	4.366	5-pt dither

### *Image reduction*

Raw data was processed using a FourStar Reduction (FSRED) pipeline developed by AJM. The pipeline preprocesses the raw image data by applying a linearity, dark and flat field correction and creates a bad pixel mask for each image starting with the known bad pixels. The pipeline also masks pixels above the saturation threshold and forward propagates those pixels to mask image persistence up to five minutes from the onset of saturation.

The pipeline creates a first pass sky frame for each raw image by combining a number (nine in this case) of adjacent dithered frames and rejecting 50% of high values (which might be stars, cosmic rays or other transients like satellite streaks, etc). For each FourStar exposure, there are four images (one for each chip) which are merged into a multi-extension fits (MEF) image that is then analyzed to locate sources using Source Extractor (Bertin & Arnouts 1996; Bertin & Arnouts 2010). The Source Extractor detection catalogues are used as input into SCAMP (Bertin 2006, 2010a), which solves for the astrometric alignment between frames and on sky using 2MASS sources as a reference (Skrutskie et al. 2006), then SWarp (Bertin et al. 2002; Bertin 2010b) is used to resample each image along with a weight image. The pipeline uses IRAF's `imcombine` (Tody 1986, 1993; National Optical Astronomy Observatories 1999) to co-add (using a median) the resampled images into a first pass mosaic image of the field.

Source Extractor is run on the first pass mosaic to detect and mask sources; for each input image, a corresponding sub-image from the mosaic and mask is created. Sources detected in the mosaic are propagated to each input mask, and the difference between each input and corresponding subsection is used to detect and mask transients (cosmic rays, satellites, etc). For each input, a second pass sky is created using a weighted average (weighted inversely by time difference or position offset from the input frame) of adjacent frames relying on the masks to reject non-sky sources. Similar to the first pass step, the sky-subtracted mef images are run through Source Extractor, SCAMP and SWARP and resampled into images which are combined, using IRAF:`imcombine`, using a weighted average into a final image mosaic.



### *FourStar photometry*

The final mosaics are photometered using Source Extractor to detect sources and DAOPHOT (Stetson 1987, 2011) to perform point spread function (PSF) photometry. The final mosaic image for each filter is run through a script which first detects sources using Source Extractor with a detection threshold of  $15\sigma$ , where  $\sigma$  is the sky background standard deviation. Then the output from Source Extractor is used to identify 200 sources to be used to create a PSF in the DAOPHOT PSF-fitting software. The image is then iterated on 3 times with decreasing detection threshold sigmas of 10, 5, and 2. In each iteration Source Extractor detects sources, then DAOPHOT:PHOT is used to perform aperture photometry at each location then DAOPHOT:ALLSTAR is used to fit the PSF and generate a PSF subtracted image for the next iteration of detection. In each iteration the new detections are simply appended to the original list and ALLSTAR is run on the original image with the appended list of detections. The PSF subtracted images are only used for detection of fainter or hidden/merged sources; it is not recommended to PSF fit an image which has already been PSF subtracted.

### *Calibration to 2MASS*

Normally, the PSF photometry would be compared against the APER photometry to determine an offset to add to the PSF phot to place it on the APER system. Then the PSF phot would be compared to 2MASS stars in the frame to determine a zero-point offset for that filter/frame. The PSF to APER correction is redundant since a single zero-point offset can be determined by comparing the raw  $JHK_S$  PSF photometry directly to 2MASS magnitudes, which simultaneously incorporates an airmass correction term.

For each mosaic, we matched the single-band photometry to 2MASS using a maximum radius of  $0.5''$  (see §4.1.3 for more details on cross-matching). We then took the median difference of the FourStar and 2MASS magnitudes for stars with FourStar single-band photometric uncertainties below 0.05 mag and 2MASS quality flags equal to “A” in all bands

( $\text{SNR} \geq 10$ ; see Skrutskie et al. 2006). All applied magnitude corrections (e.g. the values subtracted from the original FourStar magnitudes to put them on the 2MASS system) are shown as a function of airmass in Figure 4.5. We examine FourStar-2MASS color terms in §4.2.2.

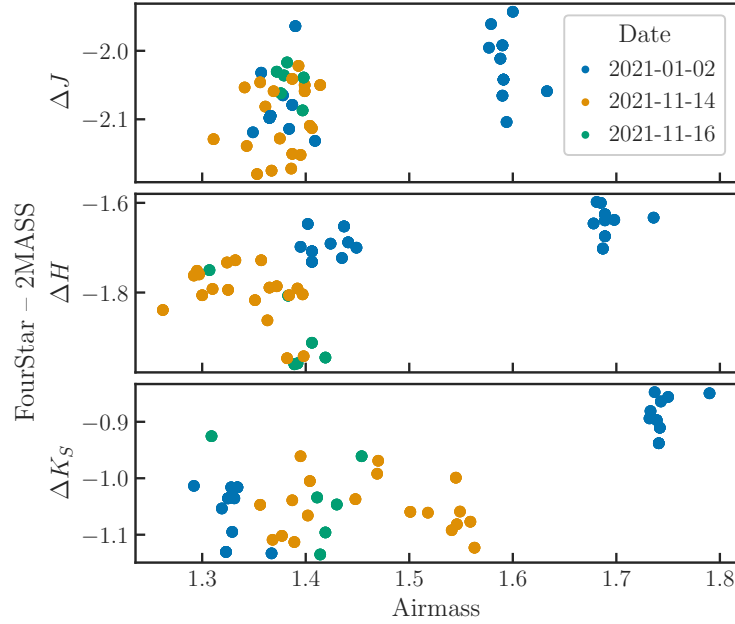


Figure 4.5: Median offsets between 2MASS and raw FourStar magnitudes as a function of airmass, colored by the date of the FourStar observations.

#### 4.1.3 Catalog matching

We adopt the same cross-matching routine to first combine all single-band photometry for *HST* and FourStar into separate multiwavelength catalogs, and then to match between respective catalogs and to archival photometry. While `hst1pass` does offer a companion routine `hst2collate` for similar such purposes (with respect to its own output catalogs at least), it is currently limited in functionality and documentation, and requires an undistorted reference image created with `AstroDrizzle`. As the majority of our *HST* fields have only one exposure per filter with no subpixel dithers, and cosmic rays in WFC3/IR data are rejected

in the ramp fitting step prior to `flt` creation, there are few if any advantages to producing drizzled reference images for our use case.

To match single-band photometry on a per-instrument basis, we use the `search_around_sky` method of the `SkyCoord` class in Astropy, with respective separation limits of  $0.1''$  for *HST* and  $0.15''$  for FourStar. These correspond to just under one pixel on each detector, which is both well above the typical astrometric scatter of these data, and well below the separation at which mismatches become a concern for the stellar surface densities at hand. While most of our targets have only one orbit or epoch of observations, not all do; for targets with repeat observations, we average the fluxes and other photometric information per filter. Sky coordinates are averaged over all available measurements in all data. The combined single-instrument catalogs include all non-matched sources, equivalent to an outer join; therefore, the order in which the matching was done does not matter.

To match between the combined multiband catalogs, and to archival catalogs as well, we take the *HST* coordinates as the astrometric reference. We match other catalogs to *HST* with the `match_to_catalog_sky` method, also of the Astropy `SkyCoord` class. This method finds the nearest match to all reference catalog sources at any distance (analogous to a left join), rather than finding all matches within a given distance. We retain angular separation information in the final matched catalogs, and make cuts as appropriate to filter out mismatches on a post-hoc basis.

In addition to our FourStar photometry and the 2MASS 6X catalogs, we consider the VISTA survey of the Magellanic Clouds (VMC, Cioni et al. 2011) as a third point of comparison. With its recent sixth data release, the VMC survey now offers deep  $YJK_S$  coverage of over  $180 \text{ deg}^2$  of the Magellanic clouds and bridge. Details of the VISTA/VIRCAM telescope, camera, and photometric system (which is itself calibrated to 2MASS) may be found in Emerson et al. (2006); Dalton et al. (2006); González-Fernández et al. (2018). In this work we adopt the VMC DR6 PSF photometry catalog (version 4)<sup>9</sup> throughout.

---

<sup>9</sup><https://www.eso.org/qi/catalog/show/401>

We show histograms of the fractions of stars from our *HST* data with matched detections in ground catalogs in Figure 4.6. Most fields have fewer than 20% of stars matched in 2MASS, whereas most have 80% or better in VMC. For FourStar matches are more evenly spread between 60 to 100%; the outlier below 10% is a field centered on another target that happened to partially overlap an *HST* pointing observed later on.

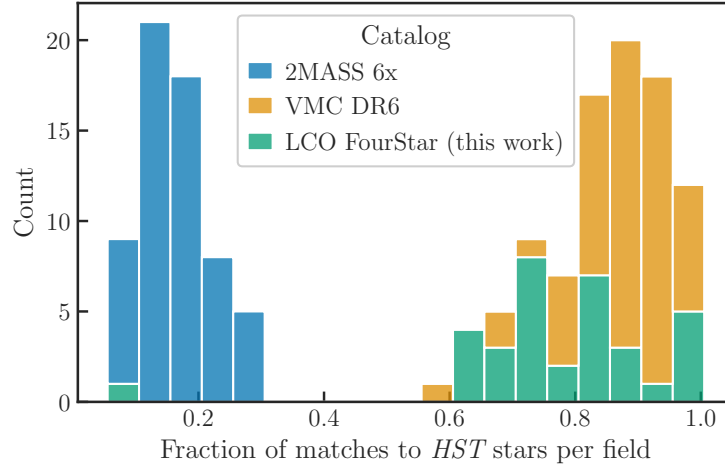


Figure 4.6: Fractions of sources in our *HST* photometry with matches in 2MASS 6X (blue), VMC (orange), and FourStar (green) catalogs.

## 4.2 Results

### 4.2.1 Color-magnitude diagrams

We show color-magnitude diagrams for all our *HST* photometry in Figures 4.7 through 4.9, the same for our FourStar photometry in Figures 4.10 and 4.11, and comparisons between matched stars in *HST*, FourStar, and 2MASS in Figure 4.12. The red giant branch and red clump are the dominant features in all *HST* and FourStar CMDs, and the upper red giant branch dominates in 2MASS. The RGB appears as a tight sequence from  $H \approx 12$ ,  $J - H \approx 0.8$  down to the detection limits, which are 1-2 mag fainter than the red clump at  $H \approx 17$  in *HST* and FourStar. The bright end of the main sequence appears as well at

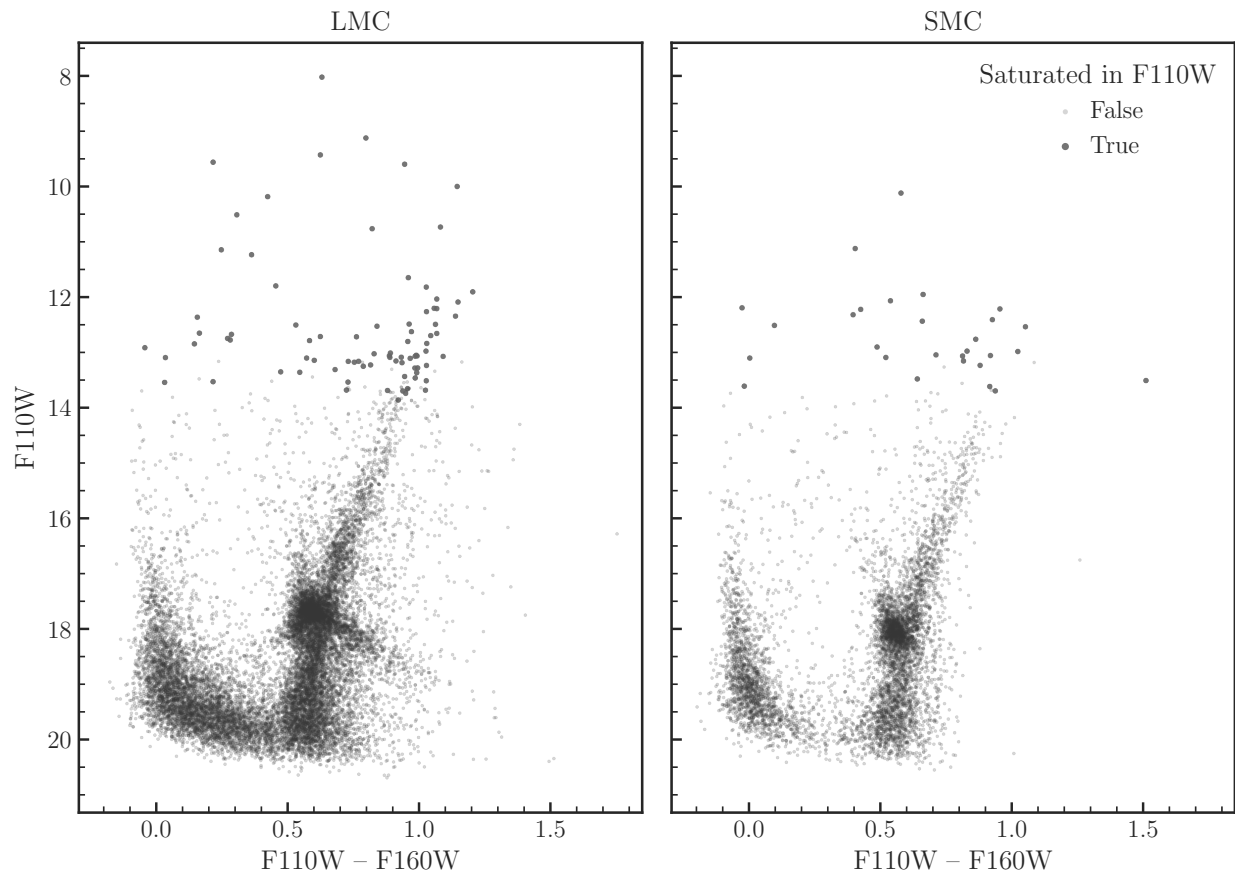


Figure 4.7: Color-magnitude diagrams of our complete *HST* catalogs in the Large (left) and Small (right) Magellanic Clouds in the F110W, F110W–F160W plane. Stars that saturate in the first read in F110W (down to just above 14th magnitude) are marked with large points, and unsaturated stars with smaller and lighter ones.

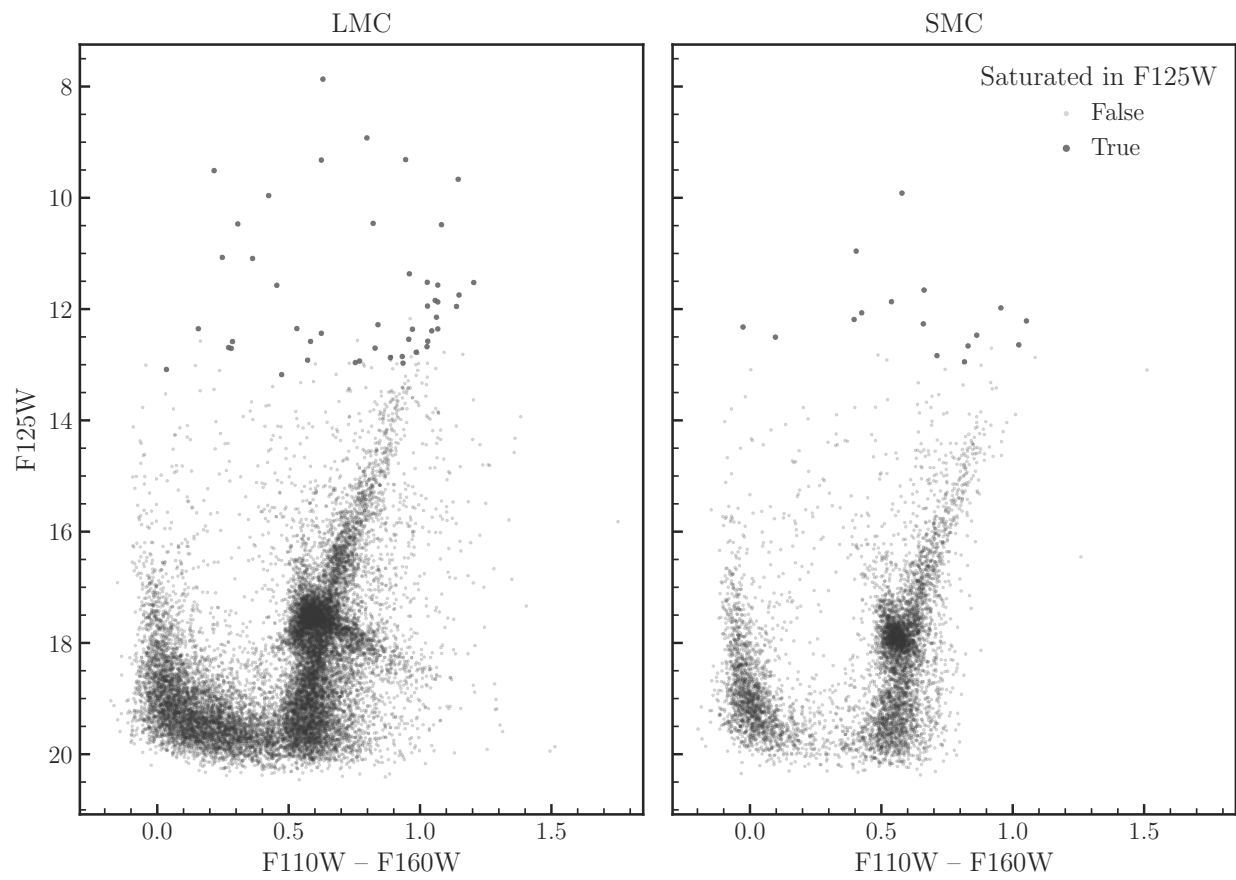


Figure 4.8: As Figure 4.7, but with F125W on the  $y$  axis. Saturation occurs at  $F125W \approx 13$ .

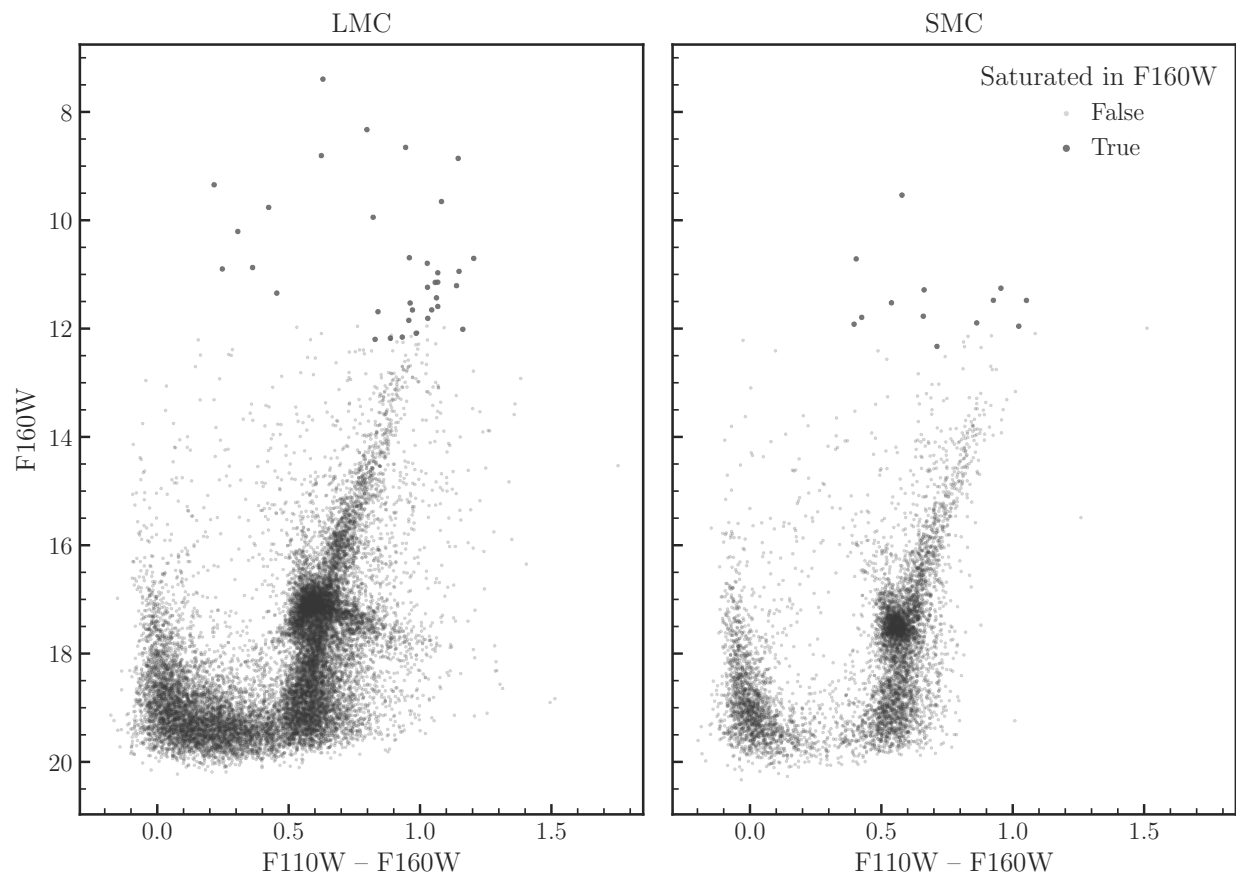


Figure 4.9: As Figure 4.7, but with F160W on the  $y$  axis. Saturation occurs at  $F160W \approx 12$ .

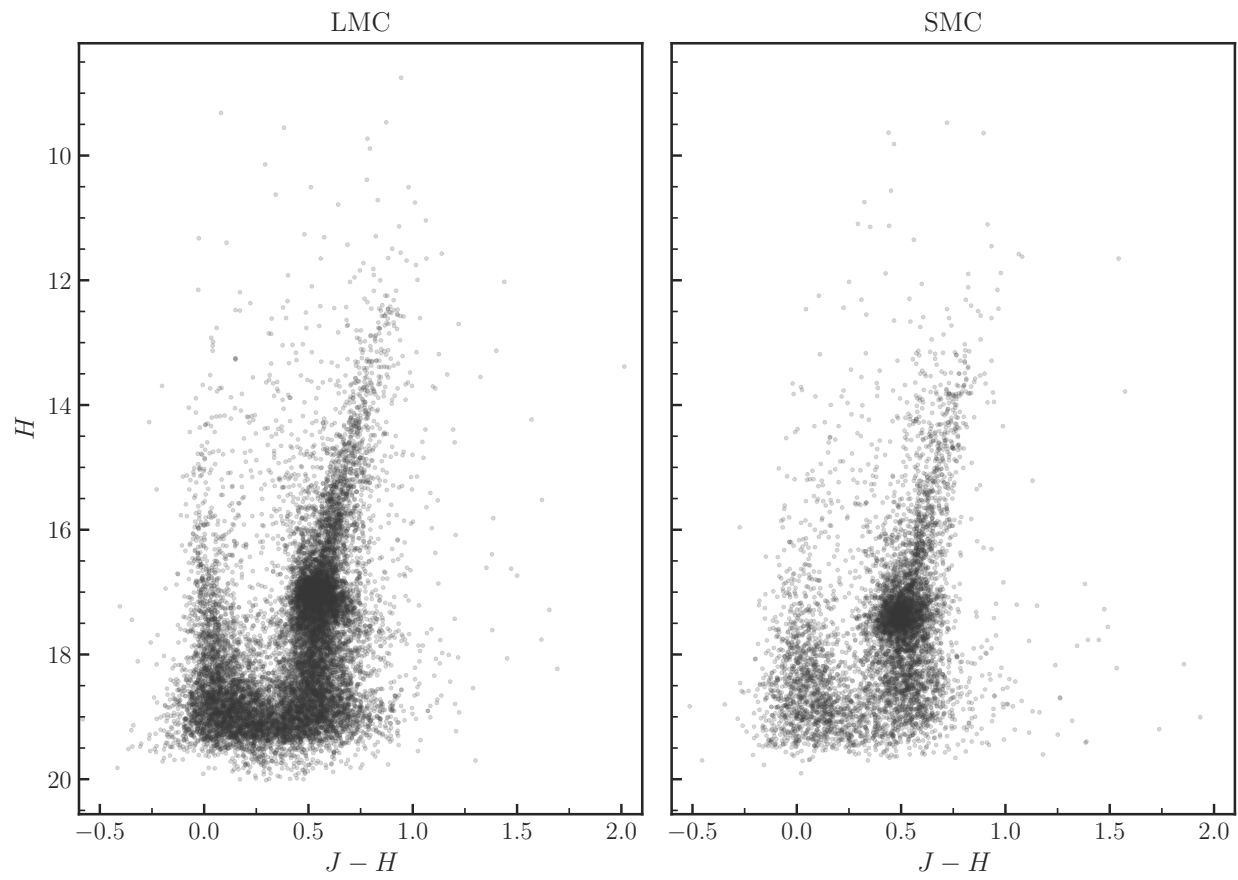


Figure 4.10: As Figure 4.7 for  $H$ ,  $J - H$  on LCO/FourStar.



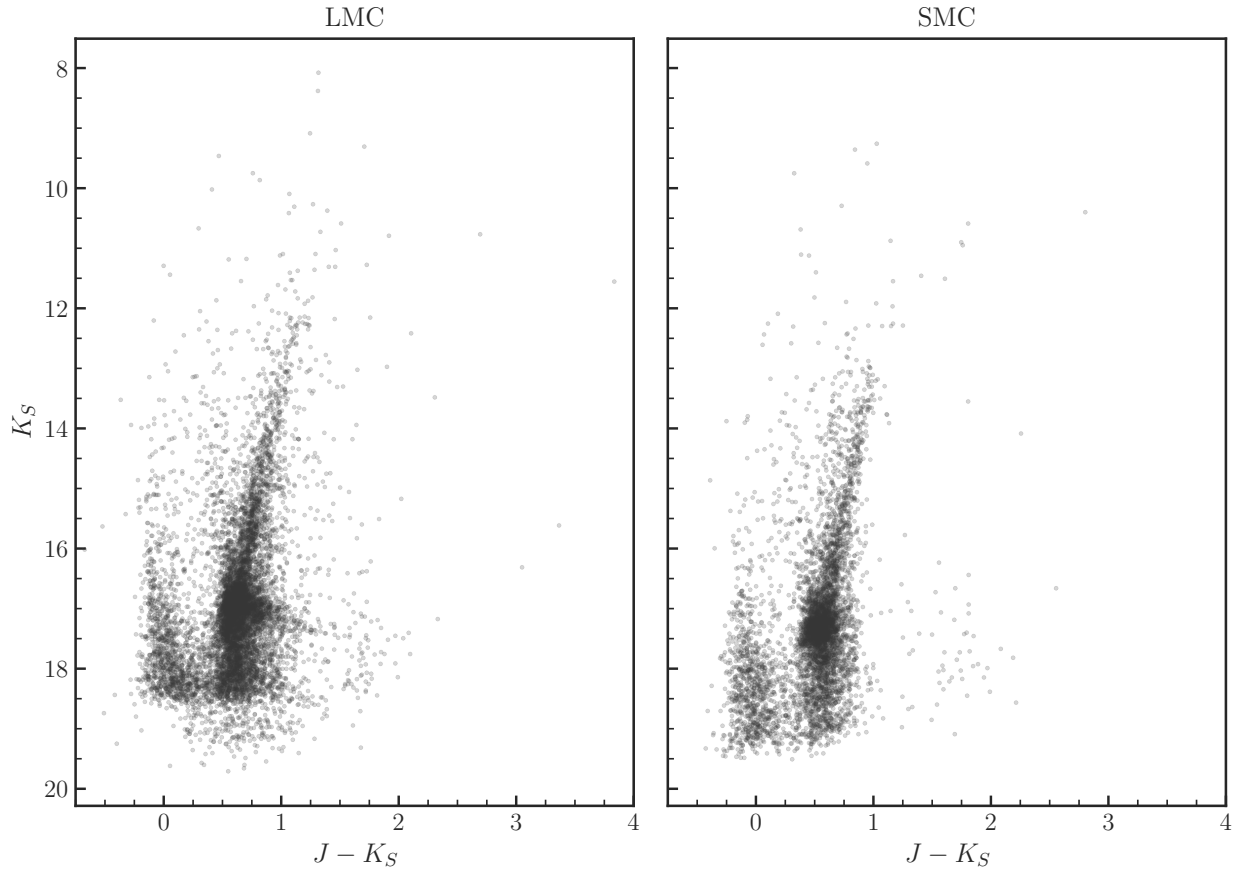


Figure 4.11: As Figure 4.10 for  $K_S$ ,  $J - K_S$  on LCO/FourStar. The population of stars dimmer than  $K_S \sim 18.5$  is from a small subset of deeper areas with repeated pointings.

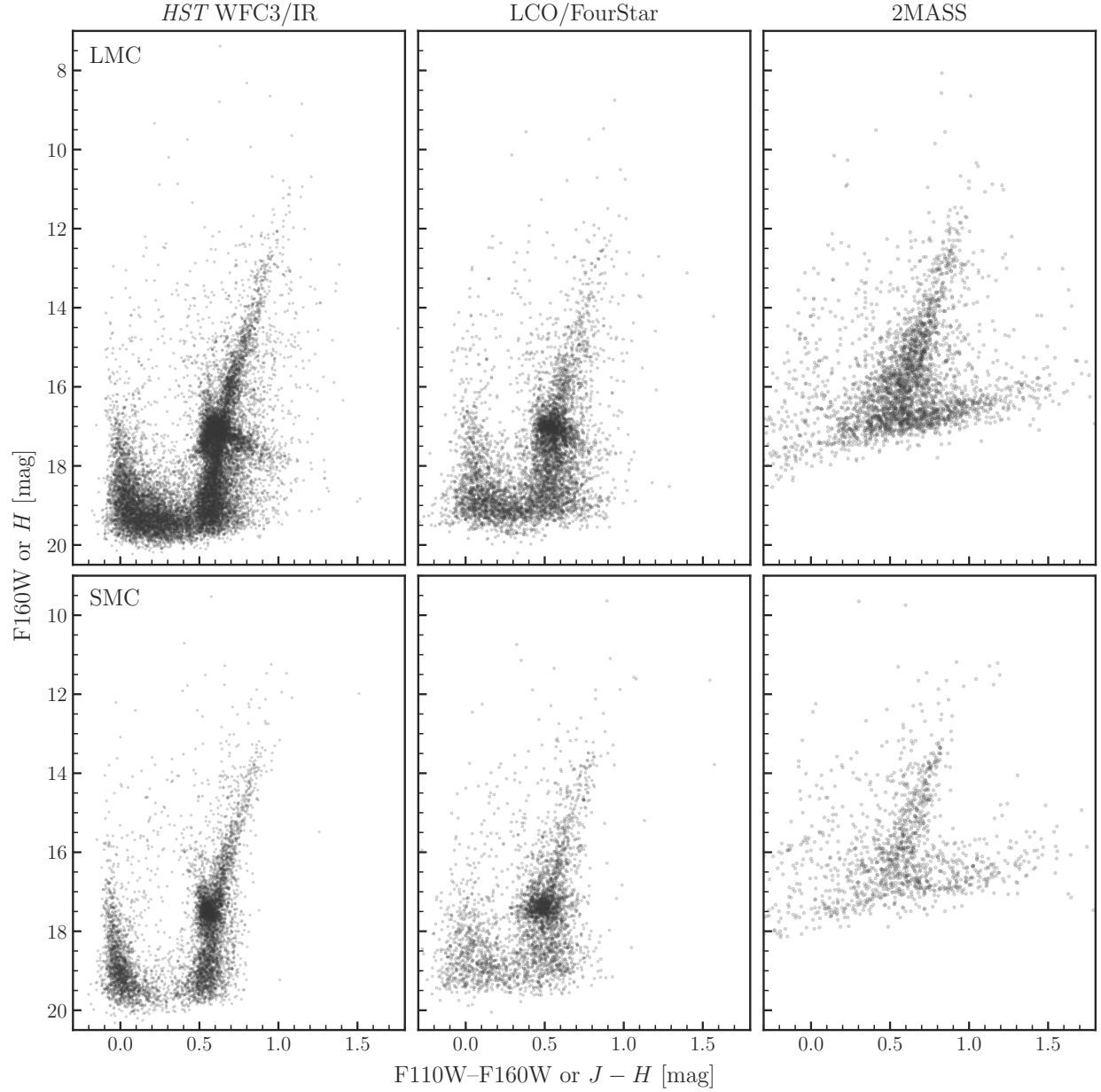


Figure 4.12: Color-magnitude diagrams of our final crossmatched sample for the Large (upper row) and Small (lower row) Magellanic Clouds. Catalogs from left to right: WFC3/IR F160W vs. F110W–F160W, FourStar  $H$  vs.  $J - H$ , and the same bands with 2MASS. Both *HST* and FourStar reach at least two magnitudes below the red clump ( $H \sim 17$ ), whereas 2MASS stops just short of it. Note the large crowding uncertainties at the 2MASS magnitude limit, where faint stars are upscattered due to photometric blending with nearby sources.

$J - H \approx 0$ . The sparse populations at colors between the main sequence and RGB are a mix of Milky Way foreground dwarfs and intermediate- to high-mass Magellanic Clouds stars at varying evolutionary stages, such as the red- and blue core helium burning sequences. Some reddening from interstellar dust is apparent in the LMC, most noticeably in the populations extending redwards of the red clump and RGB. Such effects are far less pronounced, although not entirely absent, in the SMC.

The most noticeable difference in the FourStar CMDs relative to *HST* is the larger scatter at faint magnitudes, which is expected due to the lower resolution. The faint red sources near  $H \approx 18$ ,  $J - H \approx 1.5$  not seen in the *HST* data are likely background galaxies and/or photometric blends.

In the *HST* CMDs, we mark saturated stars with heavier scatter points. First-read saturation occurs in stars brighter than 14th magnitude in F110W, 13th in F125W, and 12th in F160W. This results in saturation below the TRGB only in F110W in the LMC, and just above it in F125W and F160W. The SMC TRGB is fainter than the saturation limit in all our data. Note that there may be some unsaturated stars slightly brighter than the dimmest saturated stars; this is because saturation is affected by subpixel location, where a star falling on the center of a pixel will saturate more quickly than a star at the corner. The FourStar catalogs do not include saturation information.

#### 4.2.2 Filter transformations

##### *FourStar to 2MASS and VMC*

We first examine the residual differences between FourStar and 2MASS, and compare to VMC photometry as well for stars with high-quality photometry in common. For 2MASS this includes stars with angular separations relative to FourStar under  $0.5''$ , and photometric uncertainties below 0.05 mag and quality flags of “A” in all bands. For VMC this includes combined statistical and systematic uncertainties under 0.025 mag in  $JK_S$ , and for FourStar uncertainties under 0.025 mag in  $JHK_S$ . We also require that the absolute differences in

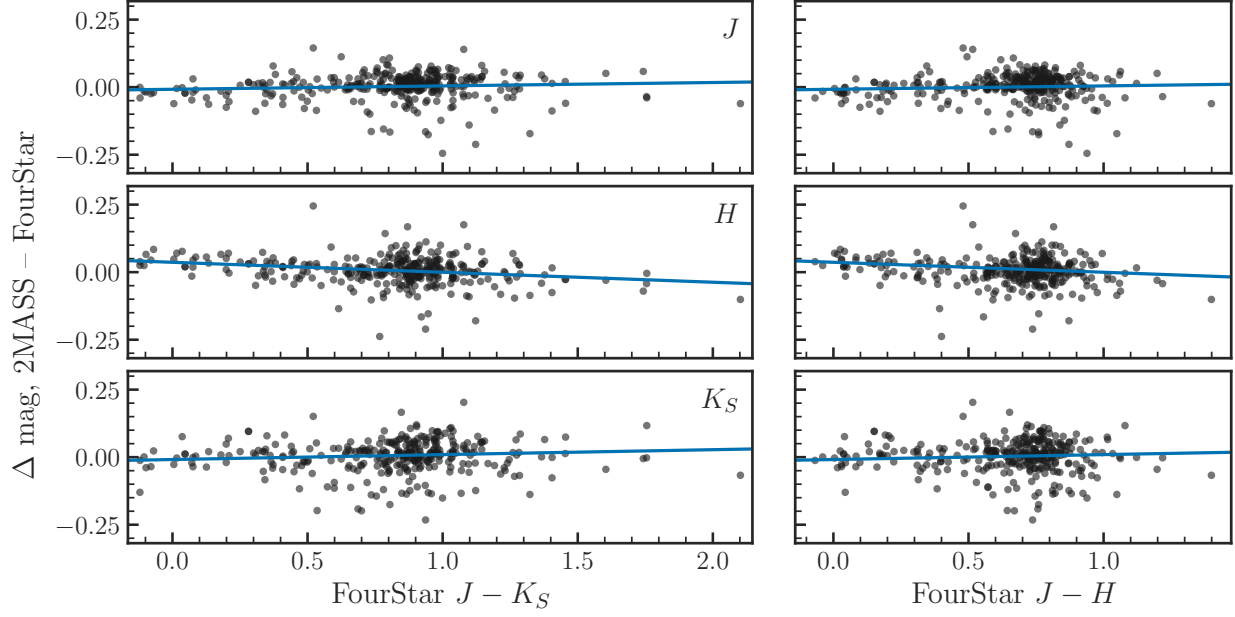


Figure 4.13: Differences between FourStar and 2MASS  $JHK_S$  bands as functions of FourStar  $J - K_S$  and  $J - H$  color.

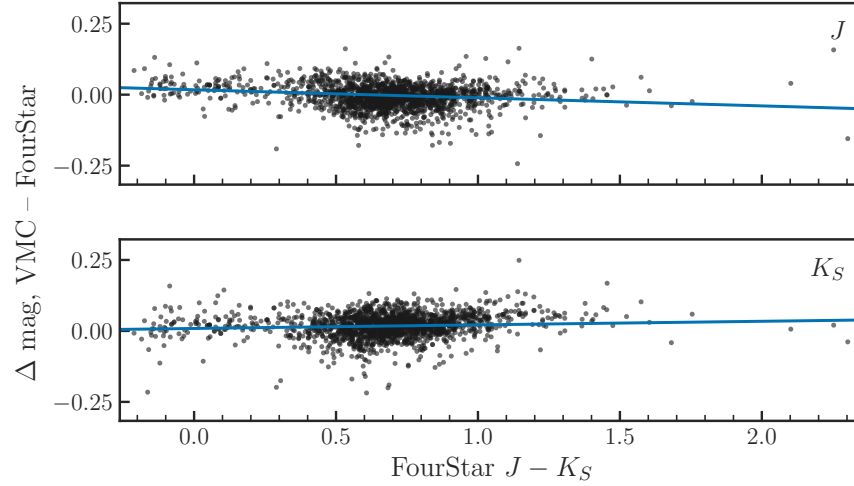


Figure 4.14: First-order transformations between FourStar and VMC  $JK_S$  bands as functions of FourStar  $J - K_S$  color.

magnitudes between FourStar and other catalogs be less than 0.25 mag in all bands to reduce the impact of sources that are blended or otherwise upscattered in one catalog but not the other, which particularly affects 2MASS.

We perform first-order least-squares fitting on all available color and magnitude combinations. Transformations take the functional form  $Y = c_0 + c_1X$ , where  $X$  is the broadband color in the FourStar system, and  $Y$  is the difference between magnitudes in the same filter, in the direction of (other catalogs – FourStar).  $\sigma_{c0}$  and  $\sigma_{c1}$  are the uncertainties on the fitted coefficients. All fits are weighted by the inverse variance of both the  $X$  and  $Y$  terms. Results are shown in Figures 4.13 and 4.14, and coefficients are listed in Table 4.6.

Table 4.6: Filter transformations: FourStar

$X$	$Y$	$c_0$	$\sigma_{c0}$	$c_1$	$\sigma_{c1}$
2MASS					
$J-H$	$\Delta J$	-0.0074	0.0068	0.0153	0.0098
	$\Delta H$	0.0302	0.0077	-0.0368	0.0109
	$\Delta K_S$	0.0060	0.0091	0.0020	0.0125
$J-K_S$	$\Delta J$	-0.0078	0.0063	0.0125	0.0073
	$\Delta H$	0.0366	0.0071	-0.0369	0.0080
	$\Delta K_S$	-0.0087	0.0083	0.0182	0.0088
VMC					
$J-K_S$	$\Delta J$	0.0172	0.0023	-0.0284	0.0029
	$\Delta K_S$	0.0087	0.0024	0.0127	0.0032

NOTE—Transformations take the functional form  $Y = c_0 + c_1X$ , where  $X$  is the broadband color in the FourStar system, and  $Y$  is the magnitude difference in the direction of (other catalog – FourStar).

Between FourStar and 2MASS, only the  $H$  band coefficients are statistically inconsistent with zero. We suspect this may be due in part to the several fields with noticeably large

offsets relative to 2MASS in our initial calibration (see Figure 4.5).

### *HST to FourStar, 2MASS, and VMC*

For transformations from ground data to the *HST* flight system, we apply the same quality criteria as described in §4.2.2, and add only the requirement that a source have measurements in all three *HST* wide bands as well. We apply the same fitting procedure as in §4.2.2.

Results of these fits are shown in Figures 4.15-4.20, and coefficients are listed in Table 4.7. Transformations take the same form as in §4.2.2.

For these fits, many of the zeropoint terms ( $c_0$ ) are statistically inconsistent with zero. This is most likely attributable to a combination of changes to the underlying Vega calibration (Cohen et al. 2003; Bohlin et al. 2014; Maíz Apellániz & Pantaleoni González 2018; Bohlin et al. 2020), and the fact that a single first-order term may not be sufficient to capture the full range of color-magnitude behavior in some filter combinations.

## **4.3 Discussion**

### *4.3.1 Comparison to literature transformations*

Riess (2011) predicted color terms between WFC3/IR F125W, F160W and 2MASS  $JH$  based on theoretical spectra. They used synthetic photometry of Castelli & Kurucz (2003) model atmospheres with  $-0.15 < J - H < 0.8$ ,  $T_{\text{eff}} \geq 3500$  K,  $\log(g)=4.5$ , and solar metallicity and abundance ratios. From these they fit the following slopes:

$$J - \text{F125W} = +0.012(\pm 0.020)(J - H) \quad (4.1)$$

$$H - \text{F160W} = -0.204(\pm 0.040)(J - H) \quad (4.2)$$

Dalcanton et al. (2012a) derived  $JH$  to F110W, F160W transformations using Padova isochrones (Girardi et al. 2008) for 10 Gyr TRGB stars with  $0.6 < J - H < 1.15$  at a range

Table 4.7: Filter transformations: *HST*

$X$	$Y$	$c_0$	$\sigma_{c0}$	$c_1$	$\sigma_{c1}$
FourStar					
$J-H$	F110W- $J$	0.0306	0.0097	0.2463	0.0138
	F125W- $J$	0.0222	0.0065	-0.0331	0.0093
	F160W- $H$	-0.0435	0.0076	0.2452	0.0107
$J-K_S$	F110W- $J$	0.0260	0.0096	0.1989	0.0109
	F125W- $J$	0.0099	0.0077	-0.0221	0.0088
	F160W- $H$	-0.0380	0.0078	0.1869	0.0086
2MASS					
$J-H$	F110W- $J$	0.0268	0.0089	0.2702	0.0126
	F125W- $J$	0.0153	0.0047	-0.0130	0.0066
	F160W- $H$	-0.0239	0.0067	0.2302	0.0094
$J-K_S$	F110W- $J$	0.0204	0.0078	0.2263	0.0089
	F125W- $J$	0.0041	0.0059	0.0002	0.0067
	F160W- $H$	-0.0055	0.0073	0.1621	0.0082
VMC					
$J-K_S$	F110W- $J$	-0.0027	0.0080	0.2695	0.0096
	F125W- $J$	-0.0116	0.0062	0.0261	0.0074

NOTE—Transformations take the form  $Y = c_0 + c_1 X$ .

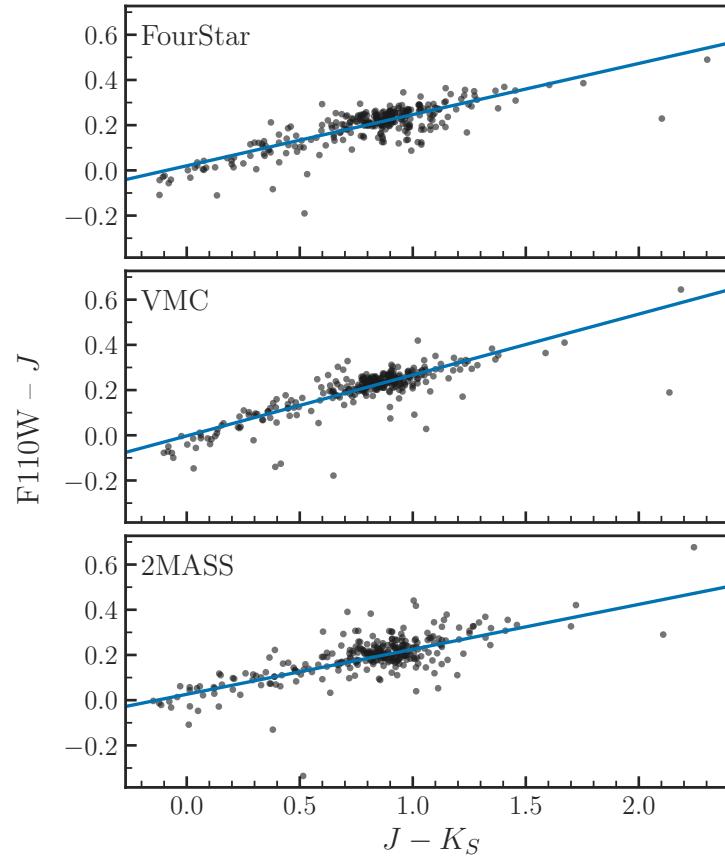


Figure 4.15: Linear fits to WFC3/IR  $F110W - J$  vs.  $J - K_S$  for the FourStar, VMC, and 2MASS  $J$  and  $K_S$  filters (top to bottom).



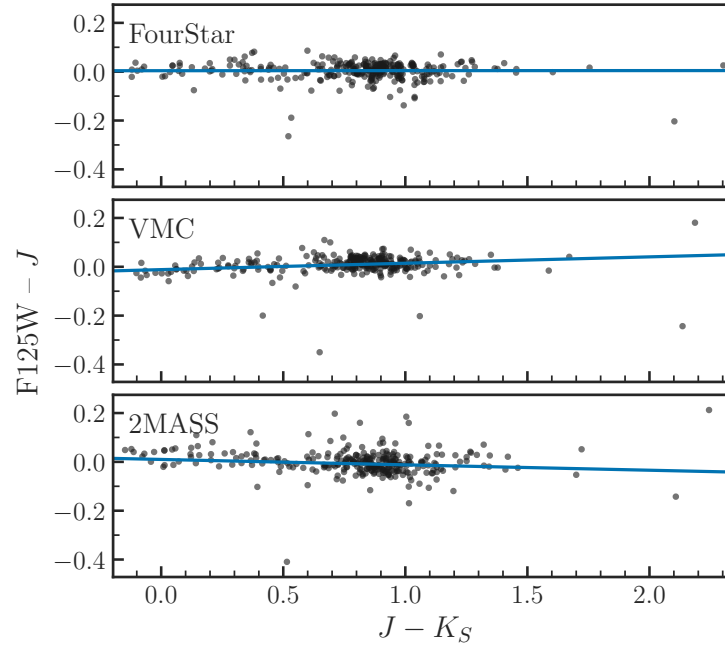


Figure 4.16: As Figure 4.15 for  $F125W - J$  vs.  $J - K_S$ .

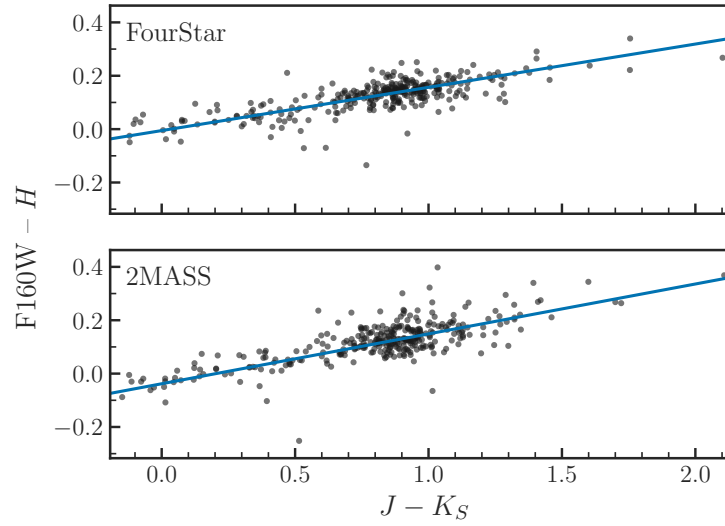


Figure 4.17: Linear fits to  $F160W - H$  vs.  $J - K_S$  for FourStar and 2MASS.

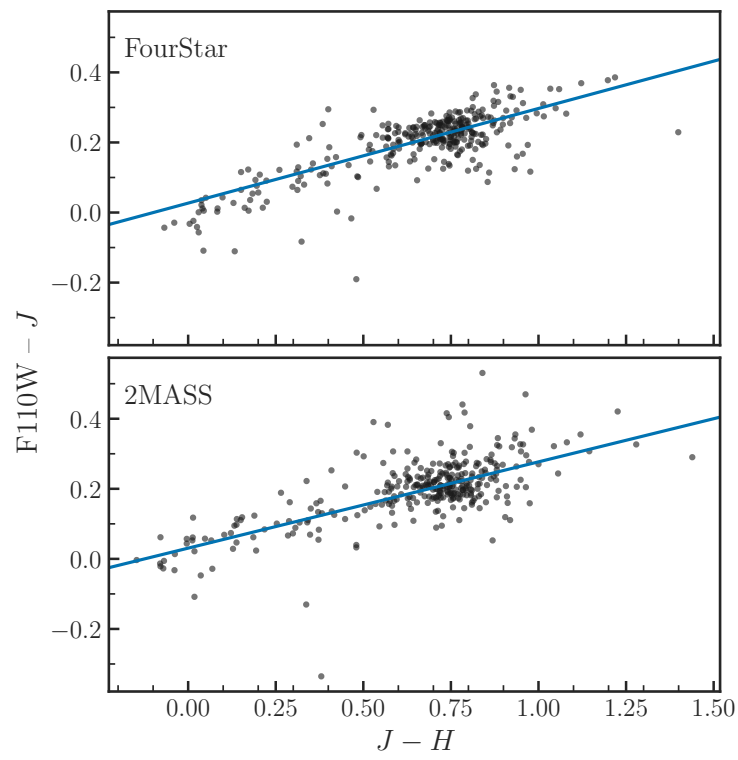


Figure 4.18: As Figure 4.17 for  $F110W - J$  vs.  $J - H$ .

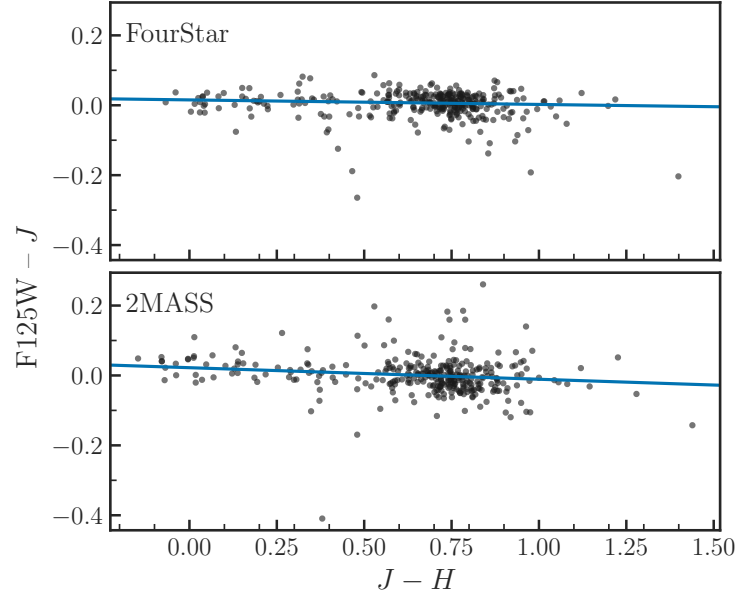


Figure 4.19: As Figure 4.17 for  $F125W - J$  vs.  $J - H$ .

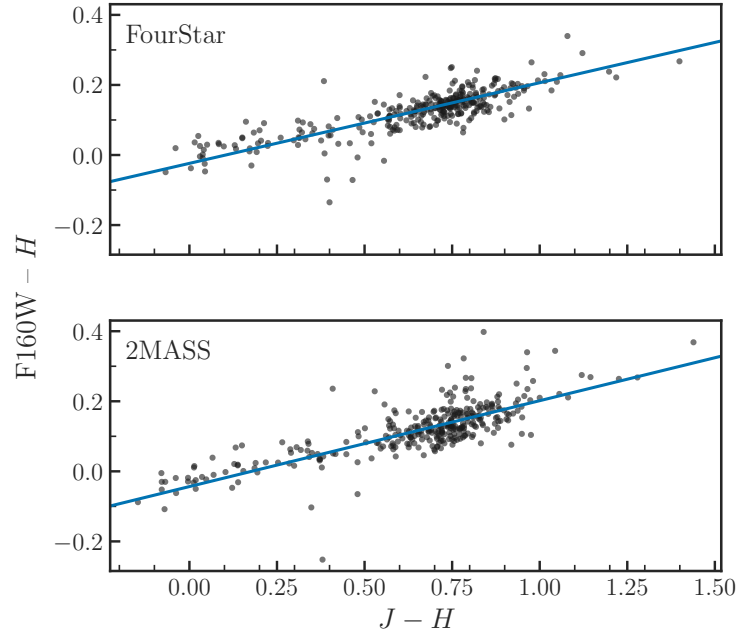


Figure 4.20: As Figure 4.17 for  $F160W - H$  vs.  $J - H$ .

of metallicities. They found:

$$\begin{aligned} \text{F160W} - H &= 0.2031 + 0.401(J - H - 0.9) \\ &\quad + 0.3498(J - H - 0.9)^2 \end{aligned} \tag{4.3}$$

$$\begin{aligned} J - H &= 0.9418 + 0.841(\text{F110W} - \text{F160W} - 1.0) \\ &\quad - 0.9053(\text{F110W} - \text{F160W} - 1.0)^2 \end{aligned} \tag{4.4}$$

We show comparisons between these two sets of transformations, as well as piecewise linear relations from synthetic photometry from the previous chapter, and color terms from this work in Figure 4.21. (We disregard zeropoint terms for the sake of comparison, as they are likely dominated by changes in the calibration of Vega and similar such factors.)

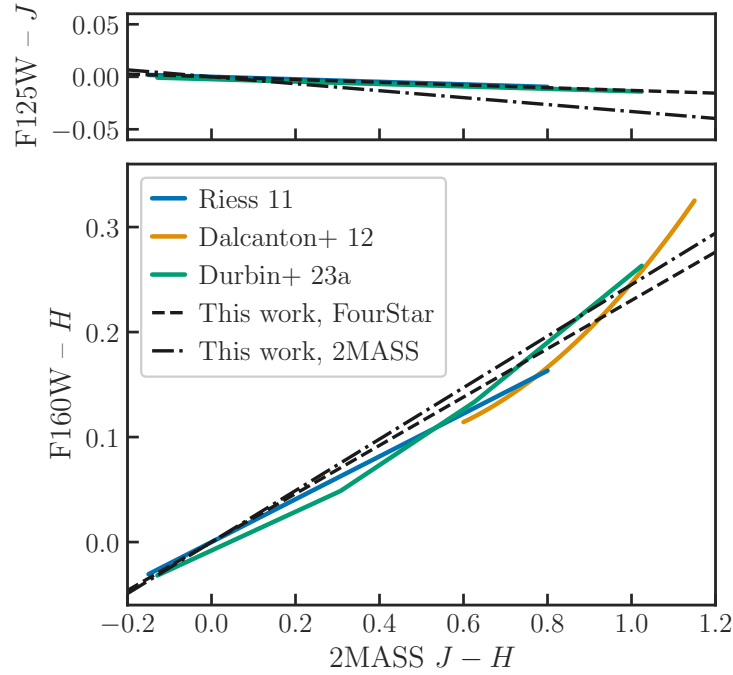


Figure 4.21: Comparisons of this work to published transformations for  $\text{F125W} - J$  (Riess 2011, Durbin et al. in prep, upper panel) and  $\text{F160W} - H$  (Riess 2011; Dalcanton et al. 2012a, Durbin et al. in prep, lower panel).

González-Fernández et al. (2018) fit for color terms between the VISTA and 2MASS

photometric systems in terms of 2MASS  $J - K_S$  color. They found:

$$J_V = J_2 - (0.031 \pm 0.006)(J - K_S)_2 \quad (4.5)$$

$$K_{S,V} = K_{S,2} - (0.006 \pm 0.007)(J - K_S)_2 \quad (4.6)$$

(their equations 7 and 9).

Combining our FourStar, 2MASS, and VMC results and rearranging, we find:

$$J_V = J_2 - (0.0352 \pm 0.0139)(J - K_S)_2 \quad (4.7)$$

$$K_{S,V} = K_{S,2} + (0.0001 \pm 0.0148)(J - K_S)_2 \quad (4.8)$$

Both of these are fully statistically consistent with those of González-Fernández et al. (2018).

#### 4.4 Conclusions

We have produced catalogs of near-infrared broadband photometry of over 35,000 Magellanic Cloud stars, mainly evolved giants, from both *HST* WFC3/IR F110W, F125W, F160W and LCO/FourStar  $JHK_S$ . Using these data, we have produced direct empirical transformations between *HST* and ground-based filter systems, including archival catalogs from the 2MASS and VMC surveys. Preliminary results show overall good agreement with literature transformations.

In a subsequent paper, we will present a library of low-resolution slitless spectra extracted from the WFC3/IR G102+G141 grism observations obtained in this program, as well as the full set of broad- and medium-band photometric coverage from both *HST* and FourStar. This spectrophotometric library will provide absolutely fluxed  $R \sim 150$  SED coverage from 0.8-1.7  $\mu\text{m}$  for dozens of IR-bright giants in the Magellanic Clouds. This will offer a valuable complement both to current ground-based NIR spectral libraries (e.g. Rayner et al. 2009; Villaume et al. 2017; Chen et al. 2014b; Gonneau et al. 2020b; Verro et al. 2022c) as well as to the gold standard CALSPEC library (Turnshek et al. 1990; Bohlin 2007; Bohlin et al. 2014; Bohlin & Deustua 2019), which largely omits cool and luminous evolved stars due to their lack of suitability as high-precision flux standards. It will additionally serve as a bridge

to the much more distant hosts accessible with *JWST*/NIRSpec (e.g. Nidever et al. 2023), and to much greater areas with *Roman*/WFI.

## Chapter 5

# CONCLUSIONS

### 5.1 *Summary*

In Chapter 2 I led an end-to-end reevaluation of the IR-TRGB color-absolute magnitude relations first presented by Dalcanton et al. (2012a, hereafter D12). The reprocessed results, when compared to two state-of-the-art suites of isochrone predictions, revealed  $\sim 0.1$  mag discrepancies between measurements and theoretical predictions for both color-magnitude and optical-IR color relations for TRGB stars. These results were consistent with theoretical investigations' conclusions that stellar physics implementations and bolometric corrections remain a dominant source of uncertainty in absolute TRGB predictions (Capozzi & Raffelt 2020; Serenelli et al. 2017; Straniero et al. 2020). Since this study, exciting progress has been made in minimizing these theoretical uncertainties (Di Luzio et al. 2022; Lopes & Lopes 2021; Pietrinferni et al. 2021; Saltas & Tognelli 2022) as well as uncertainties on the empirical optical calibration (Hoyt 2023).

In Chapter 3, I predicted filter transformations between 2MASS and WFC3/IR from synthetic photometry. These predictions were based on empirical spectra of over 1000 individual stars from four optical+IR spectral libraries, which together span nearly the full HR diagram and sample stellar populations from the solar neighborhood out to the Magellanic Clouds, covering a broad range of ages, metallicities, and other relevant stellar properties (Rayner et al. 2009; Turnshek et al. 1990; Verro et al. 2022c; Villaume et al. 2017). We found that for most stars, filter transformations were well fit by piecewise-linear relations as functions of color; however, molecular features in the coolest stars' atmospheres result in significant departures from these relations.

In Chapter 4, I showed preliminary results from a complementary approach to achieving

the same goals as in the previous chapter. I directly compared photometry of the same stars from the ground and space to achieve the same goals as in the previous chapter. Although the full complement of ground-based observations has not yet been obtained, early results are highly promising.

In the near term, I plan to continue the work of this thesis in future papers by a) extending the synthetic photometry technique described in Chapter 3 to other infrared instruments, including *JWST*/NIRCam, *Roman*/WFI, and *Euclid*/NISP; and b) incorporating the medium-band and spectroscopic observations mentioned in Chapter 4 to produce a robust absolute spectrophotometric calibration of the NIR-TRGB.



## BIBLIOGRAPHY

Aiola, S., Calabrese, E., Maurin, L., Naess, S., Schmitt, B. L., Abitbol, M. H., Addison, G. E., Ade, P. A. R., Alonso, D., Amiri, M., Amodeo, S., Angile, E., Austermann, J. E., Baidon, T., Battaglia, N., Beall, J. A., Bean, R., Becker, D. T., Bond, J. R., Bruno, S. M., Calafut, V., Campusano, L. E., Carrero, F., Chesmore, G. E., Cho, H.-m., Choi, S. K., Clark, S. E., Cothard, N. F., Crichton, D., Crowley, K. T., Darwish, O., Datta, R., Denison, E. V., Devlin, M. J., Duell, C. J., Duff, S. M., Duivenvoorden, A. J., Dunkley, J., Dünner, R., Essinger-Hileman, T., Fankhanel, M., Ferraro, S., Fox, A. E., Fuzia, B., Gallardo, P. A., Gluscevic, V., Golec, J. E., Grace, E., Gralla, M., Guan, Y., Hall, K., Halpern, M., Han, D., Hargrave, P., Hasselfield, M., Helton, J. M., Henderson, S., Hensley, B., Hill, J. C., Hilton, G. C., Hilton, M., Hincks, A. D., Hložek, R., Ho, S.-P. P., Hubmayr, J., Huppenberger, K. M., Hughes, J. P., Infante, L., Irwin, K., Jackson, R., Klein, J., Knowles, K., Koopman, B., Kosowsky, A., Lakey, V., Li, D., Li, Y., Li, Z., Lokken, M., Louis, T., Lungu, M., MacInnis, A., Madhavacheril, M., Maldonado, F., Mallaby-Kay, M., Marsden, D., McMahon, J., Menanteau, F., Moodley, K., Morton, T., Namikawa, T., Nati, F., Newburgh, L., Nibarger, J. P., Nicola, A., Niemack, M. D., Nolta, M. R., Orlowski-Sherer, J., Page, L. A., Pappas, C. G., Partridge, B., Phakathi, P., Pisano, G., Prince, H., Puddu, R., Qu, F. J., Rivera, J., Robertson, N., Rojas, F., Salatino, M., Schaan, E., Schillaci, A., Sehgal, N., Sherwin, B. D., Sierra, C., Sievers, J., Sifon, C., Sikhosana, P., Simon, S., Spergel, D. N., Staggs, S. T., Stevens, J., Storer, E., Sunder, D. D., Switzer, E. R., Thorne, B., Thornton, R., Trac, H., Treu, J., Tucker, C., Vale, L. R., Van Engelen, A., Van Lanen, J., Vavagiakis, E. M., Wagoner, K., Wang, Y., Ward, J. T., Wollack, E. J., Xu, Z., Zago, F., & Zhu, N., “The Atacama Cosmology Telescope: DR4 maps and cosmological parameters”. 2020, *JCAP*, 2020, 047

Allard, F., Homeier, D., Freytag, B., & Sharp, C. M. 2012, in EAS Publications Series, Vol. 57, EAS Publications Series, ed. C. Reyl  , C. Charbonnel, & M. Schultheis, 3–43

Allende Prieto, C., “The Shapes of Stellar Spectra”. 2023, *Atoms*, 11, 61

Alvarez, R., Lan  on, A., Plez, B., & Wood, P. R., “Optical and near-infrared spectrophotometric properties of Long Period Variables and other luminous red stars”. 2000, *A&A*, 353, 322

Anand, G. S., Tully, R. B., Rizzi, L., & Karachentsev, I. D., “The Distance and Motion of the Maffei Group”. 2019a, *ApJL*, 872, L4

Anand, G. S., Tully, R. B., Rizzi, L., Riess, A. G., & Yuan, W., “Comparing Tip of the Red Giant Branch Distance Scales: An Independent Reduction of the Carnegie-Chicago Hubble Program and the Value of the Hubble Constant”. 2022, *ApJ*, 932, 15

Anand, G. S., Tully, R. B., Rizzi, L., Shaya, E. J., & Karachentsev, I. D., “Peculiar Velocities of Galaxies Just Beyond the Local Group”. 2019b, *ApJ*, 880, 52

Anders, F., Khalatyan, A., Queiroz, A. B. A., Chiappini, C., Ardèvol, J., Casamiquela, L., Figueras, F., Jiménez-Arranz, Ó., Jordi, C., Monguió, M., Romero-Gómez, M., Altamirano, D., Antoja, T., Assaad, R., Cantat-Gaudin, T., Castro-Ginard, A., Enke, H., Girardi, L., Guiglion, G., Khan, S., Luri, X., Miglio, A., Minchev, I., Ramos, P., Santiago, B. X., & Steinmetz, M., “Photo-astrometric distances, extinctions, and astrophysical parameters for Gaia EDR3 stars brighter than  $G = 18.5$ ”. 2022, *A&A*, 658, A91

Anderson, J. 2016, “Empirical Models for the WFC3/IR PSF”, Space Telescope WFC Instrument Science Report

—. 2022, “One-Pass HST Photometry with hst1pass”, Instrument Science Report WFC3 2022-5, 55 pages

Anderson, J., & King, I. R., “Toward High-Precision Astrometry with WFPC2. I. Deriving an Accurate Point-Spread Function”. 2000, *PASP*, 112, 1360

—. 2006, “PSFs, Photometry, and Astronomy for the ACS/WFC”, Instrument Science Report ACS 2006-01

Andrae, R., Fouesneau, M., Sordo, R., Bailer-Jones, C. A. L., Dharmawardena, T. E., Rybizki, J., De Angeli, F., Lindstrøm, H. E. P., Marshall, D. J., Drimmel, R., Korn, A. J., Soubiran, C., Brouillet, N., Casamiquela, L., Rix, H. W., Abreu Aramburu, A., Álvarez, M. A., Bakker, J., Bellas-Velidis, I., Bijaoui, A., Brugaletta, E., Burlacu, A., Carballo, R., Chaoul, L., Chiavassa, A., Contursi, G., Cooper, W. J., Creevey, O. L., Dafonte, C., Dapergolas, A., de Laverny, P., Delchambre, L., Demouchy, C., Edvardsson, B., Frémat, Y., Garabato, D., García-Lario, P., García-Torres, M., Gavel, A., Gomez, A., González-Santamaría, I., Hatzidimitriou, D., Heiter, U., Jean-Antoine Piccolo, A., Kontizas, M., Kordopatis, G., Lanzafame, A. C., Lebreton, Y., Licata, E. L., Livanou, E., Lobel, A., Lorca, A., Magdaleno Romeo, A., Manteiga, M., Marocco, F., Mary, N., Nicolas, C., Ordenovic, C., Pailier, F., Palicio, P. A., Pallas-Quintela, L., Panem, C., Pichon, B., Poggio, E., Recio-Blanco, A., Riclet, F., Robin, C., Santoveña, R., Sarro, L. M., Schultheis, M. S., Segol, M., Silvelo, A., Slezak, I., Smart, R. L., Süveges, M., Thévenin, F., Torralba Elipse, G., Ulla, A., Utrilla, E., Vallenari, A., van Dillen, E., Zhao, H., & Zorec, J., “Gaia Data Release 3: Analysis of the Gaia BP/RP spectra using the General Stellar Parameterizer from Photometry”. 2022, *arXiv e-prints*, arXiv:2206.06138

Arentsen, A., Prugniel, P., Gonneau, A., Lançon, A., Trager, S., Peletier, R., Lyubenova, M., Chen, Y.-P., Falcón Barroso, J., Sánchez Blázquez, P., & Vazdekis, A., “Stellar atmospheric parameters for 754 spectra from the X-shooter Spectral Library”. 2019, *A&A*, 627, A138

Aringer, B., Girardi, L., Nowotny, W., Marigo, P., & Bressan, A., “Synthetic photometry for M and K giants and stellar evolution: hydrostatic dust-free model atmospheres and chemical abundances”. 2016, *MNRAS*, 457, 3611

Aringer, B., Marigo, P., Nowotny, W., Girardi, L., Mečina, M., & Nanni, A., “Abundances of C, N, and O in AGB Giants and Model Atmospheres”. 2019, *IAU Symposium*, 343, 93

Arthur, D., & Vassilvitskii, S. 2007, in Proceedings of the Eighteenth Annual ACM-SIAM Symposium on Discrete Algorithms, SODA '07 (Philadelphia, PA, USA: Society for Industrial and Applied Mathematics), 1027–1035

Avila, R. J., Hack, W., Cara, M., Borncamp, D., Mack, J., Smith, L., & Ubeda, L. 2015, in Astronomical Society of the Pacific Conference Series, Vol. 495, Astronomical Data Analysis Software and Systems XXIV (ADASS XXIV), ed. A. R. Taylor & E. Rosolowsky, 281

Baade, W., “The Resolution of Messier 32, NGC 205, and the Central Region of the Andromeda Nebula.”. 1944, *ApJ*, 100, 137

Bagnulo, S., Jehin, E., Ledoux, C., Cabanac, R., Melo, C., Gilmozzi, R., & ESO Paranal Science Operations Team, “The UVES Paranal Observatory Project: A Library of High-Resolution Spectra of Stars across the Hertzsprung-Russell Diagram”. 2003, *The Messenger*, 114, 10

Bailer-Jones, C. A. L., Rybizki, J., Fouesneau, M., Demleitner, M., & Andrae, R., “Estimating Distances from Parallaxes. V. Geometric and Photogeometric Distances to 1.47 Billion Stars in Gaia Early Data Release 3”. 2021, *AJ*, 161, 147

Bailer-Jones, C. A. L., Rybizki, J., Fouesneau, M., Mantelet, G., & Andrae, R., “Estimating Distance from Parallaxes. IV. Distances to 1.33 Billion Stars in Gaia Data Release 2”. 2018, *AJ*, 156, 58

Bajaj, V. 2017, “Aligning HST Images to Gaia: A Faster Mosaicking Workflow”, Space Telescope WFC Instrument Science Report

Bajaj, V., Calamida, A., Mack, J., & Som, D. 2022, “WFC3/IR Photometric Stability Stellar Cluster Study”, WFC3 Instrument Science Report 2022-07, 28 pages

Baldwin, C., McDermid, R. M., Kuntschner, H., Maraston, C., & Conroy, C., “Comparison of stellar population model predictions using optical and infrared spectroscopy”. 2018, *MNRAS*, 473, 4698

Barbary, K., “SEP: Source Extractor as a Library”. 2016, *The Journal of Open Source Software*, 1, 58

Baumgardt, H., & Vasiliev, E., “Accurate distances to Galactic globular clusters through a combination of Gaia EDR3, HST, and literature data”. 2021, *MNRAS*, 505, 5957

Beasley, A., Wolff, S., Dickinson, M., Murphy, E. J., Beaton, R., Braatz, J., Corsi, A., de Pater, I., Loomis, R., Margutti, R., Weinberger, A., & Wong, M. H., “Multiwavelength Astrophysics in the Era of the ngVLA and the US ELT Program”. 2019, *BAAS*, 51, 88

Beaton, R., Dalcanton, J., Durbin, M., Freedman, W. L., Hoyt, T., Madore, B. F., Monson, A., Neeley, J. R., Nidever, D., Rich, J. A. S., & Seibert, M. 2022, “Securing the Absolute Scale for the IR-TRGB Distance Ladder”, HST Proposal. Cycle 29, ID. #16928

Beaton, R. L., Freedman, W. L., Madore, B. F., Bono, G., Carlson, E. K., Clementini, G., Durbin, M. J., Garofalo, A., Hatt, D., Jang, I. S., Kollmeier, J. A., Lee, M. G., Monson, A. J., Rich, J. A., Scowcroft, V., Seibert, M., Sturch, L., & Yang, S.-C., “The Carnegie-Chicago Hubble Program. I. An Independent Approach to the Extragalactic Distance Scale Using Only Population II Distance Indicators”. 2016, *ApJ*, 832, 210

Beaton, R. L., Bono, G., Braga, V. F., Dall’Ora, M., Fiorentino, G., Jang, I. S., Martínez-Vázquez, C. E., Matsunaga, N., Monelli, M., Neeley, J. R., & Salaris, M., “Old-Aged Primary Distance Indicators”. 2018, *SSRv*, 214, 113

Beaton, R. L., Birrer, S., Dell’Antonio, I., Fassnacht, C., Goldstein, D., Lee, C.-H., Nugent, P., Pierce, M., Shajib, A. J., & Treu, T., “Measuring the Hubble Constant Near and Far in the Era of ELT’s”. 2019a, *BAAS*, 51, 456

Beaton, R. L., Dalcanton, J., Durbin, M., Freedman, W. L., Hoyt, T., Madore, B. F., Monson, A., Neeley, J. R., Nidever, D., Rich, J. A. S., & Seibert, M., “Securing the Absolute Scale for the IR-TRGB Distance Ladder”. 2019b, *HST PID GO-15875, Cy 27*

—. 2020, “Securing the Absolute Scale for the IR-TRGB Distance Ladder”, HST Proposal

Bell, C. P. M., Cioni, M.-R. L., Wright, A. H., Rubele, S., Nidever, D. L., Tatton, B. L., van Loon, J. T., Ivanov, V. D., Subramanian, S., Oliveira, J. M., de Grijs, R., Pennock, C. M., Choi, Y., Zaritsky, D., Olsen, K., Niederhofer, F., Choudhury, S., Martínez-Delgado, D., & Muñoz, R. R., “The intrinsic reddening of the Magellanic Clouds as traced by background

galaxies - I. The bar and outskirts of the Small Magellanic Cloud". 2019, *MNRAS*, 489, 3200

Bentley, J. L., "Multidimensional Binary Search Trees Used for Associative Searching". 1975, *Communications of the ACM*, 18, 509

Bertin, E. 2006, in Astronomical Society of the Pacific Conference Series, Vol. 351, Astronomical Data Analysis Software and Systems XV, ed. C. Gabriel, C. Arviset, D. Ponz, & S. Enrique, 112

Bertin, E. 2010a, "SCAMP: Automatic Astrometric and Photometric Calibration", ascl:1010.063

—. 2010b, "SWarp: Resampling and Co-adding FITS Images Together", ascl:1010.068

Bertin, E., & Arnouts, S., "SExtractor: Software for Source Extraction". 1996, *Astronomy and Astrophysics Supplement Series*, 117, 393

Bertin, E., & Arnouts, S. 2010, "SExtractor: Source Extractor", ascl:1010.064

Bertin, E., Mellier, Y., Radovich, M., Missonnier, G., Didelon, P., & Morin, B. 2002, in Astronomical Society of the Pacific Conference Series, Vol. 281, Astronomical Data Analysis Software and Systems XI, ed. D. A. Bohlender, D. Durand, & T. H. Handley, 228

Bessell, M., & Murphy, S., "Spectrophotometric Libraries, Revised Photonic Passbands, and Zero Points for UBVRI, Hipparcos, and Tycho Photometry". 2012, *PASP*, 124, 140

Blakeslee, J. P., Lucey, J. R., Tonry, J. L., Hudson, M. J., Narayanan, V. K., & Barris, B. J., "Early-type galaxy distances from the Fundamental Plane and surface brightness fluctuations". 2002, *MNRAS*, 330, 443

Boggs, P. T., Byrd, R. H., & Schnabel, R. B., "A Stable and Efficient Algorithm for Non-linear Orthogonal Distance Regression". 1987, *SIAM Journal on Scientific and Statistical Computing*, 8, 1052

Bohlin, R. C. 2007, in Astronomical Society of the Pacific Conference Series, Vol. 364, The Future of Photometric, Spectrophotometric and Polarimetric Standardization, ed. C. Sterken, 315

Bohlin, R. C., & Cohen, M., "NICMOS Spectrophotometry and Models for a Stars". 2008, *AJ*, 136, 1171

- Bohlin, R. C., & Deustua, S. E., “CALSPEC: Wide Field Camera 3 Infrared Grism Spectrophotometry”. 2019, *AJ*, 157, 229
- Bohlin, R. C., Deustua, S. E., & de Rosa, G., “Hubble Space Telescope Flux Calibration. I. STIS and CALSPEC”. 2019, *AJ*, 158, 211
- Bohlin, R. C., Dickinson, M. E., & Calzetti, D., “Spectrophotometric Standards from the Far-Ultraviolet to the Near-Infrared: STIS and NICMOS Fluxes”. 2001, *AJ*, 122, 2118
- Bohlin, R. C., Gordon, K. D., & Tremblay, P. E., “Techniques and Review of Absolute Flux Calibration from the Ultraviolet to the Mid-Infrared”. 2014, *PASP*, 126, 711
- Bohlin, R. C., Hubeny, I., & Rauch, T., “New Grids of Pure-hydrogen White Dwarf NLTE Model Atmospheres and the HST/STIS Flux Calibration”. 2020, *AJ*, 160, 21
- Bohlin, R. C., Mészáros, S., Fleming, S. W., Gordon, K. D., Koekemoer, A. M., & Kovács, J., “A New Stellar Atmosphere Grid and Comparisons with HST/STIS CALSPEC Flux Distributions”. 2017, *AJ*, 153, 234
- Bonatto, C., Bica, E., & Girardi, L., “Theoretical isochrones compared to 2MASS observations: Open clusters at nearly solar metallicity”. 2004, *A&A*, 415, 571
- Borlaff, A., Trujillo, I., Román, J., Beckman, J. E., Eliche-Moral, M. C., Infante-Sáinz, R., Lumbrales-Calle, A., de Almagro, R. T. S. M., Gómez-Guijarro, C., Cebrián, M., Dorta, A., Cardiel, N., Akhlaghi, M., & Martínez-Lombilla, C., “The missing light of the Hubble Ultra Deep Field”. 2019, *A&A*, 621, A133
- Botev, Z. I., Grotowski, J. F., & Kroese, D. P., “Kernel Density Estimation via Diffusion”. 2010, *The Annals of Statistics*, 38, 2916
- Bovy, J., Hogg, D. W., & Roweis, S. T., “Extreme Deconvolution: Inferring Complete Distribution Functions from Noisy, Heterogeneous and Incomplete Observations”. 2011, *The Annals of Applied Statistics*, 5, 1657
- Boyer, M. L., Girardi, L., Marigo, P., Williams, B. F., Aringer, B., Nowotny, W., Rosenfield, P., Dorman, C. E., Guhathakurta, P., Dalcanton, J. J., Melbourne, J. L., Olsen, K. A. G., & Weisz, D. R., “Is There a Metallicity Ceiling to Form Carbon Stars?—A Novel Technique Reveals a Scarcity of C stars in the Inner M31 Disk”. 2013, *ApJ*, 774, 83
- Boyer, M. L., McQuinn, K. B. W., Groenewegen, M. A. T., Zijlstra, A. A., Whitelock, P. A., van Loon, J. T., Sonneborn, G., Sloan, G. C., Skillman, E. D., Meixner, M., McDonald, I., Jones, O. C., Javadi, A., Gehrz, R. D., Britavskiy, N., & Bonanos, A. Z., “An

Infrared Census of DUST in Nearby Galaxies with Spitzer (DUSTiNGS). IV. Discovery of High-redshift AGB Analogs”. 2017, *ApJ*, 851, 152

Boyer, M. L., Williams, B. F., Aringer, B., Chen, Y., Dalcanton, J. J., Girardi, L., Guhathakurta, P., Marigo, P., Olsen, K. A. G., Rosenfield, P., & Weisz, D. R., “A Dramatic Decrease in Carbon Star Formation in M31”. 2019, *ApJ*, 879, 109

Bressan, A., Marigo, P., Girardi, L., Salasnich, B., Dal Cero, C., Rubele, S., & Nanni, A., “PARSEC: stellar tracks and isochrones with the PAdova and TRieste Stellar Evolution Code”. 2012, *MNRAS*, 427, 127

Breunig, M. M., Kriegel, H.-P., Ng, R. T., & Sander, J. 2000, in Proceedings of the 2000 ACM SIGMOD International Conference on Management of Data - SIGMOD '00 (Dallas, Texas, United States: ACM Press), 93–104

Burns, C. R., Parent, E., Phillips, M. M., Stritzinger, M., Krisciunas, K., Suntzeff, N. B., Hsiao, E. Y., Contreras, C., Anais, J., Boldt, L., Busta, L., Campillay, A., Castellón, S., Folatelli, G., Freedman, W. L., González, C., Hamuy, M., Hoefflich, P., Krzeminski, W., Madore, B. F., Morrell, N., Persson, S. E., Roth, M., Salgado, F., Serón, J., & Torres, S., “The Carnegie Supernova Project: Absolute Calibration and the Hubble Constant”. 2018, *ApJ*, 869, 56

Calamida, A., Bajaj, V., Mack, J., Marinelli, M., Medina, J., Pidgeon, A., Kozhurina-Platais, V., Shanahan, C., & Som, D., “New Photometric Calibration of the Wide Field Camera 3 Detectors”. 2022, *AJ*, 164, 32

Cantat-Gaudin, T., & Anders, F., “Clusters and mirages: cataloguing stellar aggregates in the Milky Way”. 2020, *A&A*, 633, A99

Capozzi, F., & Raffelt, G., “Axion and neutrino bounds improved with new calibrations of the tip of the red-giant branch using geometric distance determinations”. 2020, *PhRvD*, 102, 083007

Carnall, A. C., “SpectRes: A Fast Spectral Resampling Tool in Python”. 2017, *arXiv e-prints*, arXiv:1705.05165

Casagrande, L., Ramírez, I., Meléndez, J., Bessell, M., & Asplund, M., “An absolutely calibrated  $T_{eff}$  scale from the infrared flux method. Dwarfs and subgiants”. 2010, *A&A*, 512, A54

Casagrande, L., & VandenBerg, D. A., “Synthetic stellar photometry - I. General considerations and new transformations for broad-band systems”. 2014, *MNRAS*, 444, 392

—, “On the use of Gaia magnitudes and new tables of bolometric corrections”. 2018, *MNRAS*, 479, L102

Casertano, S., Riess, A. G., Anderson, J., Anderson, R. I., Bowers, J. B., Clubb, K. I., Cukierman, A. R., Filippenko, A. V., Graham, M. L., MacKenty, J. W., Melis, C., Tucker, B. E., & Upadhy, G., “Parallax of Galactic Cepheids from Spatially Scanning the Wide Field Camera 3 on the Hubble Space Telescope: The Case of SS Canis Majoris”. 2016, *ApJ*, 825, 11

Castelli, F., & Kurucz, R. L. 2003, in *Modelling of Stellar Atmospheres*, ed. N. Piskunov, W. W. Weiss, & D. F. Gray, Vol. 210, A20

Chen, B. Q., Guo, H. L., Gao, J., Yang, M., Liu, Y. L., & Jiang, B. W., “Dust distributions in the magellanic clouds”. 2022, *MNRAS*, 511, 1317

Chen, B. Q., Huang, Y., Yuan, H. B., Wang, C., Fan, D. W., Xiang, M. S., Zhang, H. W., Tian, Z. J., & Liu, X. W., “Three-dimensional interstellar dust reddening maps of the Galactic plane”. 2019a, *MNRAS*, 483, 4277

Chen, Y., Girardi, L., Fu, X., Bressan, A., Aringer, B., Dal Tio, P., Pastorelli, G., Marigo, P., Costa, G., & Zhang, X., “YBC: a stellar bolometric corrections database with variable extinction coefficients. Application to PARSEC isochrones”. 2019b, *A&A*, 632, A105

Chen, Y.-P., Trager, S. C., Peletier, R. F., Lançon, A., Vazdekis, A., Prugniel, P., Silva, D. R., & Gonneau, A., “The X-shooter Spectral Library (XSL). I. DR1: Near-ultraviolet through optical spectra from the first year of the survey”. 2014a, *A&A*, 565, A117

—, “The X-shooter Spectral Library (XSL). I. DR1: Near-ultraviolet through optical spectra from the first year of the survey”. 2014b, *A&A*, 565, A117

Choi, J., Dotter, A., Conroy, C., Cantiello, M., Paxton, B., & Johnson, B. D., “Mesa Isochrones and Stellar Tracks (MIST). I. Solar-scaled Models”. 2016, *ApJ*, 823, 102

Choi, J., Dotter, A., Conroy, C., & Ting, Y.-S., “On the Red Giant Branch: Ambiguity in the Surface Boundary Condition Leads to  $\approx 100$  K Uncertainty in Model Effective Temperatures”. 2018a, *ApJ*, 860, 131

Choi, Y., Nidever, D. L., Olsen, K., Blum, R. D., Besla, G., Zaritsky, D., van der Marel, R. P., Bell, E. F., Gallart, C., Cioni, M.-R. L., Johnson, L. C., Vivas, A. K., Saha, A., de Boer, T. J. L., Noël, N. E. D., Monachesi, A., Massana, P., Conn, B. C., Martinez-Delgado, D., Muñoz, R. R., & Stringfellow, G. S., “SMASHing the LMC: A Tidally Induced Warp in the Outer LMC and a Large-scale Reddening Map”. 2018b, *ApJ*, 866, 90



Cioni, M. R. L., Clementini, G., Girardi, L., Guandalini, R., Gullieuszik, M., Miszalski, B., Moretti, M. I., Ripepi, V., Rubele, S., Bagheri, G., Bekki, K., Cross, N., de Blok, W. J. G., de Grijs, R., Emerson, J. P., Evans, C. J., Gibson, B., Gonzales-Solares, E., Groenewegen, M. A. T., Irwin, M., Ivanov, V. D., Lewis, J., Marconi, M., Marquette, J. B., Mastropietro, C., Moore, B., Napiwotzki, R., Naylor, T., Oliveira, J. M., Read, M., Sutorius, E., van Loon, J. T., Wilkinson, M. I., & Wood, P. R., “The VMC survey. I. Strategy and first data”. 2011, *A&A*, 527, A116

Coelho, P. R. T., Bruzual, G., & Charlot, S., “To use or not to use synthetic stellar spectra in population synthesis models?”. 2020, *MNRAS*, 491, 2025

Cohen, M., Wheaton, W. A., & Megeath, S. T., “Spectral Irradiance Calibration in the Infrared. XIV. The Absolute Calibration of 2MASS”. 2003, *AJ*, 126, 1090

Cushing, M. C., Vacca, W. D., & Rayner, J. T., “Spextool: A Spectral Extraction Package for SpeX, a 0.8-5.5 Micron Cross-Dispersed Spectrograph”. 2004, *PASP*, 116, 362

Da Costa, G. S., & Armandroff, T. E., “Standard Globular Cluster Giant Branches in the (M(I), (V - I)<sub>0</sub>) Plane”. 1990, *AJ*, 100, 162

Dahmer-Hahn, L. G., Riffel, R., Rodríguez-Ardila, A., Martins, L. P., Kehrig, C., Heckman, T. M., Pastoriza, M. G., & Dametto, N. Z., “Probing evolutionary population synthesis models in the near infrared with early-type galaxies”. 2018, *MNRAS*, 476, 4459

Dalcanton, J. 2009, “A Calibration Database for Stellar Models of Asymptotic Giant Branch Stars”, HST Proposal

Dalcanton, J. J., Williams, B. F., Seth, A. C., Dolphin, A., Holtzman, J., Rosema, K., Skillman, E. D., Cole, A., Girardi, L., Gogarten, S. M., Karachentsev, I. D., Olsen, K., Weisz, D., Christensen, C., Freeman, K., Gilbert, K., Gallart, C., Harris, J., Hodge, P., de Jong, R. S., Karachentseva, V., Mateo, M., Stetson, P. B., Tavares, M., Zaritsky, D., Governato, F., & Quinn, T., “The ACS Nearby Galaxy Survey Treasury”. 2009, *ApJS*, 183, 67

Dalcanton, J. J., Williams, B. F., Melbourne, J. L., Girardi, L., Dolphin, A., Rosenfield, P. A., Boyer, M. L., de Jong, R. S., Gilbert, K., Marigo, P., Olsen, K., Seth, A. C., & Skillman, E., “Resolved Near-infrared Stellar Populations in Nearby Galaxies”. 2012a, *ApJS*, 198, 6

Dalcanton, J. J., Williams, B. F., Lang, D., Lauer, T. R., Kalirai, J. S., Seth, A. C., Dolphin, A., Rosenfield, P., Weisz, D. R., Bell, E. F., Bianchi, L. C., Boyer, M. L., Caldwell, N., Dong, H., Dorman, C. E., Gilbert, K. M., Girardi, L., Gogarten, S. M.,

Gordon, K. D., Guhathakurta, P., Hodge, P. W., Holtzman, J. A., Johnson, L. C., Larsen, S. S., Lewis, A., Melbourne, J. L., Olsen, K. A. G., Rix, H.-W., Rosema, K., Saha, A., Sarajedini, A., Skillman, E. D., & Stanek, K. Z., “The Panchromatic Hubble Andromeda Treasury”. 2012b, *ApJS*, 200, 18

Dalton, G. B., Caldwell, M., Ward, A. K., Whalley, M. S., Woodhouse, G., Edeson, R. L., Clark, P., Beard, S. M., Gallie, A. M., Todd, S. P., Strachan, J. M. D., Bezawada, N. N., Sutherland, W. J., & Emerson, J. P. 2006, in Society of Photo-Optical Instrumentation Engineers (SPIE) Conference Series, Vol. 6269, Society of Photo-Optical Instrumentation Engineers (SPIE) Conference Series, ed. I. S. McLean & M. Iye, 62690X

Davies, B., & Beasor, E. R., “The ‘red supergiant problem’: the upper luminosity boundary of Type II supernova progenitors”. 2020, *MNRAS*, 493, 468

Delchambre, L., Bailer-Jones, C. A. L., Bellas-Velidis, I., Drimmel, R., Garabato, D., Carballo, R., Hatzidimitriou, D., Marshall, D. J., Andrae, R., Dafonte, C., Livanou, E., Fouesneau, M., Licata, E. L., Lindstrom, H. E. P., Manteiga, M., Robin, C., Silvelo, A., Abreu Aramburu, A., Alvarez, M. A., Bakker, J., Bijaoui, A., Brouillet, N., Brugaletta, E., Burlacu, A., Casamiquela, L., Chaoul, L., Chiavassa, A., Contursi, G., Cooper, W. J., Creevey, O. L., Dapergolas, A., de Laverny, P., Demouchy, C., Dharmawardena, T. E., Edvardsson, B., Fremat, Y., Garcia-Lario, P., Garcia-Torres, M., Gavel, A., Gomez, A., Gonzalez-Santamaria, I., Heiter, U., Jean-Antoine Piccolo, A., Kontizas, M., Kordopatis, G., Korn, A. J., Lanzafame, A. C., Lebreton, Y., Lobel, A., Lorca, A., Magdaleno Romeo, A., Marocco, F., Mary, N., Nicolas, C., Ordenovic, C., Pailler, F., Palicio, P. A., Pallas-Quintela, L., Panem, C., Pichon, B., Poggio, E., Recio-Blanco, A., Riclet, F., Rybizki, J., Santovena, R., Sarro, L. M., Schultheis, M. S., Segol, M., Slezak, I., Smart, R. L., Sordo, R., Soubiran, C., Suveges, M., Thevenin, F., Torralba Elipse, G., Ulla, A., Utrilla, E., Vallenari, A., van Dillen, E., Zhao, H., & Zorec, J., “Gaia DR3: Apsis III – Non-stellar content and source classification”. 2022, *arXiv e-prints*, arXiv:2206.06710

Dennis, M., & Sakstein, J., “Machine Learning the Tip of the Red Giant Branch”. 2023a, *arXiv e-prints*, arXiv:2303.12069

Dennis, M. T., & Sakstein, J., “Tip of the Red Giant Branch Bounds on the Axion-Electron Coupling Revisited”. 2023b, *arXiv e-prints*, arXiv:2305.03113

Deustua, S. E., Bohlin, R., Pirzkal, N., & MacKenty, J. 2014, in Society of Photo-Optical Instrumentation Engineers (SPIE) Conference Series, Vol. 9143, Space Telescopes and Instrumentation 2014: Optical, Infrared, and Millimeter Wave, ed. J. Oschmann, Jacobus M., M. Clampin, G. G. Fazio, & H. A. MacEwen, 91433G

- Di Luzio, L., Fedele, M., Giannotti, M., Mescia, F., & Nardi, E., “Stellar evolution confronts axion models”. 2022, *JCAP*, 2022, 035
- Di Valentino, E., Mena, O., Pan, S., Visinelli, L., Yang, W., Melchiorri, A., Mota, D. F., Riess, A. G., & Silk, J., “In the realm of the Hubble tension-a review of solutions”. 2021, *Classical and Quantum Gravity*, 38, 153001
- Dixon, M., Mould, J., Flynn, C., Taylor, E. N., Lidman, C., & Duffy, A. R., “A geometric calibration of the tip of the red giant branch in the Milky Way using Gaia DR3”. 2023, *MNRAS*, 523, 2283
- Dolphin, A. E., “WFPC2 Stellar Photometry with HSTPHOT”. 2000, *PASP*, 112, 1383
- , “Numerical methods of star formation history measurement and applications to seven dwarf spheroidals”. 2002, *MNRAS*, 332, 91
- Durbin, M. 2017, “Calibrating the Near-Infrared Tip of the Red Giant Branch with Multiwavelength Photometry”, HST Proposal
- Durbin, M. J., Beaton, R. L., Dalcanton, J. J., Williams, B. F., & Boyer, M. L., “MCR-TRGB: A Multiwavelength-covariant, Robust Tip of the Red Giant Branch Measurement Method”. 2020, *ApJ*, 898, 57
- Efstathiou, G., “To  $H_0$  or not to  $H_0$ ?”. 2021, *MNRAS*, 505, 3866
- Eftekhari, E., La Barbera, F., Vazdekis, A., Allende Prieto, C., & Knowles, A. T., “Strong CO absorption features in massive ETGs”. 2022, *MNRAS*, 512, 378
- Eldridge, J. J. 2019, personal communication
- Emerson, J., McPherson, A., & Sutherland, W., “Visible and Infrared Survey Telescope for Astronomy: Progress Report”. 2006, *The Messenger*, 126, 41
- Eriksson, K., Höfner, S., & Aringer, B., “Synthetic photometry for carbon-rich giants. V. Effects of grain-size-dependent dust opacities”. 2023, *A&A*, 673, A21
- Fabrizius, C., Luri, X., Arenou, F., Babusiaux, C., Helmi, A., Muraveva, T., Reylé, C., Spoto, F., Vallenari, A., Antoja, T., Balbinot, E., Barache, C., Bauchet, N., Bragaglia, A., Busonero, D., Cantat-Gaudin, T., Carrasco, J. M., Diakité, S., Fabrizio, M., Figueras, F., Garcia-Gutierrez, A., Garofalo, A., Jordi, C., Kervella, P., Khanna, S., Leclerc, N., Licata, E., Lambert, S., Marrese, P. M., Masip, A., Ramos, P., Robichon, N., Robin, A. C., Romero-Gómez, M., Rubele, S., & Weiler, M., “Gaia Early Data Release 3. Catalogue validation”. 2021, *A&A*, 649, A5

Falcón-Barroso, J., Sánchez-Blázquez, P., Vazdekis, A., Ricciardelli, E., Cardiel, N., Cenarro, A. J., Gorgas, J., & Peletier, R. F., “An updated MILES stellar library and stellar population models”. 2011, *A&A*, 532, A95

Fischler, M. A., & Bolles, R. C. 1987, in *Readings in Computer Vision* (Elsevier), 726–740

Fitzpatrick, E. L., Massa, D., Gordon, K. D., Bohlin, R., & Clayton, G. C., “An Analysis of the Shapes of Interstellar Extinction Curves. VII. Milky Way Spectrophotometric Optical-through-ultraviolet Extinction and Its R-dependence”. 2019, *ApJ*, 886, 108

Freedman, W. L., “Measurements of the Hubble Constant: Tensions in Perspective”. 2021, *ApJ*, 919, 16

Freedman, W. L., Madore, B. F., Gibson, B. K., Ferrarese, L., Kelson, D. D., Sakai, S., Mould, J. R., Kennicutt, Robert C., J., Ford, H. C., Graham, J. A., Huchra, J. P., Hughes, S. M. G., Illingworth, G. D., Macri, L. M., & Stetson, P. B., “Final Results from the Hubble Space Telescope Key Project to Measure the Hubble Constant”. 2001, *ApJ*, 553, 47

Freedman, W. L., Madore, B. F., Hatt, D., Hoyt, T. J., Jang, I. S., Beaton, R. L., Burns, C. R., Lee, M. G., Monson, A. J., Neeley, J. R., Phillips, M. M., Rich, J. A., & Seibert, M., “The Carnegie-Chicago Hubble Program. VIII. An Independent Determination of the Hubble Constant Based on the Tip of the Red Giant Branch”. 2019, *ApJ*, 882, 34

Freedman, W. L., Madore, B. F., Hoyt, T., Jang, I. S., Beaton, R., Lee, M. G., Monson, A., Neeley, J., & Rich, J., “Calibration of the Tip of the Red Giant Branch”. 2020, *ApJ*, 891, 57

Friedmann, A., “Über die Krümmung des Raumes”. 1922, *Zeitschrift für Physik*, 10, 377

Fu, X., Bressan, A., Marigo, P., Girardi, L., Montalbán, J., Chen, Y., & Nanni, A., “New PARSEC data base of  $\alpha$ -enhanced stellar evolutionary tracks and isochrones - I. Calibration with 47 Tuc (NGC 104) and the improvement on RGB bump”. 2018, *MNRAS*, 476, 496

Gaia Collaboration, Luri, X., Chemin, L., Clementini, G., Delgado, H. E., McMillan, P. J., Romero-Gómez, M., Balbinot, E., Castro-Ginard, A., Mor, R., Ripepi, V., Sarro, L. M., Cioni, M. R. L., Fabricius, C., Garofalo, A., Helmi, A., Muraveva, T., Brown, A. G. A., Vallenari, A., Prusti, T., de Bruijne, J. H. J., Babusiaux, C., Biermann, M., Creevey, O. L., Evans, D. W., Eyer, L., Hutton, A., Jansen, F., Jordi, C., Klioner, S. A., Lammers, U., Lindegren, L., Mignard, F., Panem, C., Pourbaix, D., Randich, S., Sartoretti, P., Soubiran, C., Walton, N. A., Arenou, F., Bailer-Jones, C. A. L., Bastian, U., Cropper,

M., Drimmel, R., Katz, D., Lattanzi, M. G., van Leeuwen, F., Bakker, J., Castañeda, J., De Angeli, F., Ducourant, C., Fouesneau, M., Frémat, Y., Guerra, R., Guerrier, A., Guiraud, J., Jean-Antoine Piccolo, A., Masana, E., Messineo, R., Mowlavi, N., Nicolas, C., Nienartowicz, K., Pailier, F., Panuzzo, P., Riclet, F., Roux, W., Seabroke, G. M., Sordo, R., Tanga, P., Thévenin, F., Gracia-Abril, G., Portell, J., Teyssier, D., Altmann, M., Andrae, R., Bellas-Velidis, I., Benson, K., Berthier, J., Blomme, R., Brugaletta, E., Burgess, P. W., Busso, G., Carry, B., Cellino, A., Cheek, N., Damerdj, Y., Davidson, M., Delchambre, L., Dell'Oro, A., Fernández-Hernández, J., Galluccio, L., García-Lario, P., Garcia-Reinaldos, M., González-Núñez, J., Gosset, E., Haigron, R., Halbwachs, J. L., Hambly, N. C., Harrison, D. L., Hatzidimitriou, D., Heiter, U., Hernández, J., Hestroffer, D., Hodgkin, S. T., Holl, B., Janßen, K., Jevardat de Fombelle, G., Jordan, S., Krone-Martins, A., Lanzafame, A. C., Löffler, W., Lorca, A., Manteiga, M., Marchal, O., Maresse, P. M., Moitinho, A., Mora, A., Muinonen, K., Osborne, P., Pancino, E., Pauwels, T., Recio-Blanco, A., Richards, P. J., Riello, M., Rimoldini, L., Robin, A. C., Roegiers, T., Rybizki, J., Siopis, C., Smith, M., Sozzetti, A., Ulla, A., Utrilla, E., van Leeuwen, M., van Reeve, W., Abbas, U., Abreu Aramburu, A., Accart, S., Aerts, C., Aguado, J. J., Ajaj, M., Altavilla, G., Álvarez, M. A., Álvarez Cid-Fuentes, J., Alves, J., Anderson, R. I., Anglada Varela, E., Antoja, T., Audard, M., Baines, D., Baker, S. G., Balaguer-Núñez, L., Balog, Z., Barache, C., Barbato, D., Barros, M., Barstow, M. A., Bartolomé, S., Bassilana, J. L., Bauchet, N., Baudesson-Stella, A., Becciani, U., Bellazzini, M., Bernet, M., Bertone, S., Bianchi, L., Blanco-Cuaresma, S., Boch, T., Bombrun, A., Bossini, D., Bouquillon, S., Bragaglia, A., Bramante, L., Breedt, E., Bressan, A., Brouillet, N., Bucciarelli, B., Burlacu, A., Busonero, D., Butkevich, A. G., Buzzzi, R., Caffau, E., Cancelliere, R., Cánovas, H., Cantat-Gaudin, T., Carballo, R., Carlucci, T., Carnerero, M. I., Carrasco, J. M., Casamiquela, L., Castellani, M., Castro Sampedro, P., Chaoul, L., Charlot, P., Chiavassa, A., Comoretto, G., Cooper, W. J., Cornez, T., Cowell, S., Crifo, F., Crosta, M., Crowley, C., Dafonte, C., Dapergolas, A., David, M., David, P., de Laverny, P., De Luise, F., De March, R., De Ridder, J., de Souza, R., de Teodoro, P., de Torres, A., del Peloso, E. F., del Pozo, E., Delgado, A., Delisle, J. B., Di Matteo, P., Diakite, S., Diener, C., Distefano, E., Dolding, C., Eappachen, D., Enke, H., Esquej, P., Fabre, C., Fabrizio, M., Faigler, S., Fedorets, G., Fernique, P., Fienga, A., Figueras, F., Fouron, C., Fragkoudi, F., Fraile, E., Franke, F., Gai, M., Garabato, D., Garcia-Gutierrez, A., García-Torres, M., Gavras, P., Gerlach, E., Geyer, R., Giacobbe, P., Gilmore, G., Girona, S., Giuffrida, G., Gomez, A., Gonzalez-Santamaria, I., González-Vidal, J. J., Granvik, M., Gutiérrez-Sánchez, R., Guy, L. P., Hauser, M., Haywood, M., Hidalgo, S. L., Hilger, T., Hładczuk, N., Hobbs, D., Holland, G., Huckle, H. E., Jasiewicz, G., Jonker, P. G., Juaristi Campillo, J., Julbe, F., Karbevská, L., Kervella, P., Khanna, S., Kochoska, A., Kontizas, M., Kordopatis, G., Korn, A. J., Kostrzewa-Rutkowska, Z., Kruszyńska, K., Lambert, S., Lanza, A. F., Lasne, Y., Le Campion, J. F., Le Fustec, Y., Lebreton, Y., Lebzelter, T., Leccia, S., Leclerc, N., Lecoœur-Taïbi, I., Liao, S., Licata, E., Lindstrøm, H. E. P., Lister, T. A., Livanou, E., Lobel, A., Madrero Pardo, P., Managau, S., Mann, R. G., Marchant, J. M., Marconi,

M., Marcos Santos, M. M. S., Marinoni, S., Marocco, F., Marshall, D. J., Martin Polo, L., Martín-Fleitas, J. M., Masip, A., Massari, D., Mastrobuono-Battisti, A., Mazeh, T., Messina, S., Michalik, D., Millar, N. R., Mints, A., Molina, D., Molinaro, R., Molnár, L., Montegriffo, P., Morbidelli, R., Morel, T., Morris, D., Mulone, A. F., Munoz, D., Murphy, C. P., Musella, I., Noval, L., Ordénovic, C., Orrù, G., Osinde, J., Pagani, C., Pagano, I., Palaversa, L., Palicio, P. A., Panahi, A., Pawlak, M., Peñalosa Esteller, X., Penttilä, A., Piersimoni, A. M., Pineau, F. X., Plachy, E., Plum, G., Poggio, E., Poretti, E., Poujoulet, E., Prša, A., Pulone, L., Racero, E., Ragaini, S., Rainer, M., Raiteri, C. M., Rambaux, N., Ramos, P., Ramos-Lerate, M., Re Fiorentin, P., Regibo, S., Reylé, C., Riva, A., Rixon, G., Robichon, N., Robin, C., Roelens, M., Rohrbasser, L., Rowell, N., Royer, F., Rybicki, K. A., Sadowski, G., Sagristà Sellés, A., Sahlmann, J., Salgado, J., Salguero, E., Samaras, N., Gimenez, V. S., Sanna, N., Santoveña, R., Sarasso, M., Schultheis, M., Sciacca, E., Segol, M., Segovia, J. C., Ségransan, D., Semeux, D., Siddiqui, H. I., Siebert, A., Siltala, L., Slezak, E., Smart, R. L., Solano, E., Solitro, F., Souami, D., Souchay, J., Spagna, A., Spoto, F., Steele, I. A., Steidelmüller, H., Stephenson, C. A., Süveges, M., Szabados, L., Szegedi-Elek, E., Taris, F., Tauran, G., Taylor, M. B., Teixeira, R., Thuillot, W., Tonello, N., Torra, F., Torra, J., Turon, C., Unger, N., Vaillant, M., van Dillen, E., Vanel, O., Vecchiato, A., Viala, Y., Vicente, D., Voutsinas, S., Weiler, M., Wevers, T., Wyrzykowski, Ł., Yoldas, A., Yvard, P., Zhao, H., Zorec, J., Zucker, S., Zurbach, C., & Zwitter, T., “Gaia Early Data Release 3. Structure and properties of the Magellanic Clouds”. 2021, *A&A*, 649, A7

Gaia Collaboration, Vallenari, A., Brown, A. G. A., Prusti, T., de Bruijne, J. H. J., Arenou, F., Babusiaux, C., Biermann, M., Creevey, O. L., Ducourant, C., Evans, D. W., Eyer, L., Guerra, R., Hutton, A., Jordi, C., Klioner, S. A., Lammers, U. L., Lindegren, L., Luri, X., Mignard, F., Panem, C., Pourbaix, D., Randich, S., Sartoretti, P., Soubiran, C., Tanga, P., Walton, N. A., Bailer-Jones, C. A. L., Bastian, U., Drimmel, R., Jansen, F., Katz, D., Lattanzi, M. G., van Leeuwen, F., Bakker, J., Cacciari, C., Castañeda, J., De Angeli, F., Fabricius, C., Fouesneau, M., Frémat, Y., Galluccio, L., Guerrier, A., Heiter, U., Masana, E., Messineo, R., Mowlavi, N., Nicolas, C., Nienartowicz, K., Pailer, F., Panuzzo, P., Riclet, F., Roux, W., Seabroke, G. M., Sordoørcit, R., Thévenin, F., Gracia-Abril, G., Portell, J., Teyssier, D., Altmann, M., Andrae, R., Audard, M., Bellas-Velidis, I., Benson, K., Berthier, J., Blomme, R., Burgess, P. W., Busonero, D., Busso, G., Cánovas, H., Carry, B., Cellino, A., Cheek, N., Clementini, G., Damerdj, Y., Davidson, M., de Teodoro, P., Nuñez Campos, M., Delchambre, L., Dell’Oro, A., Esquej, P., Fernández-Hernández, J., Fraile, E., Garabato, D., García-Lario, P., Gosset, E., Haigron, R., Halbwachs, J. L., Hambly, N. C., Harrison, D. L., Hernández, J., Hestroffer, D., Hodgkin, S. T., Holl, B., Janßen, K., Jevardat de Fombelle, G., Jordan, S., Krone-Martins, A., Lanzafame, A. C., Löffler, W., Marchal, O., Marrese, P. M., Moitinho, A., Muinonen, K., Osborne, P., Pancino, E., Pauwels, T., Recio-Blanco, A., Reylé, C., Riello, M., Rimoldini, L., Roegiers, T., Rybizki, J., Sarro, L. M., Siopis, C., Smith, M., Sozzetti, A., Utrilla, E.,

van Leeuwen, M., Abbas, U., Ábrahám, P., Abreu Aramburu, A., Aerts, C., Aguado, J. J., Ajaj, M., Aldea-Montero, F., Altavilla, G., Álvarez, M. A., Alves, J., Anders, F., Anderson, R. I., Anglada Varela, E., Antoja, T., Baines, D., Baker, S. G., Balaguer-Núñez, L., Balbinot, E., Balog, Z., Barache, C., Barbato, D., Barros, M., Barstow, M. A., Bartolomé, S., Bassilana, J. L., Bauchet, N., Becciani, U., Bellazzini, M., Berihuete, A., Bernet, M., Bertone, S., Bianchi, L., Binnenfeld, A., Blanco-Cuaresma, S., Blazere, A., Boch, T., Bombrun, A., Bossini, D., Bouquillon, S., Bragaglia, A., Bramante, L., Breedt, E., Bressan, A., Brouillet, N., Brugaletta, E., Bucciarelli, B., Burlacu, A., Butkevich, A. G., Buzzi, R., Caffau, E., Cancelliere, R., Cantat-Gaudin, T., Carballo, R., Carlucci, T., Carnerero, M. I., Carrasco, J. M., Casamiquela, L., Castellani, M., Castro-Ginard, A., Chaoul, L., Charlot, P., Chemin, L., Chiaramida, V., Chiavassa, A., Chornay, N., Comoretto, G., Contursi, G., Cooper, W. J., Cornez, T., Cowell, S., Crifo, F., Cropper, M., Crosta, M., Crowley, C., Dafonte, C., Dapergolas, A., David, M., David, P., de Laverny, P., De Luise, F., De March, R., De Ridder, J., de Souza, R., de Torres, A., del Peloso, E. F., del Pozo, E., Delbo, M., Delgado, A., Delisle, J. B., Demouchy, C., Dharmawardena, T. E., Di Matteo, P., Diakite, S., Diener, C., Distefano, E., Dolding, C., Edvardsson, B., Enke, H., Fabre, C., Fabrizio, M., Faigler, S., Fedorets, G., Fernique, P., Fienga, A., Figueras, F., Fournier, Y., Fournon, C., Fragkoudi, F., Gai, M., Garcia-Gutierrez, A., Garcia-Reinaldos, M., García-Torres, M., Garofalo, A., Gavel, A., Gavras, P., Gerlach, E., Geyer, R., Giacobbe, P., Gilmore, G., Girona, S., Giuffrida, G., Gomel, R., Gomez, A., González-Núñez, J., González-Santamaría, I., González-Vidal, J. J., Granvik, M., Guillout, P., Guiraud, J., Gutiérrez-Sánchez, R., Guy, L. P., Hatzidimitriou, D., Hauser, M., Haywood, M., Helmer, A., Helmi, A., Sarmiento, M. H., Hidalgo, S. L., Hilger, T., Hładczyk, N., Hobbs, D., Holland, G., Huckle, H. E., Jardine, K., Jasiewicz, G., Jean-Antoine Piccolo, A., Jiménez-Arranz, Ó., Jorissen, A., Juaristi Campillo, J., Julbe, F., Karbevská, L., Kervella, P., Khanna, S., Kontizas, M., Kordopatis, G., Korn, A. J., Kóspál, Á., Kostrzewa-Rutkowska, Z., Kruszyńska, K., Kun, M., LaizEAU, P., Lambert, S., Lanza, A. F., Lasne, Y., Le Champion, J. F., Lebreton, Y., Lebzelter, T., Leccia, S., Leclerc, N., Lecoeur-Taibi, I., Liao, S., Licata, E. L., Lindstrøm, H. E. P., Lister, T. A., Livanou, E., Lobel, A., Lorca, A., Loup, C., Madrero Pardo, P., Magdaleno Romeo, A., Managau, S., Mann, R. G., Manteiga, M., Marchant, J. M., Marconi, M., Marcos, J., Marcos Santos, M. M. S., Marín Pina, D., Marinoni, S., Marocco, F., Marshall, D. J., Polo, L. M., Martín-Fleitas, J. M., Marton, G., Mary, N., Masip, A., Massari, D., Mastrobuono-Battisti, A., Mazeh, T., McMillan, P. J., Messina, S., Michalik, D., Millar, N. R., Mints, A., Molina, D., Molinaro, R., Molnár, L., Monari, G., Monguió, M., Montegriffo, P., Montero, A., Mor, R., Mora, A., Morbidelli, R., Morel, T., Morris, D., Muraveva, T., Murphy, C. P., Musella, I., Nagy, Z., Noval, L., Ocaña, F., Ogden, A., Ordenovic, C., Osinde, J. O., Pagani, C., Pagano, I., Palaversa, L., Palicio, P. A., Pallas-Quintela, L., Panahi, A., Payne-Wardenaar, S., Peñalosa Esteller, X., Penttilä, A., Pichon, B., Piersimoni, A. M., Pineau, F. X., Plachy, E., Plum, G., Poggio, E., Prša, A., Pulone, L., Racero, E., Ragaini, S., Rainer, M., Raiteri, C. M., Rambaux, N., Ramos, P., Ramos-Lerate, M., Re Fiorentin,

P., Regibo, S., Richards, P. J., Rios Diaz, C., Ripepi, V., Riva, A., Rix, H. W., Rixon, G., Robichon, N., Robin, A. C., Robin, C., Roelens, M., Rogues, H. R. O., Rohrbasser, L., Romero-Gómez, M., Rowell, N., Royer, F., Ruz Mieres, D., Rybicki, K. A., Sadowski, G., Sáez Núñez, A., Sagristà Sellés, A., Sahlmann, J., Salguero, E., Samaras, N., Sanchez Gimenez, V., Sanna, N., Santoveña, R., Sarasso, M., Schultheis, M., Sciacca, E., Segol, M., Segovia, J. C., Ségransan, D., Semeux, D., Shahaf, S., Siddiqui, H. I., Siebert, A., Siltala, L., Silvelo, A., Slezak, E., Slezak, I., Smart, R. L., Snaith, O. N., Solano, E., Solitro, F., Souami, D., Souchay, J., Spagna, A., Spina, L., Spoto, F., Steele, I. A., Steidelmüller, H., Stephenson, C. A., Süveges, M., Surdej, J., Szabados, L., Szegedi-Elek, E., Taris, F., Taylo, M. B., Teixeira, R., Tolomei, L., Tonello, N., Torra, F., Torra, J., Torralba Elipse, G., Trabucchi, M., Tsounis, A. T., Turon, C., Ulla, A., Unger, N., Vaillant, M. V., van Dillen, E., van Reeve, W., Vanel, O., Vecchiato, A., Viala, Y., Vicente, D., Voutsinas, S., Weiler, M., Wevers, T., Wyrzykowski, L., Yoldas, A., Yvard, P., Zhao, H., Zorec, J., Zucker, S., & Zwitter, T., “Gaia Data Release 3: Summary of the content and survey properties”. 2022a, *arXiv e-prints*, arXiv:2208.00211

Gaia Collaboration, Montegriffo, P., Bellazzini, M., De Angeli, F., Andrae, R., Barstow, M. A., Bossini, D., Bragaglia, A., Burgess, P. W., Cacciari, C., Carrasco, J. M., Chornay, N., Delchambre, L., Evans, D. W., Fouesneau, M., Fremat, Y., Garabato, D., Jordi, C., Manteiga, M., Massari, D., Palaversa, L., Pancino, E., Riello, M., Ruz Mieres, D., Sanna, N., Santoveña, R., Sordo, R., Vallenari, A., Walton, N., & DPAC, G., “Gaia Data Release 3: The Galaxy in your preferred colours. Synthetic photometry from Gaia low-resolution spectra”. 2022b, *arXiv e-prints*, arXiv:2206.06215

Gilbert, K. M., Kalirai, J. S., Guhathakurta, P., Beaton, R. L., Geha, M. C., Kirby, E. N., Majewski, S. R., Patterson, R. J., Tollerud, E. J., Bullock, J. S., Tanaka, M., & Chiba, M., “Global Properties of M31’s Stellar Halo from the SPLASH Survey. II. Metallicity Profile”. 2014, *ApJ*, 796, 76

Ginsburg, A., Parikh, M., Woillez, J., Groener, A., Liedtke, S., Sipocz, B., Robitaille, T., Deil, C., Svoboda, B., Tollerud, E., Persson, M. V., Séguin-Charbonneau, L., Armstrong, C., Mirocha, J., Droettboom, M., Allen, J., Moolekamp, F., Egeland, R., Singer, L., Barbary, K., Grollier, F., Shiga, D., Moritz Günther, H., Parejko, J., Booker, J., Rol, E., Edward, Miller, A., & Willett, K. 2017, “Astroquery: Access to Online Data Resources”, ascl:1708.004

Ginsburg, A., Sipocz, B. M., Brasseur, C. E., Cowperthwaite, P. S., Craig, M. W., Deil, C., Guillochon, J., Guzman, G., Liedtke, S., Lim, P. L., Lockhart, K. E., Mommert, M., Morris, B. M., Norman, H., Parikh, M., Persson, M. V., Robitaille, T. P., Segovia, J.-C., Singer, L. P., Tollerud, E. J., de Val-Borro, M., Valtchanov, I., Woillez, J., & The Astroquery collaboration, a subset of the astropy collaboration, “Astroquery : An



Astronomical Web-Querying Package in Python”. 2019, *The Astronomical Journal*, 157, 98

Girardi, L., Dalcanton, J., Williams, B., de Jong, R., Gallart, C., Monelli, M., Groenewegen, M. A. T., Holtzman, J. A., Olsen, K. A. G., Seth, A. C., Weisz, D. R., & ANGST/ANGRRR Collaboration, “Revised Bolometric Corrections and Interstellar Extinction Coefficients for the ACS and WFPC2 Photometric Systems”. 2008, *PASP*, 120, 583

Gonneau, A., Lançon, A., Trager, S. C., Aringer, B., Lyubenova, M., Nowotny, W., Peletier, R. F., Prugniel, P., Chen, Y. P., Dries, M., Choudhury, O. S., Falcón-Barroso, J., Koleva, M., Meneses-Goytia, S., Sánchez-Blázquez, P., & Vazdekis, A., “Carbon stars in the X-Shooter Spectral Library”. 2016, *A&A*, 589, A36

Gonneau, A., Lançon, A., Trager, S. C., Aringer, B., Nowotny, W., Peletier, R. F., Prugniel, P., Chen, Y. P., & Lyubenova, M., “Carbon stars in the X-shooter Spectral Library. II. Comparison with models”. 2017, *A&A*, 601, A141

Gonneau, A., Lyubenova, M., Lançon, A., Trager, S. C., Peletier, R. F., Arentsen, A., Chen, Y. P., Coelho, P. R. T., Dries, M., Falcón-Barroso, J., Prugniel, P., Sánchez-Blázquez, P., Vazdekis, A., & Verro, K., “The X-shooter Spectral Library (XSL): Data release 2”. 2020a, *A&A*, 634, A133

—, “The X-shooter Spectral Library (XSL): Data release 2”. 2020b, *A&A*, 634, A133

Gonzaga, S., Hack, W., Fruchter, A., & Mack, J. 2012, *The DrizzlePac Handbook* (Baltimore: STScI)

González-Fernández, C., Hodgkin, S. T., Irwin, M. J., González-Solares, E., Koposov, S. E., Lewis, J. R., Emerson, J. P., Hewett, P. C., Yoldas, A. K., & Riello, M., “The VISTA ZYJHKs photometric system: calibration from 2MASS”. 2018, *MNRAS*, 474, 5459

Gordon, K. D., Clayton, G. C., Misselt, K. A., Landolt, A. U., & Wolff, M. J., “A Quantitative Comparison of the Small Magellanic Cloud, Large Magellanic Cloud, and Milky Way Ultraviolet to Near-Infrared Extinction Curves”. 2003, *ApJ*, 594, 279

Górski, M., Pietrzyński, G., Gieren, W., Graczyk, D., Suchomska, K., Karczmarek, P., Cohen, R. E., Zgierski, B., Wielgórski, P., Pilecki, B., Taormina, M., Kołaczowski, Z., & Narloch, W., “The Araucaria Project: Multi-band Calibrations of the TRGB Absolute Magnitude”. 2018, *AJ*, 156, 278

Górski, M., Zgirski, B., Pietrzyński, G., Gieren, W., Wielgórski, P., Graczyk, D., Kudritzki, R.-P., Pilecki, B., Narloch, W., Karczmarek, P., Suchomska, K., & Taormina, M., “Empirical Calibration of the Reddening Maps in the Magellanic Clouds”. 2020, *ApJ*, 889, 179

Graczyk, D., Pietrzyński, G., Thompson, I. B., Gieren, W., Zgirski, B., Villanova, S., Górski, M., Wielgórski, P., Karczmarek, P., Narloch, W., Pilecki, B., Taormina, M., Smolec, R., Suchomska, K., Gallenne, A., Nardetto, N., Storm, J., Kudritzki, R.-P., Kałuszyński, M., & Pych, W., “A Distance Determination to the Small Magellanic Cloud with an Accuracy of Better than Two Percent Based on Late-type Eclipsing Binary Stars”. 2020, *ApJ*, 904, 13

Green, G. M., Schlafly, E., Zucker, C., Speagle, J. S., & Finkbeiner, D., “A 3D Dust Map Based on Gaia, Pan-STARRS 1, and 2MASS”. 2019, *ApJ*, 887, 93

Gregg, M. D., Silva, D., Rayner, J., Worthey, G., Valdes, F., Pickles, A., Rose, J., Carney, B., & Vacca, W. 2006, in *The 2005 HST Calibration Workshop: Hubble After the Transition to Two-Gyro Mode*, ed. A. M. Koekemoer, P. Goudfrooij, & L. L. Dressel, 209

Groenewegen, M. A. T., “Infrared excess around nearby red giant branch stars and Reimers law”. 2012, *A&A*, 540, A32

Grogin, N. A., Kocevski, D. D., Faber, S. M., Ferguson, H. C., Koekemoer, A. M., Riess, A. G., Acquaviva, V., Alexander, D. M., Almaini, O., Ashby, M. L. N., Barden, M., Bell, E. F., Bournaud, F., Brown, T. M., Caputi, K. I., Casertano, S., Cassata, P., Castellano, M., Challis, P., Chary, R.-R., Cheung, E., Cirasuolo, M., Conselice, C. J., Roshan Cooray, A., Croton, D. J., Daddi, E., Dahlen, T., Davé, R., de Mello, D. F., Dekel, A., Dickinson, M., Dolch, T., Donley, J. L., Dunlop, J. S., Dutton, A. A., Elbaz, D., Fazio, G. G., Filippenko, A. V., Finkelstein, S. L., Fontana, A., Gardner, J. P., Garnavich, P. M., Gawiser, E., Giavalisco, M., Grazian, A., Guo, Y., Hathi, N. P., Häussler, B., Hopkins, P. F., Huang, J.-S., Huang, K.-H., Jha, S. W., Kartaltepe, J. S., Kirshner, R. P., Koo, D. C., Lai, K., Lee, K.-S., Li, W., Lotz, J. M., Lucas, R. A., Madau, P., McCarthy, P. J., McGrath, E. J., McIntosh, D. H., McLure, R. J., Mobasher, B., Moustakas, L. A., Mozena, M., Nandra, K., Newman, J. A., Niemi, S.-M., Noeske, K. G., Papovich, C. J., Pentericci, L., Pope, A., Primack, J. R., Rajan, A., Ravindranath, S., Reddy, N. A., Renzini, A., Rix, H.-W., Robaina, A. R., Rodney, S. A., Rosario, D. J., Rosati, P., Salimbeni, S., Scarlata, C., Siana, B., Simard, L., Smidt, J., Somerville, R. S., Spinrad, H., Straughn, A. N., Strolger, L.-G., Telford, O., Teplitz, H. I., Trump, J. R., van der Wel, A., Villforth, C., Wechsler, R. H., Weiner, B. J., Wiklind, T., Wild, V., Wilson, G., Wuyts, S., Yan, H.-J., & Yun, M. S., “CANDELS: The Cosmic Assembly Near-infrared Deep Extragalactic Legacy Survey”. 2011, *ApJS*, 197, 35

Hack, W. J., Dencheva, N., & Fruchter, A. S. 2013, in *Astronomical Society of the Pacific Conference Series*, Vol. 475, *Astronomical Data Analysis Software and Systems XXII*, ed. D. N. Friedel, 49

Härm, H., & Schwarzschild, M., “Red Giants of Population II. III.”. 1964, *ApJ*, 139, 594

Hartig, G. F. 2009, “WFC3 SMOV Programs 11437/9: IR On-orbit PSF Evaluation”, *Space Telescope WFC Instrument Science Report*

Hasan, H., & Bely, P. Y. 1994, in *The Restoration of HST Images and Spectra - II*, ed. R. J. Hanisch & R. L. White, 157

Haschke, R., Grebel, E. K., & Duffau, S., “New Optical Reddening Maps of the Large and Small Magellanic Clouds”. 2011, *AJ*, 141, 158

Hatt, D., Beaton, R. L., Freedman, W. L., Madore, B. F., Jang, I.-S., Hoyt, T. J., Lee, M. G., Monson, A. J., Rich, J. A., Scowcroft, V., & Seibert, M., “The Carnegie-Chicago Hubble Program. II. The Distance to IC 1613: The Tip of the Red Giant Branch and RR Lyrae Period luminosity Relations”. 2017, *ApJ*, 845, 146

Hatt, D., Freedman, W. L., Madore, B. F., Beaton, R. L., Hoyt, T. J., Jang, I. S., Lee, M. G., Monson, A. J., Rich, J. A., Scowcroft, V., & Seibert, M., “The Carnegie-Chicago Hubble Program. IV. The Distance to NGC 4424, NGC 4526, and NGC 4356 via the Tip of the Red Giant Branch”. 2018a, *ApJ*, 861, 104

Hatt, D., Freedman, W. L., Madore, B. F., Jang, I. S., Beaton, R. L., Hoyt, T. J., Lee, M. G., Monson, A. J., Rich, J. A., Scowcroft, V., & Seibert, M., “The Carnegie-Chicago Hubble Program. V. The Distances to NGC 1448 and NGC 1316 via the Tip of the Red Giant Branch”. 2018b, *ApJ*, 866, 145

Hoffmann, S. L., Mack, J., Avila, R., Martlin, C., Cohen, Y., & Bajaj, V. 2021, in *American Astronomical Society Meeting Abstracts*, Vol. 53, *American Astronomical Society Meeting Abstracts*, 216.02

Holberg, J. B., & Bergeron, P., “Calibration of Synthetic Photometry Using DA White Dwarfs”. 2006, *AJ*, 132, 1221

Hoyt, T. J., “Sub-per-cent determination of the brightness at the tip of the red giant branch in the Magellanic Clouds”. 2023, *Nature Astronomy*, 7, 590

Hoyt, T. J., Freedman, W. L., Madore, B. F., Seibert, M., Beaton, R. L., Hatt, D., Jang, I. S., Lee, M. G., Monson, A. J., & Rich, J. A., “The Near-infrared Tip of the Red Giant Branch. II. An Absolute Calibration in the Large Magellanic Cloud”. 2018, *ApJ*, 858, 12

Huang, C. D., Riess, A. G., Hoffmann, S. L., Klein, C., Bloom, J., Yuan, W., Macri, L. M., Jones, D. O., Whitelock, P. A., Casertano, S., & Anderson, R. I., “A Near-infrared Period-Luminosity Relation for Miras in NGC 4258, an Anchor for a New Distance Ladder”. 2018, *ApJ*, 857, 67

Huang, C. D., Riess, A. G., Yuan, W., Macri, L. M., Zakamska, N. L., Casertano, S., Whitelock, P. A., Hoffmann, S. L., Filippenko, A. V., & Scolnic, D., “Hubble Space Telescope Observations of Mira Variables in the SN Ia Host NGC 1559: An Alternative Candle to Measure the Hubble Constant”. 2020, *ApJ*, 889, 5

Hubble, E., “A Relation between Distance and Radial Velocity among Extra-Galactic Nebulae”. 1929, *Proceedings of the National Academy of Science*, 15, 168

Imara, N., & Blitz, L., “Extinction in the Large Magellanic Cloud”. 2007, *ApJ*, 662, 969

Indebetouw, R., Mathis, J. S., Babler, B. L., Meade, M. R., Watson, C., Whitney, B. A., Wolff, M. J., Wolfire, M. G., Cohen, M., Bania, T. M., Benjamin, R. A., Clemens, D. P., Dickey, J. M., Jackson, J. M., Kobulnicky, H. A., Marston, A. P., Mercer, E. P., Stauffer, J. R., Stolovy, S. R., & Churchwell, E., “The Wavelength Dependence of Interstellar Extinction from 1.25 to 8.0  $\mu\text{m}$  Using GLIMPSE Data”. 2005, *ApJ*, 619, 931

Ita, Y., Tanabé, T., Matsunaga, N., Nakajima, Y., Nagashima, C., Nagayama, T., Kato, D., Kurita, M., Nagata, T., Sato, S., Tamura, M., Nakaya, H., & Nakada, Y., “Pulsation at the tip of the first giant branch?”. 2002, *MNRAS*, 337, L31

—, “Variable stars in the Magellanic Clouds: results from OGLE and SIRIUS”. 2004, *MNRAS*, 347, 720

Jang, I. S., & Lee, M. G., “The Tip of the Red Giant Branch Distances to Type Ia Supernova Host Galaxies. V. NGC 3021, NGC 3370, and NGC 1309 and the Value of the Hubble Constant”. 2017a, *ApJ*, 836, 74

—, “The Tip of the Red Giant Branch Distances to Type Ia Supernova Host Galaxies. IV. Color Dependence and Zero-point Calibration”. 2017b, *ApJ*, 835, 28

Jang, I. S., Hatt, D., Beaton, R. L., Lee, M. G., Freedman, W. L., Madore, B. F., Hoyt, T. J., Monson, A. J., Rich, J. A., Scowcroft, V., & Seibert, M., “The Carnegie-Chicago Hubble Program. III. The Distance to NGC 1365 via the Tip of the Red Giant Branch”. 2018, *ApJ*, 852, 60

Jang, I. S., Hoyt, T. J., Beaton, R. L., Freedman, W. L., Madore, B. F., Lee, M. G., Neeley, J. R., Monson, A. J., Rich, J. A., & Seibert, M., “The Carnegie-Chicago Hubble

Program. IX. Calibration of the Tip of the Red Giant Branch Method in the Megamaser Host Galaxy, NGC 4258 (M106)". 2021, *ApJ*, 906, 125

Jekel, C. F., & Venter, G. 2019, "Pwlf: A Python Library for Fitting 1D Continuous Piecewise Linear Functions"

Jimenez, R., Grae Jorgensen, U., & Verde, L., "Giants eating giants: Mass loss and giant planets modifying the luminosity of the Tip of the Giant Branch". 2020, *arXiv e-prints*, arXiv:2003.11499

John, T. L., "Continuous absorption by the negative hydrogen ion reconsidered". 1988, *A&A*, 193, 189

Joshi, Y. C., & Panchal, A., "Reddening map and recent star formation in the Magellanic Clouds based on OGLE IV Cepheids". 2019, *A&A*, 628, A51

Karachentsev, I. D., "The Local Group and Other Neighboring Galaxy Groups". 2005, *AJ*, 129, 178

Karachentsev, I. D., Karachentseva, V. E., Huchtmeier, W. K., & Makarov, D. I., "A Catalog of Neighboring Galaxies". 2004, *AJ*, 127, 2031

Karachentsev, I. D., Grebel, E. K., Sharina, M. E., Dolphin, A. E., Geisler, D., Guhathakurta, P., Hodge, P. W., Karachentseva, V. E., Sarajedini, A., & Seitzer, P., "Distances to nearby galaxies in Sculptor". 2003, *A&A*, 404, 93

Koekemoer, A. M., Faber, S. M., Ferguson, H. C., Grogin, N. A., Kocevski, D. D., Koo, D. C., Lai, K., Lotz, J. M., Lucas, R. A., McGrath, E. J., Ogaz, S., Rajan, A., Riess, A. G., Rodney, S. A., Strolger, L., Casertano, S., Castellano, M., Dahlen, T., Dickinson, M., Dolch, T., Fontana, A., Giavalisco, M., Grazian, A., Guo, Y., Hathi, N. P., Huang, K.-H., van der Wel, A., Yan, H.-J., Acquaviva, V., Alexander, D. M., Almaini, O., Ashby, M. L. N., Barden, M., Bell, E. F., Bournaud, F., Brown, T. M., Caputi, K. I., Cassata, P., Challis, P. J., Chary, R.-R., Cheung, E., Cirasuolo, M., Conselice, C. J., Roshan Cooray, A., Croton, D. J., Daddi, E., Davé, R., de Mello, D. F., de Ravel, L., Dekel, A., Donley, J. L., Dunlop, J. S., Dutton, A. A., Elbaz, D., Fazio, G. G., Filippenko, A. V., Finkelstein, S. L., Frazer, C., Gardner, J. P., Garnavich, P. M., Gawiser, E., Gruetzbauch, R., Hartley, W. G., Häussler, B., Herrington, J., Hopkins, P. F., Huang, J.-S., Jha, S. W., Johnson, A., Kartaltepe, J. S., Khostovan, A. A., Kirshner, R. P., Lani, C., Lee, K.-S., Li, W., Madau, P., McCarthy, P. J., McIntosh, D. H., McLure, R. J., McPartland, C., Mobasher, B., Moreira, H., Mortlock, A., Moustakas, L. A., Mozena, M., Nandra, K., Newman, J. A., Nielsen, J. L., Niemi, S., Noeske, K. G., Papovich, C. J., Pentericci, L., Pope, A., Primack, J. R., Ravindranath, S., Reddy, N. A., Renzini, A., Rix, H.-W., Robaina, A. R., Rosario,

D. J., Rosati, P., Salimbeni, S., Scarlata, C., Siana, B., Simard, L., Smidt, J., Snyder, D., Somerville, R. S., Spinrad, H., Straughn, A. N., Telford, O., Teplitz, H. I., Trump, J. R., Vargas, C., Villforth, C., Wagner, C. R., Wandro, P., Wechsler, R. H., Weiner, B. J., Wiklind, T., Wild, V., Wilson, G., Wuyts, S., & Yun, M. S., “CANDELS: The Cosmic Assembly Near-infrared Deep Extragalactic Legacy Survey—The Hubble Space Telescope Observations, Imaging Data Products, and Mosaics”. 2011, *ApJS*, 197, 36

Koekemoer, A. M., Ellis, R. S., McLure, R. J., Dunlop, J. S., Robertson, B. E., Ono, Y., Schenker, M. A., Ouchi, M., Bowler, R. A. A., Rogers, A. B., Curtis-Lake, E., Schneider, E., Charlot, S., Stark, D. P., Furlanetto, S. R., Cirasuolo, M., Wild, V., & Targett, T., “The 2012 Hubble Ultra Deep Field (UDF12): Observational Overview”. 2013, *ApJS*, 209, 3

Koornneef, J., Bohlin, R., Buser, R., Horne, K., & Turnshek, D., “Synthetic photometry and the calibration of the Hubble Space Telescope”. 1986, *Highlights of Astronomy*, 7, 833

Kunder, A., Valenti, E., Dall’Ora, M., Pietrukowicz, P., Sneden, C., Bono, G., Braga, V. F., Ferraro, I., Fiorentino, G., Iannicola, G., Marconi, M., Martínez-Vázquez, C. E., Monelli, M., Musella, I., Ripepi, V., Salaris, M., & Stetson, P. B., “Impact of Distance Determinations on Galactic Structure. II. Old Tracers”. 2018, *SSRv*, 214, 90

Kurucz, R. L. 2014, *Model Atmosphere Codes: ATLAS12 and ATLAS9* (Springer International Publishing), 39–51

Lallement, R., Babusiaux, C., Vergely, J. L., Katz, D., Arenou, F., Valette, B., Hottier, C., & Capitanio, L., “Gaia-2MASS 3D maps of Galactic interstellar dust within 3 kpc”. 2019, *A&A*, 625, A135

Lallement, R., Vergely, J. L., Babusiaux, C., & Cox, N. L. J., “Updated Gaia-2MASS 3D maps of Galactic interstellar dust”. 2022, *A&A*, 661, A147

Lallement, R., Capitanio, L., Ruiz-Dern, L., Danielski, C., Babusiaux, C., Vergely, L., Elyajouri, M., Arenou, F., & Leclerc, N., “Three-dimensional maps of interstellar dust in the Local Arm: using Gaia, 2MASS, and APOGEE-DR14”. 2018, *A&A*, 616, A132

Lançon, A., Gonneau, A., Trager, S. C., Prugniel, P., Arentsen, A., Chen, Y. P., Dries, M., Loup, C., Lyubenova, M., Peletier, R., Telliez, L., & Vazdekis, A., “Oxygen-rich Long Period Variables in the X-shooter Spectral Library”. 2018, *arXiv e-prints*, arXiv:1811.02841

Lançon, A., Gonneau, A., Verro, K., Prugniel, P., Arentsen, A., Trager, S. C., Peletier, R., Chen, Y. P., Coelho, P., Falcón-Barroso, J., Hauschildt, P., Husser, T. O., Jain, R., Lyubenova, M., Martins, L., Sánchez Blázquez, P., & Vazdekis, A., “A comparison between X-shooter spectra and PHOENIX models across the HR-diagram”. 2021, *A&A*, 649, A97

Le Borgne, J. F., Bruzual, G., Pelló, R., Lançon, A., Rocca-Volmerange, B., Sanahuja, B., Schaerer, D., Soubiran, C., & Vílchez-Gómez, R., “STELIB: A library of stellar spectra at  $R \sim 2000$ ”. 2003, *A&A*, 402, 433

Leavitt, H. S., & Pickering, E. C., “Periods of 25 Variable Stars in the Small Magellanic Cloud.”. 1912, *Harvard College Observatory Circular*, 173, 1

Lebzelter, T., & Wood, P. R., “Long period variables in 47 Tuc: direct evidence for lost mass”. 2005, *A&A*, 441, 1117

Lee, M. G., Freedman, W. L., & Madore, B. F., “The Tip of the Red Giant Branch as a Distance Indicator for Resolved Galaxies”. 1993, *ApJ*, 417, 553

Lemaître, G., “Un Univers homogène de masse constante et de rayon croissant rendant compte de la vitesse radiale des nébuleuses extra-galactiques”. 1927, *Annales de la Société Scientifique de Bruxelles*, 47, 49

Levesque, E. M., Massey, P., Olsen, K. A. G., Plez, B., Meynet, G., & Maeder, A., “The Effective Temperatures and Physical Properties of Magellanic Cloud Red Supergiants: The Effects of Metallicity”. 2006, *ApJ*, 645, 1102

Li, S., Casertano, S., & Riess, A. G., “A Maximum Likelihood Calibration of the Tip of the Red Giant Branch Luminosity from High Latitude Field Giants Using Gaia Early Data Release 3 Parallaxes”. 2022, *ApJ*, 939, 96

Lopes, J., & Lopes, I., “Dark matter capture and annihilation in stars: Impact on the red giant branch tip”. 2021, *A&A*, 651, A101

Lucas, R. A. 2015, “Basic Use of SExtractor Catalogs With TweakReg - II”, Tech. rep., Space Telescope Science Institute

Lyubenova, M., Kuntschner, H., Rejkuba, M., Silva, D. R., Kissler-Patig, M., & Tacconi-Garman, L. E., “Integrated J- and H-band spectra of globular clusters in the LMC: implications for stellar population models and galaxy age dating”. 2012, *A&A*, 543, A75

Mack, J. 2018, “New Calibration in Cycles 23-26 & Detector Monitoring Results over the WFC3 Lifetime”, Tech. rep., Space Telescope Science Institute

Madore, B. F., Mager, V., & Freedman, W. L., “Sharpening the Tip of the Red Giant Branch”. 2009, *ApJ*, 690, 389

- Madore, B. F., Freedman, W. L., Hatt, D., Hoyt, T. J., Monson, A. J., Beaton, R. L., Rich, J. A., Jang, I. S., Lee, M. G., Scowcroft, V., & Seibert, M., “The Near-infrared Tip of the Red Giant Branch. I. A Calibration in the Isolated Dwarf Galaxy IC 1613”. 2018, *ApJ*, 858, 11
- Maíz Apellániz, J., Barbá, R. H., Fernández Aranda, R., Pantaleoni González, M., Crespo Bellido, P., Sota, A., & Alfaro, E. J., “The Villafranca catalog of Galactic OB groups. II. From Gaia DR2 to EDR3 and ten new systems with O stars”. 2022, *A&A*, 657, A131
- Maíz Apellániz, J., & Pantaleoni González, M., “A reevaluation of the 2MASS zero points using CALSPEC spectrophotometry complemented with Gaia Data Release 2 parallaxes”. 2018, *A&A*, 616, L7
- Maíz Apellániz, J., & Weiler, M., “Reanalysis of the Gaia Data Release 2 photometric sensitivity curves using HST/STIS spectrophotometry”. 2018, *A&A*, 619, A180
- Maraston, C., “Evolutionary population synthesis: models, analysis of the ingredients and application to high- $z$  galaxies”. 2005, *MNRAS*, 362, 799
- Marigo, P., Girardi, L., Bressan, A., Rosenfield, P., Aringer, B., Chen, Y., Dussin, M., Nanni, A., Pastorelli, G., Rodrigues, T. S., Trabucchi, M., Bladh, S., Dalcanton, J., Groenewegen, M. A. T., Montalbán, J., & Wood, P. R., “A New Generation of PARSEC-COLIBRI Stellar Isochrones Including the TP-AGB Phase”. 2017, *ApJ*, 835, 77
- Martins, F., “Synthetic photometry of globular clusters: Uncertainties on synthetic colors”. 2018, *A&A*, 616, A164
- McDonald, I., & van Loon, J. T., “Dust, pulsation, chromospheres and their rôle in driving mass loss from red giants in Galactic globular clusters”. 2007, *A&A*, 476, 1261
- McQuinn, K. B. W., Boyer, M., Skillman, E. D., & Dolphin, A. E., “Using the Tip of the Red Giant Branch As a Distance Indicator in the Near Infrared”. 2019, *ApJ*, 880, 63
- National Optical Astronomy Observatories. 1999, “IRAF: Image Reduction and Analysis Facility”, ascl:9911.002
- Nidever, D. L., Hasselquist, S., Hayes, C. R., Hawkins, K., Povick, J., Majewski, S. R., Smith, V. V., Anguiano, B., Stringfellow, G. S., Sobeck, J. S., Cunha, K., Beers, T. C., Bestenlehner, J. M., Cohen, R. E., Garcia-Hernandez, D. A., Jönsson, H., Nitschelm, C., Shetrone, M., Lacerna, I., Allende Prieto, C., Beaton, R. L., Dell’Agli, F., Fernández-Trincado, J. G., Feuillet, D., Gallart, C., Hearty, F. R., Holtzman, J., Machado, A., Muñoz, R. R., O’Connell, R., & Rosado, M., “The Lazy Giants: APOGEE Abundances Reveal Low Star Formation Efficiencies in the Magellanic Clouds”. 2020, *ApJ*, 895, 88



Nidever, D. L., Gilbert, K., Tollerud, E., Siders, C., Escala, I., Allende Prieto, C., Smith, V., Cunha, K., Debattista, V. P., Ting, Y.-S., & Kirby, E. N., “The Prevalence of the  $\alpha$ -bimodality: First JWST  $\alpha$ -abundance Results in M31”. 2023, *arXiv e-prints*, arXiv:2306.04688

Odland, T. 2018, “Tommyod/KDEpy: Kernel Density Estimation in Python”, Zenodo, doi:10.5281/ZENODO.2392268

Origlia, L., Rood, R. T., Fabbri, S., Ferraro, F. R., Fusi Pecci, F., & Rich, R. M., “The First Empirical Mass-Loss Law for Population II Giants”. 2007, *ApJL*, 667, L85

Parzen, E., “On Estimation of a Probability Density Function and Mode”. 1962, *The Annals of Mathematical Statistics*, 33, 1065

Pasquato, M., de Luca, A., Raimondo, G., Carini, R., Moraghan, A., Chung, C., Brocato, E., & Lee, Y.-W., “Stellar Encounter Driven Red-giant Star Mass Loss in Globular Clusters”. 2014, *ApJ*, 789, 28

Perivolaropoulos, L., & Skara, F., “Challenges for  $\Lambda$ CDM: An update”. 2022, *NewAR*, 95, 101659

Persson, S. E., Murphy, D. C., Smee, S., Birk, C., Monson, A. J., Uomoto, A., Koch, E., Sackett, S., Barkhouser, R., Orndorff, J., Hammond, R., Harding, A., Scharfstein, G., Kelson, D., Marshall, J., & McCarthy, P. J., “FourStar: The Near-Infrared Imager for the 6.5 m Baade Telescope at Las Campanas Observatory”. 2013, *PASP*, 125, 654

Pietrinferni, A., Cassisi, S., Salaris, M., & Hidalgo, S., “The BaSTI Stellar Evolution Database: models for extremely metal-poor and super-metal-rich stellar populations”. 2013, *A&A*, 558, A46

Pietrinferni, A., Hidalgo, S., Cassisi, S., Salaris, M., Savino, A., Mucciarelli, A., Verma, K., Silva Aguirre, V., Aparicio, A., & Ferguson, J. W., “Updated BaSTI Stellar Evolution Models and Isochrones. II.  $\alpha$ -enhanced Calculations”. 2021, *ApJ*, 908, 102

Pietrzyński, G., Graczyk, D., Gieren, W., Thompson, I. B., Pilecki, B., Udalski, A., Soszyński, I., Kozłowski, S., Konorski, P., Suchomska, K., Bono, G., Moroni, P. G. P., Villanova, S., Nardetto, N., Bresolin, F., Kudritzki, R. P., Storm, J., Gallenne, A., Smolec, R., Minniti, D., Kubiak, M., Szymański, M. K., Poleski, R., Wyrzykowski, Ł., Ulaczyk, K., Pietrukowicz, P., Górski, M., & Karczmarek, P., “An eclipsing-binary distance to the Large Magellanic Cloud accurate to two per cent”. 2013, *Nature*, 495, 76

Pietrzyński, G., Graczyk, D., Gallenne, A., Gieren, W., Thompson, I. B., Pilecki, B., Karczmarek, P., Górski, M., Suchomska, K., Taormina, M., Zgirski, B., Wielgórski, P., Kołaczkowski, Z., Konorski, P., Villanova, S., Nardetto, N., Kervella, P., Bresolin, F., Kudritzki, R. P., Storm, J., Smolec, R., & Narloch, W., “A distance to the Large Magellanic Cloud that is precise to one per cent”. 2019, *Nature*, 567, 200

Planck Collaboration, Aghanim, N., Akrami, Y., Ashdown, M., Aumont, J., Baccigalupi, C., Ballardini, M., Banday, A. J., Barreiro, R. B., Bartolo, N., Basak, S., Battye, R., Benabed, K., Bernard, J. P., Bersanelli, M., Bielewicz, P., Bock, J. J., Bond, J. R., Borrill, J., Bouchet, F. R., Boulanger, F., Bucher, M., Burigana, C., Butler, R. C., Calabrese, E., Cardoso, J. F., Carron, J., Challinor, A., Chiang, H. C., Chluba, J., Colombo, L. P. L., Combet, C., Contreras, D., Crill, B. P., Cuttaia, F., de Bernardis, P., de Zotti, G., Delabrouille, J., Delouis, J. M., Di Valentino, E., Diego, J. M., Doré, O., Douspis, M., Ducout, A., Dupac, X., Dusini, S., Efstathiou, G., Elsner, F., Enßlin, T. A., Eriksen, H. K., Fantaye, Y., Farhang, M., Fergusson, J., Fernandez-Cobos, R., Finelli, F., Forastieri, F., Frailis, M., Fraisse, A. A., Franceschi, E., Frolov, A., Galeotta, S., Galli, S., Ganga, K., Génova-Santos, R. T., Gerbino, M., Ghosh, T., González-Nuevo, J., Górski, K. M., Gratton, S., Gruppuso, A., Gudmundsson, J. E., Hamann, J., Handley, W., Hansen, F. K., Herranz, D., Hildebrandt, S. R., Hivon, E., Huang, Z., Jaffe, A. H., Jones, W. C., Karacki, A., Keihänen, E., Keskitalo, R., Kiiveri, K., Kim, J., Kisner, T. S., Knox, L., Krachmalnicoff, N., Kunz, M., Kurki-Suonio, H., Lagache, G., Lamarre, J. M., Lasenby, A., Lattanzi, M., Lawrence, C. R., Le Jeune, M., Lemos, P., Lesgourgues, J., Levrier, F., Lewis, A., Liguori, M., Lilje, P. B., Lilley, M., Lindholm, V., López-Caniego, M., Lubin, P. M., Ma, Y. Z., Macías-Pérez, J. F., Maggio, G., Maino, D., Mandolesi, N., Mangilli, A., Marcos-Caballero, A., Maris, M., Martin, P. G., Martinelli, M., Martínez-González, E., Matarrese, S., Mauri, N., McEwen, J. D., Meinhold, P. R., Melchiorri, A., Mennella, A., Migliaccio, M., Millea, M., Mitra, S., Miville-Deschênes, M. A., Molinari, D., Montier, L., Morgante, G., Moss, A., Natoli, P., Nørgaard-Nielsen, H. U., Pagano, L., Paoletti, D., Partridge, B., Patanchon, G., Peiris, H. V., Perrotta, F., Pettorino, V., Piacentini, F., Polastri, L., Polenta, G., Puget, J. L., Rachen, J. P., Reinecke, M., Remazeilles, M., Renzi, A., Rocha, G., Rosset, C., Roudier, G., Rubiño-Martín, J. A., Ruiz-Granados, B., Salvati, L., Sandri, M., Savelainen, M., Scott, D., Shellard, E. P. S., Sirignano, C., Sirri, G., Spencer, L. D., Sunyaev, R., Suur-Uski, A. S., Tauber, J. A., Tavagnacco, D., Tenti, M., Toffolatti, L., Tomasi, M., Trombetti, T., Valenziano, L., Valiviita, J., Van Tent, B., Vibert, L., Vielva, P., Villa, F., Vittorio, N., Wandelt, B. D., Wehus, I. K., White, M., White, S. D. M., Zaccchi, A., & Zonca, A., “Planck 2018 results. VI. Cosmological parameters”. 2020, *A&A*, 641, A6

Prugniel, P., & Soubiran, C., “A database of high and medium-resolution stellar spectra”. 2001, *A&A*, 369, 1048

—, “New release of the ELODIE library”. 2004, *arXiv e-prints*, astro

Prugniel, P., Soubiran, C., Koleva, M., & Le Borgne, D., “New release of the ELODIE library: Version 3.1”. 2007, *arXiv e-prints*, astro

Rayner, J. T., Cushing, M. C., & Vacca, W. D., “The Infrared Telescope Facility (IRTF) Spectral Library: Cool Stars”. 2009, *ApJS*, 185, 289

Rayner, J. T., Toomey, D. W., Onaka, P. M., Denault, A. J., Stahlberger, W. E., Vacca, W. D., Cushing, M. C., & Wang, S., “SpeX: A Medium-Resolution 0.8-5.5 Micron Spectrograph and Imager for the NASA Infrared Telescope Facility”. 2003, *PASP*, 115, 362

Reid, M. J., Pesce, D. W., & Riess, A. G., “An Improved Distance to NGC 4258 and Its Implications for the Hubble Constant”. 2019, *ApJL*, 886, L27

Rich, J. A., Madore, B. F., Monson, A. J., Freedman, W. L., Beaton, R. L., Clementini, G., Garofalo, A., Hatt, D., Hoyt, T., Jang, I.-S., Kollmeier, J. A., Lee, M. G., Neeley, J. R., Scowcroft, V., & Seibert, M., “The Carnegie-Chicago Hubble Program: Calibration of the Near-infrared RR Lyrae Period-Luminosity Relation with HST”. 2018, *ApJ*, 869, 82

Riess, A. G. 2011, “An Independent Determination of WFC3-IR Zeropoints and Count Rate Non-Linearity from 2MASS Asterisms”, Space Telescope WFC Instrument Science Report

Riess, A. G., Casertano, S., Yuan, W., Macri, L. M., & Scolnic, D., “Large Magellanic Cloud Cepheid Standards Provide a 1% Foundation for the Determination of the Hubble Constant and Stronger Evidence for Physics beyond  $\Lambda$ CDM”. 2019, *ApJ*, 876, 85

Riess, A. G., Macri, L., Casertano, S., Sosey, M., Lampeitl, H., Ferguson, H. C., Filippenko, A. V., Jha, S. W., Li, W., Chornock, R., & Sarkar, D., “A Redetermination of the Hubble Constant with the Hubble Space Telescope from a Differential Distance Ladder”. 2009, *ApJ*, 699, 539

Riess, A. G., Macri, L. M., Hoffmann, S. L., Scolnic, D., Casertano, S., Filippenko, A. V., Tucker, B. E., Reid, M. J., Jones, D. O., Silverman, J. M., Chornock, R., Challis, P., Yuan, W., Brown, P. J., & Foley, R. J., “A 2.4% Determination of the Local Value of the Hubble Constant”. 2016, *ApJ*, 826, 56

Riess, A. G., Yuan, W., Macri, L. M., Scolnic, D., Brout, D., Casertano, S., Jones, D. O., Murakami, Y., Anand, G. S., Breuval, L., Brink, T. G., Filippenko, A. V., Hoffmann, S., Jha, S. W., D’arcy Kenworthy, W., Mackenty, J., Stahl, B. E., & Zheng, W., “A Comprehensive Measurement of the Local Value of the Hubble Constant with 1 km s<sup>-1</sup> Mpc<sup>-1</sup> Uncertainty from the Hubble Space Telescope and the SH0ES Team”. 2022, *ApJL*, 934, L7

Ripepi, V., Cioni, M.-R. L., Moretti, M. I., Marconi, M., Bekki, K., Clementini, G., de Grijs, R., Emerson, J., Groenewegen, M. A. T., Ivanov, V. D., Molinaro, R., Muraveva, T., Oliveira, J. M., Piatti, A. E., Subramanian, S., & van Loon, J. T., “The VMC survey - XXV. The 3D structure of the Small Magellanic Cloud from Classical Cepheids”. 2017, *MNRAS*, 472, 808

Ripepi, V., Chemin, L., Molinaro, R., Cioni, M.-R. L., Bekki, K., Clementini, G., de Grijs, R., De Somma, G., El Yousoufi, D., Girardi, L., Groenewegen, M. A. T., Ivanov, V., Marconi, M., McMillan, P. J., & van Loon, J. T., “The VMC survey - XLVIII. Classical cepheids unveil the 3D geometry of the LMC”. 2022, *MNRAS*, 512, 563

Roman-Duval, J., Proffitt, C. R., Taylor, J. M., Monroe, T. R., Fischer, T. C., Fischer, W. J., Fullerton, A. W., Aloisi, A., Britt, C. T., Busko, I., Carlberg, J. K., De Rosa, G., Jędrzejewski, R. I., Lockwood, S., Frazer, E. M., Hernandez, S., James, B. L., Oliveira, C., Plesha, R. J., Riedel, A. R., Riley, A., Sahnou, D. J., Sankrit, R., Shaw, R. A., Smith, L. J., Sohn, S. T., Som, D., Ubeda, L., & Welty, D. E., “Ultraviolet Legacy Library of Young Stars as Essential Standards (ULLYSES): Data Release I”. 2020, *Research Notes of the American Astronomical Society*, 4, 205

Rosenblatt, M., “Remarks on Some Nonparametric Estimates of a Density Function”. 1956, *The Annals of Mathematical Statistics*, 27, 832

Sahai, R., Morris, M., Sánchez Contreras, C., & Claussen, M., “Preplanetary Nebulae: A Hubble Space Telescope Imaging Survey and a New Morphological Classification System”. 2007, *AJ*, 134, 2200

Salaris, M., & Cassisi, S., “The ‘tip’ of the red giant branch as a distance indicator: results from evolutionary models”. 1997, *MNRAS*, 289, 406

—. 2005, *Evolution of Stars and Stellar Populations* (Wiley)

—. 2006, *Evolution of Stars and Stellar Populations*, 1st edn. (Wiley)

Salaris, M., Cassisi, S., & Weiss, A., “Red Giant Branch Stars: The Theoretical Framework”. 2002, *PASP*, 114, 375

Saltas, I. D., & Tognelli, E., “New calibrated models for the tip of the red giant branch luminosity and a thorough analysis of theoretical uncertainties”. 2022, *MNRAS*, 514, 3058

Sánchez-Blázquez, P., Peletier, R. F., Jiménez-Vicente, J., Cardiel, N., Cenarro, A. J., Falcón-Barroso, J., Gorgas, J., Selam, S., & Vazdekis, A., “Medium-resolution Isaac Newton Telescope library of empirical spectra”. 2006, *MNRAS*, 371, 703

Sanders, J. L., “The period-luminosity relation for Mira variables in the Milky Way using Gaia DR3: a further distance anchor for  $H_0$ ”. 2023, *MNRAS*, 523, 2369

Savitzky, A., & Golay, M. J. E., “Smoothing and Differentiation of Data by Simplified Least Squares Procedures.”. 1964, *Analytical Chemistry*, 36, 1627

Schlafly, E. F., & Finkbeiner, D. P., “Measuring Reddening with Sloan Digital Sky Survey Stellar Spectra and Recalibrating SFD”. 2011, *ApJ*, 737, 103

Schmidt, S. J., West, A. A., Hawley, S. L., & Pineda, J. S., “Colors and Kinematics of L Dwarfs from the Sloan Digital Sky Survey”. 2010, *AJ*, 139, 1808

Scolnic, D., Brout, D., Carr, A., Riess, A. G., Davis, T. M., Dwomoh, A., Jones, D. O., Ali, N., Charvu, P., Chen, R., Peterson, E. R., Popovic, B., Rose, B. M., Wood, C. M., Brown, P. J., Chambers, K., Coulter, D. A., Dettman, K. G., Dimitriadis, G., Filippenko, A. V., Foley, R. J., Jha, S. W., Kilpatrick, C. D., Kirshner, R. P., Pan, Y.-C., Rest, A., Rojas-Bravo, C., Siebert, M. R., Stahl, B. E., & Zheng, W., “The Pantheon+ Analysis: The Full Data Set and Light-curve Release”. 2022, *ApJ*, 938, 113

Scolnic, D. M., Jones, D. O., Rest, A., Pan, Y. C., Chornock, R., Foley, R. J., Huber, M. E., Kessler, R., Narayan, G., Riess, A. G., Rodney, S., Berger, E., Brout, D. J., Challis, P. J., Drout, M., Finkbeiner, D., Lunnan, R., Kirshner, R. P., Sanders, N. E., Schlafly, E., Smartt, S., Stubbs, C. W., Tonry, J., Wood-Vasey, W. M., Foley, M., Hand, J., Johnson, E., Burgett, W. S., Chambers, K. C., Draper, P. W., Hodapp, K. W., Kaiser, N., Kudritzki, R. P., Magnier, E. A., Metcalfe, N., Bresolin, F., Gall, E., Kotak, R., McCrum, M., & Smith, K. W., “The Complete Light-curve Sample of Spectroscopically Confirmed SNe Ia from Pan-STARRS1 and Cosmological Constraints from the Combined Pantheon Sample”. 2018, *ApJ*, 859, 101

Sculley, D. 2010, in Proceedings of the 19th International Conference on World Wide Web - WWW '10 (Raleigh, North Carolina, USA: ACM Press), 1177

Serenelli, A., Weiss, A., Cassisi, S., Salaris, M., & Pietrinferni, A., “The brightness of the red giant branch tip. Theoretical framework, a set of reference models, and predicted observables”. 2017, *A&A*, 606, A33

Singh, S., Yu, B., & Seljak, U., “Fundamental Plane of BOSS galaxies: correlations with galaxy properties, density field, and impact on RSD measurements”. 2021, *MNRAS*, 501, 4167

Skowron, D. M., Skowron, J., Udalski, A., Szymański, M. K., Soszyński, I., Wyrzykowski, Ł., Ulaczyk, K., Poleski, R., Kozłowski, S., Pietrukowicz, P., Mróz, P., Rybicki, K., Iwanek,

P., Wrona, M., & Gromadzki, M., “OGLE-ing the Magellanic System: Optical Reddening Maps of the Large and Small Magellanic Clouds from Red Clump Stars”. 2021, *ApJS*, 252, 23

Skrutskie, M. F., Cutri, R. M., Stiening, R., Weinberg, M. D., Schneider, S., Carpenter, J. M., Beichman, C., Capps, R., Chester, T., Elias, J., Huchra, J., Liebert, J., Lonsdale, C., Monet, D. G., Price, S., Seitzer, P., Jarrett, T., Kirkpatrick, J. D., Gizis, J. E., Howard, E., Evans, T., Fowler, J., Fullmer, L., Hurt, R., Light, R., Kopan, E. L., Marsh, K. A., McCallon, H. L., Tam, R., Van Dyk, S., & Wheelock, S., “The Two Micron All Sky Survey (2MASS)”. 2006, *AJ*, 131, 1163

Sobel, I., & Feldman, G. 1968, “An Isotropic 3x3 Image Gradient Operator”, Presentation at Stanford A.I. Project

Som, D., Bajaj, V., Mack, J., & Calamida, A. 2021, “Photometric Repeatability and Sensitivity Evolution of WFC3/IR”, Space Telescope WFC Instrument Science Report

Soszyński, I., Udalski, A., Szymański, M. K., Kubiak, M., Pietrzyński, G., Wyrzykowski, Ł., Szewczyk, O., Ulaczyk, K., & Poleski, R., “The Optical Gravitational Lensing Experiment. The OGLE-III Catalog of Variable Stars. IV. Long-Period Variables in the Large Magellanic Cloud”. 2009, *AcA*, 59, 239

Soszyński, I., Udalski, A., Szymański, M. K., Kubiak, M., Pietrzyński, G., Wyrzykowski, Ł., Ulaczyk, K., Poleski, R., Kozłowski, S., & Pietrukowicz, P., “The Optical Gravitational Lensing Experiment. The OGLE-III Catalog of Variable Stars. XIII. Long-Period Variables in the Small Magellanic Cloud”. 2011, *AcA*, 61, 217

Stetson, P. B., “DAOPHOT: A Computer Program for Crowded-Field Stellar Photometry”. 1987, *PASP*, 99, 191

—. 2011, “DAOPHOT: Crowded-field Stellar Photometry Package”, ascl:1104.011

Straatman, C. M. S., Spitler, L. R., Quadri, R. F., Labbé, I., Glazebrook, K., Persson, S. E., Papovich, C., Tran, K.-V. H., Brammer, G. B., Cowley, M., Tomczak, A., Nanayakkara, T., Alcorn, L., Allen, R., Broussard, A., van Dokkum, P., Forrest, B., van Houdt, J., Kacprzak, G. G., Kawinwanichakij, L., Kelson, D. D., Lee, J., McCarthy, P. J., Mehrrens, N., Monson, A., Murphy, D., Rees, G., Tilvi, V., & Whitaker, K. E., “The FourStar Galaxy Evolution Survey (ZFOURGE): Ultraviolet to Far-infrared Catalogs, Medium-bandwidth Photometric Redshifts with Improved Accuracy, Stellar Masses, and Confirmation of Quiescent Galaxies to  $z \sim 3.5$ ”. 2016, *ApJ*, 830, 51

Straizys, V., “Synthetic Photometry Experiments in the Vicinity of the Paschen Jump”. 1998, *Baltic Astronomy*, 7, 571

Straniero, O., Pallanca, C., Dalessandro, E., Domínguez, I., Ferraro, F. R., Giannotti, M., Mirizzi, A., & Piersanti, L., “The RGB tip of galactic globular clusters and the revision of the axion-electron coupling bound”. 2020, *A&A*, 644, A166

Strömgren, B. 1937, *Aufgaben und Probleme der Astrophotometrie*, Vol. 26 (Akademische verlagsgesellschaft M.B.H., Leipzig), 319

STSCI Development Team. 2012, “DrizzlePac: HST Image Software”, ascl:1212.011

STScI Development Team. 2020, “stsynphot: synphot for HST and JWST”, ascl:2010.003

Swam, M. S., Lubow, S., & Hurt, L. 2004, in *Astronomical Society of the Pacific Conference Series*, Vol. 314, *Astronomical Data Analysis Software and Systems (ADASS) XIII*, ed. F. Ochsenbein, M. G. Allen, & D. Egret, 824

Sweigart, A. V., & Gross, P. G., “Evolutionary sequences for red giant stars.”. 1978, *ApJS*, 36, 405

Taylor, B. J., “Transformation Equations and Other Aids for VRI Photometry”. 1986, *ApJS*, 60, 577

Tej, A., Lançon, A., Scholz, M., & Wood, P. R., “Optical and near-IR spectra of O-rich Mira variables: A comparison between models and observations”. 2003, *A&A*, 412, 481

Thomas, H. C., “Sternentwicklung VIII. Der Helium-Flash bei einem Stern von 1. 3 Sonnenmassen”. 1967, *ZA*, 67, 420

Tody, D. 1986, in *Society of Photo-Optical Instrumentation Engineers (SPIE) Conference Series*, Vol. 627, *Instrumentation in astronomy VI*, ed. D. L. Crawford, 733

Tody, D. 1993, in *Astronomical Society of the Pacific Conference Series*, Vol. 52, *Astronomical Data Analysis Software and Systems II*, ed. R. J. Hanisch, R. J. V. Brissenden, & J. Barnes, 173

Tonry, J. L., Stubbs, C. W., Lykke, K. R., Doherty, P., Shivvers, I. S., Burgett, W. S., Chambers, K. C., Hodapp, K. W., Kaiser, N., Kudritzki, R. P., Magnier, E. A., Morgan, J. S., Price, P. A., & Wainscoat, R. J., “The Pan-STARRS1 Photometric System”. 2012, *ApJ*, 750, 99

Torres, G., Andersen, J., & Giménez, A., “Accurate masses and radii of normal stars: modern results and applications”. 2010, *A&A Rev*, 18, 67

Trager, S. C. 2012, in Astronomical Society of India Conference Series, Vol. 6, Astronomical Society of India Conference Series, ed. P. Prugniel & H. P. Singh, 1

Trujillo, I., Beasley, M. A., Borlaff, A., Carrasco, E. R., Di Cintio, A., Filho, M., Monelli, M., Montes, M., Román, J., Ruiz-Lara, T., Sánchez Almeida, J., Valls-Gabaud, D., & Vazdekis, A., “A distance of 13 Mpc resolves the claimed anomalies of the galaxy lacking dark matter”. 2019, *MNRAS*, 486, 1192

Tully, R. B., Courtois, H. M., & Sorce, J. G., “Cosmicflows-3”. 2016, *AJ*, 152, 50

Tully, R. B., Rizzi, L., Dolphin, A. E., Karachentsev, I. D., Karachentseva, V. E., Makarov, D. I., Makarova, L., Sakai, S., & Shaya, E. J., “Associations of Dwarf Galaxies”. 2006, *AJ*, 132, 729

Tully, R. B., Courtois, H. M., Dolphin, A. E., Fisher, J. R., Héraudeau, P., Jacobs, B. A., Karachentsev, I. D., Makarov, D., Makarova, L., Mitronova, S., Rizzi, L., Shaya, E. J., Sorce, J. G., & Wu, P.-F., “Cosmicflows-2: The Data”. 2013, *AJ*, 146, 86

Turnshek, D. A., Bohlin, R. C., Williamson, R. L., I., Lupie, O. L., Koornneef, J., & Morgan, D. H., “An Atlas of Hubble Space Telescope Photometric, Spectrophotometric, and Polarimetric Calibration Objects”. 1990, *AJ*, 99, 1243

Vacca, W. D., Cushing, M. C., & Rayner, J. T., “A Method of Correcting Near-Infrared Spectra for Telluric Absorption”. 2003, *PASP*, 115, 389

—, “Nonlinearity Corrections and Statistical Uncertainties Associated with Near-Infrared Arrays”. 2004, *PASP*, 116, 352

Valdes, F., Gupta, R., Rose, J. A., Singh, H. P., & Bell, D. J., “The Indo-US Library of Coudé Feed Stellar Spectra”. 2004, *ApJS*, 152, 251

van Leeuwen, F., “Validation of the new Hipparcos reduction”. 2007, *A&A*, 474, 653

VandenBerg, D. A., Swenson, F. J., Rogers, F. J., Iglesias, C. A., & Alexander, D. R., “Models for Old, Metal-poor Stars with Enhanced  $\alpha$ -Element Abundances. I. Evolutionary Tracks and ZAHB Loci; Observational Constraints”. 2000, *ApJ*, 532, 430

Vergely, J. L., Lallement, R., & Cox, N. L. J., “Three-dimensional extinction maps: Inverting inter-calibrated extinction catalogues”. 2022a, *A&A*, 664, A174



—, “Three-dimensional extinction maps: Inverting inter-calibrated extinction catalogues”. 2022b, *A&A*, 664, A174

Verro, K., Trager, S. C., Peletier, R. F., Lançon, A., Arentsen, A., Chen, Y. P., Coelho, P. R. T., Dries, M., Falcón-Barroso, J., Gonneau, A., Lyubenova, M., Martins, L., Prugniel, P., Sánchez-Blázquez, P., & Vazdekis, A., “Modelling simple stellar populations in the near-ultraviolet to near-infrared with the X-shooter Spectral Library (XSL)”. 2022a, *A&A*, 661, A50

Verro, K., Trager, S. C., Peletier, R. F., Lançon, A., Gonneau, A., Vazdekis, A., Prugniel, P., Chen, Y. P., Coelho, P. R. T., Sánchez-Blázquez, P., Martins, L., Arentsen, A., Lyubenova, M., Falcón-Barroso, J., & Dries, M., “The X-shooter Spectral Library (XSL): Data Release 3”. 2022b, *A&A*, 660, A34

—, “The X-shooter Spectral Library (XSL): Data Release 3”. 2022c, *A&A*, 660, A34

Vilardell, F., Ribas, I., Jordi, C., Fitzpatrick, E. L., & Guinan, E. F., “The distance to the Andromeda galaxy from eclipsing binaries”. 2010, *A&A*, 509, A70

Villaume, A., Conroy, C., Johnson, B., Rayner, J., Mann, A. W., & van Dokkum, P., “The Extended IRTF Spectral Library: Expanded Coverage in Metallicity, Temperature, and Surface Gravity”. 2017, *ApJS*, 230, 23

Wang, C., Liu, X. W., Huang, Y., Xiang, M. S., Ren, J. J., Yuan, H. B., Chen, B. Q., Tian, Z. J., Bai, J. M., Sun, N. C., Zuo, F., Zhang, H. W., Zhang, Y. W., Fan, Z., Luo, A. L., Shi, J. R., Li, J., & Shao, Y. L., “LEMONY - a library of empirical medium-resolution spectra by observations with the NAOC Xinglong 2.16-m and YNAO Gaomeigu 2.4-m telescopes”. 2018, *MNRAS*, 480, 4766

Williams, B. F., Olsen, K., Khan, R., Pirone, D., & Rosema, K., “Reducing and Analyzing the PHAT Survey with the Cloud”. 2018, *ApJS*, 236, 4

Williams, B. F., Lang, D., Dalcanton, J. J., Dolphin, A. E., Weisz, D. R., Bell, E. F., Bianchi, L., Byler, N., Gilbert, K. M., Girardi, L., Gordon, K., Gregersen, D., Johnson, L. C., Kalirai, J., Lauer, T. R., Monachesi, A., Rosenfield, P., Seth, A., & Skillman, E., “The Panchromatic Hubble Andromeda Treasury. X. Ultraviolet to Infrared Photometry of 117 Million Equidistant Stars”. 2014, *ApJS*, 215, 9

Wood, P. R., “The pulsation modes, masses and evolution of luminous red giants”. 2015, *MNRAS*, 448, 3829

Wu, P.-F., Tully, R. B., Rizzi, L., Dolphin, A. E., Jacobs, B. A., & Karachentsev, I. D., “Infrared Tip of the Red Giant Branch and Distances to the Maffei/IC 342 Group”. 2014, *AJ*, 148, 7

Yan, R., Chen, Y., Lazarz, D., Bizyaev, D., Maraston, C., Stringfellow, G. S., McCarthy, K., Meneses-Goytia, S., Law, D. R., Thomas, D., Falcon Barroso, J., Sánchez-Gallego, J. R., Schlafly, E., Zheng, Z., Argudo-Fernández, M., Beaton, R. L., Beers, T. C., Bershad, M., Blanton, M. R., Brownstein, J., Bundy, K., Chambers, K. C., Cherinka, B., De Lee, N., Drory, N., Galbany, L., Holtzman, J., Imig, J., Kaiser, N., Kinemuchi, K., Liu, C., Luo, A. L., Magnier, E., Majewski, S., Nair, P., Oravetz, A., Oravetz, D., Pan, K., Sobeck, J., Stassun, K., Talbot, M., Tremonti, C., Waters, C., Weijmans, A.-M., Wilhelm, R., Zasowski, G., Zhao, G., & Zhao, Y.-H., “SDSS-IV MaStar: A Large and Comprehensive Empirical Stellar Spectral Library—First Release”. 2019, *ApJ*, 883, 175

Yuan, H. B., Liu, X. W., & Xiang, M. S., “Empirical extinction coefficients for the GALEX, SDSS, 2MASS and WISE passbands”. 2013, *MNRAS*, 430, 2188

Yuan, W., Riess, A. G., Macri, L. M., Casertano, S., & Scolnic, D. M., “Consistent Calibration of the Tip of the Red Giant Branch in the Large Magellanic Cloud on the Hubble Space Telescope Photometric System and a Redetermination of the Hubble Constant”. 2019, *ApJ*, 886, 61

## Appendix A

### MCR-TRGB: TESTS ON ARTIFICIAL DATA

In this section, we diagnose potential biases and systematics induced by the MCR technique by applying it to simulated CMDs with known theoretical TRGB magnitudes. We use the results of this analysis to determine bias corrections to our final tip magnitudes and to refine the uncertainties on our measurements.

We first generate a set of idealized (i.e., error-free) photometry of artificial RGB sequences with MATCH based on the PARSEC model suite. Serenelli et al. (2017) demonstrated that metallicity is the primary driver of variation in TRGB colors and magnitudes for old ages, so we hold all parameters except metallicity constant. We use a Chabrier IMF with a slope of 1.3, a binary fraction of 0.3, and a constant star formation rate with an age range of 100 Myr to 14 Gyr. We vary metallicity between  $-2.0 < [\text{Fe}/\text{H}] < -0.5$  dex with a spacing of 0.1 dex, which covers a color range representative of our data. We constrain the output magnitudes to  $\sim 1$  mag brighter than the TRGB to  $\sim 2.5$  mag dimmer for each filter:  $-5.0 < \text{F814W} < -1.5$  mag,  $-6.0 < \text{F110W} < -3.0$  mag, and  $-7.0 < \text{F160W} < -3.5$  mag.

We choose to model a constant SFR rather than a single-age population for two reasons. First, most of our data (see star-formation histories in D12) show evidence for stellar sequences from young populations, and as such, mono-age populations are not realistic representations of our data. Second, for a mono-age population, the full color or magnitude range of the TRGB is small enough to be comparable to the typical errors on the data points. In this limit, XDGMM cannot resolve the underlying distribution of TRGB color and magnitude, and thus its performance cannot be tested.

We add fiducial photometric errors to the simulated stellar population using the aggregate of all of our AST results, which were determined for each galaxy in our dataset in section 2.2.3.

We do not incorporate a net photometric bias or photometric incompleteness, both of which are negligible at the TRGB for the majority of our sample.

For all tests, we randomly subsample the artificial data to reach a desired total number of RGB stars less than 1 magnitude fainter than the fiducial-TRGB ( $N_{\star}^{T+1}$ ) in the filter used to measure the Sobel edge. We also adjust all magnitudes by a value randomly generated from a Gaussian with a mean of 0 mag and standard deviation set to the star’s photometric uncertainty.

### A.1 Luminosity function sampling

Here we test our method against  $N_{\star}^{T+1}$  over a range of  $200 \leq N_{\star}^{T+1} \leq 5000$  stars, which spans the  $N_{\star}^{T+1}$  values for the majority of the galaxies in our sample. At each  $N_{\star}^{T+1}$  we run 20 end-to-end XDGMM tip fitting iterations and calculate the offsets  $\Delta M_{\text{TRGB}} \equiv M_{\text{TRGB}}(\text{measured}) - M_{\text{TRGB}}(\text{true})$  for each filter. We repeat these tests at four different metallicities ( $[\text{Fe}/\text{H}] = \{-1.7, -1.3, -1.0, -0.7\}$  dex) to check for possible color-dependent effects.

Figure A.1 shows the median per-filter differences in the measured versus theoretical TRGB values against  $N_{\star}^{T+1}$  for each of the four metallicities. The error bars on the points in Figure A.1 show the interquartile range of the results. The dashed horizontal lines are color-coded to match the filter and show the range of the per-filter mean uncertainty on the tip-fitting results; we define the uncertainty as the quadrature sum of the XDGMM fitting uncertainty and the median photometric error of the tip stars.

For all but  $[\text{Fe}/\text{H}] = -0.7$  dex, the results are largely consistent: the offsets  $\Delta M_{\text{TRGB}}$  start out around 0.04 mag in the most undersampled case, increase approximately with  $N_{\star}^{T+1}$  for  $N_{\star}^{T+1} \lesssim 1000$  stars in all filters, and then begin to level off near  $\Delta M_{\text{TRGB}} \sim 0.01$  mag. These results are broadly similar to what is seen for traditional edge detection methods. Madore et al. (2009) found that Sobel edge detection is prone to bias when the RGB luminosity function is undersampled, and that a sample of  $N_{\star}^{T+1} \gtrsim 500$  stars is required for edge detection to function accurately.

For  $[\text{Fe}/\text{H}] = -0.7$  dex, where the edge detection and initial tip star selection are done in

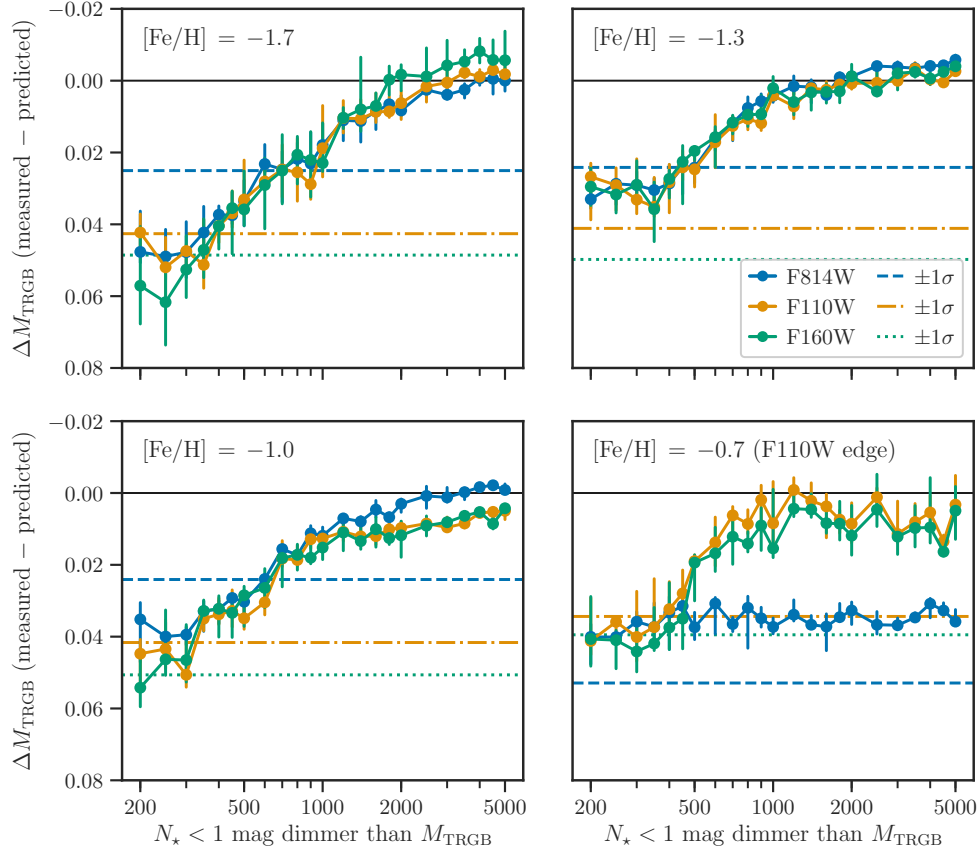


Figure A.1: Differences between measured and theoretical TRGB magnitude versus  $N_{\star}^{T+1}$  (the number of stars within 1 mag fainter of the TRGB), for  $[\text{Fe}/\text{H}] = -1.7$  dex (top left),  $-1.3$  dex (top right),  $-1.0$  dex (bottom left), and  $-0.7$  dex (bottom right). The error bars on the points show the interquartile range of the results. The various dashed horizontal lines show the mean per-filter uncertainties on the tip fitting results, which we define as the quadrature sum of the XDGMM fitting uncertainty and the mean photometric uncertainty of the tip stars. The bias in the XDGMM edge measurement is typically within the  $1\text{-}\sigma$  TRGB uncertainty, with the exception of poorly populated CMDs ( $N_{\star}^{T+1} < \sim 500$  stars).

F110W rather than F814W, we see behavior similar to the lower metallicities in the NIR, but not in F814W, which hovers at 0.04 mag throughout. This foreshadows a possible selection effect when using F110W for the primary edge detection, which we investigate further in section A.2.

## A.2 Metallicity

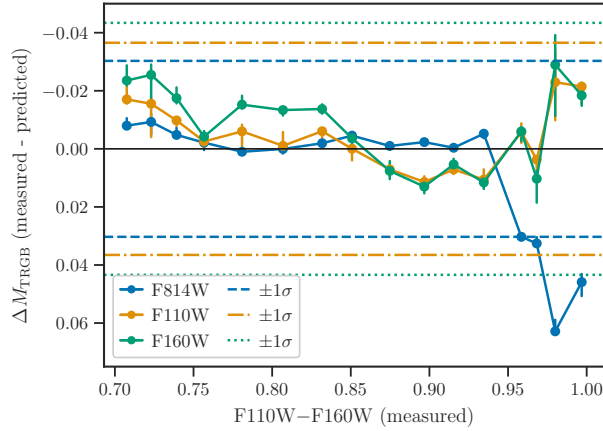


Figure A.2: The difference between measured and theoretical TRGB values against the median measured NIR tip color for the ensemble of simulated datasets. Results for F814W, F110W, and F160W are shown in blue, orange, and green, respectively. The horizontal lines show  $\pm 1\sigma$ , where  $\sigma$  is the mean quadrature sum of the photometric and fitting errors for each filter. This bias is within the TRGB detection uncertainty in almost all cases.

For each metallicity in our artificial dataset, we run 20 end-to-end tip fitting iterations with  $N_{\star}^{T+1} = 4000$  stars, in the regime where sampling effects are minimal. Figure A.2 shows the median per-filter differences in the measured versus the theoretical TRGB values against the measured IR-TRGB color; the IR-TRGB color increases approximately monotonically with metallicity in the artificial data.

The jump in offset values at  $F110W - F160W > 0.95$  mag corresponds to the switch from using F814W to using F110W for the Sobel edge detection. We hypothesize that this jump is due to a difference in which stars are selected as candidate tip stars. At high metallicity, stars

that have similar magnitudes in F110W may have a large range of magnitudes in F814W due to the increasingly steep TRGB-color slope in F814W. The stars that are the brightest in F814W are relatively dim in F110W and so may not fall within the F110W tip star selection window and, thus, our measured F814W tip magnitudes are skewed faint relative to the predicted values.

### A.3 Photometric uncertainties

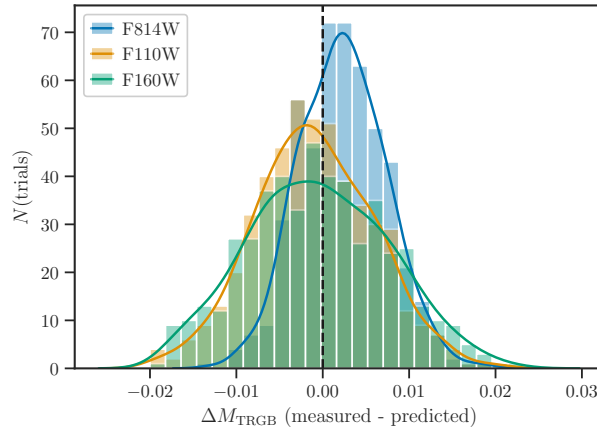


Figure A.3: Histograms of the difference between the measured and predicted  $M_{\text{TRGB}}$  for the with  $N_{\star}^{T+1} = 2000$  stars and  $[\text{Fe}/\text{H}] = -1.0$  dex artificial dataset for 500 trials, where each trial modifies the stellar magnitude randomly in proportion to its photometric error. The blue histogram is for F814W, the orange is for F110W, and the green is for F160W. As expected, the widths of all histograms are smaller than the reported photometric uncertainties at the tip.

To isolate the impact of photometric uncertainties on our TRGB-measurements, we use the artificial dataset with  $N_{\star}^{T+1} = 2000$  stars and  $[\text{Fe}/\text{H}] = -1.0$  dex. For each of 500 trials, we vary the input magnitudes by a different random value drawn from a Gaussian whose standard deviation is each star's photometric uncertainty. The results of this test are shown in Figure A.3. We find that for all filters the standard deviation of the resulting distribution of offsets is roughly a third of the typical photometric uncertainty at the tip.

#### A.4 XDGMM vs. Sobel edge detection

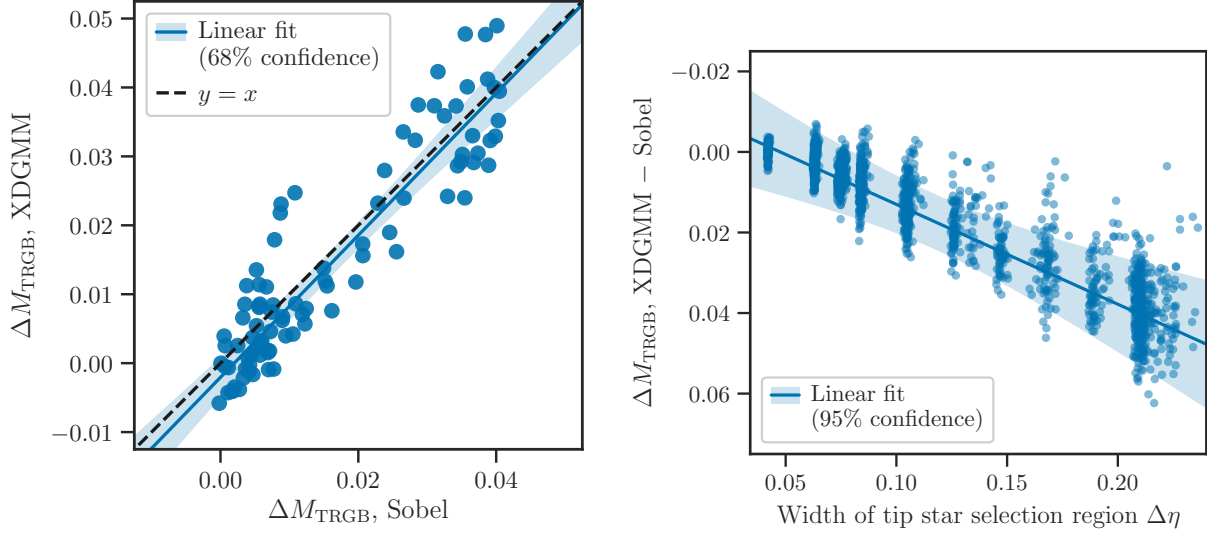


Figure A.4: Top: The median difference between XDGMM-fitted and theoretical tip magnitudes versus the median difference between the Sobel edge magnitude and theoretical tip magnitude in either F814W or F110W. Each point is the median result for one set of trials with fixed metallicity and  $N_{\star}^{T+1}$ . The solid line and flanking filled region show a linear fit to the data and its 68% confidence interval, whereas the dashed line shows a one-to-one relation. Bottom: Difference between the XDGMM-fitted mean and Sobel edge magnitude versus  $\Delta\eta$ , which is the width in magnitudes of the tip star selection region in the luminosity function. Each point represents the offset for a single trial with fixed metallicity and  $N_{\star}^{T+1}$ . The solid line and flanking filled region show a linear fit to the data and its a 95% confidence interval, respectively.

Here we investigate the behavior of XDGMM tip fitting relative to the standard method of Sobel edge detection using the same set of trials as in section A.1. As our method for XDGMM tip fitting itself uses Sobel edge detection to set the color-magnitude center of the initial tip star selection window, we can make a fully self-consistent comparison of the Sobel edge magnitudes to the XDGMM mean magnitudes for detections in F814W and F110W. (We do not perform edge detection on F160W in our method and so do not make the comparison.)



The top panel of Figure A.4 shows the relation between the median difference between the XDGMM-fitted mean and the theoretical tip versus the median difference between the Sobel edge and theoretical tip. The linear fit to the data is consistent within  $1\sigma$  with a one-to-one relation, indicating that the methods produce overall consistent tip magnitudes.

The bottom panel of Figure A.4 shows the relation between the width of the tip star selection region,  $\Delta\eta$ , and the difference between the XDGMM- and Sobel-derived tip magnitudes,  $\Delta M_{\text{TRGB}}$ . The quantities are correlated, albeit with some scatter on the order of 0.01 mag, and are fit by the linear relation  $\Delta M_{\text{TRGB}}^{\text{X-S}} = 0.25(\Delta\eta) - 0.01$  mag.

### A.5 Adjustments to measurements

In the previous sections, a number of tests were performed to quantify the statistical and systematic uncertainties of the MCR method using artificial photometry. Here we match our observed galaxies to their artificial tests to determine both systematic terms that are applied in the form of bias corrections and statistical terms that are applied in the form of inflating the algorithmic uncertainties. The corrections are parameterized by two key observables: (i) how well populated the RGB is as a proxy for the total mass, and (ii) the F814W–F160W color as a proxy for the underlying stellar population properties. All such adjustments are summarized in Table A.1 and if a given target does not appear in the table, then it did not require a modification.

For each target, we determine the most appropriate sets of tests to use to determine the bias based on  $N_{\star}^{T+1}$  and F814W–F160W color. The quoted adjustment values are adopted from the relevant set of trials, with uncertainties determined as the median and interquartile range of the offsets (measured – predicted value) in each filter. We subtract the offsets from the measured TRGB apparent magnitude and add the associated uncertainty in quadrature to the fitting uncertainty. We also modify all relevant colors based on these adjustments.

The first four targets in Table A.1 (KDG73, NGC2403-HALO-6, SCL-DE1, and UGCA292) all have  $N_{\star}^{T+1} < 500$  stars. (Although these targets do not all have the same colors, we found that differences between offsets were negligible at the relevant colors.) For

Table A.1: Applied bias corrections

Target name	Value( $\pm$ error) subtracted from $m_{\text{TRGB}}$		
	F814W	F110W	F160W
KDG73	$0.04 \pm 0.02$	$0.04 \pm 0.02$	$0.04 \pm 0.02$
NGC2403-HALO-6	$0.04 \pm 0.02$	$0.04 \pm 0.02$	$0.04 \pm 0.02$
SCL-DE1	$0.04 \pm 0.02$	$0.04 \pm 0.02$	$0.04 \pm 0.02$
UGCA292	$0.04 \pm 0.02$	$0.04 \pm 0.02$	$0.04 \pm 0.02$
NGC0300	$0.03 \pm 0.01$		
NGC2976-DEEP	$0.03 \pm 0.01$		
NGC3077-PHOENIX	$0.03 \pm 0.01$		
SN-NGC2403-PR	$0.03 \pm 0.01$		
M81-DEEP	$0.06 \pm 0.01$	$-0.02 \pm 0.02$	$-0.02 \pm 0.02$

these we take the median and interquartile range of offsets for all trials with  $N_{\star}^{T+1} < 500$  stars and  $[\text{Fe}/\text{H}] \leq -1.0$  dex.

The remaining targets (NGC0300, NGC2976-DEEP, NGC3077-PHOENIX, SN-NGC2403-PR, and M81-DEEP) use F110W as the edge detection filter. All but M81-DEEP have colors  $\text{F814W} - \text{F160W} \sim 2$  mag, whereas M81-DEEP has  $\text{F814W} - \text{F160W} \sim 2.25$  mag. We match these colors by adopting the median and interquartile range of offsets for trials with  $-0.8 \leq [\text{Fe}/\text{H}] \leq -0.7$  dex for all but M81-DEEP, and  $-0.6 \leq [\text{Fe}/\text{H}] \leq -0.5$  dex for M81-DEEP.

## Appendix B

### MCR-TRGB: FIGURE SETS

Figure B.1: Stellar surface density maps

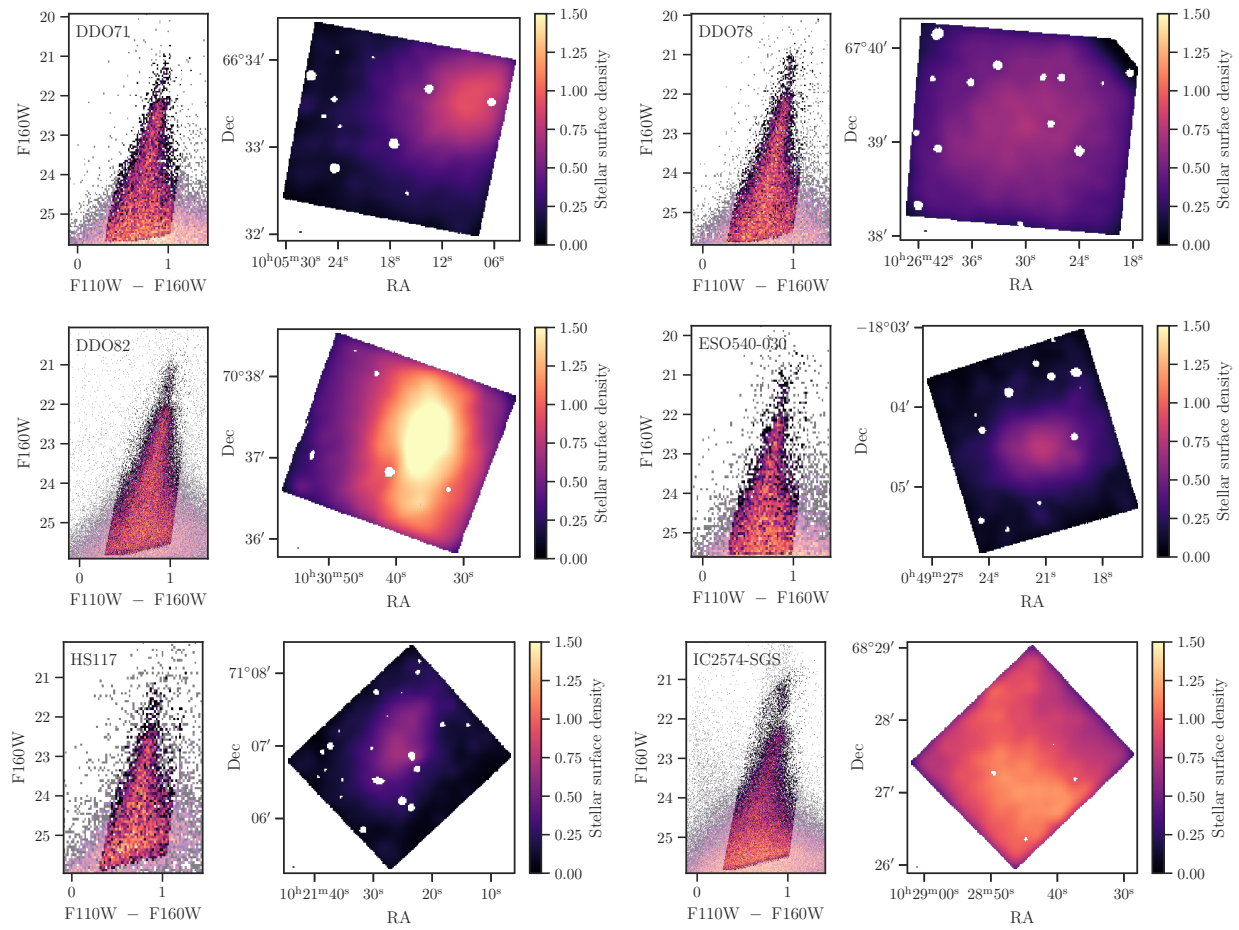


Figure B.1: —CONTINUED

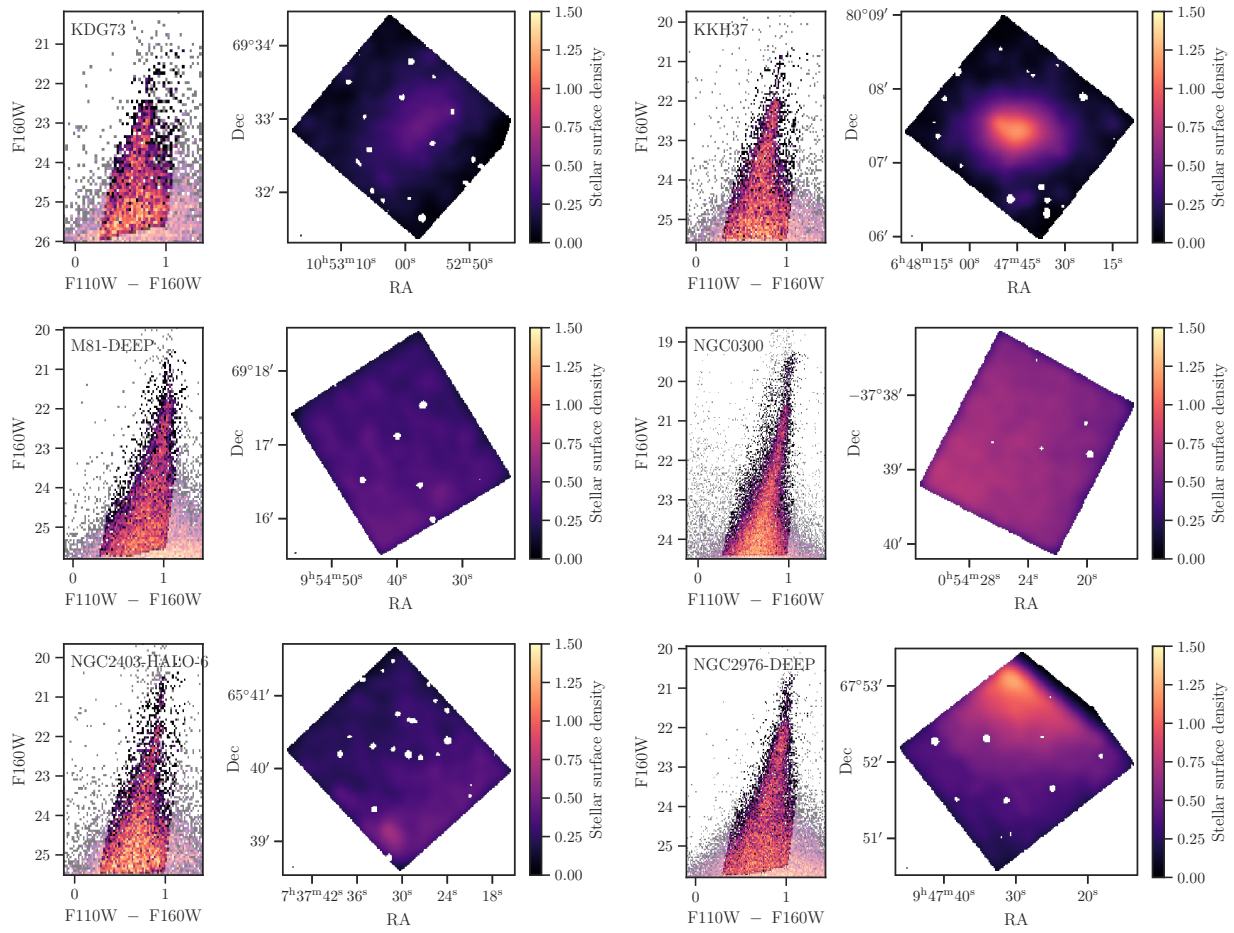


Figure B.1: —CONTINUED

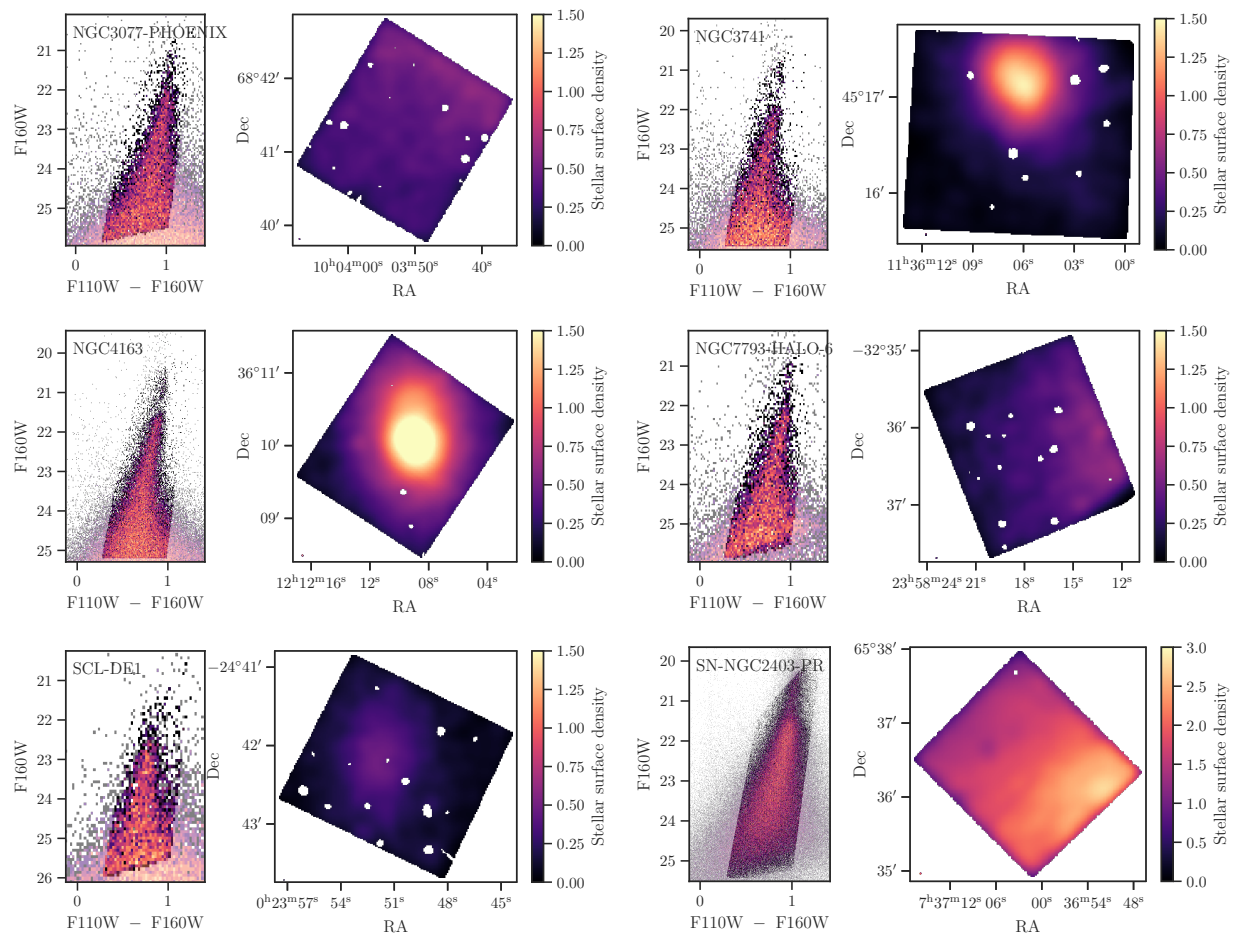


Figure B.1: —CONTINUED

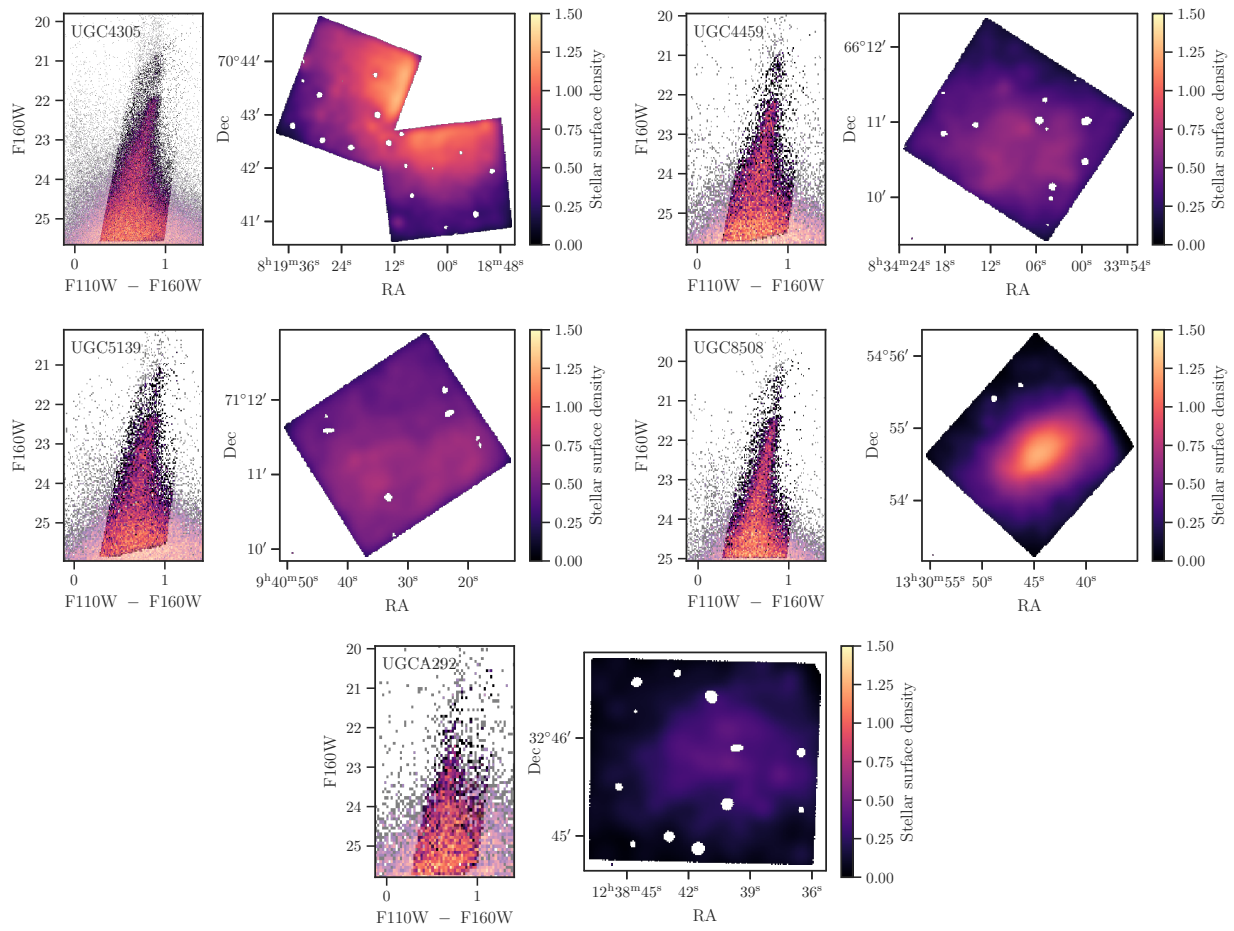


Figure B.2: Old to new photometry comparisons

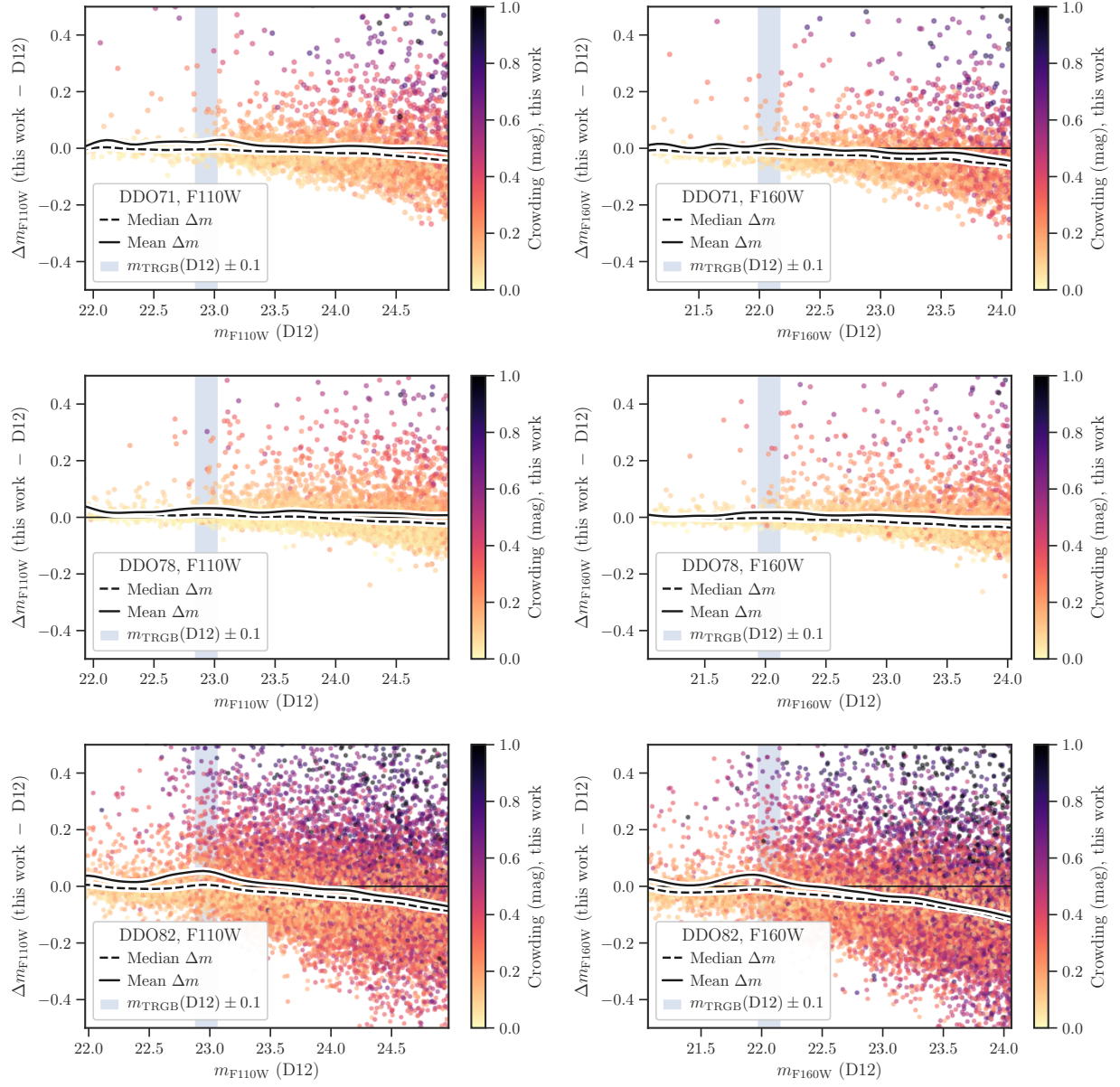




Figure B.3: —CONTINUED

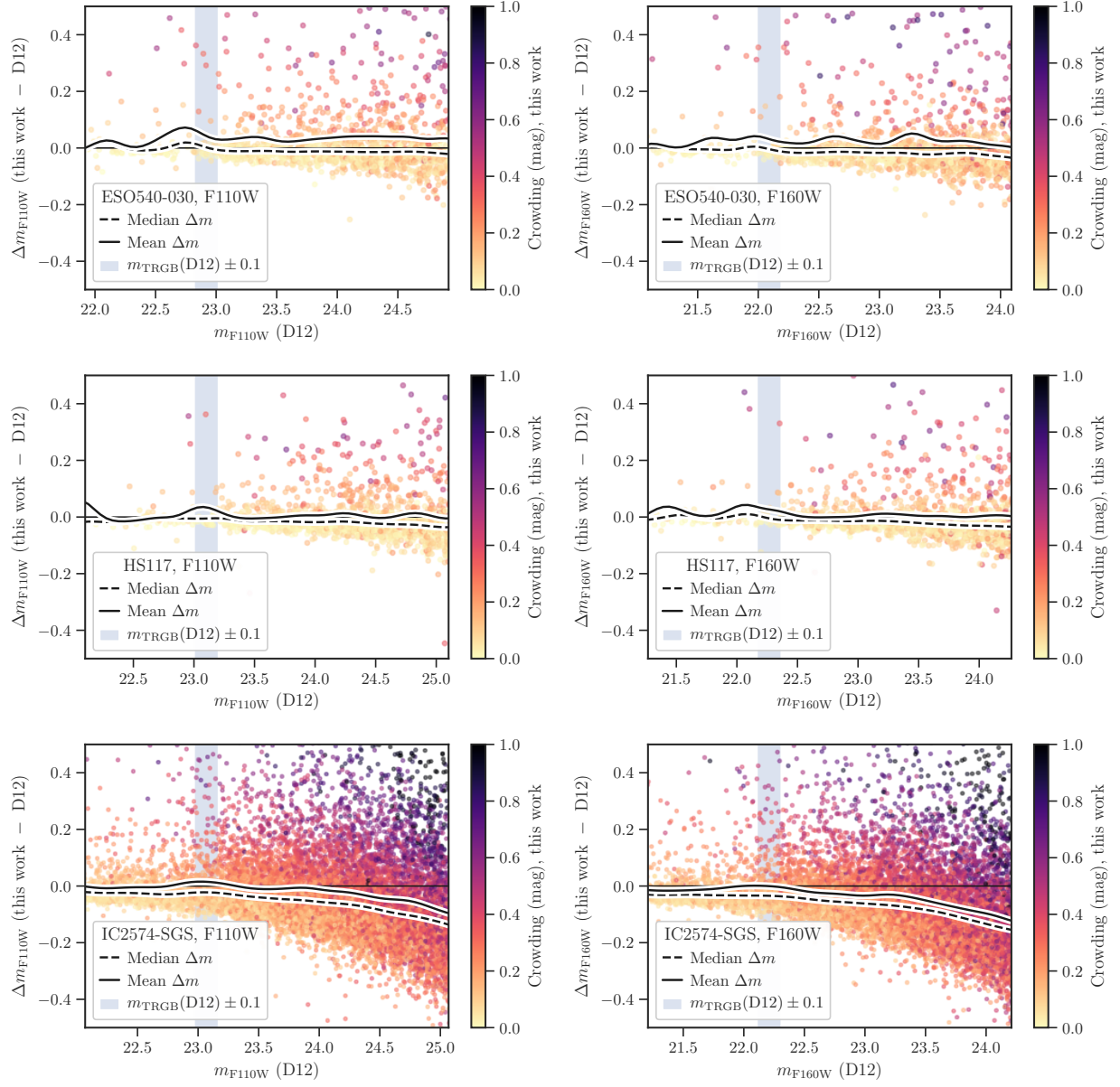




Figure B.3: —CONTINUED

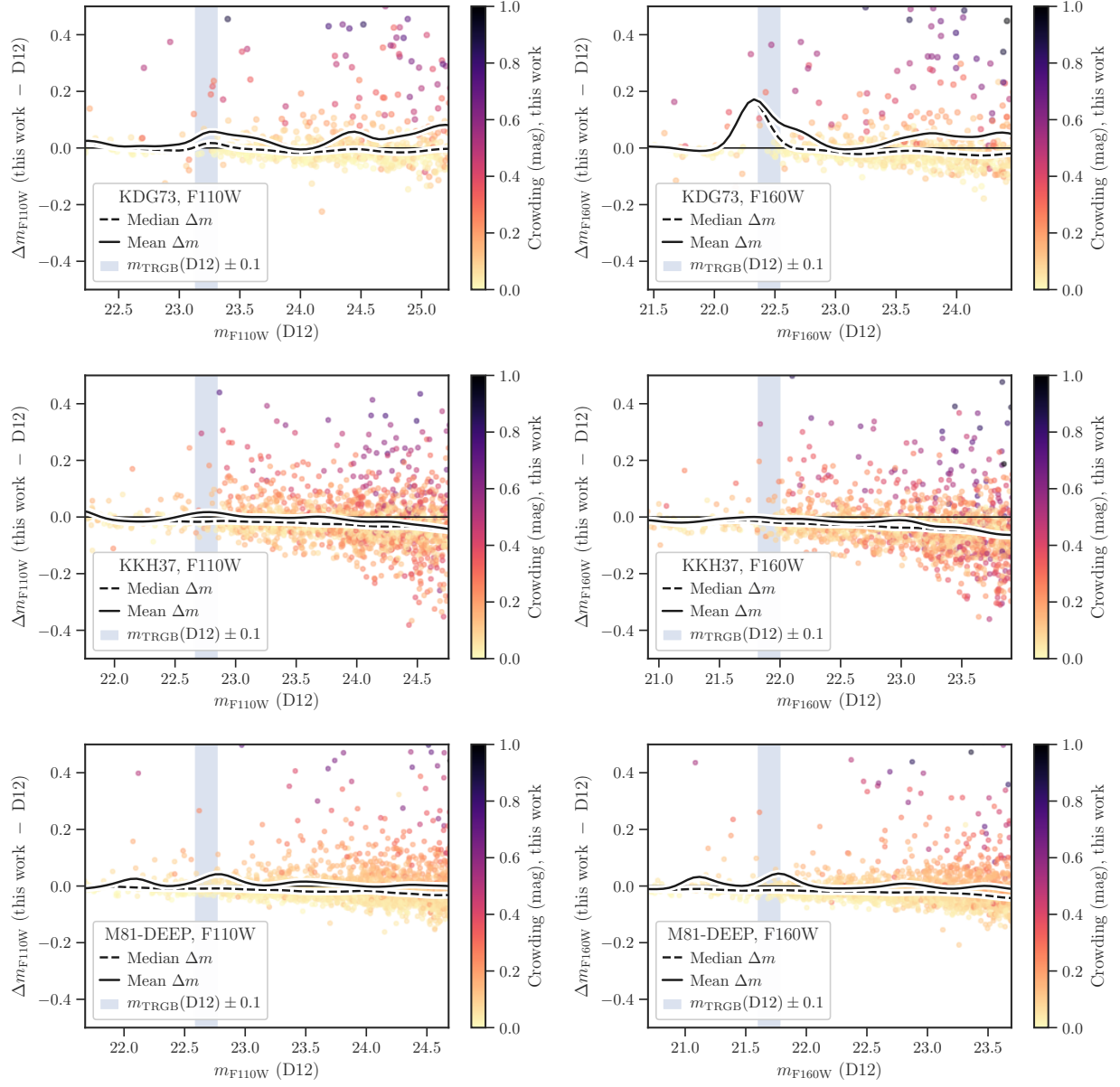


Figure B.3: —CONTINUED

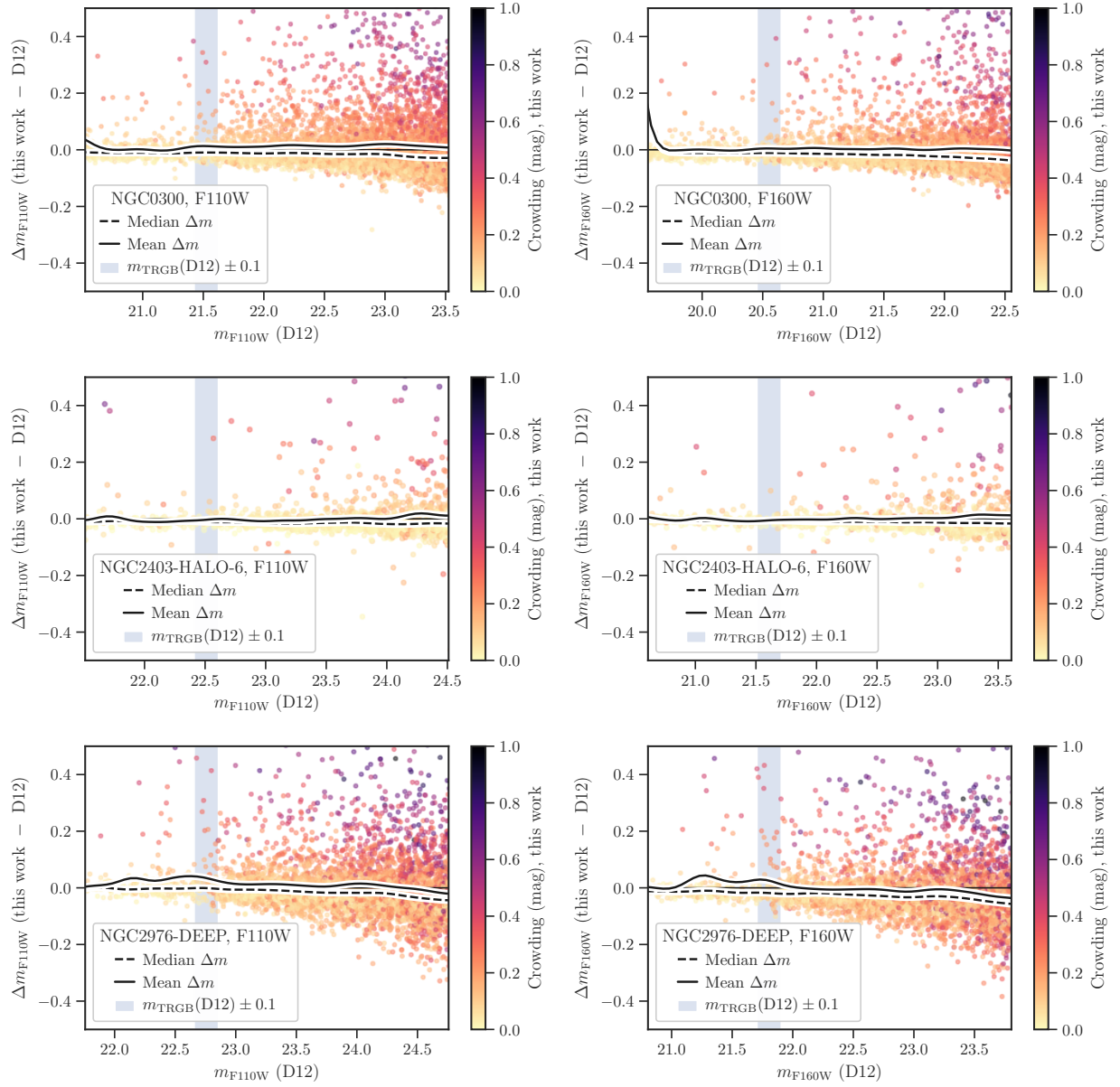


Figure B.3: —CONTINUED

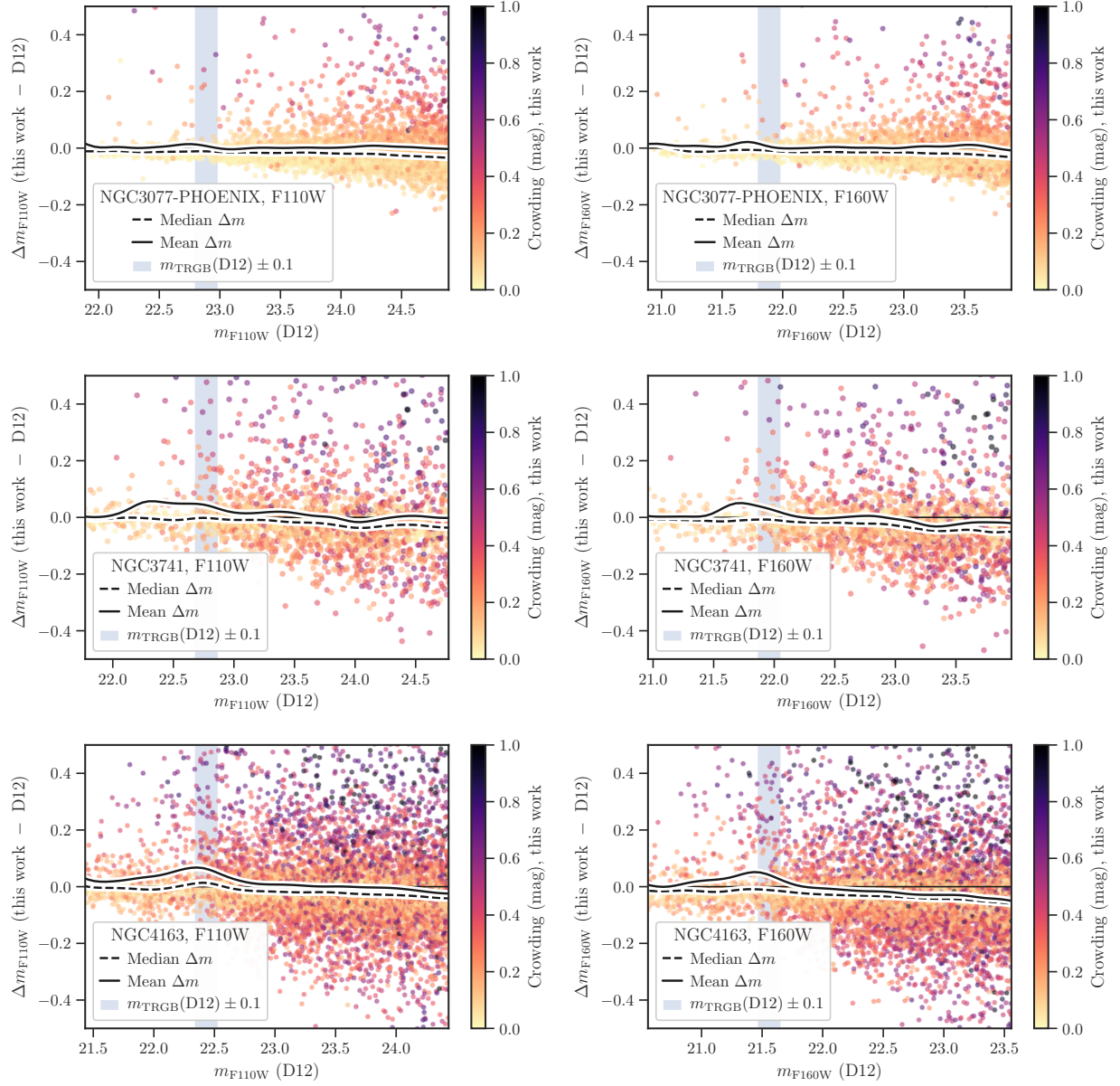


Figure B.3: —CONTINUED

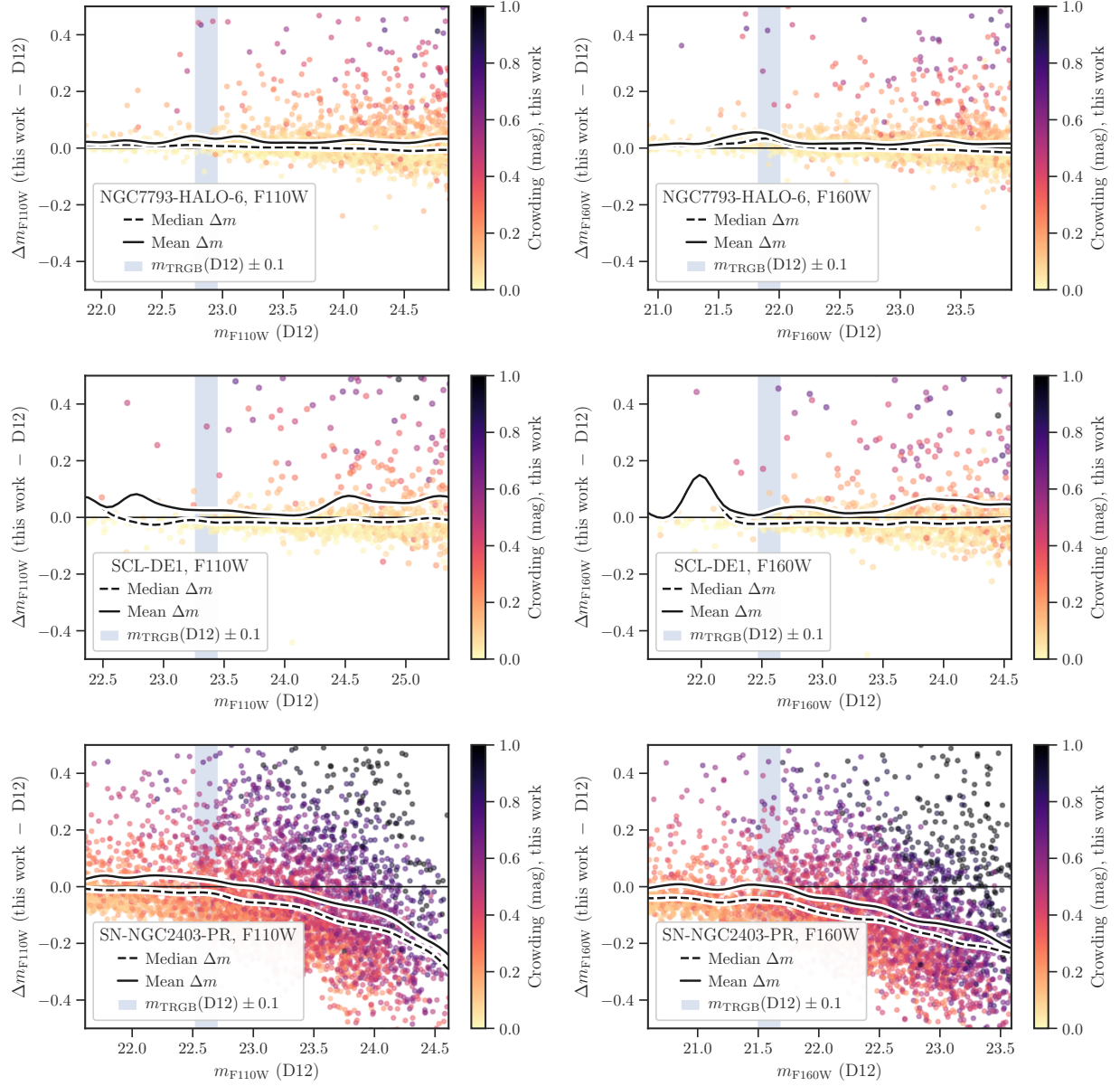


Figure B.3: —CONTINUED

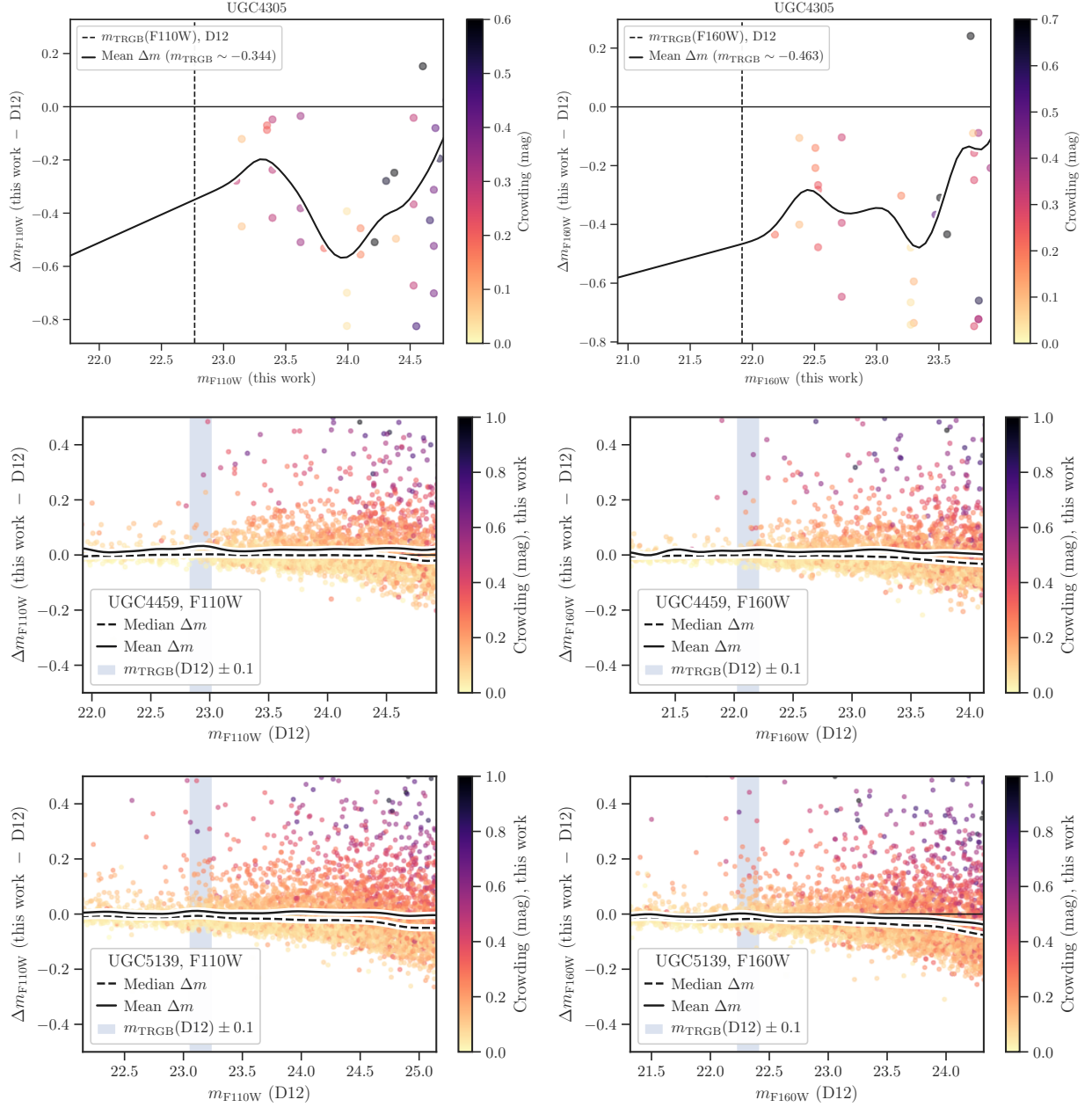


Figure B.3: —CONTINUED

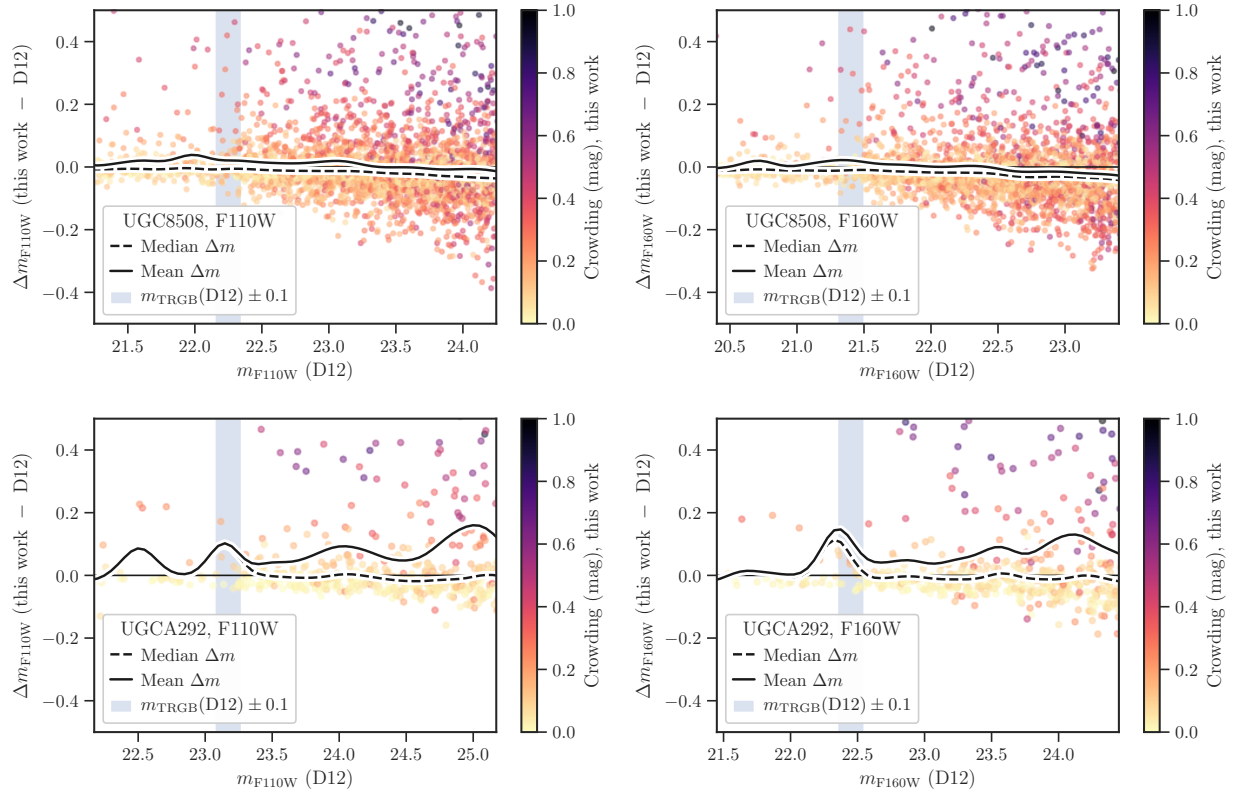




Figure B.4: CMDs showing individual RGB-sequence probabilities.

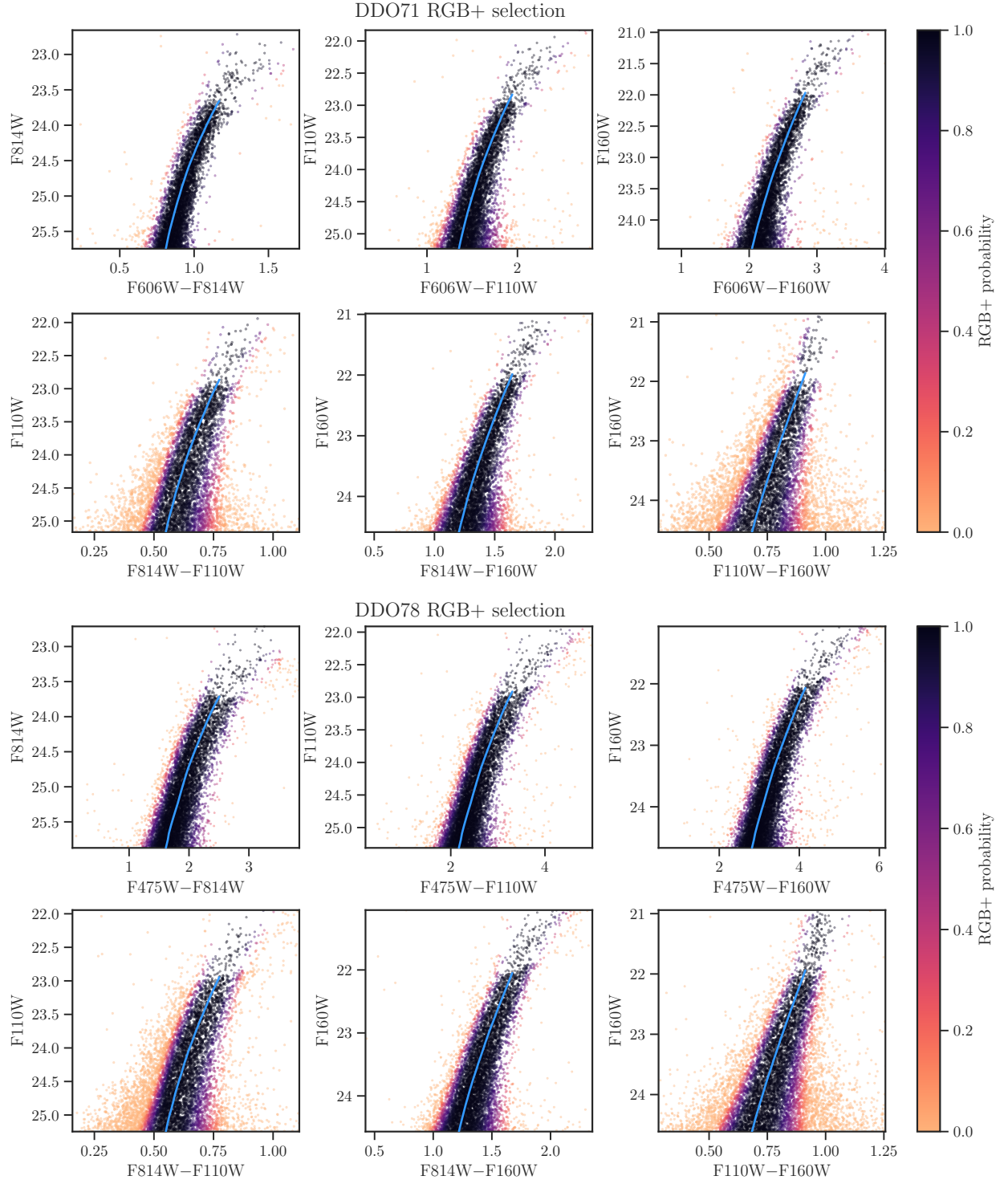


Figure B.4: —CONTINUED

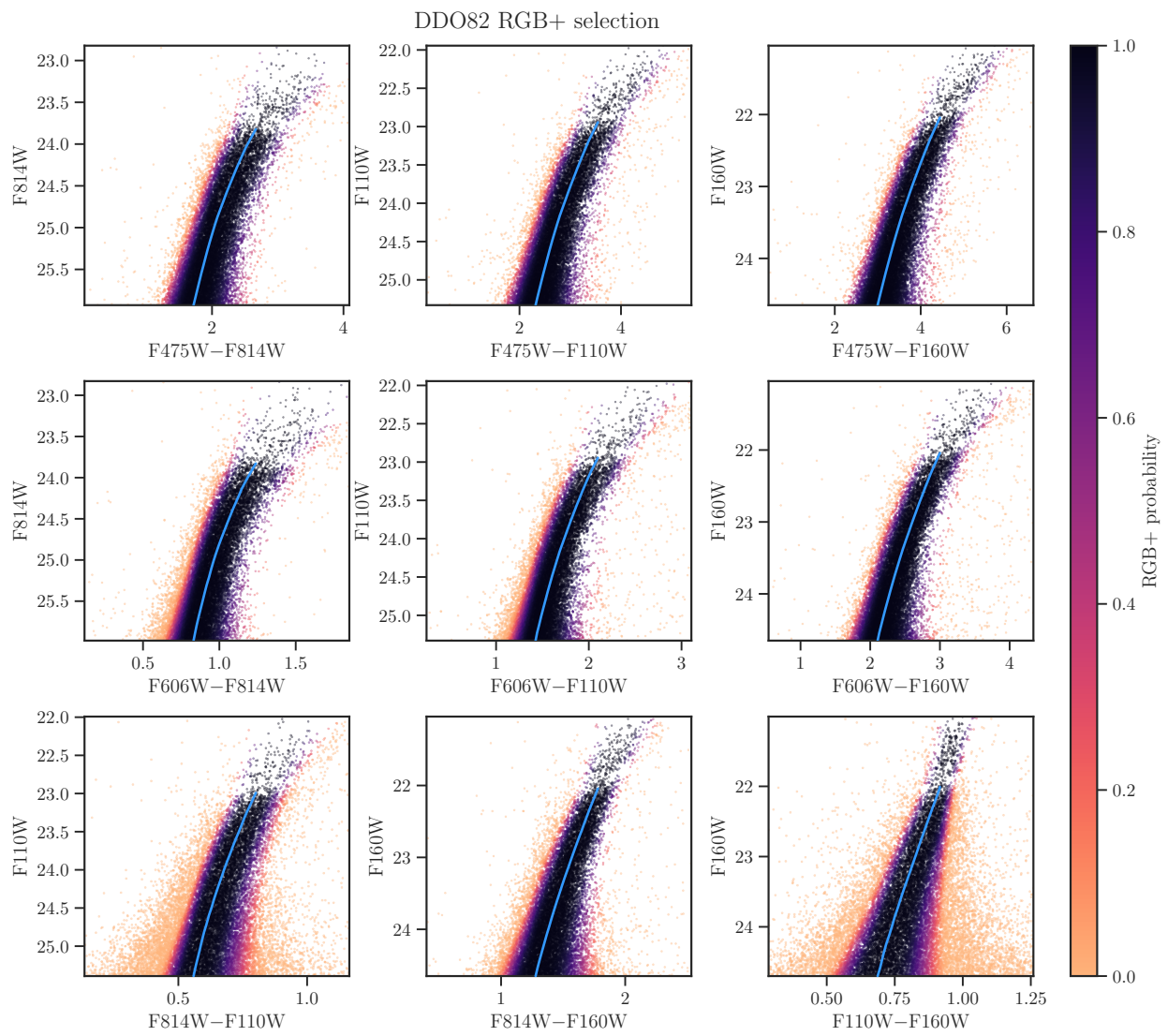




Figure B.4: —CONTINUED

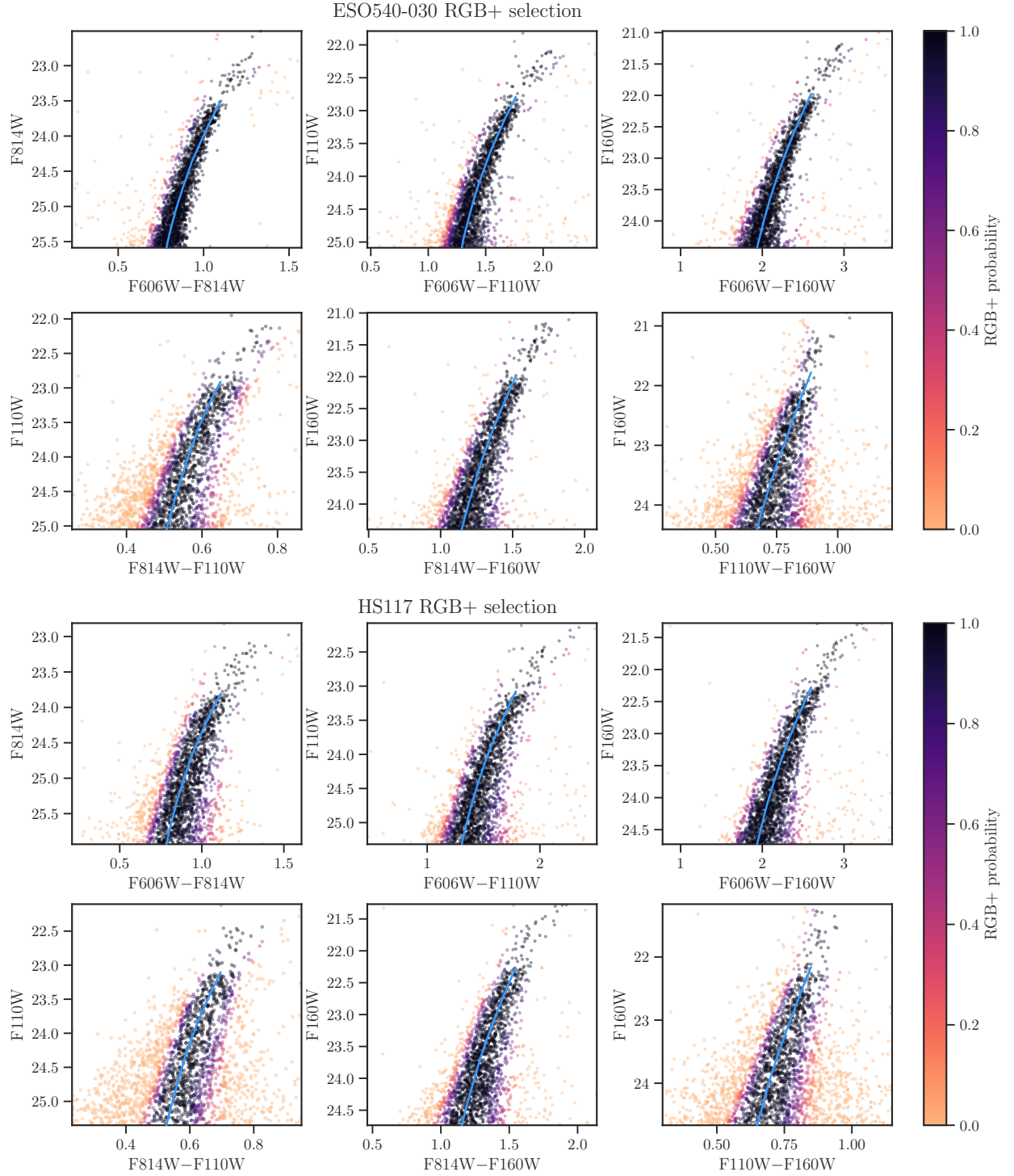


Figure B.4: —CONTINUED

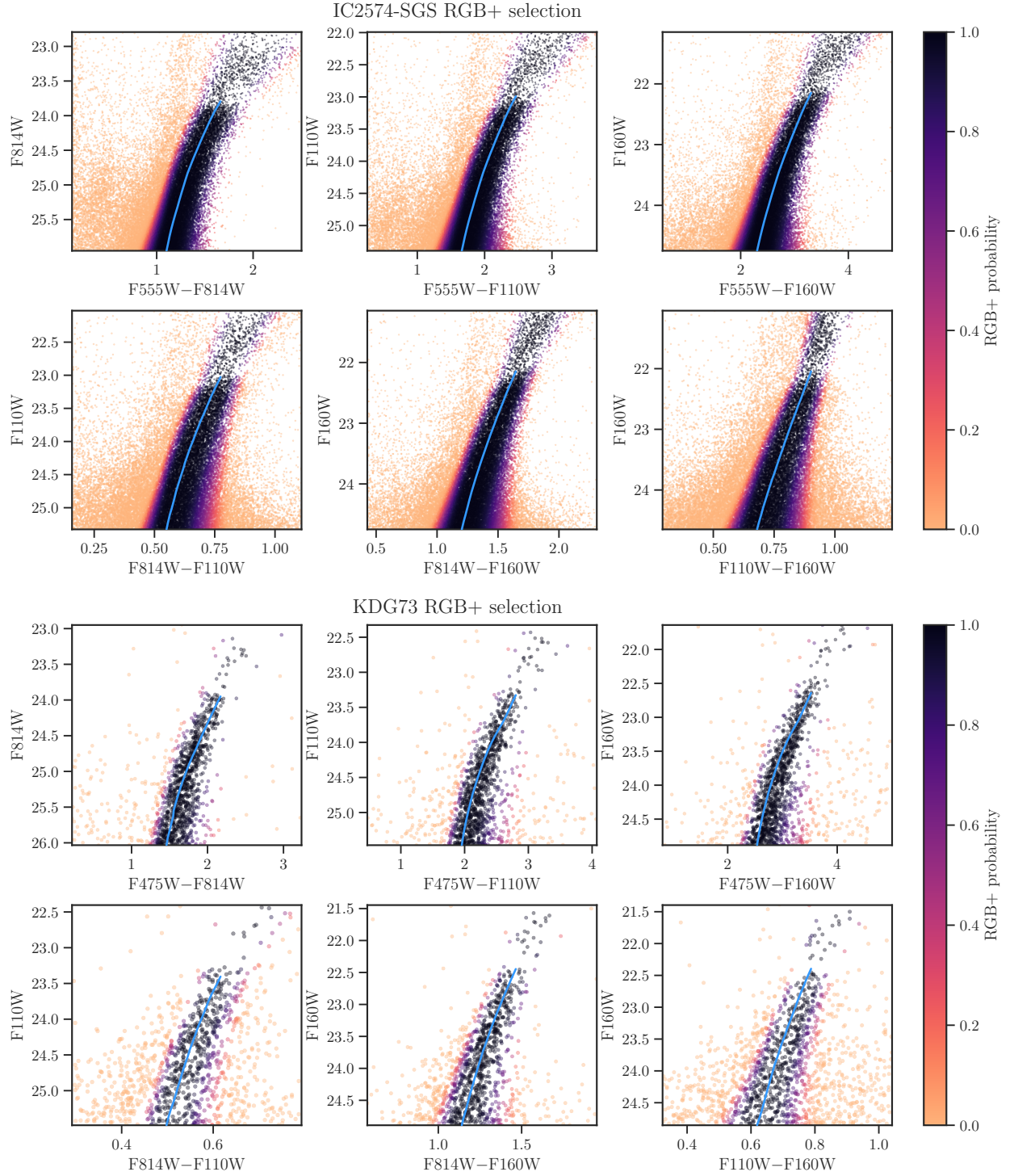


Figure B.4: —CONTINUED

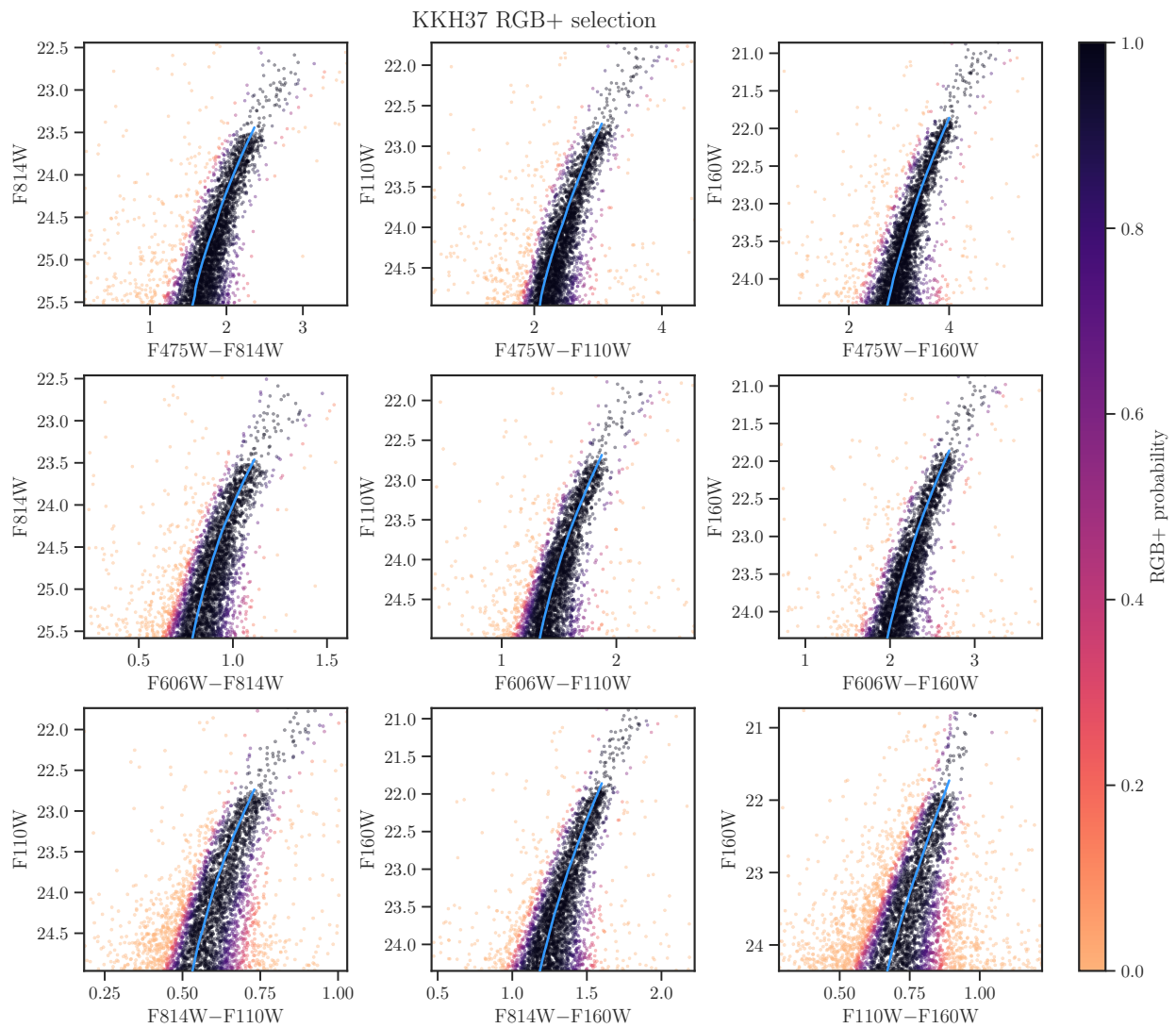


Figure B.4: —CONTINUED

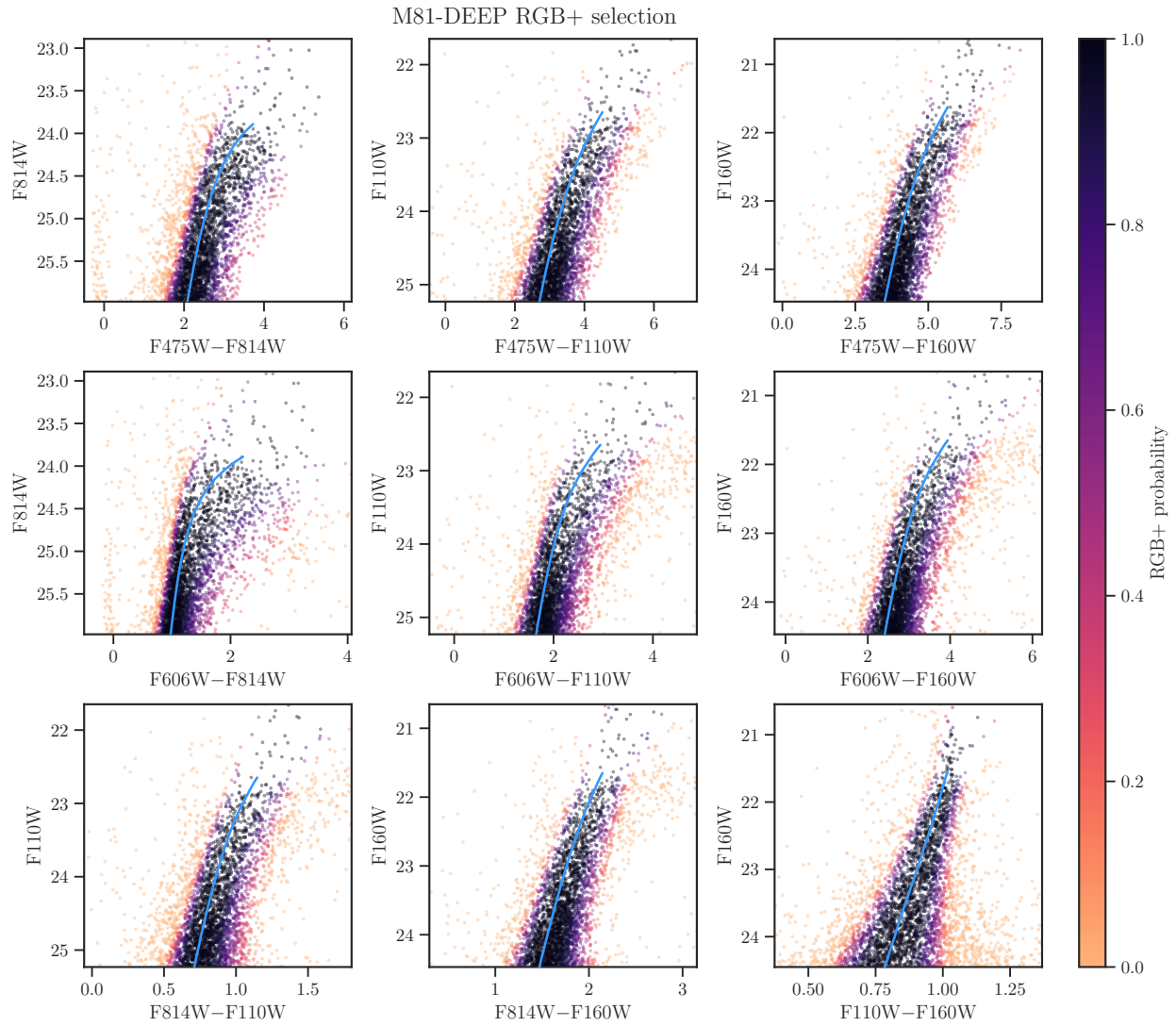




Figure B.4: —CONTINUED

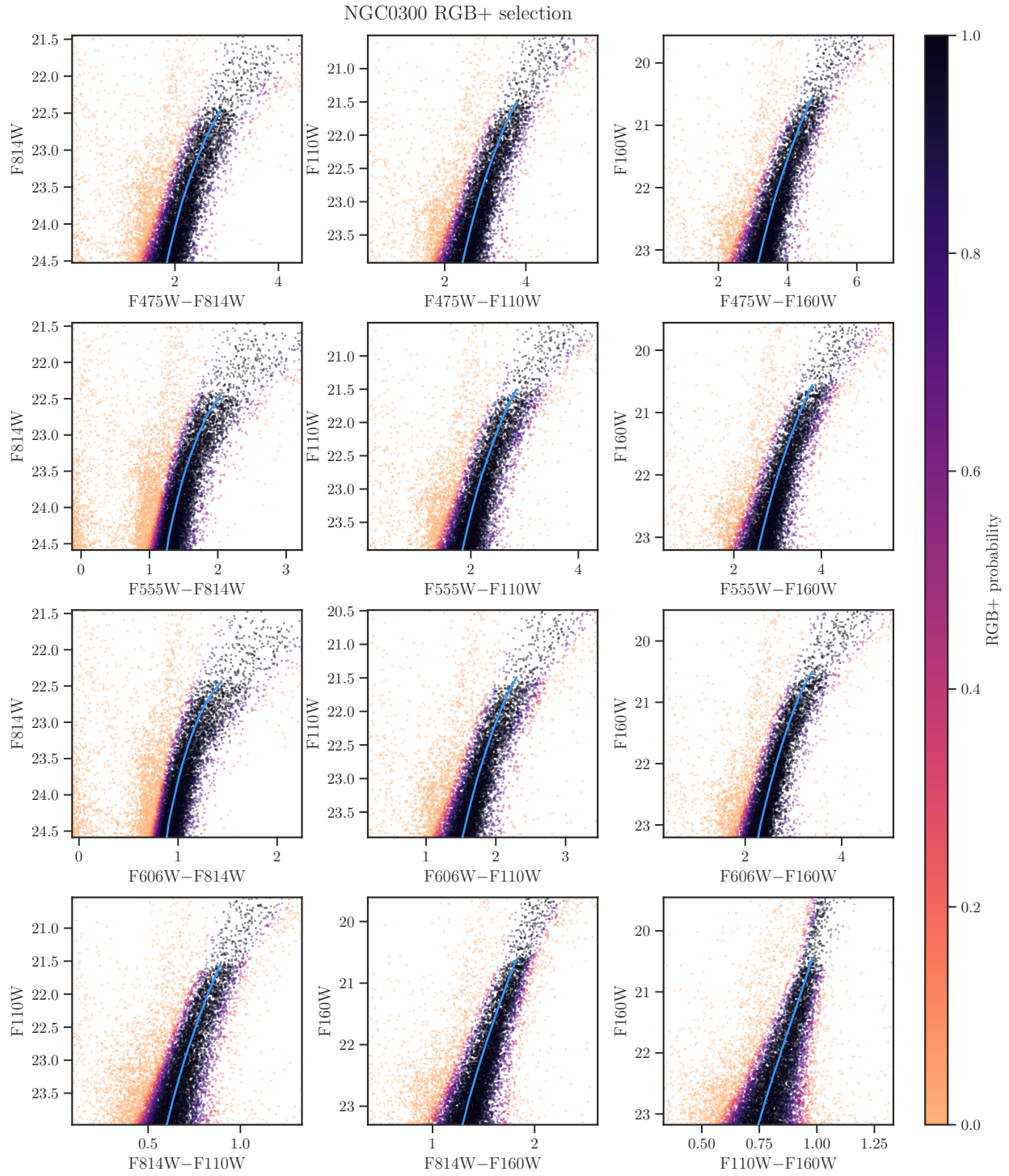


Figure B.4: —CONTINUED

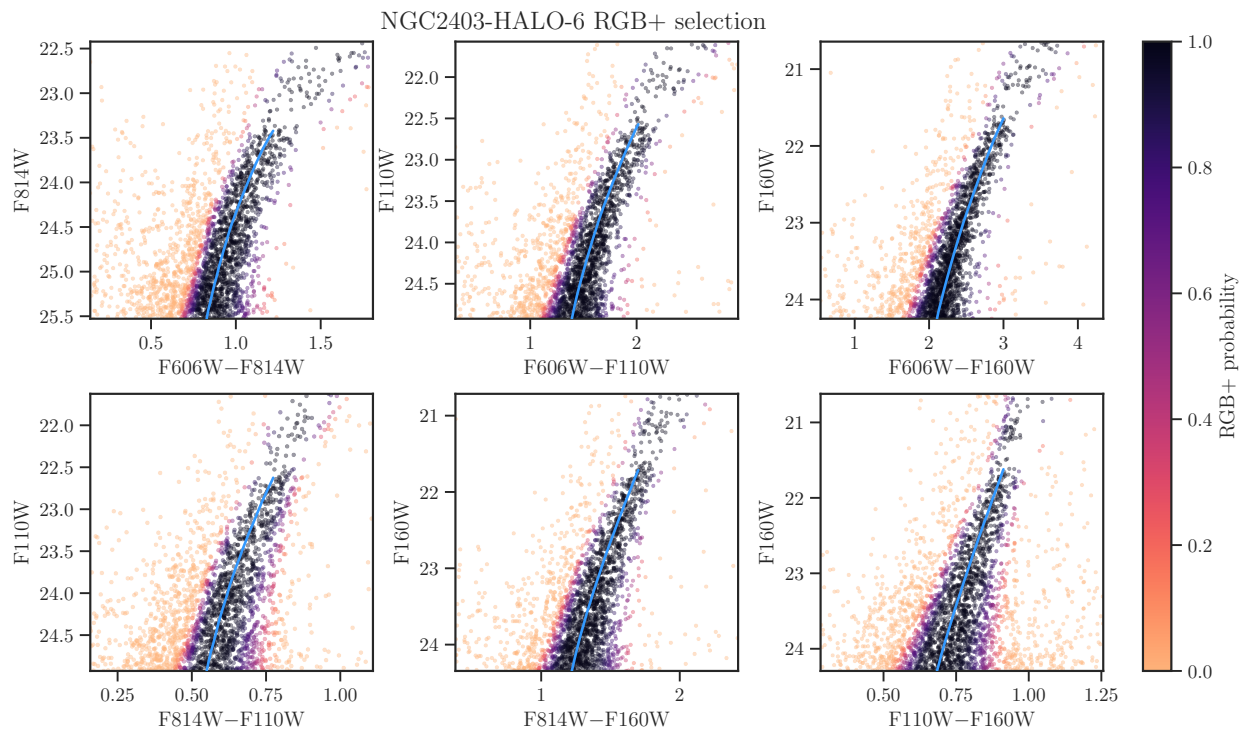


Figure B.4: —CONTINUED

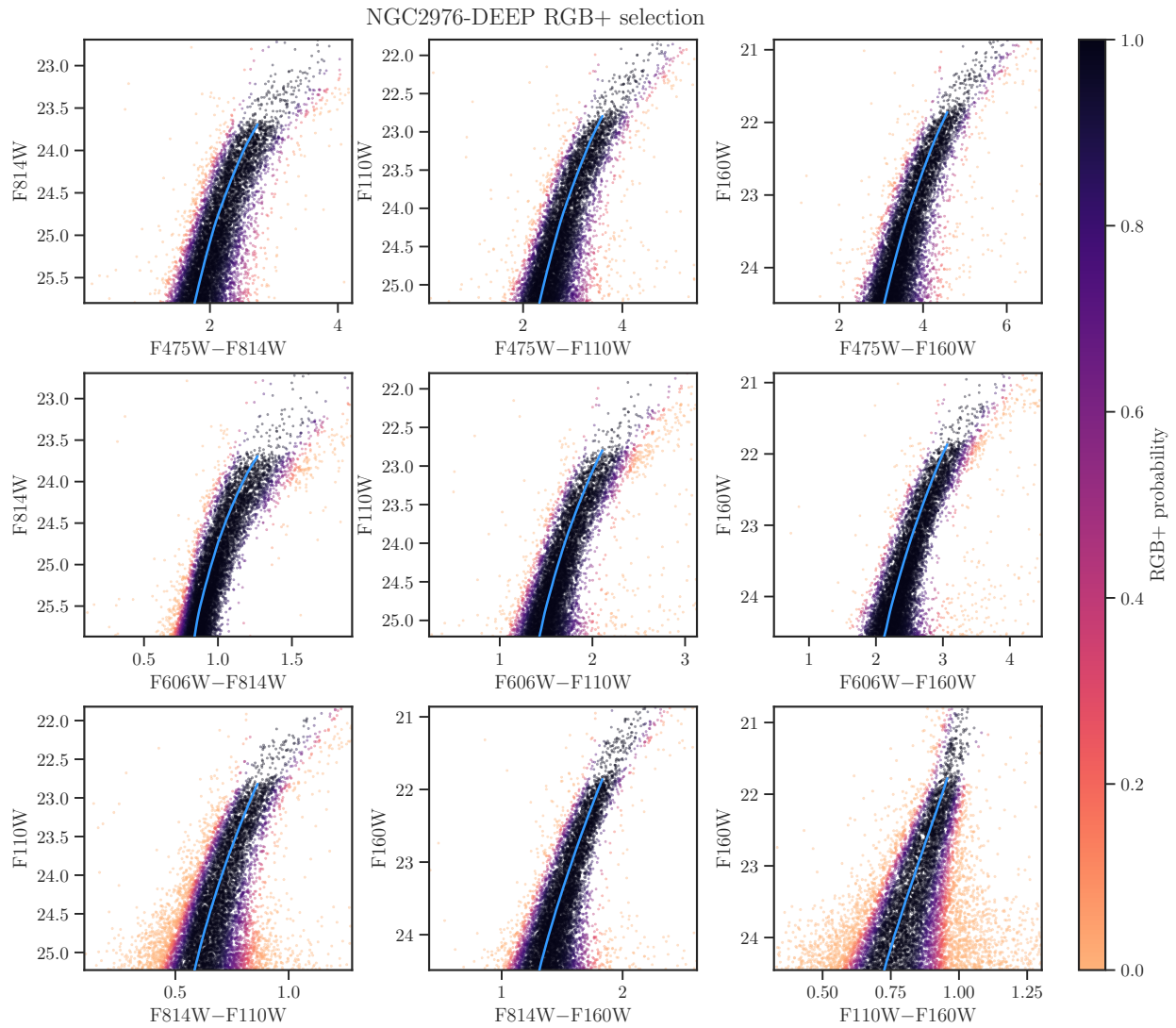


Figure B.4: —CONTINUED

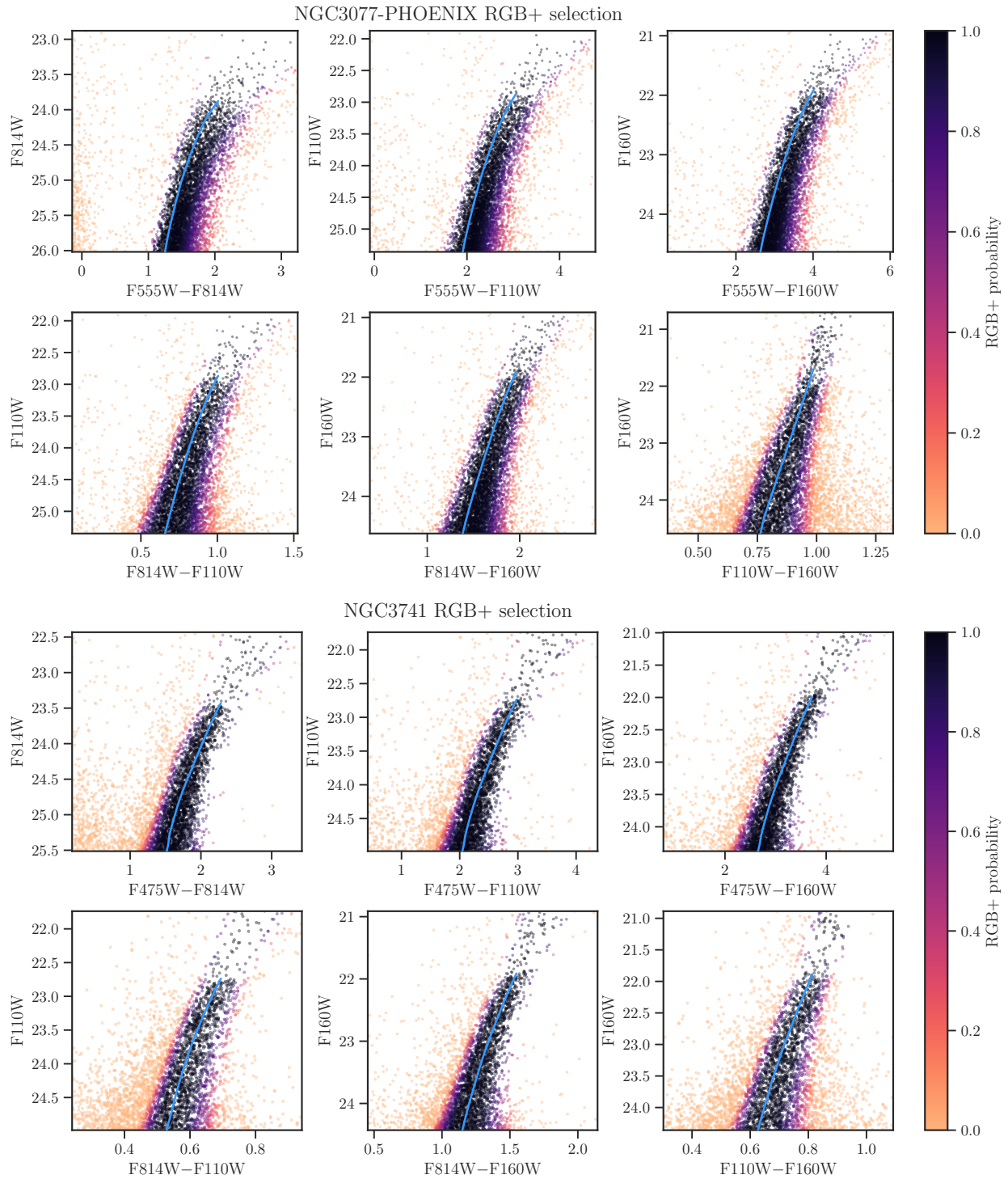




Figure B.4: —CONTINUED

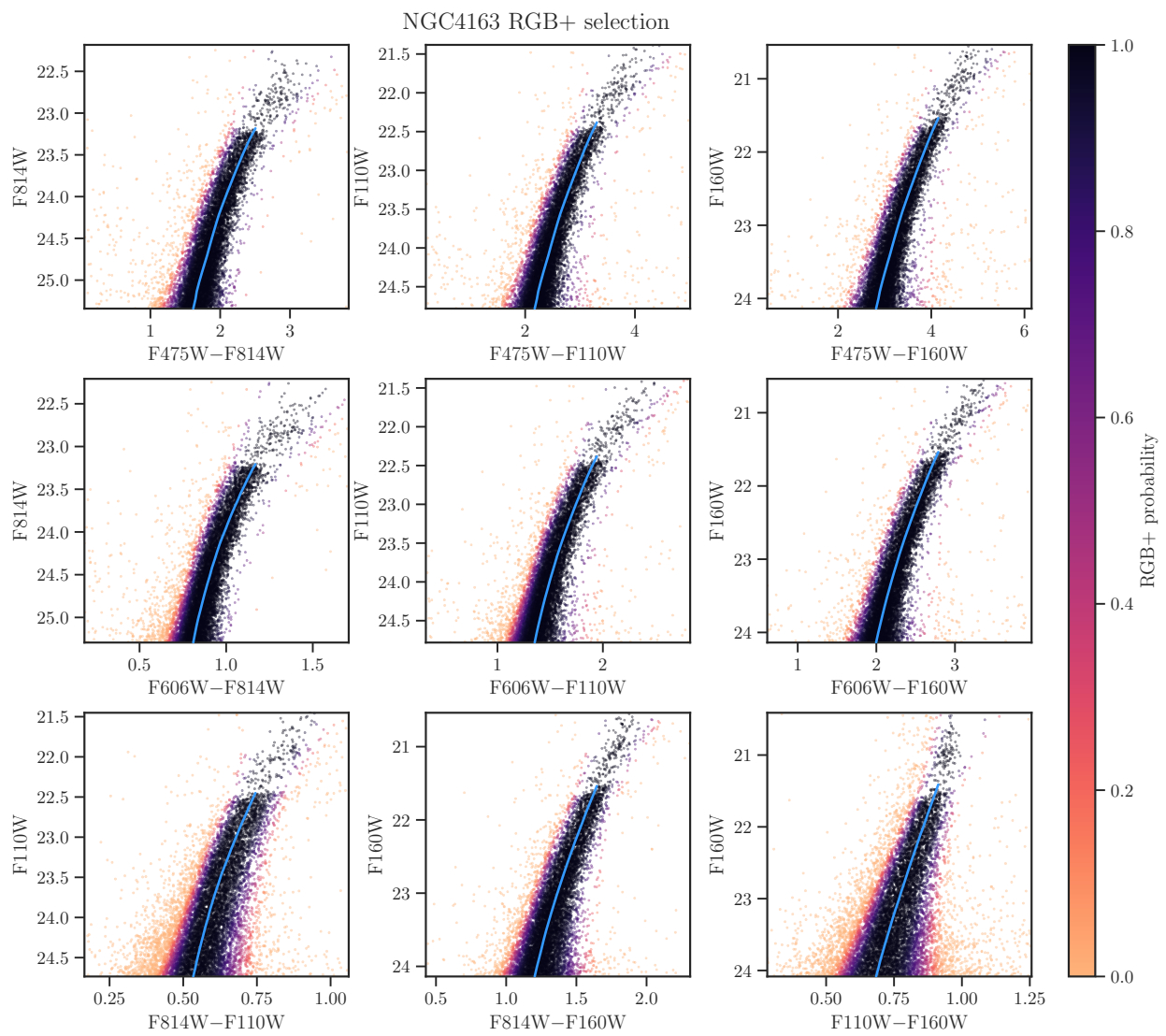


Figure B.4: —CONTINUED

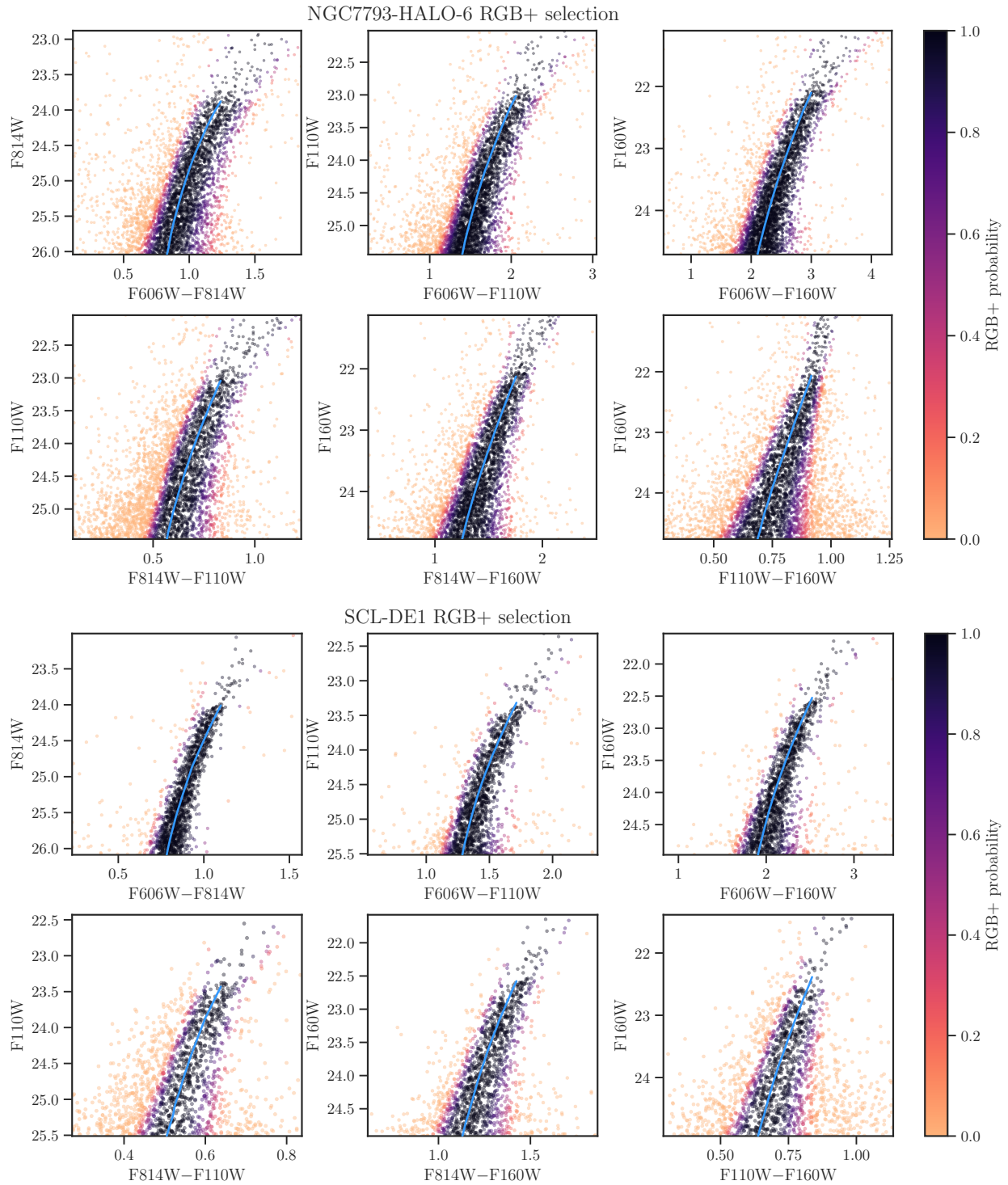


Figure B.4: —CONTINUED

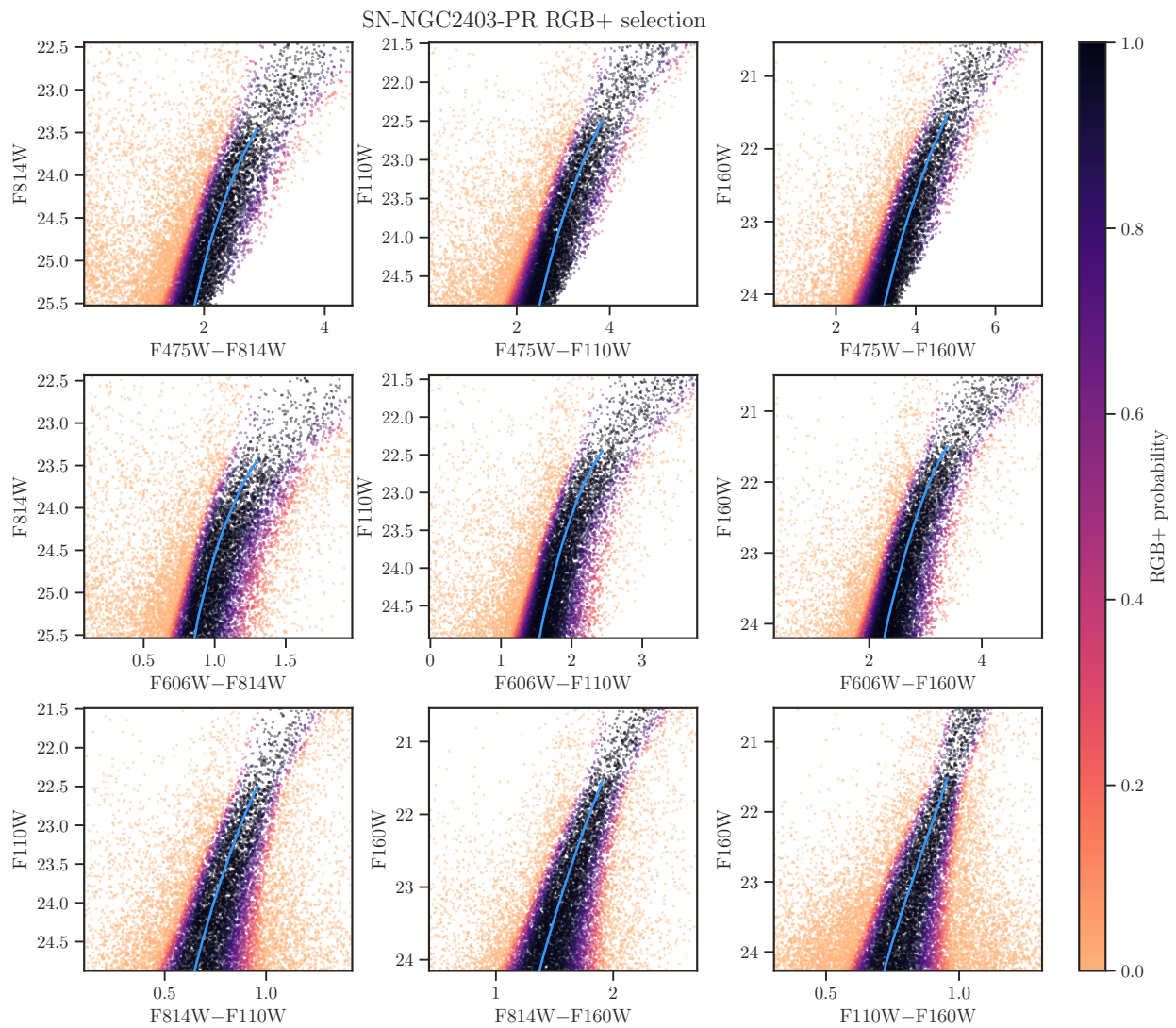


Figure B.4: —CONTINUED

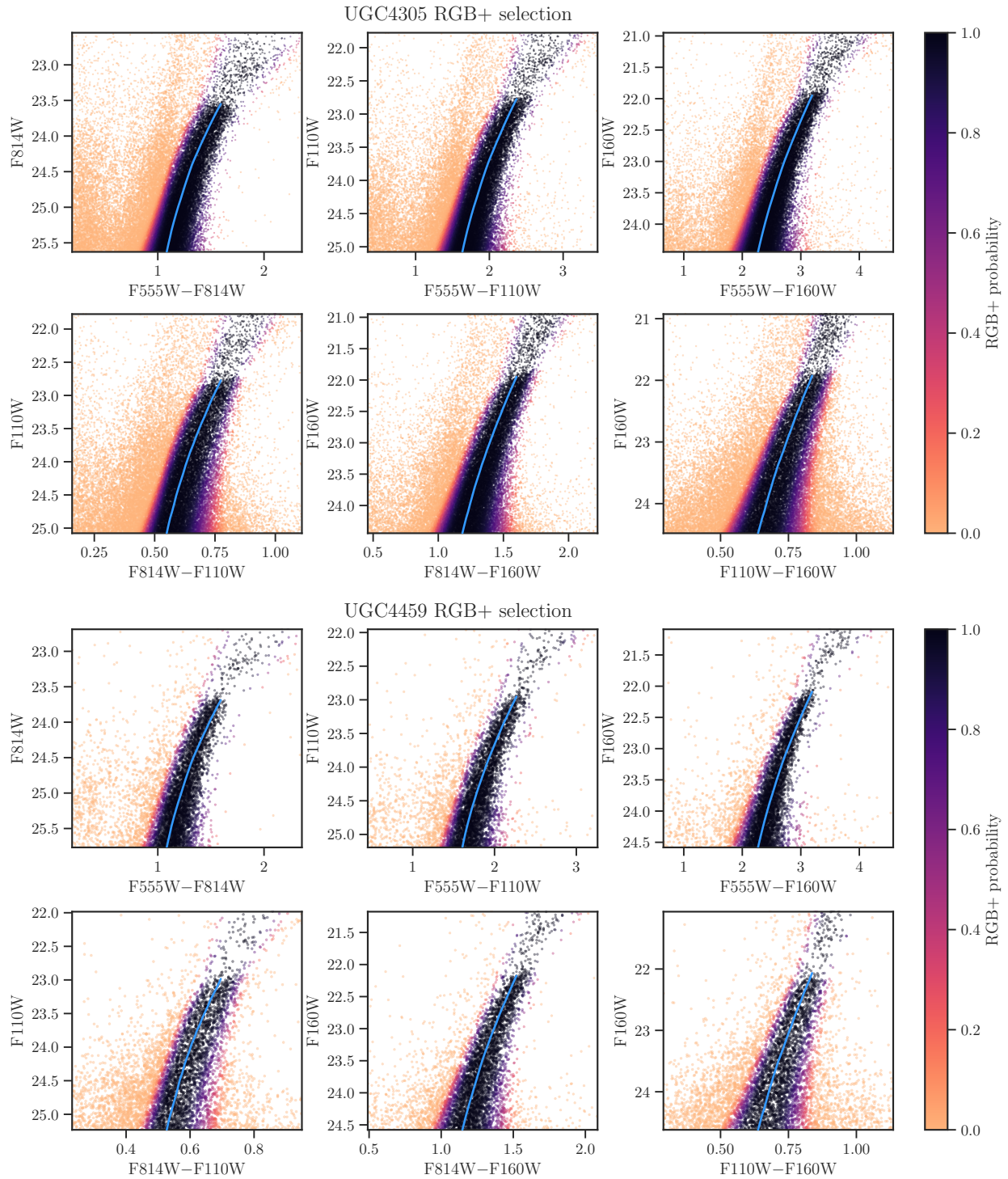




Figure B.4: —CONTINUED

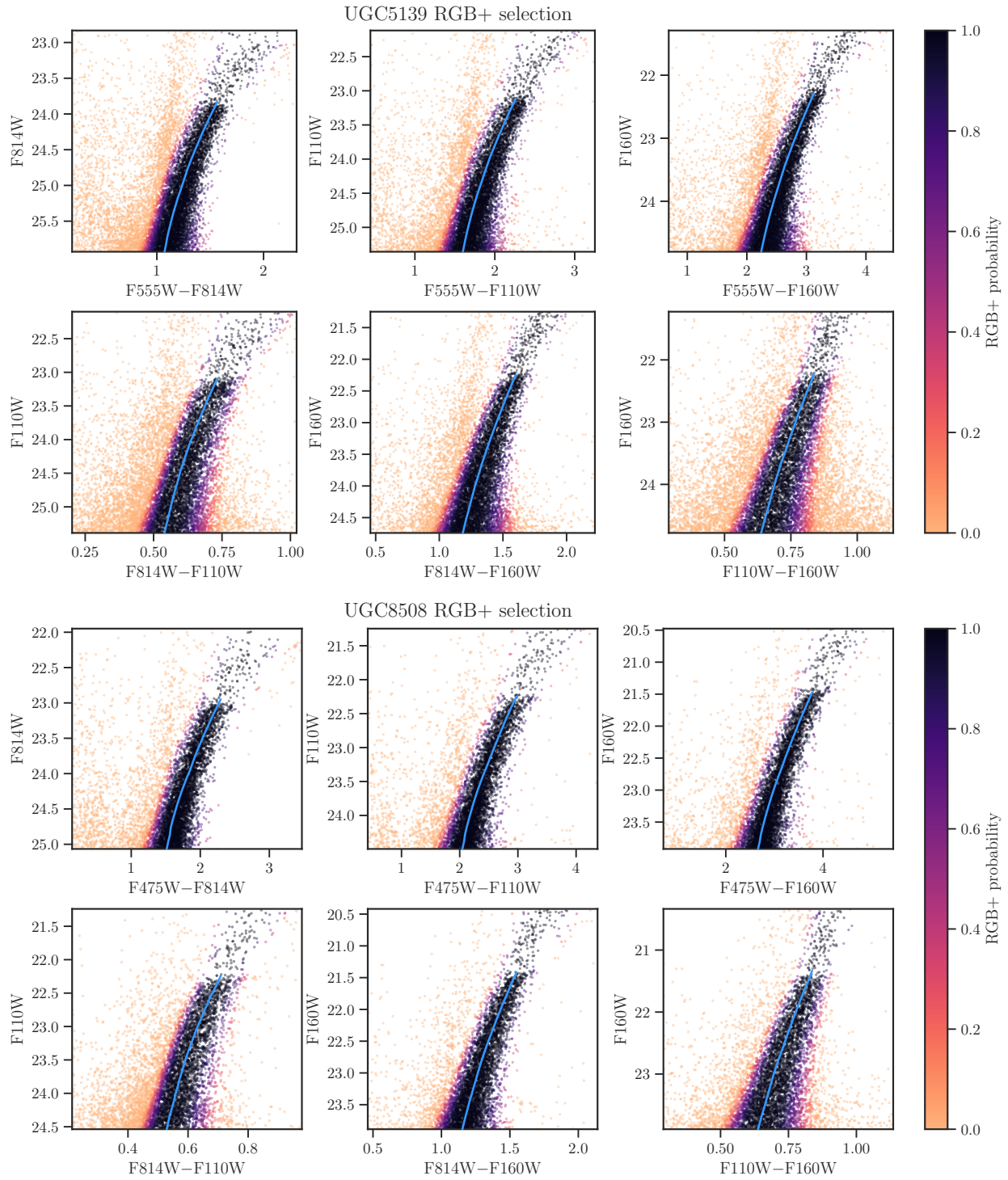


Figure B.4: —CONTINUED

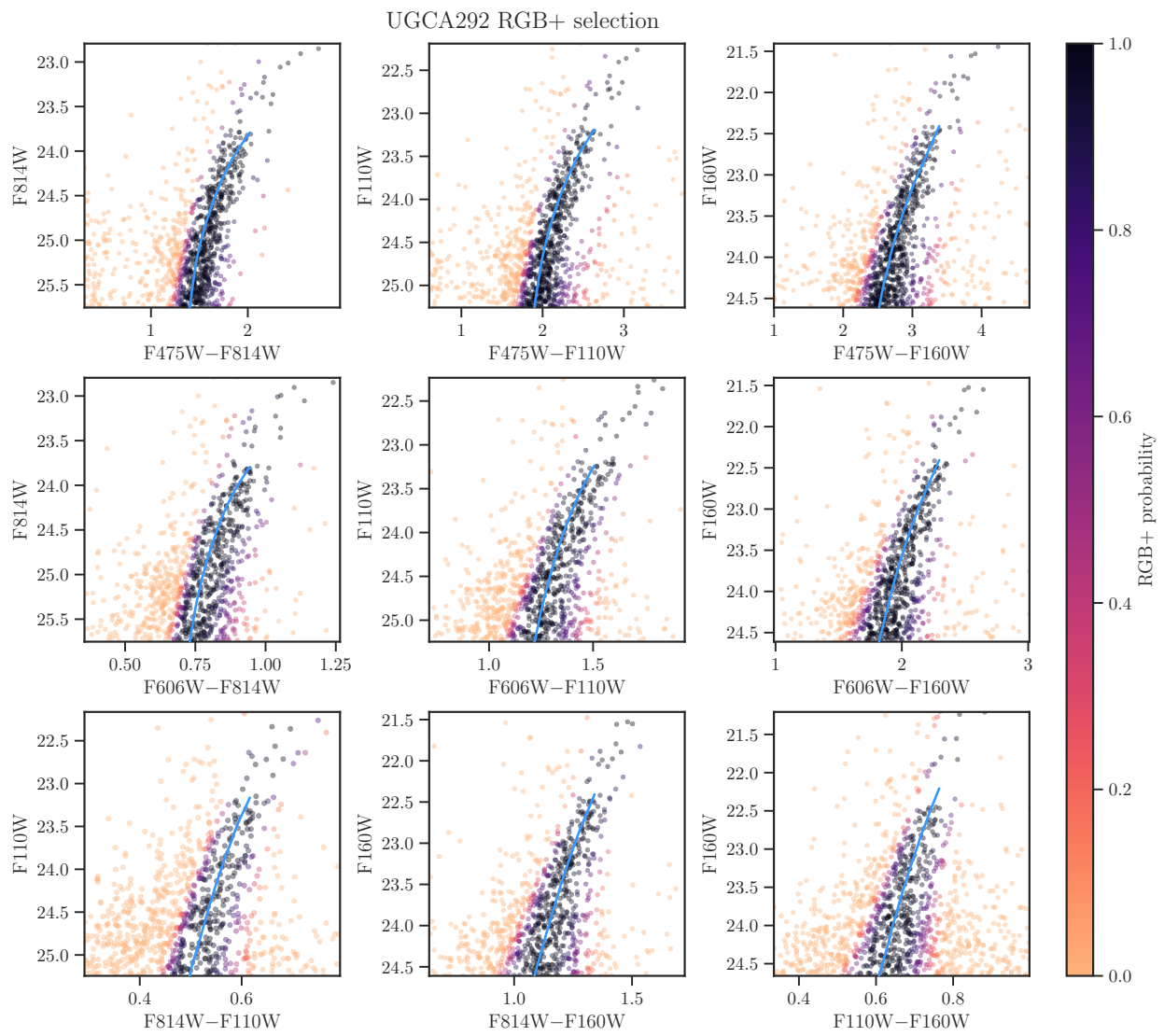


Figure B.5: Initial TRGB star selection

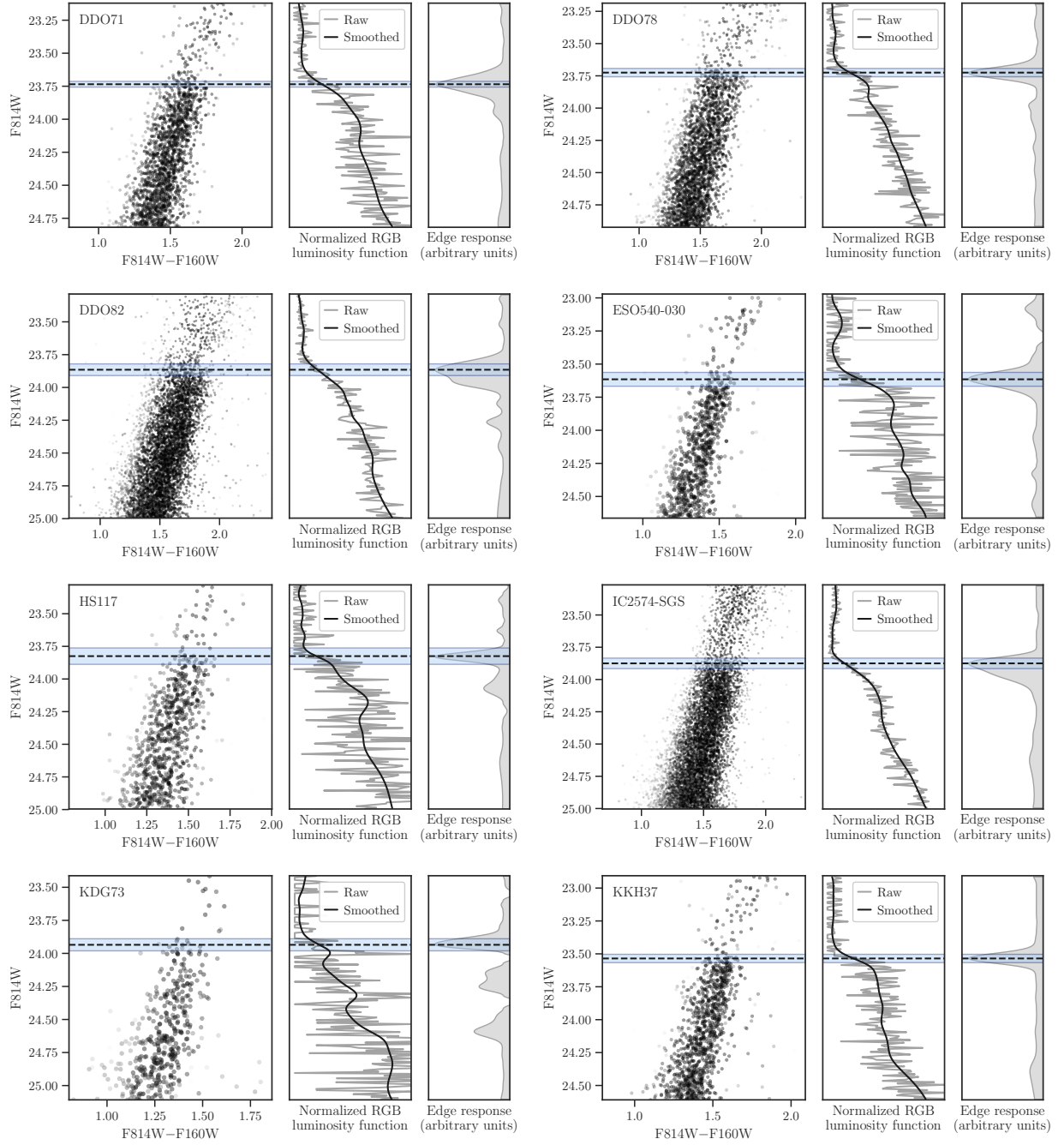


Figure B.5: —CONTINUED

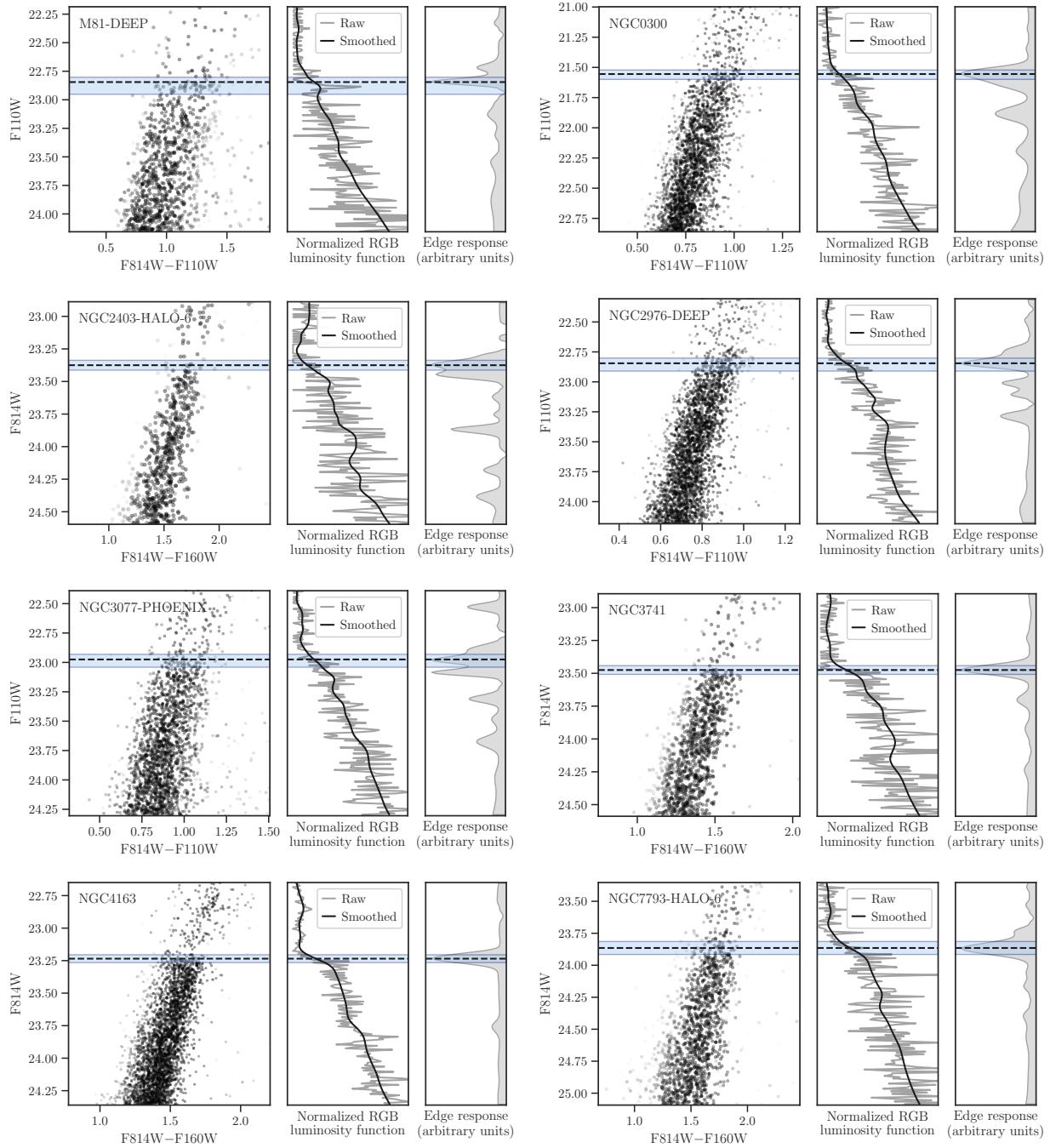




Figure B.5: —CONTINUED

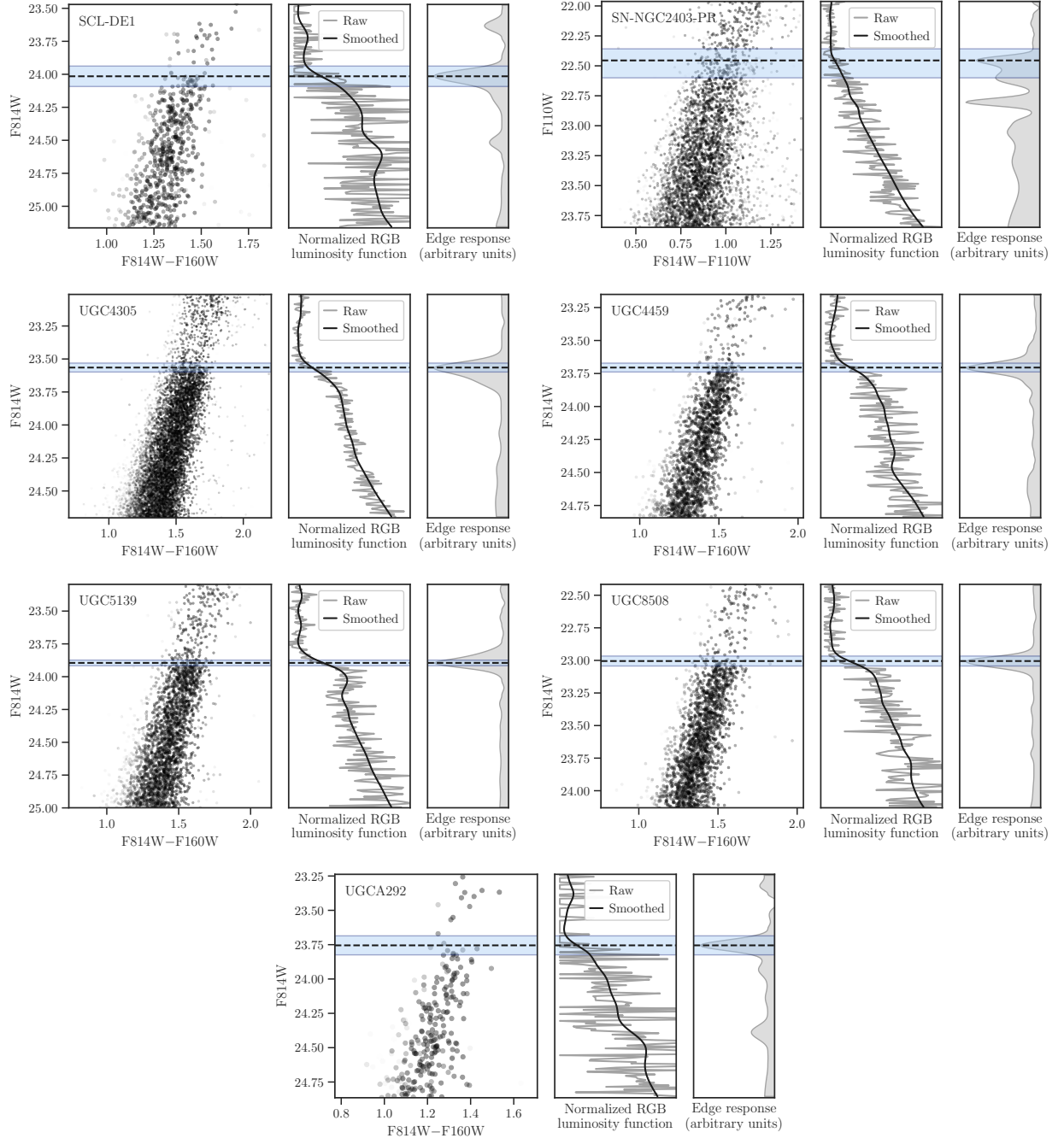


Figure B.6: Initial TRGB star selection

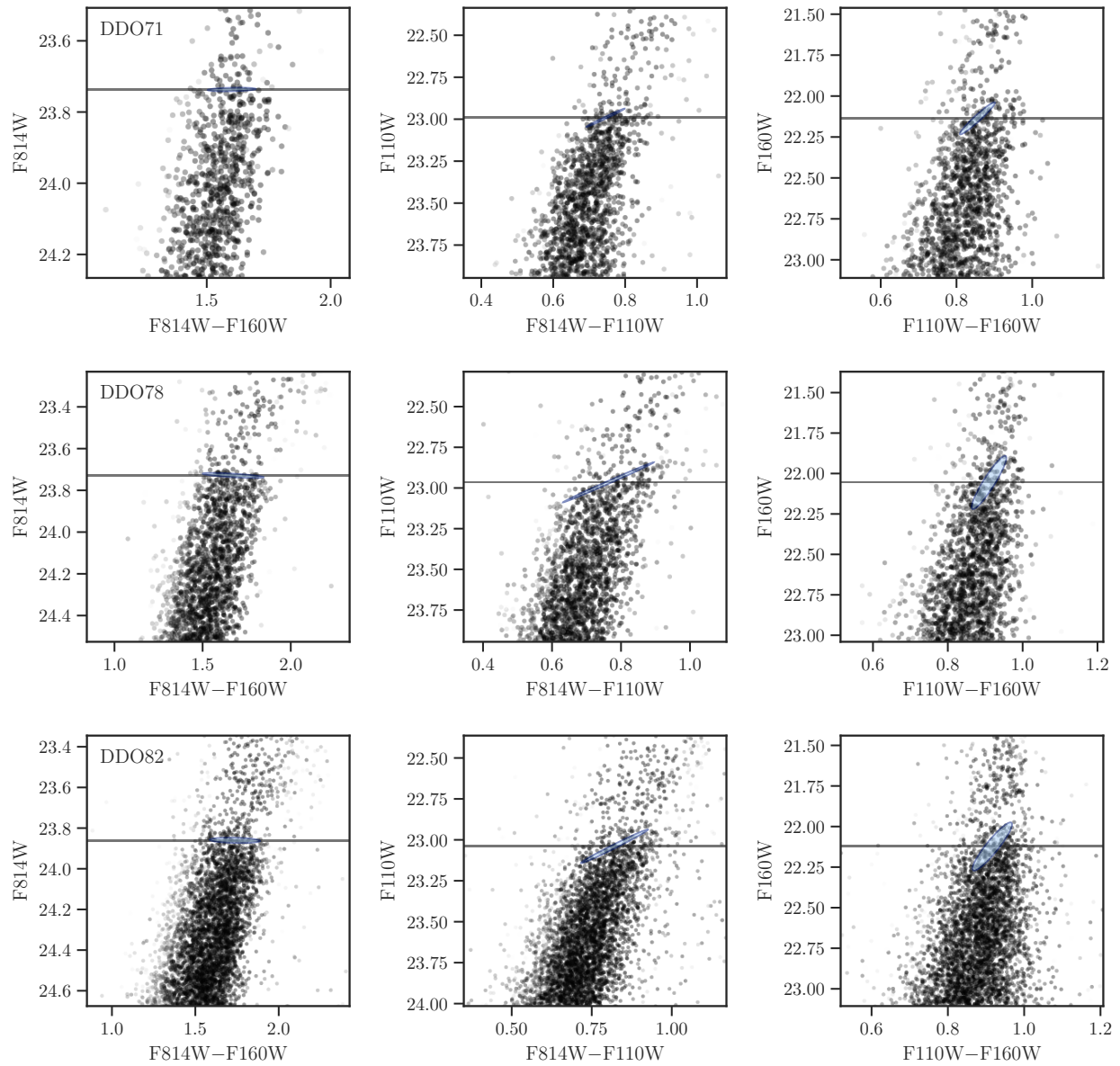


Figure B.6: —CONTINUED

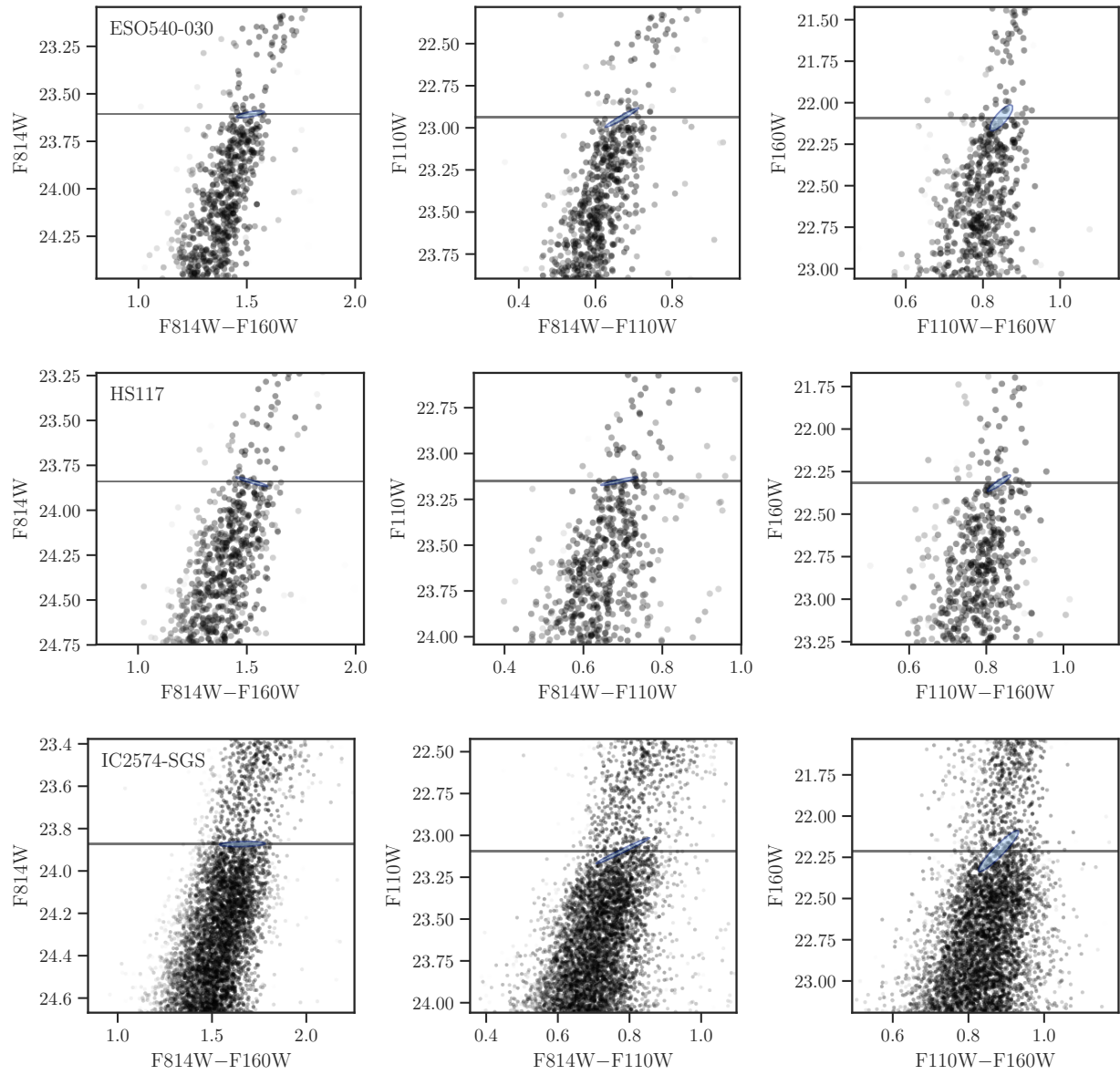


Figure B.6: —CONTINUED

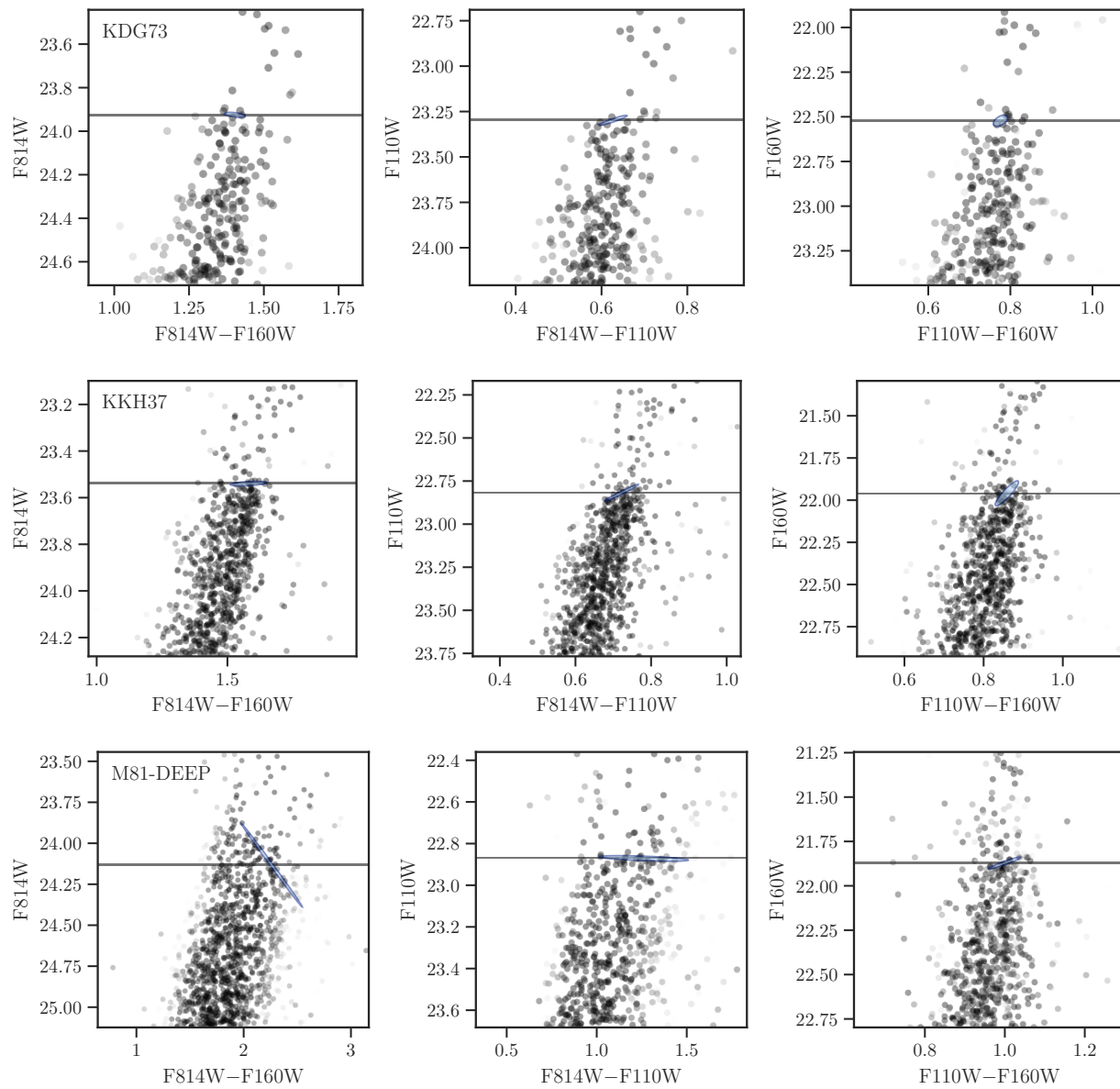


Figure B.6: —CONTINUED

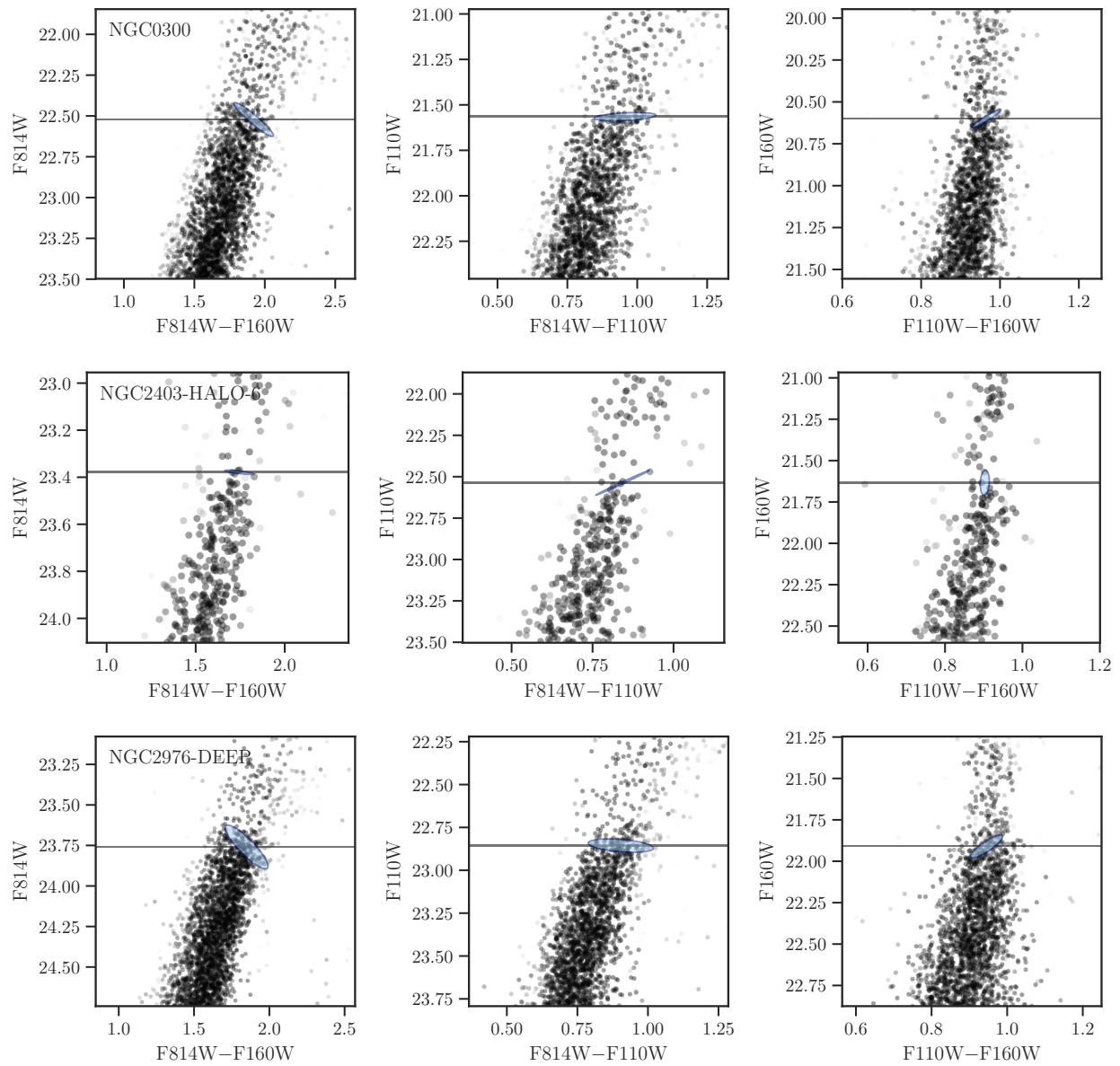


Figure B.6: —CONTINUED

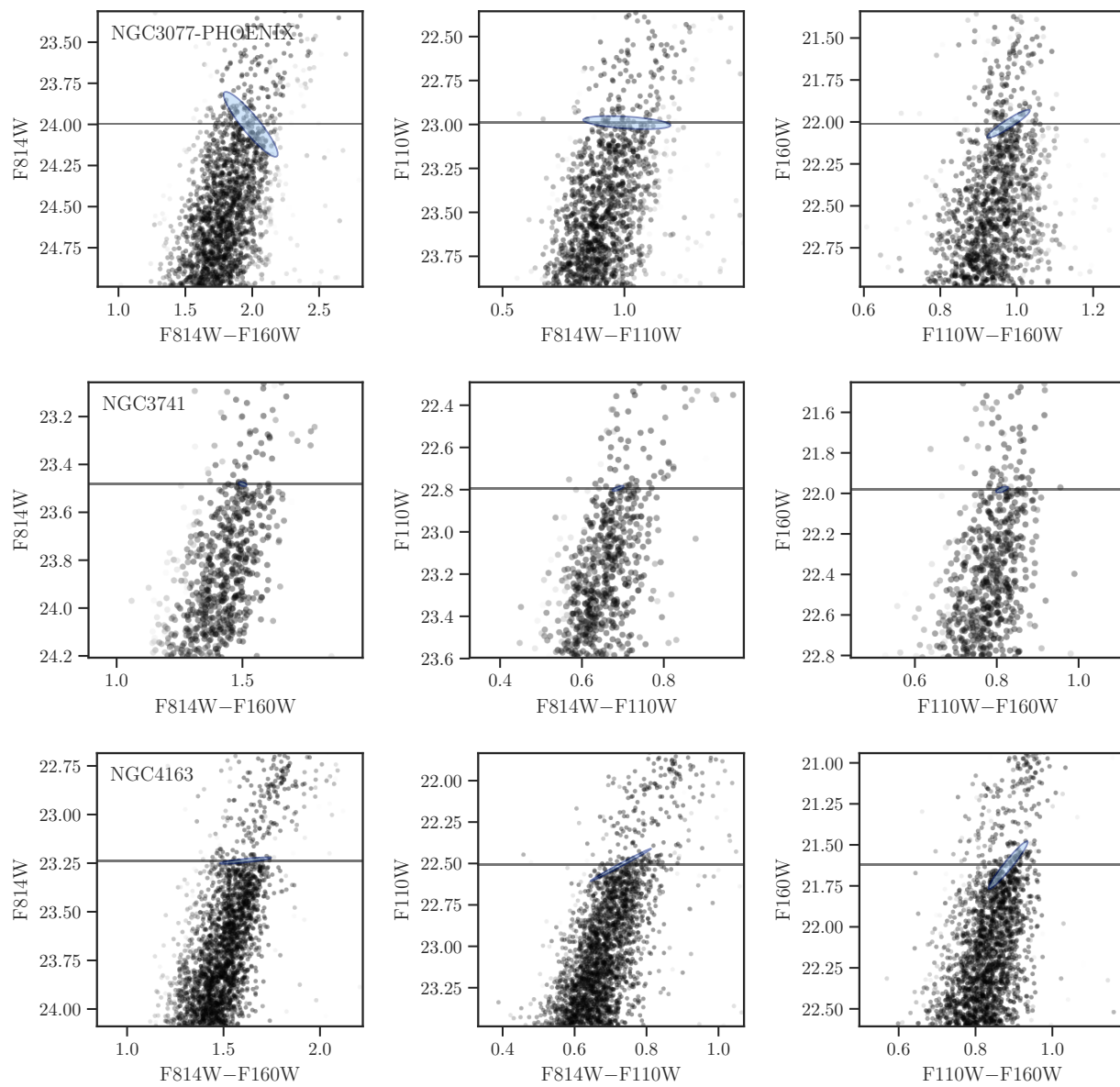




Figure B.6: —CONTINUED

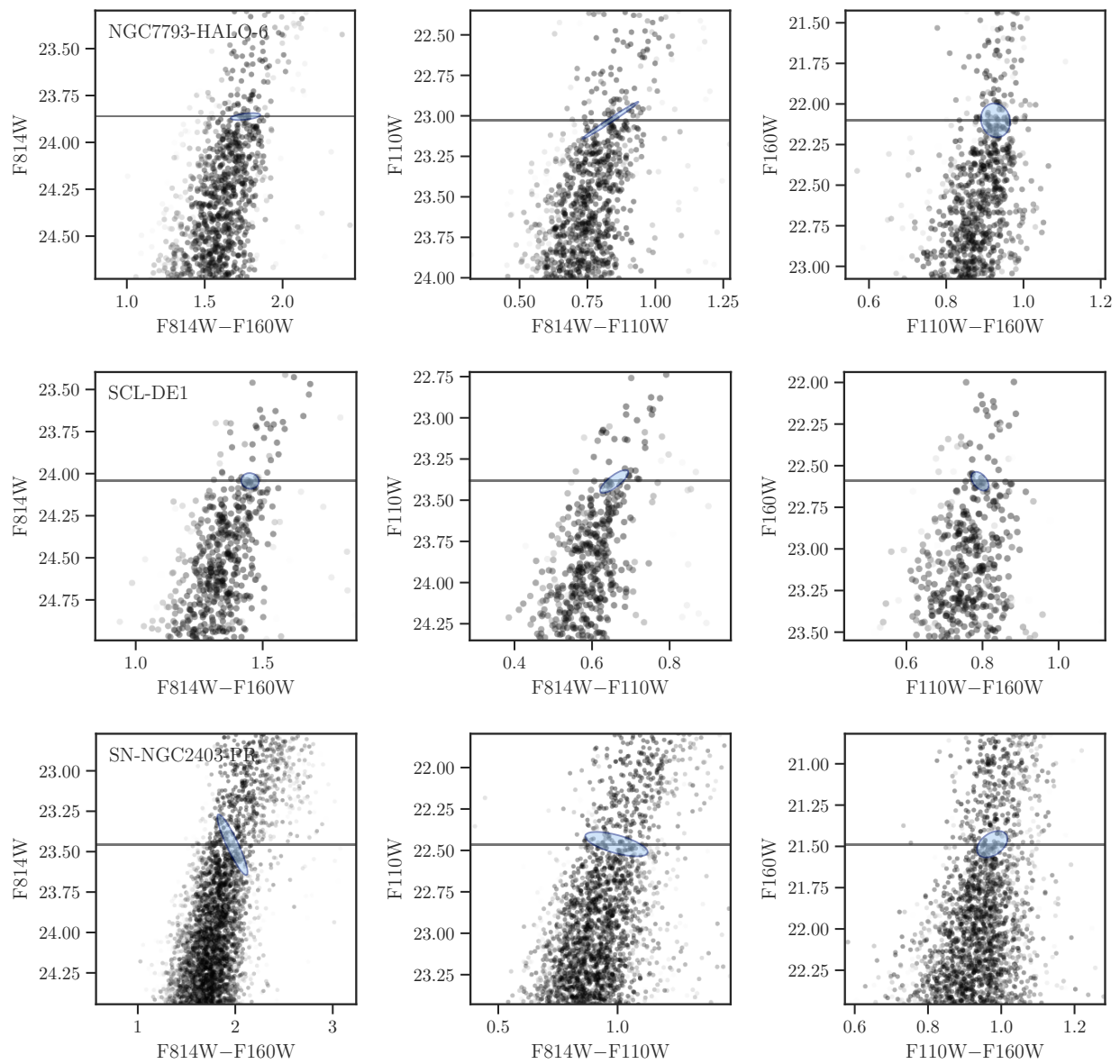


Figure B.6: —CONTINUED

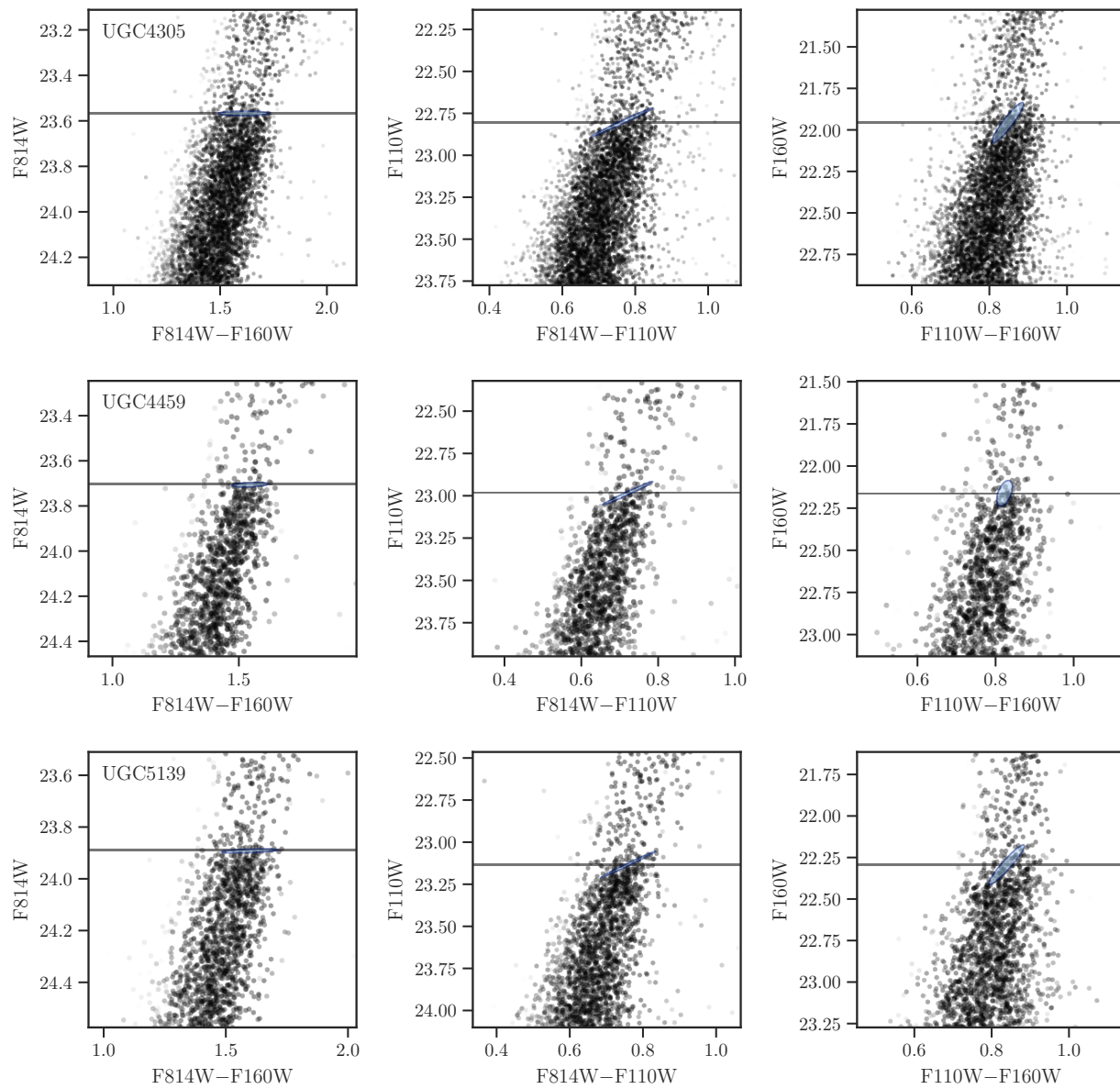
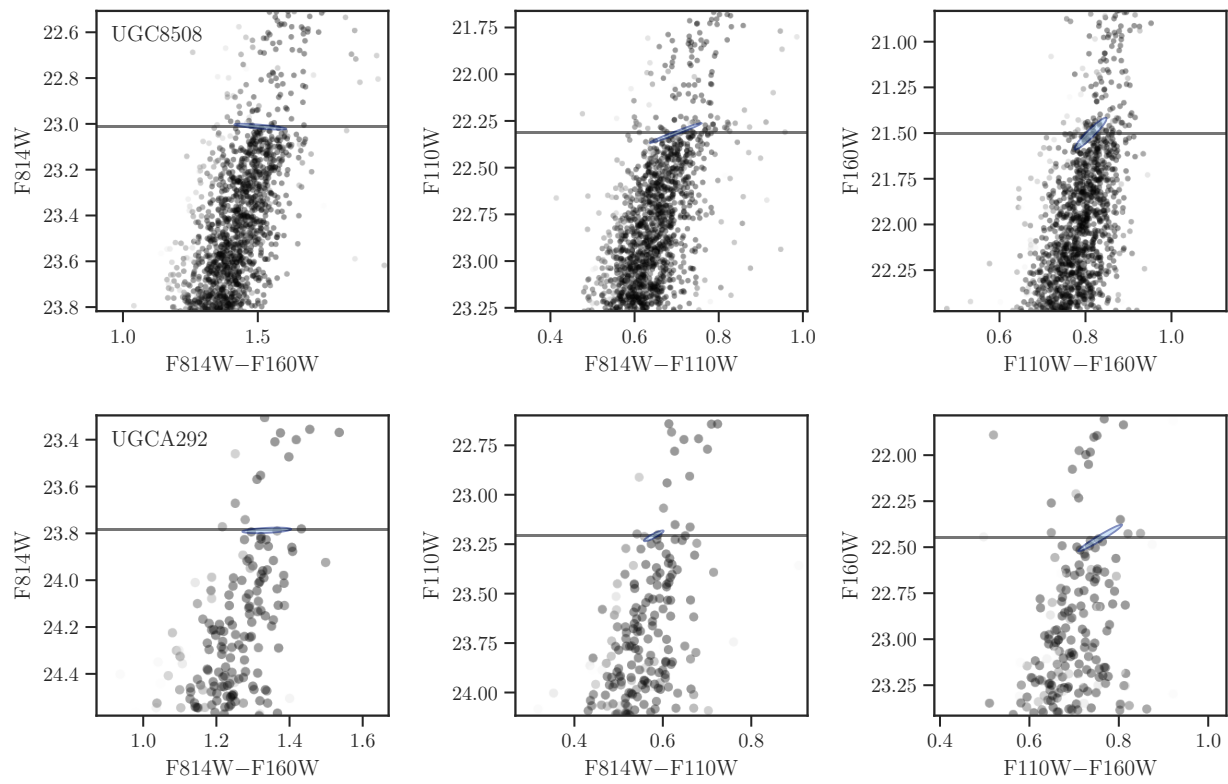




Figure B.6: —CONTINUED



Appendix C

**SYNTHETIC PHOTOMETRY TABLE**

Table C.1: Synthetic 2MASS and *HST* magnitudes

Spectrum Name	<i>J</i>	<i>H</i>	<i>K<sub>S</sub></i>	F110W	F125W	F160W
CALSPEC						
109vir_stis_003	3.675	3.668	3.673	3.667	3.675	3.672
10lac_stis_007	5.273	5.388	5.486	5.212	5.273	5.356
16cygb_stis_003	5.017	4.676	4.635	5.140	5.012	4.732
1732526_stisnic_007	12.264	12.216	12.210	12.287	12.263	12.220
1740346_stisnic_005	12.059	11.977	11.967	12.101	12.059	11.990
1743045_stisnic_007	12.933	12.820	12.805	12.990	12.933	12.838
1757132_stiswfc_004	11.262	11.159	11.156	11.305	11.261	11.176
1802271_stiswfcnic_004	11.827	11.811	11.803	11.825	11.825	11.819
1805292_stisnic_006	12.017	11.973	11.972	12.037	12.017	11.978
1808347_stiswfc_004	11.623	11.539	11.550	11.665	11.622	11.554
1812095_stisnic_006	11.324	11.255	11.256	11.348	11.322	11.266
1812524_nic_005	11.888	11.822	11.809	11.915	11.886	11.836
18sco_stis_003	4.295	3.955	3.915	4.417	4.290	4.011
2m003618_stiswfcnic_006	12.444	11.585	11.040	12.950	12.521	11.946
2m055914_stiswfcnic_005	13.777	13.570	13.588	14.412	14.025	13.909
agk_81d266_stisnic_007	12.678	12.807	12.921	12.603	12.677	12.770
alpha_lyr_stis_011	0.000	0.000	0.000	0.000	0.000	0.000
bd02d3375_stis_006	8.770	8.442	8.417	8.886	8.764	8.495

Table C.1: — continued

Spectrum Name	$J$	$H$	$K_S$	F110W	F125W	F160W
bd21d0607_stis_006	8.172	7.885	7.862	8.279	8.168	7.929
bd26d2606_stis_006	8.641	8.356	8.332	8.749	8.637	8.400
bd29d2091_stis_006	9.079	8.723	8.688	9.202	9.073	8.782
bd54d1216_stis_005	8.628	8.303	8.276	8.744	8.623	8.354
bd60d1753_stiswfc_004	9.613	9.606	9.610	9.607	9.612	9.609
bd_17d4708_stisnic_007	8.391	8.080	8.048	8.498	8.386	8.133
c26202_stiswfcnic_005	15.329	15.044	15.030	15.435	15.324	15.088
delumi_stis_004	4.257	4.243	4.242	4.257	4.256	4.248
eta1dor_stis_004	5.715	5.726	5.738	5.704	5.715	5.724
etauma_stis_007	2.216	2.282	2.336	2.179	2.217	2.263
feige110_stisnic_008	12.508	12.635	12.757	12.436	12.508	12.597
g191b2b_stiswfcnic_004	12.520	12.638	12.738	12.456	12.520	12.606
gd153_stiswfcnic_004	14.055	14.169	14.287	13.997	14.056	14.136
gd71_stiswfcnic_004	13.710	13.820	13.918	13.656	13.710	13.786
gj7541a_stis_004	12.343	12.359	12.393	12.336	12.343	12.349
grw_70d5824_stiswfcnic_003	13.247	13.318	13.395	13.219	13.247	13.291
hd009051_stis_007	7.237	6.761	6.698	7.393	7.229	6.847
hd031128_stis_006	8.036	7.746	7.715	8.149	8.032	7.791
hd074000_stis_006	8.645	8.351	8.328	8.755	8.641	8.397
hd101452_stis_003	6.954	6.844	6.827	7.007	6.953	6.858
hd106252_stis_006	6.279	5.954	5.919	6.397	6.274	6.007
hd111980_stis_006	7.203	6.851	6.818	7.325	7.197	6.910
hd115169_stis_003	8.022	7.673	7.635	8.144	8.017	7.731
hd116405_stis_006	8.402	8.424	8.443	8.384	8.402	8.420

Table C.1: — continued

Spectrum Name	$J$	$H$	$K_S$	F110W	F125W	F160W
hd128998_stis_003	5.792	5.787	5.792	5.787	5.791	5.790
hd142331_stis_004	7.462	7.105	7.066	7.587	7.456	7.165
hd14943_stis_005	5.543	5.474	5.458	5.582	5.543	5.482
hd158485_stis_005	6.199	6.153	6.135	6.228	6.199	6.158
hd159222_stis_007	5.374	5.056	5.018	5.492	5.369	5.107
hd160617_stis_005	7.605	7.274	7.250	7.721	7.600	7.327
hd163466_stis_005	6.442	6.368	6.352	6.482	6.442	6.379
hd165459_stisnic_006	6.621	6.571	6.568	6.646	6.620	6.577
hd167060_stis_004	7.746	7.407	7.367	7.868	7.741	7.463
hd172728_stis_002	5.768	5.782	5.799	5.752	5.768	5.780
hd180609_stis_006	9.119	9.084	9.081	9.136	9.119	9.090
hd185975_stis_007	6.858	6.504	6.460	6.984	6.852	6.563
hd200654_stis_007	7.607	7.168	7.119	7.750	7.600	7.246
hd205905_stis_007	5.607	5.291	5.254	5.724	5.602	5.342
hd209458_stisnic_008	6.610	6.328	6.300	6.718	6.607	6.374
hd2811_stis_004	7.140	7.069	7.055	7.170	7.139	7.081
hd37725_stiswfc_004	7.953	7.907	7.899	7.978	7.952	7.912
hd37962_stis_008	6.636	6.283	6.245	6.759	6.630	6.342
hd38949_stis_007	6.715	6.411	6.380	6.828	6.710	6.459
hd55677_stis_004	9.186	9.156	9.151	9.196	9.186	9.163
hd93521_stis_007	7.519	7.631	7.726	7.460	7.518	7.600
kf01t5_nic_004	11.705	11.156	11.053	11.881	11.697	11.274
kf06t1_nic_004	11.493	10.932	10.851	11.663	11.486	11.047
kf06t2_stiswfcnic_005	11.823	11.201	11.111	12.009	11.814	11.332
kf08t3_stisnic_004	11.550	11.038	10.958	11.708	11.544	11.137

Table C.1: — continued

Spectrum Name	$J$	$H$	$K_S$	F110W	F125W	F160W
ksi2ceti_stis_006	4.336	4.347	4.359	4.324	4.336	4.345
lamlep_stis_007	4.821	4.931	5.023	4.759	4.821	4.900
lds749b_stisnic_008	14.918	14.959	15.020	14.889	14.918	14.938
mucol_stis_007	5.768	5.886	5.984	5.705	5.768	5.853
p041c_stisnic_009	10.868	10.564	10.521	10.982	10.865	10.615
p177d_stisnic_009	12.240	11.902	11.837	12.362	12.236	11.961
p330e_stiswfcnic_005	11.772	11.436	11.393	11.890	11.766	11.495
sdssj151421_stis_005	16.428	16.524	16.629	16.375	16.428	16.492
sf1615_001a_stisnic_010	15.242	14.897	14.870	15.348	15.235	14.957
sirius_stis_005	-1.421	-1.410	-1.406	-1.421	-1.421	-1.414
snap1_stisnic_008	15.996	15.947	16.017	15.974	15.996	15.961
snap2_stiswfcnic_004	14.942	14.586	14.545	15.067	14.937	14.645
vb8_stiswfcnic_004	9.773	9.155	8.790	10.109	9.804	9.402
wd0148_467_stiswfc_001	12.764			12.756	12.764	12.767
wd0227_050_stiswfc_002	13.265			13.238	13.266	13.297
wd0308_565_stis_009	14.576	14.671	14.754	14.541	14.576	14.643
wd0320_539_stis_005	15.622	15.731	15.832	15.567	15.622	15.698
wd0809_177_stiswfc_002	13.769			13.752	13.768	13.781
wd0947_857_stis_006	16.457	16.574	16.674	16.396	16.457	16.541
wd1026_453_stis_006	16.814	16.930	17.031	16.756	16.815	16.897
wd1057_719_stisnic_011	15.447	15.558	15.737	15.389	15.447	15.524
wd1105_048_stiswfc_002	13.420			13.405	13.419	13.429
wd1105_340_stiswfc_002	13.914			13.911	13.913	13.912
wd1202_232_stiswfc_002	12.419			12.463	12.417	12.306
wd1327_083_stiswfc_004	12.634			12.626	12.633	12.657

Table C.1: — continued

Spectrum Name	$J$	$H$	$K_S$	F110W	F125W	F160W
wd1544_377_stiswfc_002	12.912			12.942	12.913	12.847
wd1657_343_stiswfcnic_006	17.149	17.274	17.367	17.081	17.149	17.241
wd1713_695_stiswfc_002	13.653			13.637	13.652	13.669
wd1911_536_stiswfc_001	13.635			13.614	13.635	13.655
wd1919_145_stiswfc_001	13.321			13.310	13.317	13.306
wd2039_682_stiswfc_001	13.698			13.679	13.697	13.709
wd2117_539_stiswfc_002	12.673			12.669	12.673	12.677
wd2126_734_stiswfc_002	13.206			13.193	13.205	13.218
wd2149_021_stiswfc_001	13.176			13.154	13.176	13.200
wd2341_322_stiswfc_004	13.130			13.131	13.129	13.126
Extended IRTF Spectral Library (EIRTF)						
BD+002058A	9.143	8.844	8.815	9.257	9.142	8.894
BD+012916	7.184	6.523	6.408	7.382	7.176	6.664
BD+053080	7.448	6.968	6.900	7.601	7.441	7.061
BD+112998	7.575	7.178	7.117	7.707	7.564	7.237
BD+130013	6.822	6.337	6.232	6.979	6.815	6.443
BD+172473	8.675	8.203	8.103	8.825	8.669	8.292
BD+182890	8.229	7.760	7.701	8.376	8.223	7.841
BD+290366	7.567	7.226	7.184	7.688	7.563	7.282
BD+302611	6.846	6.166	6.054	7.046	6.835	6.306
BD+312360	9.433	8.879	8.798	9.602	9.425	8.985
BD+430699	7.123	6.590	6.494	7.287	7.117	6.701
BD+501021	8.821	8.341	8.264	8.980	8.815	8.435
BD+511696	8.679	8.304	8.282	8.808	8.672	8.365

Table C.1: — continued

Spectrum Name	$J$	$H$	$K_S$	F110W	F125W	F160W
BD-010306	7.873	7.536	7.504	7.987	7.870	7.590
BD-011792	7.586	7.095	7.038	7.744	7.581	7.190
BD-060855	9.245	8.859	8.806	9.373	9.236	8.919
BD-103166	8.600	8.212	8.125	8.750	8.606	8.303
BD-182065	7.843	7.316	7.224	8.016	7.838	7.422
CD-2809374	8.623	8.140	8.069	8.772	8.614	8.228
G171-010	6.820	6.219	5.922	7.100	6.822	6.389
HD001461	5.323	4.998	4.850	5.443	5.310	5.033
HD001918	5.793	5.277	5.204	5.960	5.789	5.382
HD003546	2.662	2.151	2.057	2.826	2.652	2.246
HD003567	8.194	7.895	7.842	8.307	8.190	7.944
HD003574	2.525	1.771	1.598	2.754	2.521	1.960
HD004307	4.998	4.671	4.627	5.116	4.994	4.719
HD004744	5.619	4.998	4.896	5.805	5.606	5.117
HD004906	7.242	6.786	6.738	7.397	7.235	6.864
HD006497	4.648	4.037	3.916	4.835	4.634	4.166
HD006755	6.162	5.683	5.642	6.326	6.162	5.780
HD007106	2.839	2.270	2.140	3.027	2.838	2.400
HD007351	2.749	1.900	1.656	3.001	2.731	2.106
HD009919	4.801	4.593	4.568	4.890	4.802	4.631
HD011397	7.650	7.290	7.248	7.774	7.645	7.355
HD013520	2.244	1.508	1.357	2.459	2.240	1.681
HD013783	7.011	6.634	6.555	7.146	7.009	6.706
HD017361	2.912	2.340	2.223	3.096	2.905	2.461
HD017491	1.601	0.707	0.431	1.876	1.588	0.929

Table C.1: — continued

Spectrum Name	$J$	$H$	$K_S$	F110W	F125W	F160W
HD017548	7.053	6.775	6.757	7.161	7.049	6.818
HD018191	0.238	-0.651	-0.933	0.528	0.224	-0.428
HD019373	3.120	2.848	2.805	3.226	3.123	2.898
HD020893	2.975	2.369	2.238	3.176	2.975	2.518
HD021581	6.903	6.409	6.349	7.045	6.893	6.492
HD022879	5.537	5.237	5.205	5.644	5.530	5.286
HD023439A	6.609	6.152	6.087	6.761	6.606	6.241
HD023439B	6.942	6.412	6.338	7.110	6.936	6.515
HD024341	6.566	6.143	6.059	6.712	6.558	6.221
HD024421	5.785	5.490	5.422	5.898	5.784	5.548
HD025673	7.982	7.504	7.450	8.138	7.977	7.595
HD026297	5.353	4.718	4.597	5.531	5.338	4.844
HD027371	1.991	1.543	1.462	2.151	1.986	1.643
HD027771	7.594	7.197	7.130	7.739	7.592	7.274
HD030649	5.798	5.452	5.401	5.923	5.793	5.510
HD031128	8.090	7.777	7.635	8.206	8.089	7.831
HD031767	2.168	1.523	1.326	2.375	2.163	1.672
HD033608	5.126	4.923	4.885	5.211	5.123	4.952
HD034411	3.425	3.128	3.071	3.540	3.423	3.179
HD035179	7.647	7.132	7.049	7.804	7.627	7.219
HD036003	5.588	4.985	4.886	5.767	5.570	5.101
HD036395	4.970	4.261	4.074	5.187	4.958	4.424
HD037160	2.431	1.864	1.785	2.604	2.425	1.979
HD037828	4.818	4.163	4.014	5.004	4.802	4.288
HD037984	2.958	2.343	2.246	3.141	2.945	2.465



Table C.1: — continued

Spectrum Name	$J$	$H$	$K_S$	F110W	F125W	F160W
HD038393	2.837	2.603	2.565	2.930	2.824	2.625
HD039364	2.136	1.575	1.467	2.306	2.124	1.689
HD039833	6.487	6.174	6.118	6.606	6.481	6.227
HD042543	1.447	0.743	0.545	1.703	1.466	0.973
HD044030	5.034	4.264	4.110	5.256	5.020	4.426
HD045282	6.567	6.143	6.070	6.706	6.563	6.218
HD045829	4.037	3.456	3.311	4.237	4.042	3.610
HD054719	2.429	1.835	1.703	2.619	2.427	1.973
HD055496	6.523	5.980	5.903	6.694	6.520	6.093
HD058551	5.538	5.273	5.241	5.638	5.533	5.307
HD061935	2.277	1.770	1.680	2.441	2.270	1.878
HD065583	5.502	5.117	5.093	5.633	5.497	5.183
HD073394	5.601	5.007	4.939	5.770	5.580	5.111
HD074011	6.183	5.822	5.777	6.305	6.171	5.870
HD074377	6.709	6.164	6.087	6.882	6.703	6.270
HD074462	6.627	6.054	6.017	6.810	6.629	6.169
HD074721	8.527	8.528	8.427	8.531	8.522	8.525
HD075318	6.535	6.147	6.090	6.668	6.530	6.217
HD075691	1.960	1.302	1.187	2.165	1.953	1.449
HD076151	4.824	4.522	4.460	4.937	4.814	4.563
HD076932	4.716	4.402	4.367	4.834	4.719	4.464
HD077236	5.390	4.753	4.660	5.584	5.385	4.893
HD082074	4.721	4.257	4.191	4.874	4.716	4.348
HD082734	3.426	2.977	2.907	3.586	3.423	3.071
HD083212	6.234	5.667	5.586	6.409	6.225	5.778

Table C.1: — continued

Spectrum Name	$J$	$H$	$K_S$	F110W	F125W	F160W
HD083632	5.614	4.838	4.646	5.834	5.600	5.005
HD086986	7.607	7.497	7.425	7.646	7.603	7.510
HD087141	4.783	4.538	4.500	4.884	4.777	4.572
HD088230	3.899	3.220	3.072	4.103	3.884	3.368
HD088446	6.771	6.464	6.406	6.877	6.755	6.490
HD088725	6.548	6.188	6.100	6.678	6.542	6.249
HD088986	5.235	4.907	4.855	5.358	5.231	4.964
HD089010	4.752	4.409	4.353	4.879	4.747	4.467
HD091347	6.370	6.043	6.000	6.488	6.364	6.094
HD094028	7.134	6.818	6.785	7.251	7.141	6.872
HD095128	4.048	3.760	3.727	4.158	4.048	3.809
HD096360	4.030	3.168	2.862	4.291	4.025	3.377
HD097855	5.550	5.285	5.239	5.650	5.533	5.310
HD099109	7.600	7.210	7.144	7.746	7.595	7.279
HD100906	7.991	7.523	7.456	8.146	7.993	7.620
HD102328	3.455	2.875	2.734	3.642	3.428	2.992
HD103095	4.917	4.446	4.374	5.068	4.910	4.536
HD104307	3.917	3.295	3.179	4.115	3.911	3.433
HD105452	3.537	3.378	3.359	3.602	3.535	3.403
HD105546	7.186	6.697	6.605	7.343	7.170	6.776
HD105740	6.478	5.905	5.822	6.650	6.462	6.011
HD106038	9.082	8.768	8.731	9.203	9.081	8.821
HD107213	5.377	5.141	5.105	5.475	5.374	5.175
HD108564	7.522	6.961	6.881	7.690	7.518	7.071
HD109443	8.332	8.163	8.156	8.398	8.329	8.182

Table C.1: — continued

Spectrum Name	$J$	$H$	$K_S$	F110W	F125W	F160W
HD114038	3.448	2.857	2.740	3.636	3.444	2.988
HD114606	7.532	7.137	7.068	7.673	7.532	7.213
HD114710	3.272	3.004	2.949	3.383	3.269	3.049
HD115589	8.109	7.685	7.571	8.272	8.123	7.782
HD115617	3.331	2.986	2.927	3.457	3.327	3.052
HD116316	6.668	6.427	6.393	6.768	6.665	6.465
HD117176	3.853	3.500	3.449	3.980	3.847	3.563
HD117200	5.920	5.713	5.671	6.013	5.921	5.750
HD117635	5.814	5.392	5.334	5.952	5.813	5.476
HD117876	4.570	4.025	3.940	4.742	4.562	4.134
HD118244	5.882	5.621	5.594	5.979	5.880	5.662
HD119288	5.368	5.159	5.071	5.464	5.369	5.192
HD120136	3.719	3.571	3.582	3.788	3.710	3.580
HD125451	4.577	4.413	4.395	4.651	4.571	4.426
HD126141	5.399	5.232	5.221	5.478	5.401	5.254
HD126614	7.446	7.110	7.019	7.567	7.430	7.160
HD126778	6.408	5.888	5.810	6.575	6.404	5.990
HD128959	7.903	7.588	7.552	8.016	7.900	7.640
HD130095	7.751	7.722	7.724	7.755	7.751	7.725
HD130322	6.667	6.281	6.234	6.812	6.671	6.359
HD130705	4.723	4.167	4.034	4.924	4.728	4.303
HD130817	5.288	5.091	5.056	5.381	5.289	5.126
HD132142	6.239	5.824	5.799	6.376	6.228	5.895
HD132475	7.289	6.942	6.889	7.410	7.283	7.000
HD134063	6.016	5.513	5.424	6.179	6.008	5.603

Table C.1: — continued

Spectrum Name	$J$	$H$	$K_S$	F110W	F125W	F160W
HD134083	4.121	3.918	3.874	4.207	4.110	3.930
HD134440	7.765	7.258	7.165	7.928	7.758	7.357
HD134987	5.301	4.997	4.927	5.415	5.295	5.048
HD136064	4.279	4.001	3.961	4.391	4.277	4.047
HD137391	3.866	3.728	3.712	3.943	3.878	3.757
HD137471	1.960	1.175	0.994	2.191	1.947	1.364
HD138290	5.833	5.663	5.632	5.911	5.833	5.691
HD138776	7.449	7.133	7.076	7.576	7.453	7.195
HD139641	3.680	3.190	3.179	3.834	3.661	3.279
HD142575	7.670	7.486	7.468	7.749	7.670	7.510
HD144585	5.139	4.870	4.821	5.247	5.135	4.918
HD145148	4.301	3.815	3.715	4.460	4.289	3.909
HD145976	5.672	5.495	5.465	5.749	5.668	5.512
HD150177	5.272	5.012	4.987	5.364	5.262	5.046
HD152601	3.492	2.966	2.868	3.666	3.489	3.084
HD154733	3.344	2.725	2.626	3.535	3.342	2.866
HD155763	3.569	3.610	3.593	3.531	3.567	3.597
HD157089	5.761	5.424	5.374	5.884	5.759	5.485
HD157881	4.933	4.292	4.158	5.125	4.925	4.440
HD161149	5.244	5.082	5.053	5.325	5.241	5.107
HD162211	3.188	2.656	2.559	3.367	3.184	2.774
HD164349	2.575	2.012	1.918	2.755	2.567	2.139
HD166460	3.310	2.730	2.607	3.489	3.294	2.852
HD170737	6.474	5.974	5.887	6.634	6.469	6.065
HD171496	6.129	5.616	5.542	6.296	6.121	5.715

Table C.1: — continued

Spectrum Name	$J$	$H$	$K_S$	F110W	F125W	F160W
HD173740	5.722	5.165	4.932	5.951	5.718	5.309
HD174912	6.025	5.726	5.633	6.145	6.026	5.779
HD175535	3.528	3.098	3.010	3.678	3.525	3.191
HD175640	6.136	6.207	6.263	6.095	6.130	6.179
HD182572	3.593	3.259	3.259	3.720	3.593	3.325
HD185657	4.706	4.189	4.099	4.873	4.698	4.293
HD189558	6.500	6.177	6.146	6.609	6.489	6.223
HD190178	8.322	8.068	8.073	8.427	8.324	8.116
HD190360	4.468	4.124	4.074	4.596	4.449	4.170
HD192640	4.517	4.435	4.430	4.557	4.513	4.429
HD196755	4.053	3.698	3.632	4.176	4.043	3.755
HD199191	5.349	4.794	4.717	5.529	5.351	4.912
HD200527	2.244	1.407	1.149	2.496	2.222	1.612
HD200779	6.002	5.427	5.324	6.183	5.998	5.558
HD201891	6.257	5.937	5.897	6.373	6.254	5.993
HD203638	3.377	2.833	2.710	3.558	3.368	2.957
HD204155	7.335	7.007	6.975	7.456	7.335	7.069
HD204587	6.634	5.980	5.841	6.828	6.623	6.117
HD204613	7.098	6.780	6.734	7.221	7.114	6.852
HD205153	7.130	6.856	6.816	7.232	7.120	6.894
HD205512	3.325	2.789	2.692	3.499	3.314	2.900
HD207222	8.349	8.331	8.342	8.359	8.350	8.335
HD210295	7.772	7.240	7.177	7.933	7.770	7.344
HD213042	5.843	5.207	5.025	6.055	5.837	5.346
HD216131	1.761	1.273	1.191	1.917	1.750	1.368

Table C.1: — continued

Spectrum Name	$J$	$H$	$K_S$	F110W	F125W	F160W
HD216174	3.611	2.943	2.704	3.815	3.608	3.092
HD217107	4.999	4.644	4.489	5.133	4.989	4.699
HD218640	3.290	3.065	3.012	3.384	3.292	3.102
HD219734	1.483	0.652	0.420	1.731	1.472	0.854
HD221148	4.611	4.070	3.853	4.797	4.603	4.192
HD221377	6.593	6.363	6.335	6.684	6.591	6.399
HD221830	5.654	5.316	5.264	5.779	5.650	5.375
HD223524	3.917	3.356	3.248	4.085	3.882	3.458
HD224458	6.341	5.779	5.679	6.528	6.334	5.892
HD284248	8.147	7.866	7.836	8.255	8.142	7.910
HD285773	7.496	7.106	7.042	7.640	7.494	7.178
HD345957	7.681	7.372	7.361	7.790	7.671	7.415
M71_I	9.259	8.563	8.473	9.440	9.239	8.704
M79_160	10.888	10.240	10.165	11.064	10.880	10.375
M79_223	10.532	9.835	9.714	10.723	10.528	9.990
NGC288-77	10.739	10.072	9.971	10.909	10.716	10.198
NGC6791-R19	10.952	10.278	10.094	11.156	10.942	10.436
NGC6791-R4	8.867	8.024	7.744	9.133	8.850	8.221
IRTF Spectral Library (IRTF)						
C-J4.5IIIIa:C26j6_HD70138	5.763	4.777	4.382	5.987	5.673	5.248
C-J5-C25-j4_HD57160	4.327	3.230	2.726	4.612	4.263	3.674
C-N4.5C24.5_HD92055	0.771	-0.322	-0.744	1.066	0.723	0.082
C-N4.5C25.5MS3_HD76221	1.602	0.491	-0.087	1.896	1.549	0.914
C-N4C23.5_HD44984	1.938	0.979	0.616	2.198	1.898	1.355
C-N5C26-_HD48664	3.986	2.882	2.365	4.275	3.927	3.337

Table C.1: — continued

Spectrum Name	$J$	$H$	$K_S$	F110W	F125W	F160W
C-R2+IIIa:C22.5_HD76846	7.310	6.762	6.622	7.515	7.308	6.977
C7,6e(N4)_HD31996	2.269	0.886	-0.199	2.641	2.236	1.319
F0III-IVn_HD13174	4.244	4.078	4.065	4.319	4.241	4.101
F0IIIa_HD89025	2.751	2.579	2.552	2.815	2.736	2.599
F0II_HD6130	4.419	4.287	4.281	4.448	4.413	4.316
F0IV_HD27397	4.964	4.846	4.858	5.022	4.965	4.866
F0Ia_HD7927	3.339	3.192	3.143	3.364	3.331	3.233
F0Ib-II_HD135153	4.071	3.919	3.877	4.116	4.071	3.964
F0V(n)_HD108519	7.091	6.940	6.904	7.146	7.088	6.965
F1II_HD173638	3.645	3.587	3.633	3.638	3.644	3.607
F1V_HD213135	5.253	5.064	5.048	5.331	5.252	5.095
F2-F5Ib_BD+38_2803	7.615	7.294	7.224	7.730	7.608	7.349
F2III-IV_HD40535	5.496	5.296	5.259	5.579	5.492	5.328
F2Ib_HD182835	2.754	2.629	2.640	2.791	2.759	2.667
F2V_HD113139	4.166	3.972	3.951	4.248	4.144	3.988
F3V_HD26015	5.147	5.016	5.032	5.217	5.145	5.033
F4III_HD21770	4.465	4.269	4.246	4.548	4.466	4.299
F4V_HD16232	6.073	5.849	5.821	6.162	6.078	5.890
F4V_HD87822	5.365	5.167	5.135	5.456	5.367	5.196
F5.5III-IV_HD75555	7.217	6.991	6.955	7.317	7.215	7.025
F5II-III_HD186155	4.368	4.196	4.162	4.450	4.373	4.221
F5III_HD17918	5.388	5.186	5.183	5.476	5.389	5.219
F5Ib-G1Ib_HD213306	2.808	2.443	2.386	2.929	2.792	2.508
F5V_HD218804	4.974	4.716	4.667	5.060	4.948	4.749
F5V_HD27524	5.959	5.763	5.740	6.040	5.954	5.783

Table C.1: — continued

Spectrum Name	$J$	$H$	$K_S$	F110W	F125W	F160W
F6III-IV_HD160365	4.874	4.692	4.726	4.946	4.872	4.717
F6IV_HD11443	2.450	2.189	2.111	2.538	2.444	2.230
F6V_HD215648	3.291	3.046	3.016	3.383	3.273	3.072
F7II-_HD201078	4.633	4.404	4.347	4.715	4.624	4.442
F7III_HD124850	3.117	2.854	2.831	3.226	3.119	2.900
F7V_HD126660	3.142	2.909	2.854	3.232	3.133	2.940
F8.5IV-V_HD102870	2.584	2.315	2.279	2.687	2.576	2.351
F8III_HD220657	3.518	3.166	3.067	3.641	3.501	3.220
F8IV_HD111844	6.687	6.573	6.567	6.746	6.685	6.588
F8Ia_HD190323	4.999	4.788	4.785	5.076	4.999	4.829
F8Ib_HD51956	5.966	5.655	5.602	6.084	5.962	5.707
F8V_HD219623	4.637	4.357	4.313	4.744	4.633	4.408
F8V_HD27383	5.793	5.561	5.547	5.883	5.784	5.597
F9.5V_HD114710	3.174	2.961	2.970	3.263	3.165	2.982
F9IIIa_HD6903	4.519	4.178	4.121	4.643	4.514	4.236
F9V_HD176051	4.035	3.688	3.642	4.150	4.022	3.743
F9Vmetalweak_HD165908	3.439	3.188	3.136	3.522	3.423	3.221
G0Ib-II_HD185018	4.324	3.959	3.909	4.449	4.319	4.033
G0V_HD109358	3.191	2.875	2.849	3.299	3.183	2.926
G1-VFe-0.5_HD95128	4.000	3.703	3.667	4.123	4.001	3.753
G1.5V_HD20619	5.878	5.506	5.444	6.013	5.880	5.576
G1II-III:Fe-1CH0.5_ HD216219	6.259	5.971	5.925	6.360	6.244	6.010
G1III:CH-1:_HD21018	4.711	4.368	4.311	4.833	4.706	4.434
G1Ib_HD74395	3.141	2.762	2.693	3.285	3.143	2.847



Table C.1: — continued

Spectrum Name	$J$	$H$	$K_S$	F110W	F125W	F160W
G1V_HD10307	3.962	3.656	3.629	4.072	3.957	3.710
G2II-III_HD219477	5.132	4.802	4.757	5.250	5.127	4.860
G2IV_HD126868	3.486	3.142	3.080	3.605	3.486	3.207
G2Ib-II_HD3421	3.652	3.259	3.204	3.785	3.648	3.346
G2Ib_HD39949	5.073	4.669	4.603	5.214	5.063	4.745
G2Ib_HD42454	4.862	4.504	4.454	4.987	4.848	4.565
G2V_HD76151	4.853	4.523	4.453	4.969	4.844	4.582
G3IIIbFe-1_HD88639	4.498	4.071	4.018	4.648	4.495	4.156
G3II_HD176123	4.485	4.089	4.046	4.620	4.478	4.168
G3Ib-IIWkH&Kcomp:_ HD192713	3.478	3.029	2.944	3.641	3.480	3.137
G3Va_HD10697	5.022	4.665	4.589	5.144	4.999	4.716
G4III-IIIb_HD94481	4.191	3.759	3.692	4.335	4.184	3.844
G4III_HD108477	4.776	4.350	4.272	4.921	4.767	4.437
G4Ia_HD6474	3.993	3.722	3.680	4.075	3.985	3.777
G40-Ia_HD179821	4.862	4.623	4.516	4.928	4.840	4.668
G4V_HD214850	4.462	4.036	3.942	4.586	4.453	4.117
G5:III:CN-3CH-2H_delta-1_ HD18474	3.535	3.094	3.071	3.677	3.533	3.180
G5IIIa_HD193896	4.677	4.204	4.105	4.839	4.667	4.298
G5Ib_HD190113	5.100	4.582	4.489	5.273	5.094	4.702
G5V_HD165185	4.825	4.546	4.499	4.923	4.815	4.589
G6.5V_HD115617	3.277	2.969	2.956	3.391	3.279	3.020
G6III_HD27277	6.072	5.666	5.623	6.215	6.072	5.751
G6IIb_HD58367	3.393	2.921	2.838	3.549	3.385	3.027

Table C.1: — continued

Spectrum Name	$J$	$H$	$K_S$	F110W	F125W	F160W
G6Ib-IIaCa1Ba0.5_HD202314	4.580	4.097	3.968	4.745	4.579	4.224
G6IbH_delta1_HD161664	3.181	2.656	2.557	3.360	3.166	2.779
G7.5IIIIa_HD16139	6.098	5.628	5.532	6.254	6.095	5.728
G7IIIIa_HD182694	4.388	3.946	3.855	4.534	4.378	4.032
G7II_HD25877	4.146	3.787	3.772	4.263	4.142	3.861
G7IV_HD114946	3.666	3.177	3.097	3.824	3.667	3.277
G7IV_HD20618	4.512	4.037	3.953	4.665	4.502	4.130
G7Ia_HD333385	3.904	3.603	3.501	4.023	3.899	3.658
G8:III:Fe-5_HD122563	4.374	3.814	3.727	4.536	4.354	3.915
G8IIIBa1CN-1CH1_HD104979	2.594	2.068	1.982	2.753	2.586	2.178
G8IIIFe-1_HD135722	1.650	1.116	1.007	1.807	1.637	1.225
G8Ib_HD208606	3.336	2.815	2.714	3.503	3.329	2.957
G8V_HD101501	3.995	3.633	3.583	4.120	3.987	3.703
G8V_HD75732	4.504	4.103	4.019	4.640	4.491	4.190
G9IICN1H_delta1_HD170820	4.109	3.528	3.384	4.315	4.100	3.678
G9III_HD222093	4.129	3.583	3.491	4.297	4.116	3.697
K0.5IIICN1_HD9852	5.066	4.517	4.450	5.233	5.059	4.651
K0.5IIb_HD164349	2.473	1.973	1.917	2.639	2.460	2.091
K0III_HD100006	3.900	3.324	3.232	4.077	3.890	3.450
K0II_HD179870	4.631	4.205	4.198	4.779	4.609	4.290
K0Ia_HD165782	2.941	2.607	2.514	3.079	2.938	2.687
K0Ib_HD44391	5.117	4.584	4.469	5.290	5.110	4.713
K0V_HD145675	5.138	4.765	4.715	5.278	5.135	4.836
K1-IIIFe-0.5_HD36134	3.792	3.213	3.130	3.973	3.787	3.339
K1-IIIBCN1.5Ca1_HD91810	4.833	4.256	4.138	5.023	4.825	4.393

Table C.1: — continued

Spectrum Name	$J$	$H$	$K_S$	F110W	F125W	F160W
K1.5IIIFe-0.5_HD124897_ shape	-2.195	-2.895	-3.016	-2.004	-2.210	-2.745
K1III_HD25975	4.526	4.064	4.000	4.673	4.519	4.159
K1IV_HD165438	4.304	3.810	3.723	4.466	4.292	3.909
K1IVa_HD142091	3.018	2.521	2.448	3.180	3.012	2.629
K1Ia-Iab_HD63302	3.548	2.917	2.719	3.776	3.549	3.103
K1V_HD10476	3.810	3.372	3.291	3.951	3.793	3.449
K2.5II_HD23082	3.535	2.870	2.739	3.741	3.523	3.046
K2IIIFe-1_HD2901	4.890	4.253	4.174	5.088	4.891	4.393
K2III_HD132935	4.391	3.698	3.559	4.589	4.376	3.855
K2III_HD137759	1.325	0.708	0.582	1.520	1.314	0.850
K20-Ia_HD212466	2.027	1.708	1.590	2.138	2.040	1.825
K2V_HD3765	5.682	5.227	5.157	5.830	5.663	5.307
K3+IIIFe-0.5_HD99998	2.163	1.363	1.180	2.397	2.150	1.549
K3.5IIIbCN0.5CH0.5_ HD114960	4.089	3.420	3.281	4.300	4.087	3.586
K3II-III_HD16068	4.397	3.722	3.621	4.598	4.384	3.891
K3IIIFe1_HD35620	2.824	2.161	2.008	3.025	2.799	2.323
K3III_HD178208	4.408	3.769	3.640	4.614	4.393	3.920
K3III_HD221246	3.813	3.119	3.001	4.021	3.803	3.287
K3Iab-Ib_HD187238	3.027	2.402	2.294	3.224	3.021	2.579
K3V_HD219134	3.960	3.407	3.304	4.135	3.944	3.517
K4-III_HD207991	3.930	3.122	2.948	4.159	3.917	3.310
K4Ib-II_HD201065	4.202	3.581	3.495	4.361	4.189	3.746
K4Ib_HD185622A	1.802	1.042	0.830	2.026	1.787	1.250

Table C.1: — continued

Spectrum Name	$J$	$H$	$K_S$	F110W	F125W	F160W
K4V_HD45977	7.038	6.518	6.427	7.199	7.027	6.624
K5.5III_HD120477	1.286	0.487	0.286	1.524	1.277	0.680
K5III_HD181596	4.787	4.009	3.826	5.015	4.768	4.191
K5Ib_HD216946	1.773	0.873	0.589	2.049	1.759	1.103
K5V_HD36003	5.594	4.993	4.885	5.771	5.582	5.113
K6IIa_HD3346	2.214	1.389	1.172	2.448	2.203	1.587
K7III_HD194193	3.046	2.184	1.977	3.280	3.022	2.385
K7IIa_HD181475	2.666	1.862	1.639	2.901	2.644	2.064
K7V_HD201092	3.428	2.837	2.706	3.581	3.384	2.946
K7V_HD237903	6.115	5.459	5.347	6.309	6.104	5.600
L0.5_2MASSJ0746+2000AB	11.730	10.958	10.476	12.178	11.782	11.261
L1_2MASSJ0208+2542	14.024	13.144	12.583		14.052	13.471
L1_2MASSJ1439+1929	12.748	12.000	11.523	13.210	12.824	12.328
L2_Kelu-1AB	13.332	12.381	11.756		13.392	12.747
L3.5_2MASSJ0036+1821	12.450	11.564	11.034	12.959	12.533	11.928
L3_2MASSJ1146+2230AB	14.118	13.167	12.574		14.172	13.529
L3_2MASSJ1506+1321	13.330	12.364	11.723		13.387	12.738
L4.5_2MASSJ2224-0158	14.011	12.794	12.012		14.040	13.181
L5_2MASSJ1507-1627	12.804	11.853	11.307		12.897	12.232
L5_SDSSJ0539-0059	14.055	13.125	12.624		14.153	13.506
L6(NIR)_2MASSJ1515+4847	14.082	13.066	12.456		14.169	13.439
L7.5_2MASSJ0825+2115	15.013	13.794	13.026		15.099	14.209
L8_DENISJ0255-4700	13.233	12.151	11.552	13.771	13.364	12.544
M0.5Ib_HD236697	4.393	3.607	3.389	4.637	4.385	3.819
M0.5V_HD209290	6.182	5.503	5.314	6.394	6.167	5.653

Table C.1: — continued

Spectrum Name	$J$	$H$	$K_S$	F110W	F125W	F160W
M0IIIb_HD213893	3.861	3.056	2.872	4.091	3.848	3.241
M0V_HD19305	6.478	5.796	5.638	6.678	6.471	5.948
M1+III_HD204724	1.589	0.815	0.581	1.808	1.568	1.020
M1-Iab-Ib_HD14404	3.066	2.339	2.138	3.300	3.063	2.552
M1-M2Ia-Iab_HD39801	-3.216	-3.940	-4.056	-2.966	-3.217	-3.724
M1.5Iab-Ib_HD35601	2.488	1.693	1.431	2.720	2.444	1.905
M1.5Ib_BD+60_265	3.450	2.700	2.449	3.681	3.434	2.907
M1.5V_HD36395	4.902	4.172	3.998	5.122	4.892	4.340
M10+III_IRAS14086-0703	6.569	4.434	2.598	7.295	6.717	5.156
M1Ia_HD339034	2.227	1.538	1.289	2.486	2.226	1.772
M1V_HD42581	5.079	4.424	4.243	5.284	5.065	4.574
M2-Ia_HD206936	-0.873	-1.548	-1.841	-0.656	-0.887	-1.323
M2.5IIIBa0.5_HD219734	1.484	0.616	0.387	1.739	1.478	0.832
M2.5V_G1381	7.004	6.397	6.192	7.239	7.010	6.552
M2.5V_G1581	6.659	6.080	5.840	6.888	6.663	6.235
M2III_HD120052	1.851	0.956	0.704	2.097	1.825	1.163
M2II_HD23475	0.331	-0.496	-0.715	0.551	0.294	-0.291
M2Ib_HD10465	2.450	1.689	1.447	2.685	2.426	1.894
M2V_G1806	7.309	6.699	6.543	7.509	7.286	6.832
M2V_HD95735	4.134	3.569	3.391	4.345	4.130	3.712
M3-M4Iab_HD14469	2.430	1.656	1.371	2.694	2.437	1.907
M3.5IIICa-0.5_HD28487	2.569	1.661	1.408	2.832	2.563	1.895
M3.5IabFe-1var:_HD14488	2.692	1.795	1.399	2.954	2.682	2.049
M3.5V_G1273	5.681	5.106	4.865	5.922	5.679	5.265
M3III_HD39045	2.472	1.611	1.377	2.718	2.456	1.820

Table C.1: — continued

Spectrum Name	$J$	$H$	$K_S$	F110W	F125W	F160W
M3IIb_HD40239	0.273	-0.644	-0.923	0.536	0.248	-0.415
M3Iab-Ia_CD-31_49	4.078	3.280	3.035	4.338	4.086	3.520
M3V_G1388	5.413	4.798	4.599	5.642	5.406	4.952
M3toM4Ia-Iab_RW_Cyg	1.082	0.356	0.144	1.287	1.070	0.579
M4+III_HD214665	1.119	0.095	-0.225	1.432	1.107	0.344
M4+IIIIa_HD19058	-0.753	-1.698	-1.980	-0.481	-0.759	-1.454
M4-III_HD27598	2.941	2.061	1.808	3.204	2.947	2.294
M4.5IIIIa_HD204585	1.039	0.205	-0.019	1.307	1.034	0.421
M4.5V_G1268AB	6.706	6.108	5.841	6.973	6.716	6.274
M4IIII_HD4408	1.399	0.483	0.198	1.664	1.389	0.708
M4V_G1213	7.126	6.597	6.364	7.373	7.134	6.758
M4V_G1299	8.393	7.913	7.655	8.642	8.406	8.078
M5.5IIII:_HD94705	0.420	-0.478	-0.801	0.710	0.407	-0.249
M5IIII_HD175865	-0.763	-1.624	-1.848	-0.492	-0.779	-1.408
M5Ib-II_HD156014	-2.592	-3.262	-3.358	-2.342	-2.594	-3.077
M5V_G151	8.593	7.985	7.703	8.873	8.605	8.167
M5V_G1866ABC	6.515	5.882	5.561	6.821	6.528	6.081
M5e-M9eIIII_HD14386	-0.914	-1.558	-2.003	-0.549	-0.843	-1.172
M6-III:_HD18191	0.258	-0.681	-0.980	0.558	0.248	-0.438
M6.5StoM7SIIII:_HD142143	0.769	-0.179	-0.605	1.111	0.745	0.072
M6.5V_GJ1111	8.201	7.598	7.232	8.516	8.200	7.800
M6IIII_HD196610	0.145	-0.707	-0.986	0.428	0.126	-0.489
M6V_G1406	7.073	6.436	6.071	7.392	7.080	6.630
M6e-M9eIIII_HD69243	0.641	-0.268	-0.794	1.191	0.753	0.183
M7-8IIII_BRIB2339-0447	9.032	8.123	7.672	9.321	9.077	8.427

Table C.1: — continued

Spectrum Name	$J$	$H$	$K_S$	F110W	F125W	F160W
M7-III:_HD108849	0.513	-0.397	-0.784	0.894	0.548	-0.104
M7-III:_HD207076	-0.494	-1.265	-1.529	-0.189	-0.495	-1.037
M7-M7.5I_MY_Cep	3.587	2.432	1.865	3.994	3.624	2.791
M7V_G1644C	9.765	9.171	8.793	10.098	9.788	9.404
M8-9III_IRAS14303-1042	6.272	5.497	4.991	6.702	6.447	6.067
M8-9III_IRAS14436-0703	5.546	4.815	4.354	6.013	5.688	5.340
M8-9III_IRAS21284-0747	6.117	5.251	4.693	6.632	6.239	5.748
M8III_IRAS01037+1219	7.315	4.858	3.253	8.050	7.424	5.531
M8V_G1752B	9.843	9.203	8.777	10.213	9.879	9.462
M8V_LP412-31	11.757	11.038	10.607	12.133	11.776	11.280
M9.5V_BRIB0021-0214	11.870	11.072	10.549	12.296	11.884	11.363
M9III_BRIB1219-1336	8.560	7.809	7.335	8.991	8.667	8.234
M9III_IRAS15060+0947	5.397	4.103	2.999	5.837	5.440	4.549
M9V_DENIS-PJ1048-3956	9.490	8.875	8.462	9.885	9.545	9.156
M9V_LHS2065	11.215	10.423	9.916	11.621	11.226	10.689
M9V_LHS2924	11.962	11.201	10.728	12.382	11.995	11.483
M9V_LP944-20	10.697	9.993	9.528	11.125	10.744	10.289
S2.5Zr2_BD+44_2267	6.219	5.392	5.151	6.472	6.193	5.609
S4.5Zr2Ti4_HD64332	3.436	2.560	2.287	3.706	3.430	2.782
S5-S6Zr3to4Ti0_HD62164	2.700	1.663	1.256	2.997	2.646	1.931
SC5.5Zr0.5_HD44544	3.077	2.006	1.633	3.411	3.057	2.323
T2_SDSSJ1254-0122	14.824	14.067	13.881		15.025	14.501
T4.5_2MASSJ0559-1404	13.782	13.603	13.608		14.022	13.934
kA9hF2mF2(IV)_HD164136	2.971	2.748	2.732	3.062	2.972	2.790

Table C.1: — continued

Spectrum Name	$J$	$H$	$K_S$	F110W	F125W	F160W
X-Shooter Spectral Library (XSL)						
MD002_merged_scl	11.562	10.911	10.725	11.790	11.554	11.070
MD003_merged_scl	8.111	7.472	7.265	8.344	8.100	7.621
MD004_merged_scl	10.114	9.416	9.172	10.365	10.103	9.579
MD005_merged_scl	11.372	10.773	10.538	11.607	11.365	10.915
MD006_merged_scl	12.004	11.316	11.086	12.241	11.994	11.475
MD007_merged_scl	8.013	7.569	7.356	8.251	8.019	7.720
MD008_merged_scl	11.934	11.312	11.077	12.186	11.929	11.468
MD010_merged_scl	12.921	12.388	12.138	13.189	12.925	12.557
MD011_merged_scl	10.732	10.110	9.848	10.983	10.730	10.280
MD012_merged_scl	12.895	12.193	11.953	13.144	12.886	12.361
MD013_merged_scl	11.031	10.428	10.218	11.266	11.027	10.602
MD014_merged_scl	10.476	9.848	9.662	10.682	10.465	10.013
MD017_merged_scl	9.995	9.385	9.145	10.246	9.988	9.535
MD018_merged_scl	10.779	10.152	9.834	11.054	10.780	10.321
MD020_merged_scl	11.779	11.203	10.984	12.033	11.778	11.358
MD021_merged_scl	7.331	6.557	6.132	7.658	7.324	6.770
MD022_merged_scl	11.933	11.285	10.953	12.201	11.930	11.454
X0003_merged_scl	13.480	12.723	12.580	13.699	13.470	12.903
X0004_merged	10.398	9.485	9.076	10.716	10.429	9.781
X0005_merged	9.498	8.669	8.434	9.758	9.499	8.892
X0006_merged	9.726	8.925	8.716	9.964	9.725	9.133
X0007_merged	7.023	6.585	6.530	7.163	7.011	6.655
X0012_merged_ncl	11.982	10.919	10.432	12.286	11.957	11.327
X0013_merged_ncl	11.588	10.590	10.184	11.892	11.564	10.962



Table C.1: — continued

Spectrum Name	$J$	$H$	$K_S$	F110W	F125W	F160W
X0020_merged	10.701	9.874	9.432	11.158	10.782	10.288
X0021_merged	9.578	8.803	8.512	9.847	9.596	9.042
X0022_merged_scl	6.441	6.501	6.540	6.410	6.436	6.477
X0023_merged	6.548	5.797	5.677	6.749	6.535	5.958
X0024_merged	10.805	10.687	10.681	10.857	10.793	10.696
X0026_merged_scl	13.250	12.403	12.238	13.504	13.232	12.601
X0031_merged_scl	13.035	12.395	12.288	13.216	13.025	12.533
X0037_merged	9.876	8.945	8.552	10.143	9.914	9.266
X0038_merged_ncl	12.139	11.004	10.426	12.451	12.089	11.401
X0039_merged_ncl	12.230	11.001	10.354	12.590	12.202	11.452
X0040_merged_ncl	12.342	11.283	10.783	12.643	12.292	11.633
X0041_merged	8.965	8.227	8.002	9.213	8.973	8.427
X0042_merged_scl	6.404	6.026	5.967	6.530	6.395	6.084
X0043_merged_scl	5.622	5.169	5.118	5.770	5.611	5.245
X0044_merged	8.368	7.533	7.229	8.664	8.382	7.788
X0045_merged_ncl	10.510	9.539	9.017	10.958	10.567	10.015
X0048_merged_ncl	10.030	9.206	8.732	10.425	10.112	9.625
X0050_merged	8.911	8.172	7.805	9.262	8.980	8.517
X0057_merged_ncl	10.372	9.466	9.099	10.786	10.435	9.880
X0059_merged_scl	12.297	11.461	11.231	12.551	12.290	11.682
X0065_merged	8.724	8.425	8.389	8.828	8.717	8.473
X0066_merged_scl	4.136	3.623	3.571	4.291	4.125	3.718
X0070_merged	6.925	6.603	6.568	7.043	6.917	6.654
X0071_merged	5.870	5.582	5.535	5.982	5.863	5.629
X0072_merged	8.162	7.857	7.823	8.267	8.150	7.905

Table C.1: — continued

Spectrum Name	$J$	$H$	$K_S$	F110W	F125W	F160W
X0073_merged	5.606	5.544	5.521	5.639	5.602	5.552
X0074_merged	5.513	5.476	5.459	5.514	5.508	5.480
X0075_merged	6.846	6.315	6.217	7.004	6.836	6.415
X0077_merged	6.269	5.715	5.635	6.443	6.258	5.813
X0081_merged_scl	6.264	6.257	6.274	6.252	6.259	6.248
X0082_merged_scl	5.747	5.608	5.592	5.809	5.740	5.615
X0084_merged_scl	4.738	4.241	4.170	4.907	4.731	4.338
X0089_merged	5.256	4.860	4.812	5.392	5.247	4.921
X0092_merged	6.332	5.782	5.709	6.499	6.321	5.876
X0094_merged_scl	6.143	5.500	5.415	6.330	6.136	5.635
X0096_merged_scl	5.196	4.912	4.862	5.304	5.185	4.949
X0097_merged_scl	5.568	4.955	4.891	5.745	5.561	5.080
X0099_merged_scl	11.576	10.740	10.518	11.827	11.572	10.960
X0106_merged_scl	3.561	2.802	2.543	3.791	3.559	3.016
X0110_merged_scl	3.807	3.257	3.190	3.967	3.809	3.401
X0113_merged	6.727	6.772	6.813	6.703	6.722	6.751
X0118_merged	9.198	8.389	8.057	9.454	9.224	8.649
X0119_merged	8.794	7.938	7.636	9.110	8.825	8.228
X0120_merged	8.870	8.030	7.755	9.150	8.878	8.283
X0121_merged_ncl_ncge	10.435	9.541	9.127	10.806	10.470	9.870
X0122_merged	6.353	5.835	5.767	6.515	6.344	5.930
X0123_merged	6.645	6.212	6.166	6.785	6.635	6.286
X0131_merged_ncge	11.332	10.578	10.082	11.704	11.329	10.823
X0133_merged	6.913	6.996	7.073	6.868	6.907	6.961
X0134_merged	6.288	5.470	5.174	6.584	6.321	5.753

Table C.1: — continued

Spectrum Name	$J$	$H$	$K_S$	F110W	F125W	F160W
X0136_merged_ncl_ncge	13.395	12.455	11.872	13.876	13.430	12.809
X0137_merged	12.711	12.081	12.053	12.891	12.700	12.209
X0138_merged	12.303	11.766	11.761	12.456	12.296	11.881
X0139_merged	12.267	11.670	11.652	12.429	12.258	11.790
X0140_merged	6.202	5.851	5.841	6.322	6.195	5.907
X0141_merged	5.549	5.262	5.258	5.659	5.543	5.307
X0142_merged	5.459	4.933	4.868	5.629	5.449	5.036
X0143_merged	8.282	7.873	7.854	8.411	8.273	7.943
X0144_merged_ncl	8.636	7.862	7.663	8.832	8.632	8.063
X0145_merged_ncge	7.622	6.928	6.660	7.935	7.648	7.189
X0146_merged_ncl_ncge	8.529	7.845	7.502	8.806	8.610	8.249
X0147_merged_ncl_ncge	8.709	7.958	7.678	8.953	8.761	8.293
X0148_merged	9.291	8.356	8.044	9.616	9.327	8.667
X0149_merged	5.543	4.692	4.315	5.786	5.602	5.047
X0151_merged	12.486	12.004	12.052	12.629	12.477	12.093
X0152_merged	12.469	11.934	11.934	12.617	12.467	12.073
X0153_merged	9.688	8.908	8.747	9.897	9.680	9.109
X0154_merged	9.191	8.361	8.170	9.463	9.214	8.634
X0155_merged_ncl_ncge	7.480	6.494	6.105	7.937	7.524	6.844
X0156_merged_ncl_ncge	9.864	9.222	8.906	10.202	9.885	9.465
X0157_merged	9.221	8.842	8.826	9.345	9.215	8.909
X0158_merged_ncl_ncge	7.695	6.959	6.729	7.971	7.750	7.290
X0159_merged_ncl_ncge	8.714	8.004	7.785	8.914	8.754	8.319
X0160_merged	8.421	7.548	7.313	8.688	8.437	7.808
X0161_merged	6.639	6.519	6.538	6.678	6.636	6.545

Table C.1: — continued

Spectrum Name	$J$	$H$	$K_S$	F110W	F125W	F160W
X0162_merged	4.551	4.192	4.205	4.645	4.551	4.283
X0163_merged	6.155	6.100	6.135	6.143	6.152	6.117
X0164_merged	7.290	7.142	7.158	7.342	7.286	7.167
X0165_merged	5.500	4.871	4.786	5.678	5.493	5.010
X0168_merged_ncl_ncge	7.626	6.829	6.558	7.905	7.682	7.174
X0169_merged_ncl	9.278	8.430	8.221	9.537	9.272	8.652
X0170_merged	11.452	10.794	10.807	11.603	11.440	10.930
X0171_merged	12.486	12.010	12.035	12.619	12.476	12.096
X0172_merged	8.065	7.263	7.123	8.272	8.061	7.470
X0173_merged_ncl	8.852	7.996	7.776	9.127	8.854	8.230
X0174_merged_scl	6.622	5.922	5.773	6.832	6.618	6.092
X0175_merged	7.157	6.932	6.903	7.248	7.152	6.967
X0176_merged	8.967	8.657	8.629	9.072	8.962	8.709
X0177_merged	6.421	5.956	5.880	6.560	6.416	6.053
X0178_merged	6.053	5.935	5.915	6.092	6.049	5.955
X0179_merged	7.310	6.970	6.933	7.429	7.304	7.028
X0180_merged	6.470	5.740	5.608	6.674	6.461	5.904
X0181_merged_ncl	10.199	9.152	8.707	10.496	10.257	9.534
X0184_merged_ncl	10.612	9.839	9.389	11.010	10.716	10.293
X0185_merged_ncl_ncge	8.827	8.179	7.845	9.131	8.892	8.554
X0186_merged_ncl_ncge	6.976	5.947	5.442	7.478	7.024	6.310
X0187_merged_ncl	8.162	7.418	7.152	8.436	8.205	7.721
X0188_merged_ncl	8.534	7.843	7.609	8.757	8.610	8.211
X0189_merged_ncl	8.960	8.271	7.977	9.241	9.033	8.665
X0190_merged_ncl_ncge	8.082	7.328	7.006	8.286	8.137	7.655

Table C.1: — continued

Spectrum Name	$J$	$H$	$K_S$	F110W	F125W	F160W
X0191_merged_ncl	8.655	7.899	7.659	8.892	8.677	8.149
X0192_merged_ncl_ncge	8.487	7.775	7.453	8.829	8.556	8.141
X0193_merged_ncl	7.818	7.032	6.729	8.041	7.864	7.339
X0194_merged_scl	6.345	6.268	6.282	6.358	6.342	6.277
X0195_merged	4.590	4.144	4.064	4.739	4.583	4.233
X0196_merged	6.649	6.648	6.662	6.641	6.646	6.652
X0197_merged_ncge	6.287	5.792	5.710	6.449	6.283	5.903
X0198_merged	9.299	8.961	8.929	9.418	9.293	9.017
X0199_merged	6.311	6.334	6.364	6.278	6.308	6.328
X0200_merged	7.133	6.817	6.778	7.246	7.127	6.868
X0201_merged	6.170	5.482	5.301	6.373	6.158	5.639
X0202_merged_ncl	6.499	5.855	5.513	6.805	6.508	6.057
X0203_merged	5.663	5.356	5.303	5.792	5.659	5.409
X0205_merged	8.327	7.490	7.147	8.612	8.343	7.748
X0206_merged	14.292	13.584	13.568	14.500	14.281	13.727
X0207_merged	4.732	4.235	4.130	4.898	4.731	4.351
X0208_merged_ncge	4.860	4.629	4.546	4.930	4.859	4.690
X0209_merged	13.021	12.244	12.057	13.282	13.012	12.422
X0210_merged	4.556	3.796	3.675	4.764	4.552	3.972
X0211_merged	5.825	5.377	5.306	5.942	5.826	5.485
X0212_merged	5.644	5.152	5.085	5.803	5.636	5.246
X0213_merged	7.667	7.325	7.290	7.793	7.663	7.384
X0216_merged	6.258	5.944	5.908	6.374	6.253	5.994
X0217_merged	5.543	5.248	5.209	5.666	5.539	5.297
X0218_merged_ncl_ncge	7.939	7.155	6.758	8.199	8.011	7.540

Table C.1: — continued

Spectrum Name	$J$	$H$	$K_S$	F110W	F125W	F160W
X0220_merged	7.116	6.995	6.981	7.158	7.113	7.013
X0221_merged	6.138	6.175	6.212	6.114	6.137	6.165
X0222_merged	6.572	6.337	6.302	6.672	6.567	6.374
X0223_merged	9.096	8.797	8.772	9.209	9.090	8.845
X0224_merged	5.288	5.323	5.363	5.263	5.287	5.314
X0225_merged	10.125	9.767	9.731	10.256	10.119	9.829
X0228_merged	6.353	6.348	6.346	6.355	6.353	6.357
X0230_merged_ncl	8.061	7.334	6.945	8.316	8.145	7.748
X0231_merged_ncl	7.759	6.956	6.627	8.003	7.783	7.214
X0232_merged	4.571	3.983	3.905	4.733	4.561	4.104
X0238_merged	14.388	13.691	13.660	14.600	14.376	13.835
X0241_merged	8.860	8.025	7.718	9.148	8.879	8.279
X0242_merged	5.595	4.728	4.257	5.895	5.662	5.101
X0243_merged	8.718	8.727	8.752	8.707	8.716	8.729
X0245_merged	6.016	6.012	6.026	6.011	6.014	6.016
X0246_merged	7.691	7.097	6.980	7.818	7.704	7.290
X0247_merged	9.548	8.988	8.738	9.691	9.548	9.142
X0248_merged	7.132	6.589	5.875	7.218	7.124	6.754
X0249_merged	5.733	5.257	5.210	5.879	5.722	5.347
X0250_merged_ncl_ncge	7.871	7.232	7.063	8.072	7.913	7.515
X0251_merged	7.669	7.141	7.093	7.736	7.692	7.343
X0252_merged_ncl_ncge	8.086	7.396	7.066	8.493	8.172	7.798
X0253_merged	9.057	8.390	8.179	9.305	9.099	8.694
X0254_merged	8.877	8.133	7.917	9.069	8.884	8.336
X0255_merged_ncl_ncge	8.925	7.962	7.578	9.342	8.930	8.232

Table C.1: — continued

Spectrum Name	$J$	$H$	$K_S$	F110W	F125W	F160W
X0256_merged_ncl	8.626	7.777	7.488	8.946	8.631	8.022
X0257_merged	10.183	9.349	9.165	10.410	10.176	9.563
X0258_merged	6.556	5.847	5.726	6.756	6.547	6.005
X0259_merged_ncl	10.016	8.970	8.547	10.354	10.070	9.343
X0260_merged	8.487	7.659	7.311	8.767	8.502	7.916
X0263_merged_scl	14.303	13.588	13.471	14.502	14.294	13.752
X0264_merged_ncl	10.586	9.836	9.435	10.919	10.687	10.270
X0265_merged	9.121	8.320	8.102	9.369	9.122	8.540
X0266_merged	9.350	8.535	8.259	9.626	9.365	8.789
X0267_merged	6.287	6.192	6.189	6.314	6.283	6.211
X0268_merged	5.854	5.417	5.350	5.983	5.851	5.518
X0269_merged	5.333	4.942	4.875	5.441	5.328	5.027
X0270_merged	6.262	6.253	6.228	6.254	6.256	6.247
X0271_merged	7.198	6.965	6.928	7.297	7.191	6.994
X0272_merged	4.808	4.288	4.188	4.975	4.803	4.405
X0273_merged	4.680	3.940	3.820	4.888	4.671	4.106
X0274_merged	6.450	5.964	5.883	6.615	6.443	6.065
X0275_merged	7.458	7.072	7.002	7.597	7.449	7.135
X0276_merged	7.535	7.312	7.275	7.633	7.528	7.341
X0277_merged	6.287	5.610	5.422	6.494	6.274	5.762
X0278_merged	6.417	6.109	6.069	6.533	6.410	6.157
X0279_merged	5.652	5.362	5.318	5.769	5.644	5.404
X0280_merged	5.435	5.472	5.509	5.406	5.430	5.455
X0281_merged	5.945	5.631	5.579	6.071	5.937	5.676
X0282_merged	8.389	8.008	7.962	8.524	8.377	8.065

Table C.1: — continued

Spectrum Name	$J$	$H$	$K_S$	F110W	F125W	F160W
X0283_merged	7.273	7.163	7.156	7.321	7.270	7.177
X0285_merged	7.232	7.163	7.160	7.266	7.227	7.166
X0286_merged	6.612	5.905	5.785	6.814	6.603	6.060
X0287_merged	5.945	5.704	5.686	6.042	5.940	5.737
X0288_merged	6.702	6.717	6.748	6.686	6.696	6.702
X0289_merged	6.361	6.404	6.449	6.325	6.357	6.384
X0290_merged	7.179	6.886	6.858	7.292	7.172	6.929
X0291_merged	6.111	6.015	6.018	6.151	6.105	6.020
X0292_merged	6.466	6.027	5.964	6.603	6.463	6.118
X0293_merged_nc1	9.271	8.457	8.234	9.494	9.261	8.663
X0294_merged	6.257	6.310	6.338	6.224	6.251	6.288
X0295_merged	6.689	6.466	6.437	6.781	6.682	6.494
X0296_merged_ncge	8.356	7.637	7.381	8.613	8.415	7.968
X0297_merged	4.629	4.199	4.131	4.777	4.621	4.279
X0298_merged_sc1	4.498	3.944	3.864	4.681	4.492	4.063
X0299_merged	4.298	3.696	3.555	4.484	4.296	3.849
X0300_merged	5.712	5.299	5.120	5.845	5.705	5.383
X0302_merged_ncge	4.933	4.715	4.639	5.007	4.930	4.774
X0306_merged_sc1	5.747	5.609	5.596	5.809	5.741	5.619
X0308_merged_sc1	6.322	5.641	5.511	6.515	6.319	5.815
X0309_merged_sc1	6.747	5.976	5.855	6.956	6.733	6.147
X0310_merged	4.310	4.103	4.061	4.402	4.304	4.129
X0311_merged_sc1	5.757	5.611	5.596	5.812	5.749	5.619
X0313_merged	5.583	5.572	5.582	5.574	5.580	5.572
X0318_merged_sc1	5.231	4.917	4.827	5.331	5.218	4.960



Table C.1: — continued

Spectrum Name	$J$	$H$	$K_S$	F110W	F125W	F160W
X0319_merged_scl	4.253	3.531	3.385	4.454	4.250	3.718
X0320_merged_scl	5.372	4.644	4.488	5.539	5.357	4.841
X0323_merged	5.241	4.467	4.288	5.466	5.234	4.653
X0325_merged	5.910	4.949	4.586	6.170	5.871	5.403
X0326_merged	4.260	4.036	4.006	4.347	4.255	4.079
X0327_merged	5.713	5.717	5.733	5.697	5.709	5.711
X0328_merged	5.535	4.754	4.575	5.761	5.531	4.946
X0333_merged_scl	3.957	3.189	3.033	4.176	3.945	3.360
X0334_merged_scl	4.848	4.191	4.086	5.045	4.844	4.343
X0347_merged	6.347	5.754	5.663	6.540	6.339	5.876
X0348_merged	9.434	8.669	8.475	9.658	9.433	8.863
X0349_merged	9.489	9.065	9.059	9.606	9.484	9.155
X0350_merged	9.597	9.388	9.415	9.625	9.589	9.427
X0351_merged	11.267	10.676	10.668	11.416	11.264	10.822
X0352_merged	9.187	8.657	8.648	9.319	9.177	8.761
X0353_merged_ncge	8.959	7.673	7.005	9.303	8.930	8.120
X0354_merged	9.175	8.537	8.502	9.321	9.165	8.671
X0355_merged	8.768	8.188	8.119	8.935	8.760	8.313
X0356_merged	8.592	8.074	7.993	8.763	8.584	8.183
X0357_merged	9.550	9.640	9.718	9.490	9.538	9.602
X0358_merged	7.658	7.513	7.492	7.720	7.655	7.538
X0359_merged	11.144	10.854	10.863	11.245	11.138	10.900
X0360_merged	8.026	7.380	7.285	8.218	8.017	7.519
X0361_merged	10.949	10.554	10.524	11.083	10.943	10.628
X0363_merged	9.173	8.633	8.567	9.335	9.163	8.742

Table C.1: — continued

Spectrum Name	$J$	$H$	$K_S$	F110W	F125W	F160W
X0364_merged	7.649	6.785	6.660	7.872	7.647	7.004
X0365_merged	6.142	5.810	5.766	6.250	6.136	5.878
X0366_merged	8.132	7.771	7.729	8.264	8.125	7.833
X0367_merged	5.786	5.445	5.439	5.887	5.779	5.506
X0368_merged_nc1	8.279	7.537	7.167	8.584	8.338	7.923
X0370_merged	7.786	7.769	7.767	7.791	7.781	7.767
X0371_merged	6.533	6.417	6.389	6.585	6.523	6.416
X0372_merged	5.199	4.617	4.547	5.369	5.192	4.737
X0373_merged	5.709	5.324	5.271	5.849	5.702	5.392
X0374_merged	7.532	7.072	7.007	7.684	7.524	7.158
X0375_merged	7.413	6.980	6.930	7.567	7.404	7.054
X0376_merged	7.851	7.496	7.454	7.995	7.842	7.553
X0377_merged	7.058	6.472	6.337	7.247	7.051	6.610
X0378_merged	8.833	8.231	8.152	9.012	8.821	8.346
X0379_merged	6.617	6.071	5.979	6.791	6.605	6.177
X0380_merged	9.917	9.175	9.077	10.115	9.908	9.336
X0381_merged	10.380	9.671	9.596	10.564	10.355	9.825
X0382_merged	5.034	4.693	4.663	5.166	5.025	4.740
X0383_merged	7.861	7.370	7.298	8.015	7.850	7.459
X0384_merged	6.648	6.262	6.211	6.791	6.640	6.327
X0385_merged_ncge	13.775	13.066	12.919	14.024	13.759	13.297
X0386_merged	5.429	5.425	5.436	5.419	5.424	5.421
X0387_merged	9.055	8.789	8.773	9.159	9.048	8.824
X0388_merged	11.788	11.283	11.280	11.933	11.777	11.364
X0389_merged	12.160	11.744	11.801	12.290	12.151	11.803

Table C.1: — continued

Spectrum Name	$J$	$H$	$K_S$	F110W	F125W	F160W
X0390_merged	7.425	6.785	6.666	7.620	7.413	6.920
X0391_merged	7.422	6.765	6.635	7.611	7.411	6.905
X0392_merged	8.488	8.031	7.982	8.637	8.482	8.117
X0393_merged	7.710	7.002	6.890	7.901	7.697	7.145
X0394_merged	7.151	6.460	6.359	7.348	7.142	6.599
X0395_merged	6.246	5.727	5.655	6.406	6.236	5.825
X0396_merged_ncl	7.741	7.007	6.626	8.052	7.797	7.341
X0397_merged	7.475	6.734	6.360	7.783	7.535	7.073
X0398_merged_ncl	9.116	8.345	8.135	9.333	9.109	8.544
X0399_merged	8.681	7.913	7.705	8.914	8.673	8.109
X0400_merged	12.573	12.178	12.195	12.691	12.571	12.273
X0401_merged	12.342	11.956	11.976	12.459	12.338	12.048
X0402_merged	11.579	10.884	10.802	11.758	11.575	11.058
X0403_merged	10.411	9.720	9.631	10.574	10.399	9.879
X0405_merged	11.519	10.989	10.973	11.658	11.510	11.103
X0406_merged_scl	12.907	12.322	12.201	13.093	12.900	12.452
X0407_merged	9.698	8.977	8.881	9.880	9.687	9.132
X0408_merged	11.930	11.403	11.404	12.077	11.921	11.501
X0409_merged	6.422	5.887	5.804	6.584	6.414	5.991
X0410_merged	5.788	5.613	5.579	5.869	5.783	5.634
X0411_merged	13.254	12.523	12.329	13.514	13.273	12.727
X0412_merged	8.376	7.970	7.910	8.520	8.369	8.045
X0413_merged	5.231	4.547	4.394	5.427	5.219	4.696
X0414_merged	7.243	6.945	6.910	7.351	7.238	6.993
X0415_merged	7.347	6.875	6.801	7.495	7.340	6.964

Table C.1: — continued

Spectrum Name	$J$	$H$	$K_S$	F110W	F125W	F160W
X0416_merged	8.033	7.434	7.339	8.207	8.022	7.550
X0417_merged	7.146	6.493	6.386	7.332	7.135	6.625
X0418_merged	6.807	6.300	6.219	6.958	6.799	6.397
X0419_merged	12.862	12.379	12.407	12.997	12.853	12.472
X0420_merged	11.142	10.231	9.975	11.454	11.145	10.493
X0421_merged	9.346	9.282	9.288	9.351	9.339	9.290
X0422_merged	6.257	5.577	5.441	6.454	6.250	5.737
X0423_merged	5.264	4.767	4.704	5.410	5.256	4.861
X0426_merged	12.569	12.101	12.066	12.719	12.550	12.196
X0427_merged	12.638	12.107	12.069	12.807	12.632	12.229
X0428_merged	7.809	7.036	6.730	8.029	7.840	7.302
X0430_merged	5.748	5.226	5.130	5.923	5.737	5.331
X0432_merged	4.889	4.600	4.556	4.991	4.882	4.645
X0433_merged	6.317	6.260	6.256	6.351	6.311	6.261
X0434_merged	6.687	6.038	5.923	6.874	6.672	6.171
X0435_merged_ncge	7.706	7.160	7.072	7.895	7.708	7.316
X0436_merged	5.209	4.714	4.629	5.374	5.201	4.814
X0437_merged	6.042	5.425	5.321	6.227	6.028	5.548
X0438_merged	5.357	4.766	4.656	5.544	5.351	4.900
X0439_merged	6.603	5.938	5.795	6.796	6.588	6.074
X0440_merged	7.563	6.964	6.673	7.830	7.565	7.134
X0441_merged	7.715	7.166	7.079	7.881	7.703	7.268
X0442_merged	5.421	4.819	4.717	5.602	5.409	4.931
X0443_merged	7.007	7.060	7.082	6.983	7.002	7.038
X0444_merged	5.757	5.179	5.078	5.926	5.745	5.289

Table C.1: — continued

Spectrum Name	$J$	$H$	$K_S$	F110W	F125W	F160W
X0445_merged	9.268	8.961	8.924	9.379	9.262	9.008
X0446_merged	6.323	5.773	5.684	6.492	6.313	5.876
X0447_merged	6.013	5.374	5.268	6.207	6.006	5.516
X0448_merged	10.902	11.001	11.099	10.844	10.897	10.961
X0449_merged	5.840	5.365	5.268	5.999	5.839	5.466
X0450_merged	6.542	6.496	6.469	6.563	6.541	6.507
X0451_merged	6.750	6.577	6.532	6.816	6.749	6.616
X0452_merged	4.707	4.396	4.336	4.800	4.706	4.468
X0453_merged	5.701	5.109	5.038	5.879	5.695	5.238
X0454_merged	8.736	8.196	8.117	8.906	8.730	8.314
X0455_merged	5.886	5.633	5.615	5.986	5.881	5.668
X0456_merged	7.176	6.738	6.699	7.327	7.170	6.823
X0458_merged	5.562	4.924	4.826	5.743	5.551	5.054
X0459_merged	7.382	7.301	7.288	7.410	7.375	7.309
X0460_merged	7.590	7.592	7.596	7.581	7.583	7.579
X0461_merged	8.226	8.114	8.088	8.251	8.218	8.122
X0463_merged	10.915	11.025	11.142	10.860	10.906	10.968
X0464_merged	7.754	7.332	7.316	7.877	7.746	7.407
X0465_merged	8.659	8.576	8.597	8.682	8.655	8.589
X0466_merged_scl	4.716	4.239	4.181	4.865	4.711	4.340
X0467_merged	6.343	6.414	6.526	6.289	6.338	6.392
X0468_merged	6.874	6.791	6.813	6.882	6.870	6.806
X0469_merged	6.331	6.251	6.270	6.352	6.328	6.262
X0470_merged	7.053	7.098	7.191	6.994	7.049	7.087
X0471_merged	5.378	4.897	4.860	5.524	5.376	5.010

Table C.1: — continued

Spectrum Name	$J$	$H$	$K_S$	F110W	F125W	F160W
X0472_merged	7.585	7.502	7.521	7.610	7.580	7.515
X0473_merged	5.816	5.340	5.296	5.966	5.812	5.446
X0474_merged	5.306	4.959	4.929	5.422	5.299	5.027
X0475_merged	5.947	5.764	5.765	6.016	5.943	5.794
X0476_merged	5.891	5.691	5.693	5.961	5.886	5.725
X0477_merged	6.199	5.849	5.840	6.308	6.193	5.910
X0478_merged_nc1	8.063	7.251	7.019	8.316	8.080	7.505
X0479_merged_ncge	7.973	7.431	7.308	8.176	7.982	7.669
X0480_merged	9.363	9.036	9.041	9.469	9.356	9.089
X0481_merged	5.782	5.230	5.180	5.948	5.776	5.345
X0482_merged	5.425	4.925	4.875	5.580	5.418	5.026
X0483_merged	6.741	6.589	6.601	6.802	6.736	6.610
X0484_merged	6.305	5.833	5.802	6.450	6.298	5.925
X0485_merged	7.165	7.004	7.011	7.217	7.161	7.028
X0486_merged	7.169	6.736	6.698	7.317	7.161	6.817
X0487_merged	7.690	6.928	6.677	7.897	7.711	7.172
X0488_merged	5.291	5.077	5.075	5.366	5.284	5.109
X0489_merged	7.743	6.946	6.712	7.967	7.781	7.228
X0490_merged	5.850	5.371	5.353	6.004	5.839	5.454
X0491_merged	12.170	11.618	11.665	12.314	12.162	11.732
X0492_merged	7.219	6.396	6.108	7.536	7.270	6.718
X0493_merged	9.592	8.812	8.740	9.794	9.580	8.986
X0494_merged	10.100	9.470	9.437	10.269	10.093	9.613
X0495_merged	5.751	4.872	4.706	5.980	5.741	5.079
X0496_merged	8.577	8.067	8.047	8.716	8.566	8.161

Table C.1: — continued

Spectrum Name	$J$	$H$	$K_S$	F110W	F125W	F160W
X0498_merged	5.470	4.802	4.665	5.680	5.462	4.944
X0500_merged	6.915	6.276	6.194	7.105	6.903	6.401
X0501_merged	6.925	6.295	6.211	7.111	6.912	6.416
X0502_merged	9.131	8.522	8.471	9.287	9.122	8.651
X0504_merged	11.059	10.368	10.256	11.263	11.051	10.523
X0505_merged_ncl	12.815	11.543	10.787	13.175	12.796	11.984
X0506_merged	10.746	9.985	9.826	10.966	10.740	10.163
X0508_merged	7.723	7.038	6.905	7.928	7.713	7.183
X0509_merged	12.822	12.047	11.858	13.107	12.832	12.251
X0510_merged	13.499	12.633	12.522	13.746	13.484	12.825
X0511_merged	10.534	9.590	9.332	10.824	10.544	9.872
X0514_merged	11.093	10.318	10.107	11.357	11.160	10.672
X0515_merged	13.042	11.929	11.307	13.389	13.029	12.317
X0516_merged	12.759	11.590	10.886	13.113	12.753	11.984
X0517_merged	12.119	11.211	10.930	12.415	12.120	11.454
X0518_merged	10.322	10.042	10.003	10.417	10.317	10.103
X0519_merged	12.657	11.901	11.657	12.957	12.672	12.148
X0520_merged	6.866	6.382	6.347	7.022	6.858	6.473
X0521_merged	10.312	9.633	9.596	10.486	10.299	9.770
X0522_merged	10.924	10.248	10.232	11.097	10.911	10.385
X0523_merged	10.589	9.870	9.842	10.766	10.577	10.021
X0524_merged	12.796	12.132	12.131	12.987	12.790	12.283
X0526_merged	5.422	4.833	4.721	5.605	5.413	4.956
X0527_merged	7.736	6.984	6.665	7.965	7.777	7.262
X0529_merged	6.118	5.830	5.769	6.230	6.114	5.880

Table C.1: — continued

Spectrum Name	$J$	$H$	$K_S$	F110W	F125W	F160W
X0530_merged	12.373	11.587	11.359	12.661	12.398	11.870
X0531_merged	12.445	11.524	11.289	12.727	12.452	11.775
X0532_merged	12.431	11.459	11.231	12.741	12.450	11.747
X0533_merged_ncl	12.268	11.329	11.079	12.599	12.280	11.601
X0534_merged_ncl	12.784	11.479	10.801	13.133	12.770	11.917
X0535_merged	7.310	7.177	7.188	7.356	7.306	7.196
X0536_merged	6.204	5.683	5.645	6.359	6.194	5.780
X0537_merged	5.560	4.982	4.909	5.735	5.552	5.102
X0538_merged	5.281	4.835	4.783	5.434	5.275	4.924
X0539_merged	7.262	7.327	7.384	7.226	7.258	7.306
X0540_merged	5.783	5.234	5.017	5.999	5.784	5.376
X0542_merged	8.407	8.168	8.078	8.501	8.403	8.224
X0543_merged_ncl	12.190	11.238	10.907	12.526	12.204	11.516
X0544_merged	13.440	12.032	11.023	13.825	13.423	12.446
X0545_merged	7.241	7.024	6.960	7.330	7.234	7.051
X0546_merged	5.823	5.491	5.447	5.956	5.815	5.544
X0547_merged	6.671	6.335	6.315	6.782	6.663	6.389
X0548_merged	5.282	4.661	4.570	5.465	5.270	4.779
X0549_merged	6.370	5.784	5.713	6.530	6.359	5.898
X0550_merged	5.451	4.738	4.582	5.671	5.446	4.909
X0551_merged	12.804	11.936	11.745	13.046	12.798	12.149
X0552_merged	5.875	5.218	5.097	6.076	5.869	5.366
X0553_merged	5.577	4.892	4.749	5.794	5.576	5.057
X0554_merged	5.448	5.085	5.016	5.584	5.441	5.149
X0555_merged	6.706	6.186	6.100	6.873	6.693	6.279



Table C.1: — continued

Spectrum Name	$J$	$H$	$K_S$	F110W	F125W	F160W
X0556_merged	5.504	4.846	4.731	5.705	5.501	5.002
X0557_merged	7.152	6.247	5.895	7.423	7.178	6.526
X0558_merged	7.646	7.236	7.168	7.791	7.639	7.313
X0559_merged	5.591	5.091	5.000	5.763	5.587	5.202
X0560_merged	5.784	5.230	5.127	5.969	5.772	5.345
X0561_merged	7.960	7.498	7.430	8.121	7.951	7.586
X0562_merged	5.471	4.742	4.599	5.681	5.462	4.909
X0563_merged	5.144	4.581	4.474	5.320	5.143	4.727
X0564_merged	5.750	5.528	5.500	5.846	5.744	5.562
X0565_merged	4.640	4.114	4.034	4.801	4.629	4.221
X0566_merged	5.490	5.058	5.007	5.633	5.478	5.134
X0567_merged	6.359	5.843	5.755	6.525	6.350	5.948
X0568_merged	7.247	6.558	6.425	7.448	7.240	6.722
X0569_merged	5.617	5.330	5.340	5.721	5.606	5.369
X0570_merged	7.579	7.072	6.995	7.740	7.571	7.172
X0571_merged	7.956	7.554	7.500	8.090	7.949	7.626
X0572_merged	11.003	10.439	10.349	11.172	10.990	10.548
X0573_merged	7.947	7.702	7.653	8.048	7.942	7.737
X0574_merged_ncge	8.069	6.738	5.980	8.427	8.029	7.198
X0576_merged_ncl	7.364	6.292	5.777	7.623	7.306	6.650
X0577_merged_ncl_ncge	7.872	6.641	5.637	8.472	8.017	7.278
X0578_merged	5.331	4.887	4.791	5.481	5.327	4.978
X0579_merged	6.488	6.259	6.200	6.584	6.482	6.291
X0580_merged	6.628	6.459	6.402	6.707	6.624	6.485
X0581_merged	4.728	4.183	4.071	4.905	4.721	4.296

Table C.1: — continued

Spectrum Name	$J$	$H$	$K_S$	F110W	F125W	F160W
X0582_merged	6.953	7.042	7.099	6.895	6.949	7.014
X0583_merged	5.650	5.133	5.026	5.819	5.642	5.237
X0584_merged	5.461	4.778	4.608	5.678	5.454	4.941
X0585_merged	5.987	5.686	5.612	6.110	5.980	5.733
X0586_merged	6.248	5.775	5.674	6.402	6.241	5.869
X0587_merged	7.278	6.438	6.207	7.518	7.268	6.643
X0588_merged	5.397	4.680	4.493	5.617	5.389	4.851
X0589_merged	6.894	6.135	5.885	7.125	6.900	6.323
X0590_merged	6.962	6.699	6.634	7.060	6.955	6.744
X0591_merged_nc1	7.532	6.458	6.053	7.868	7.522	6.833
X0592_merged	12.307	11.379	11.127	12.603	12.303	11.620
X0593_merged	6.599	6.016	5.934	6.777	6.588	6.130
X0594_merged	6.693	6.072	5.975	6.871	6.685	6.207
X0595_merged	7.618	7.228	7.151	7.768	7.613	7.310
X0596_merged	5.655	5.500	5.475	5.733	5.651	5.523
X0597_merged	5.122	4.764	4.703	5.258	5.117	4.833
X0598_merged	6.931	6.305	6.210	7.113	6.923	6.437
X0599_merged_ncge	6.765	6.709	6.709	6.764	6.763	6.736
X0600_merged	6.515	5.944	5.847	6.687	6.505	6.060
X0601_merged	12.469	11.870	11.831	12.644	12.459	11.990
X0602_merged	8.980	8.555	8.505	9.121	8.972	8.636
X0604_merged	8.607	8.140	8.083	8.759	8.595	8.224
X0605_merged_ncge	8.828	7.595	6.962	9.145	8.781	8.032
X0606_merged_ncge	8.794	7.567	6.941	9.111	8.747	8.003
X0607_merged	9.026	8.738	8.721	9.135	9.018	8.779

Table C.1: — continued

Spectrum Name	$J$	$H$	$K_S$	F110W	F125W	F160W
X0609_merged_nc1	7.489	6.425	6.041	7.815	7.482	6.810
X0610_merged	11.210	10.645	10.586	11.364	11.209	10.792
X0611_merged	8.544	8.274	8.258	8.645	8.537	8.314
X0613_merged	8.621	8.335	8.311	8.728	8.614	8.378
X0614_merged	8.859	8.855	8.866	8.854	8.854	8.855
X0615_merged	9.440	8.678	8.485	9.661	9.435	8.867
X0616_merged	8.886	8.582	8.545	8.979	8.879	8.638
X0617_merged	4.947	4.858	4.841	4.987	4.940	4.862
X0618_merged	6.052	5.549	5.479	6.216	6.041	5.641
X0619_merged	9.606	9.406	9.397	9.648	9.593	9.440
X0620_merged	6.934	6.288	6.207	7.125	6.925	6.424
X0621_merged	9.244	8.713	8.662	9.380	9.236	8.819
X0622_merged	12.602	12.300	12.297	12.716	12.596	12.344
X0623_merged	13.182	12.930	12.971	13.281	13.175	12.962
X0624_merged	14.086	13.873	13.982	14.193	14.080	13.890
X0625_merged	6.930	6.303	6.185	7.121	6.916	6.433
X0626_merged	8.776	8.757	8.765	8.777	8.772	8.759
X0627_merged	6.455	5.804	5.709	6.646	6.441	5.931
X0628_merged	5.226	4.626	4.443	5.443	5.217	4.768
X0629_merged	5.256	5.042	5.019	5.361	5.251	5.074
X0630_merged	10.819	10.424	10.385	10.939	10.809	10.488
X0631_merged	13.045	12.805	12.844	13.149	13.038	12.831
X0632_merged	4.999	4.746	4.722	5.081	4.991	4.795
X0633_merged	5.419	5.326	5.315	5.458	5.413	5.333
X0634_merged	6.901	6.258	6.175	7.090	6.887	6.382

Table C.1: — continued

Spectrum Name	$J$	$H$	$K_S$	F110W	F125W	F160W
X0635_merged_ncge	8.909	7.637	6.984	9.231	8.877	8.104
X0636_merged	7.742	7.551	7.539	7.818	7.735	7.573
X0637_merged_ncge	9.901	9.404	9.303	10.071	9.901	9.569
X0638_merged	7.866	7.035	6.753	8.130	7.895	7.310
X0639_merged	6.410	6.297	6.295	6.462	6.406	6.314
X0640_merged	11.258	11.079	11.123	11.309	11.251	11.109
X0641_merged	5.245	4.696	4.609	5.413	5.240	4.828
X0642_merged	7.434	6.688	6.389	7.639	7.459	6.930
X0643_merged	7.263	6.616	6.538	7.437	7.251	6.748
X0644_merged	7.393	6.646	6.347	7.608	7.418	6.888
X0645_merged	5.945	5.845	5.831	5.988	5.940	5.857
X0646_merged	5.752	5.726	5.760	5.738	5.746	5.732
X0647_merged	6.530	5.708	5.363	6.832	6.568	6.004
X0648_merged	7.425	7.353	7.351	7.460	7.420	7.358
X0649_merged	8.941	8.380	8.192	9.139	8.938	8.520
X0650_merged	7.671	7.105	6.992	7.863	7.659	7.213
X0651_merged	8.193	7.538	7.402	8.387	8.182	7.681
X0652_merged	12.736	12.301	12.305	12.867	12.734	12.405
X0653_merged	5.897	5.992	6.092	5.854	5.892	5.964
X0654_merged	7.244	7.095	7.078	7.317	7.239	7.113
X0655_merged	6.158	6.136	6.155	6.140	6.153	6.142
X0656_merged	7.592	7.570	7.591	7.590	7.587	7.569
X0657_merged	7.241	7.214	7.229	7.251	7.237	7.215
X0658_merged	5.799	5.312	5.245	5.952	5.794	5.421
X0659_merged	7.509	6.940	6.720	7.753	7.507	7.088

Table C.1: — continued

Spectrum Name	$J$	$H$	$K_S$	F110W	F125W	F160W
X0660_merged	11.602	11.294	11.328	11.673	11.594	11.351
X0661_merged	9.442	8.829	8.779	9.588	9.433	8.962
X0662_merged	7.410	7.376	7.434	7.380	7.404	7.384
X0663_merged	7.088	6.436	6.321	7.275	7.074	6.572
X0664_merged	6.010	5.580	5.528	6.147	6.003	5.668
X0665_merged	7.818	7.138	6.986	8.015	7.805	7.289
X0666_merged	6.614	6.570	6.568	6.634	6.610	6.573
X0667_merged	5.883	5.320	5.196	6.071	5.880	5.464
X0668_merged	6.901	6.756	6.743	6.978	6.896	6.770
X0669_merged	5.565	4.936	4.849	5.748	5.554	5.062
X0670_merged	7.323	6.800	6.740	7.473	7.313	6.899
X0671_merged	6.375	6.182	6.158	6.464	6.369	6.207
X0672_merged	7.068	6.336	6.067	7.301	7.103	6.621
X0673_merged	7.458	7.330	7.321	7.517	7.452	7.345
X0674_merged	6.914	6.818	6.823	6.942	6.908	6.829
X0675_merged	7.945	7.170	6.933	8.184	7.967	7.424
X0676_merged	6.465	6.527	6.588	6.418	6.462	6.506
X0677_merged	6.278	6.075	6.043	6.365	6.272	6.103
X0678_merged	5.422	4.808	4.722	5.595	5.412	4.932
X0679_merged	6.585	6.366	6.348	6.674	6.579	6.394
X0680_merged	4.601	4.384	4.376	4.681	4.595	4.416
X0681_merged	11.971	11.464	11.457	12.116	11.961	11.558
X0682_merged	8.964	8.691	8.673	9.067	8.957	8.728
X0683_merged	8.514	7.818	7.642	8.725	8.501	7.975
X0684_merged	8.510	7.817	7.641	8.724	8.497	7.972

Table C.1: — continued

Spectrum Name	$J$	$H$	$K_S$	F110W	F125W	F160W
X0685_merged	7.606	7.289	7.240	7.734	7.600	7.343
X0686_merged	7.575	7.259	7.212	7.702	7.568	7.311
X0687_merged	6.170	5.827	5.797	6.289	6.162	5.878
X0688_merged	6.208	5.868	5.837	6.325	6.201	5.921
X0689_merged	7.481	6.752	6.454	7.713	7.509	6.987
X0690_merged	7.644	6.914	6.615	7.866	7.670	7.147
X0691_merged	5.660	5.513	5.500	5.727	5.655	5.531
X0692_merged_ncge	9.569	9.534	9.551	9.541	9.563	9.530
X0694_merged	5.915	5.244	5.108	6.125	5.909	5.388
X0695_merged	7.479	7.422	7.420	7.505	7.475	7.425
X0696_merged	6.685	6.434	6.407	6.790	6.677	6.467
X0697_merged	7.838	7.472	7.435	7.971	7.831	7.532
X0698_merged	12.594	12.009	11.935	12.781	12.589	12.155
X0699_merged	11.885	11.367	11.352	12.029	11.875	11.462
X0700_merged	8.455	7.900	7.822	8.625	8.442	8.003
X0701_merged_scl	13.264	12.815	12.816	13.372	13.252	12.896
X0702_merged	9.719	9.019	8.935	9.904	9.704	9.163
X0703_merged	10.647	10.106	10.080	10.794	10.638	10.219
X0705_merged	11.503	10.970	10.939	11.657	11.492	11.076
X0706_merged_scl	13.191	12.822	12.820	13.276	13.179	12.883
X0712_merged	10.040	9.341	9.270	10.215	10.029	9.498
X0713_merged	12.201	11.702	11.765	12.359	12.194	11.794
X0714_merged	12.999	12.412	12.262	13.157	12.990	12.536
X0715_merged	6.223	5.695	5.606	6.393	6.213	5.788
X0716_merged	6.212	5.680	5.591	6.386	6.201	5.774

Table C.1: — continued

Spectrum Name	$J$	$H$	$K_S$	F110W	F125W	F160W
X0717_merged	6.482	5.952	5.867	6.653	6.472	6.047
X0718_merged	10.573	9.910	9.858	10.746	10.563	10.056
X0719_merged	11.039	10.384	10.325	11.218	11.029	10.526
X0720_merged	10.877	10.220	10.149	11.051	10.866	10.363
X0721_merged	8.978	8.463	8.376	9.148	8.967	8.560
X0722_merged	8.694	8.183	8.097	8.861	8.684	8.279
X0723_merged	8.586	8.077	7.991	8.753	8.575	8.173
X0727_merged	7.534	7.432	7.416	7.574	7.528	7.439
X0728_merged	7.576	7.471	7.453	7.616	7.571	7.478
X0729_merged	7.569	7.470	7.457	7.612	7.564	7.476
X0730_merged	8.505	8.470	8.476	8.523	8.499	8.463
X0731_merged	8.413	8.378	8.384	8.426	8.406	8.370
X0732_merged	8.654	8.615	8.622	8.670	8.648	8.609
X0733_merged	6.360	5.805	5.745	6.523	6.348	5.905
X0734_merged	10.653	10.010	9.982	10.818	10.641	10.142
X0735_merged	12.270	11.770	11.788	12.404	12.262	11.872
X0736_merged	8.480	7.768	7.640	8.684	8.464	7.918
X0737_merged	7.416	6.786	6.541	7.676	7.412	6.947
X0738_merged_ncge	8.080	7.517	7.374	8.289	8.093	7.769
X0739_merged	6.971	6.454	6.382	7.140	6.961	6.557
X0741_merged	12.277	11.772	11.768	12.421	12.270	11.876
X0742_merged_scl	13.184	12.749	12.766	13.291	13.178	12.840
X0743_merged_scl	8.382	8.106	8.099	8.488	8.380	8.156
X0744_merged	7.260	6.617	6.507	7.449	7.247	6.744
X0746_merged	9.241	8.486	8.377	9.434	9.228	8.653

Table C.1: — continued

Spectrum Name	$J$	$H$	$K_S$	F110W	F125W	F160W
X0747_merged	5.681	5.601	5.587	5.716	5.676	5.611
X0748_merged	9.961	9.354	9.291	10.116	9.954	9.494
X0749_merged	7.247	6.968	6.926	7.350	7.239	7.009
X0750_merged_ncge	7.794	7.249	7.151	7.973	7.796	7.407
X0751_merged	6.939	6.458	6.369	7.088	6.930	6.556
X0752_merged	6.918	6.309	6.220	7.078	6.905	6.427
X0753_merged	7.380	6.933	6.883	7.513	7.371	7.014
X0754_merged_scl	13.262	12.890	12.823	13.380	13.254	12.964
X0755_merged	11.884	11.361	11.266	12.073	11.875	11.465
X0756_merged	9.633	8.749	8.544	9.877	9.624	8.961
X0757_merged	12.063	11.982	12.012	12.087	12.053	11.999
X0760_merged	13.929	13.439	13.420	14.076	13.919	13.525
X0761_merged	7.472	6.750	6.373	7.700	7.512	7.034
X0762_merged_scl	13.113	12.666	12.685	13.228	13.108	12.762
X0763_merged	8.306	7.621	7.467	8.509	8.293	7.772
X0764_merged_ncge	7.965	7.431	7.268	8.166	7.976	7.677
X0765_merged	11.079	10.177	9.917	11.346	11.084	10.435
X0767_merged	9.533	8.697	8.555	9.761	9.528	8.902
X0768_merged	7.263	6.767	6.710	7.419	7.254	6.859
X0769_merged	7.253	6.755	6.695	7.410	7.244	6.848
X0770_merged	8.801	8.517	8.493	8.901	8.795	8.564
X0771_merged	7.439	7.511	7.575	7.388	7.435	7.489
X0772_merged	6.924	6.428	6.348	7.085	6.919	6.537
X0774_merged_scl	9.350	9.082	9.067	9.457	9.346	9.125
X0775_merged	8.873	8.648	8.630	8.952	8.868	8.686



Table C.1: — continued

Spectrum Name	$J$	$H$	$K_S$	F110W	F125W	F160W
X0778_merged	7.681	7.333	7.312	7.808	7.667	7.382
X0782_merged	8.181	8.071	8.066	8.229	8.177	8.089
X0783_merged	12.757	11.912	11.716	13.004	12.735	12.116
X0786_merged	9.835	9.058	8.764	10.089	9.858	9.316
X0787_merged	6.366	5.863	5.817	6.521	6.362	5.970
X0788_merged	6.493	6.020	5.984	6.648	6.489	6.119
X0789_merged	6.471	5.979	5.941	6.621	6.467	6.082
X0791_merged	4.803	4.557	4.538	4.904	4.794	4.588
X0792_merged	6.775	6.164	5.981	7.002	6.770	6.312
X0793_merged	6.087	5.815	5.811	6.193	6.080	5.853
X0794_merged	7.711	7.631	7.670	7.744	7.705	7.632
X0795_merged	9.131	8.824	8.844	9.236	9.123	8.868
X0796_merged	6.495	6.241	6.254	6.592	6.487	6.273
X0797_merged	10.735	9.931	9.828	10.951	10.726	10.114
X0798_merged	12.892	12.022	11.865	13.138	12.883	12.234
X0801_merged	13.908	13.053	12.952	14.158	13.895	13.246
X0803_merged_ncl	12.989	11.702	10.951	13.356	12.974	12.118
X0804_merged	13.458	12.585	12.476	13.690	13.445	12.779
X0805_merged_scl	14.332	13.540	13.414	14.553	14.321	13.727
X0806_merged_scl	14.379	13.583	13.458	14.600	14.370	13.772
X0807_merged	13.244	12.354	12.147	13.520	13.250	12.595
X0809_merged	13.191	12.402	12.159	13.462	13.203	12.642
X0811_merged	12.298	11.391	11.222	12.544	12.288	11.610
X0813_merged_ncl	12.004	11.024	10.748	12.329	12.001	11.283
X0815_merged	11.134	10.193	9.891	11.455	11.143	10.469

Table C.1: — continued

Spectrum Name	$J$	$H$	$K_S$	F110W	F125W	F160W
X0816_merged	6.293	6.095	6.105	6.365	6.285	6.121
X0817_merged	7.454	7.499	7.595	7.408	7.449	7.482
X0821_merged	12.275	11.432	11.141	12.574	12.287	11.715
X0824_merged	9.233	8.768	8.801	9.338	9.225	8.868
X0825_merged	9.970	9.121	8.938	10.204	9.963	9.337
X0826_merged	5.401	4.693	4.609	5.601	5.392	4.852
X0827_merged	6.084	5.437	5.377	6.261	6.072	5.567
X0828_merged	6.243	5.498	5.343	6.460	6.238	5.688
X0829_merged	5.366	4.783	4.671	5.556	5.367	4.937
X0831_merged	7.224	7.051	7.055	7.291	7.218	7.075
X0832_merged	6.484	6.164	6.146	6.604	6.475	6.213
X0834_merged	7.409	7.361	7.353	7.419	7.405	7.371
X0835_merged	10.102	9.572	9.498	10.262	10.098	9.691
X0836_merged	6.092	5.619	5.534	6.249	6.084	5.715
X0837_merged	4.813	4.568	4.522	4.904	4.806	4.615
X0838_merged	6.159	5.998	5.964	6.235	6.154	6.021
X0839_merged	5.182	4.651	4.537	5.355	5.180	4.781
X0840_merged	5.397	4.837	4.723	5.573	5.391	4.965
X0841_merged	7.206	6.634	6.529	7.380	7.197	6.756
X0842_merged	4.744	4.443	4.379	4.855	4.734	4.490
X0843_merged	7.620	7.132	7.085	7.776	7.609	7.218
X0844_merged	6.993	6.162	5.986	7.221	6.984	6.361
X0845_merged	5.365	4.514	4.316	5.603	5.352	4.717
X0846_merged	7.811	7.504	7.484	7.932	7.803	7.550
X0847_merged	7.546	7.448	7.441	7.593	7.540	7.457

Table C.1: — continued

Spectrum Name	$J$	$H$	$K_S$	F110W	F125W	F160W
X0848_merged	6.247	6.157	6.144	6.282	6.241	6.170
X0849_merged	5.610	4.684	4.440	5.870	5.603	4.930
X0850_merged	5.485	4.582	4.339	5.727	5.477	4.825
X0851_merged	6.105	5.698	5.625	6.251	6.097	5.776
X0852_merged	6.899	6.063	5.867	7.128	6.889	6.265
X0853_merged	7.546	7.052	6.981	7.703	7.535	7.141
X0854_merged	5.046	4.621	4.511	5.191	5.038	4.707
X0855_merged	6.136	5.690	5.598	6.286	6.129	5.781
X0856_merged	6.903	6.779	6.735	6.971	6.898	6.797
X0857_merged	6.672	6.558	6.516	6.718	6.668	6.576
X0858_merged	6.185	5.655	5.584	6.355	6.180	5.772
X0859_merged	7.363	6.657	6.548	7.570	7.356	6.822
X0860_merged	7.259	6.071	5.464	7.567	7.222	6.558
X0861_merged	5.368	4.714	4.566	5.560	5.364	4.873
X0862_merged_ncl	9.302	7.999	7.226	9.677	9.276	8.389
X0863_merged	8.599	8.306	8.273	8.713	8.591	8.350
X0864_merged_ncl	9.127	7.839	7.154	9.476	9.098	8.320
X0865_merged	5.282	5.000	4.956	5.404	5.276	5.044
X0866_merged	7.121	6.507	6.407	7.306	7.110	6.627
X0867_merged	7.341	7.065	7.038	7.444	7.336	7.107
X0868_merged	9.754	9.476	9.457	9.859	9.747	9.516
X0869_merged	5.279	4.432	4.228	5.517	5.270	4.637
X0870_merged	8.793	8.600	8.599	8.875	8.787	8.622
X0871_merged	5.602	5.119	5.044	5.770	5.596	5.224
X0872_merged	10.201	9.896	9.884	10.325	10.190	9.938

Table C.1: — continued

Spectrum Name	$J$	$H$	$K_S$	F110W	F125W	F160W
X0873_merged	6.570	6.153	6.087	6.721	6.562	6.226
X0874_merged	8.590	8.543	8.550	8.608	8.585	8.544
X0875_merged	6.545	6.202	6.148	6.677	6.536	6.252
X0876_merged_ncl_ncge	7.494	6.576	6.030	7.954	7.592	7.037
X0877_merged	6.390	6.061	6.006	6.518	6.385	6.121
X0878_merged	5.623	4.917	4.731	5.843	5.618	5.068
X0879_merged	6.078	5.921	5.895	6.158	6.073	5.945
X0880_merged	6.043	5.268	5.125	6.258	6.032	5.446
X0881_merged	7.385	6.958	6.917	7.524	7.378	7.039
X0882_merged	9.102	8.762	8.737	9.224	9.092	8.817
X0883_merged	8.270	7.657	7.572	8.455	8.270	7.810
X0884_merged	10.520	9.983	9.881	10.689	10.512	10.095
X0885_merged	8.443	8.385	8.372	8.471	8.439	8.397
X0886_merged	7.990	7.525	7.458	8.149	7.981	7.611
X0887_merged	4.947	4.394	4.289	5.129	4.937	4.510
X0888_merged	9.116	8.348	8.033	9.397	9.163	8.694
X0889_merged	10.529	10.000	9.816	10.745	10.534	10.155
X0890_merged	6.808	6.321	6.253	6.969	6.803	6.428
X0891_merged	7.361	6.779	6.701	7.533	7.354	6.903
X0893_merged	5.027	4.701	4.609	5.144	5.031	4.786
X0894_merged	5.850	5.804	5.803	5.876	5.847	5.818
X0895_merged	5.382	5.237	5.220	5.444	5.380	5.267
X0897_merged	5.859	5.233	5.143	6.051	5.851	5.359
X0898_merged	5.132	4.916	4.885	5.242	5.123	4.937
X0899_merged	8.371	8.182	8.171	8.454	8.362	8.202

Table C.1: — continued

Spectrum Name	$J$	$H$	$K_S$	F110W	F125W	F160W
X0900_merged	7.805	7.447	7.411	7.932	7.796	7.505
X0901_merged	6.763	6.388	6.349	6.905	6.752	6.446
X0902_merged	8.504	7.954	7.888	8.678	8.497	8.071
X0903_merged	5.739	5.066	4.927	5.943	5.722	5.208
X0904_merged	6.345	5.866	5.813	6.498	6.335	5.950
X0905_merged	8.046	7.314	6.971	8.291	8.098	7.632
X0906_merged	11.338	10.821	10.695	11.528	11.327	10.925
X0907_merged	5.592	4.835	4.676	5.807	5.578	5.006
X0908_merged	6.644	5.780	5.637	6.859	6.636	5.989
X0909_merged	6.724	5.825	5.667	6.947	6.716	6.044
X0910_merged	7.960	7.259	6.886	8.187	8.026	7.614
X0911_merged	8.157	7.459	7.101	8.381	8.224	7.811

## Appendix D

### EXTINCTION MAP COMPARISONS

We investigated a number of available line-of-sight extinction estimates for our sample of library stars, both from large-scale extinction maps and from parameter fits to individual stars. Of these, five are from three-dimensional (3D) maps derived from aggregate spectrophotometric and parallax information (Vergely et al. 2022b; Lallement et al. 2022, 2018; Green et al. 2019; Chen et al. 2019a); three are from SED fitting techniques applied to individual library stars, including the values adopted for or derived from the original spectral library data (Anders et al. 2022; Andrae et al. 2022); and the remaining three are from two-dimensional (2D) total line-of-sight maps (Delchambre et al. 2022; Skowron et al. 2021; Schlafly & Finkbeiner 2011).

A summary of all extinction data sources we considered is given in Table D.1, including primary references, applied conversion factors from original data units to  $E(B - V)$  if needed, and numbers of library stars for which extinction data are a) available for a given star or distance-independent line of sight, and b) of those how many are considered valid measurements. For 3D maps we follow the `dustmaps` convention, where  $E(B - V)$  values are considered valid for a given sightline within a specified range of distances. We consider single-star  $E(B - V)$  measurements valid if they are free from data or fitting quality flags as defined by respective references, if available.

Figure D.1 shows pairwise comparisons for  $E(B - V)$  values from the 3D maps and individual stellar fits, and median absolute deviations of each of these are given in Table D.2. The majority of  $E(B - V)$  measurements agree to within 0.05 or 0.1 mag, with the exception of GSP-Phot, which shows deviations of up to 0.25 mag.

Table D.1: Summary of extinction data sources

Kind	Name	$N_{\text{total}}^*$	$N_{\text{valid}}^*$	$E(B - V)$ conversion	Reference(s)	Comments
3D maps	G-TOMO v2	980	808	$3.1^{-1}$	Vergely et al. 2022b	
	G-TOMO v1	980	808	$3.1^{-1}$	Lallement et al. 2022	
	StillSM	939	724	—	Lallement et al. 2018	
	Bayestar19	891	238	0.884	Green et al. 2019	
	Chen+19	480	377	0.75	Chen et al. 2019a	<i>Gaia</i> DR2 passbands
Single-star	StarHorse2021	619	425	$3.3^{-1}$	Anders et al. 2022	
	GSP-Phot	533	533	$3.1^{-1}$	Andrae et al. 2022	
	Library values	926	926	—	Rayner et al. 2009, Villaume et al. 2017, Verro et al. 2022b	
2D maps	<i>Gaia</i> TGE	1020	1020	$3.1^{-1}$	Delchambre et al. 2022	
	SFD	1063	1063	—	Schlafly & Finkbeiner 2011	
	OGLE	76	76	0.808	Skowron et al. 2021	Magellanic Clouds only

Table D.2: Median absolute deviations of pairwise  $E(B - V)$  differences for 3D maps and single-star fits

	G-TOMO v2	G-TOMO v1	StillISM	Bayestar19	Chen+19	StarHorse2021	GSP-Phot	Library
G-TOMO v2	—	0.010	0.014	0.070	0.056	0.055	0.111	0.049
G-TOMO v1	0.010	—	0.016	0.086	0.066	0.058	0.110	0.050
StillISM	0.014	0.016	—	0.059	0.045	0.045	0.087	0.042
Bayestar19	0.070	0.086	0.059	—	0.053	0.050	0.243	0.072
Chen+19	0.056	0.066	0.045	0.053	—	0.064	0.250	0.076
StarHorse2021	0.055	0.058	0.045	0.050	0.064	—	0.105	0.056
GSP-Phot	0.111	0.110	0.087	0.243	0.250	0.105	—	0.169
Library	0.049	0.050	0.042	0.072	0.076	0.056	0.169	—



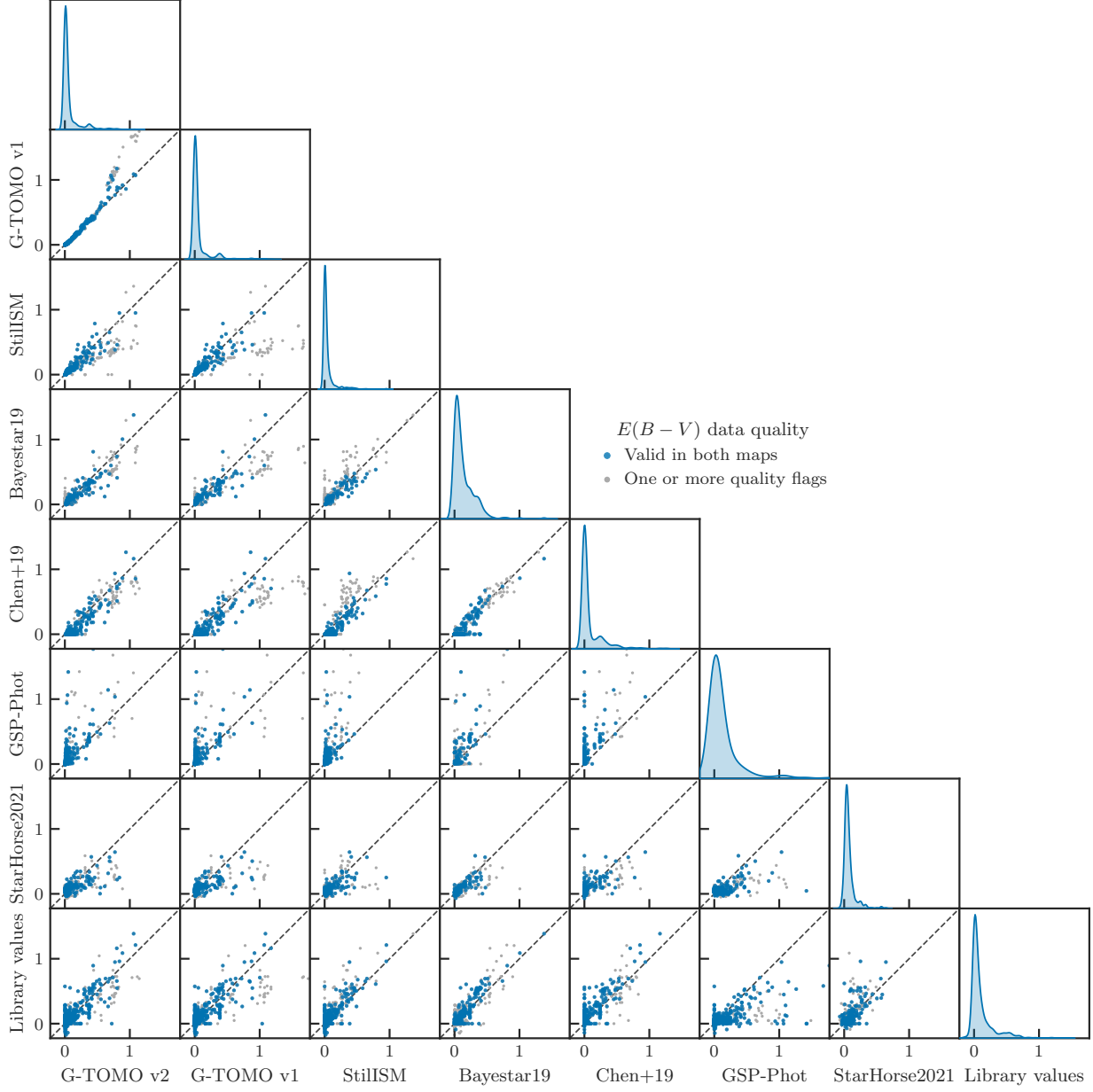


Figure D.1: Pair plots of  $E(B - V)$  measurements for stars common to different extinction catalogs. Stars with high-quality measurements in both  $E(B - V)$  maps per pair are shown by blue points, and stars with data quality flags in one or both maps are shown in light gray. Summary data for individual tables are given in Table D.1, and median absolute deviations of pairwise differences in Table D.2.